BEILSTEIN JOURNAL OF NANOTECHNOLOGY

Radiation-induced nanostructures: Formation processes and applications

Edited by Michael Huth

Imprint

Beilstein Journal of Nanotechnology
www.bjnano.org
ISSN 2190-4286
Email: journals-support@beilstein-institut.de

The *Beilstein Journal of Nanotechnology* is published by the Beilstein-Institut zur Förderung der Chemischen Wissenschaften.

Beilstein-Institut zur Förderung der Chemischen Wissenschaften
Trakehner Straße 7–9
60487 Frankfurt am Main
Germany
www.beilstein-institut.de

Beilstein Journal of Nanotechnology

Radiation-induced nanostructures: Formation processes and applications

Michael Huth

Editorial

Open Access

Address:
Physikalisches Institut, Max-von-Laue-Str. 1, Goethe-Universität, 60438 Frankfurt am Main, Germany

Email:
Michael Huth - michael.huth@physik.uni-frankfurt.de

Keywords:
radiation-induced nanostructures

Beilstein J. Nanotechnol. **2012,** *3,* 533–534.
doi:10.3762/bjnano.3.61

Received: 11 July 2012
Accepted: 13 July 2012
Published: 25 July 2012

This article is part of the Thematic Series "Radiation-induced nanostructures: Formation processes and applications".

Editor-in-Chief: T. Schimmel

Radiation-induced nanostructure formation is ubiquitous. It is routinely used in lithography employing photons and masks, or in the form of focused electron beams following a maskless approach for pattern definition in a radiation-sensitive resist, also commonly known as electron beam lithography. Examples of this are found in this Thematic Series covering the topics of selected-area silicon nanowire growth by the vapor–liquid–solid approach and the preparation of monolayers of metal–organic frameworks attached to the functional groups of a self-assembled monolayer (see, e.g., [1-4]).

Not as wide-spread, but rapidly developing, is the technique of focused electron beam induced deposition (FEBID) [5]. In this technique a previously adsorbed molecular precursor is dissociated by the electron beam, leaving behind a permanent deposit of an amorphous, nanogranular [6,7] or polycrystalline microstructure with a minimum feature size well below 10 nm. Selected aspects of this technique and its application are reviewed in this Thematic Series. In a somewhat analogous fashion, swift heavy ions can be used as nanopore-forming, seeding probes. When passing through thin polymer foils they leave behind a damage track, which can be further processed to form nanopores or nanochannels to be applied in biochemical analytics or as templates for the (galvanic) growth of metallic or semiconducting nanowires, as is also reviewed in one of the following contributions. In close connection to this, highly energetic particles, in particular those from the sun, pose a risk for astronauts as they can induce severe DNA damage upon passing through body tissues. On the other hand, this same observation has led to the rise of charged-particle cancer therapy over the past 20 years.

Conceptually speaking, electrons that locally drive molecular dissociations, as well as swift heavy ions that locally cause damage in polymers or living tissue, define a principle of nanostructure formation by destructive means. But there is a deeper connection on the microscopic level.

In FEBID the dominating contribution to the dissociation yield stems from low-energy electrons in the energy range between a few to several hundred electron volts. Different processes, such as dissociative electron attachment, neutral dissociation or dissociative ionization act together in breaking selected bonds in (mostly) metal–organic precursor molecules. On the other

hand, low-energy electrons also play a role in the radiation damage induced by ionizing radiation in living tissue, which causes different types of DNA damage on bases, as well as single- and double-bond breaks. High-energy particles travel in straight trajectories and have a relatively well-defined stopping point, at which the majority of the energy is deposited. In the tracks, the linear energy transfer, i.e., the rate at which ionization is created along the particle trajectory, can amount to more than 100 keV/µm. Proximal tissue, in contrast, only receives radiation by means of the excited secondary electrons whose trajectories are transverse to the particle track. For the electrons in the low-energy part of the energy spectrum, i.e., below about 5 keV, the biological effectiveness increases strongly. This increased effectiveness indicates a parallel to the FEBID process and points towards an analogous increase in the dissociation cross section at low electron energies.

A full microscopic understanding of the different dissociation pathways and bond-breaking mechanisms would be highly valuable. On the one hand, for FEBID this holds the promise of developing this technique towards electron-controlled chemistry on the nanometer scale. For cancer therapy and the understanding of DNA damage, a deeper insight into the biological effectiveness and long-term risks caused by low-energy electrons could be expected. On the theoretical level, this poses a highly complex problem on multiple scales, ranging from the sub-nanometer to the mesoscopic range, at time scales from femtoseconds to microseconds. This can only be mastered with a broad basis of different experimental and theoretical methods. For the latter, this comprises the development of new theoretical approaches that show reliable scaling behavior, and the application of established state-of-the-art methods for a proper description of the relevant vibronic and electronic degrees of freedom when molecules are organized to form larger complexes.

Research in the fields of FEBID, electron-controlled chemical lithography, radiation biophysics, and nanowires or nanochannels is conducted in a range of different communities. This Thematic Series is intended to provide a forum that brings together selected contributions from these fields. It is hoped that the reader originally interested in only one of the presented topics may be willing to digress a bit from his or her usual main path and take a look into the other research areas. Ultimately, the connections between these fields, as alluded to above, may receive some appreciation and will eventually lead to a mutual reinforcement and fruitful developments.

Michael Huth

Frankfurt, July 2012

References

1. Cohen, S. R.; Sagiv, J. *Beilstein J. Nanotechnol.* **2011,** *2,* 824–825. doi:10.3762/bjnano.2.91
2. Paz, Y. *Beilstein J. Nanotechnol.* **2011,** *2,* 845–861. doi:10.3762/bjnano.2.94
3. Schröter, A.; Kalus, M.; Hartmann, N. *Beilstein J. Nanotechnol.* **2012,** *3,* 65–74. doi:10.3762/bjnano.3.8
4. She, Z.; DiFalco, A.; Hähner, G.; Buck, M. *Beilstein J. Nanotechnol.* **2012,** *3,* 101–113. doi:10.3762/bjnano.3.11
5. Utke, I.; Hoffmann, P.; Melngailis, J. *J. Vac. Sci. Technol. B* **2008,** *26,* 1197–1276. doi:10.1116/1.2955728
6. Porrati, F.; Sachser, R.; Schwalb, C. H.; Frangakis, A. S.; Huth, M. *J. Appl. Phys.* **2011,** *109,* 063715. doi:10.1063/1.3559773
7. Sachser, R.; Porrati, F.; Schwalb, C. H.; Huth, M. *Phys. Rev. Lett.* **2011,** *107,* 206803. doi:10.1103/PhysRevLett.107.206803

License and Terms

Beilstein Journal of Nanotechnology

Directed deposition of silicon nanowires using neopentasilane as precursor and gold as catalyst

Britta Kämpken[1], Verena Wulf[1], Norbert Auner[1], Marcel Winhold[2], Michael Huth[2], Daniel Rhinow[3] and Andreas Terfort[*1]

Full Research Paper

Open Access

Address:
[1]Institute of Inorganic Chemistry, University of Frankfurt, Max-von-Laue-Straße 7, 60438 Frankfurt am Main, Germany, [2]Institute of Physics, University of Frankfurt, Max-von-Laue-Straße 1, 60438 Frankfurt am Main, Germany and [3]Department of Structural Biology, Max Planck Institute of Biophysics, Max-von-Laue-Straße 3, 60438 Frankfurt am Main, Germany

Email:
Andreas Terfort[*] - aterfort@chemie.uni-frankfurt.de

* Corresponding author

Keywords:
chemical vapor deposition; gold; nanoparticle; patterning; radiation-induced nanostructures; vapor-liquid-solid mechanism

Beilstein J. Nanotechnol. **2012,** *3,* 535–545.
doi:10.3762/bjnano.3.62

Received: 30 April 2012
Accepted: 11 July 2012
Published: 25 July 2012

This article is part of the Thematic Series "Radiation-induced nanostructures: Formation processes and applications".

Associate Editor: J. J. Schneider

Abstract

In this work the applicability of neopentasilane ($Si(SiH_3)_4$) as a precursor for the formation of silicon nanowires by using gold nanoparticles as a catalyst has been explored. The growth proceeds via the formation of liquid gold/silicon alloy droplets, which excrete the silicon nanowires upon continued decomposition of the precursor. This mechanism determines the diameter of the Si nanowires. Different sources for the gold nanoparticles have been tested: the spontaneous dewetting of gold films, thermally annealed gold films, deposition of preformed gold nanoparticles, and the use of "liquid bright gold", a material historically used for the gilding of porcelain and glass. The latter does not only form gold nanoparticles when deposited as a thin film and thermally annealed, but can also be patterned by using UV irradiation, providing access to laterally structured layers of silicon nanowires.

Introduction

One of the goals of nanoscience is the development of new materials. Nanowires offer unique insights into low-dimensional physics [1] and could play an important role as building blocks for nanosized devices [2]. Especially semiconducting nanowires can be usefully applied in the fields of biosensors [3] and chemical sensors [4], nanoelectronics [5], photonics [6] and photovoltaics [7]. In this context, it is important to be able to control parameters such as the diameter and length of the nanowires, as well as their localization [8]. Various techniques have been used in order to produce nanosized wires (NW) of silicon including thermal evaporation [9], molecular beam epitaxy [10], laser ablation [11], chemical vapor deposition (CVD) [12] and CVD in combination with the vapor–liquid–solid (VLS) method [13]. In the VLS mechanism, small solid metal particles catalyze the decomposition of the vaporous silicon precursor, forming a liquid Si–metal alloy. As more of the precursor is added to the

system, crystalline silicon NWs are excreted from the alloy due to oversaturation. One effect of this mechanism is that the diameter of the NW is directly correlated to the particle size of the catalytic metal [14].

The most frequently used catalytic metal is gold [15] although other metals are known to catalyze the growth of silicon NWs as well [16-18]. If gold is used as a catalyst, e.g., by deposition of Au nanoparticles on the substrate, the VLS-growth process is reported to start above the eutectic point of the silicon–gold alloy at 363 °C. However, the best results are achieved at temperatures of 450 °C or higher [19]. Typical deposition methods for the metal include sputtering [20], or its adsorption in the form of nanoclusters [21] or nanoparticles [22]. The sputtering process requires no further treatment of the substrate before the VLS process. In contrast to this, organic molecules typically participate in the adsorption process of nanoparticles. Firstly, the nanoparticles themselves are almost always coated with a stabilizer to prevent agglomeration [23]. Secondly, the deposition process of nanoparticles often requires other reagents, e.g., for micelle nanolithography or chemisorption at surface-attached organic monolayers [24,25]. These organic additives (stabilizer/monolayer) might disturb the growth process of the silicon NWs and lead to contaminations, thus they need to be removed after the adsorption step in order to permit the undisturbed growth of silicon NWs. Depending on the nature of the stabilizer as well as the monolayer, positive results have been reported by simple thermolysis [26] or treatment of the substrates with either hydrogen or oxygen plasma [27]. An alternative way to prepare nanoparticles on surfaces was reported by He et al. [28]. They achieved the formation of gold nanoparticles on oxidic substrates by annealing of sputtered gold films. Variation of the thickness of the sputtered layer results in nanoparticles with a variety of sizes. Since the method is also applicable to other metals [29], it could prove to be a versatile way to create well-defined silicon NWs on metal-sputtered surfaces.

For the formation of silicon NWs by the CVD–VLS process, mainly monosilanes such as silane (SiH_4) or tetrachlorosilane ($SiCl_4$) have been used as starting materials due to their low cost and commercial accessibility [30-32]. Of these, silane bears the significant disadvantage of being a highly pyrophoric material, which upon contact with air immediately explodes, thus posing severe danger in the manufacturing process [33,34]. Tetrachlorosilane on the other hand is much safer but requires a reducing agent, such as hydrogen, for the formation of elemental silicon [35]. It also bears the possibility of contaminating the deposited silicon with chlorine atoms, which will significantly change the conduction behavior of the Si NWs. Different precursors such as octachlorotrisilane [36] and disilane [37] have similar properties to their monomeric analogues, although both of these precursors are reported to have an exceptionally high growth rate compared to their analogous monosilanes. This is due to the fact that the dissociation energy of the Si–Si bond is relatively small and can be supplied by thermal activation [38,39].

We herein report the first usage of neopentasilane ($Si(SiH_3)_4$, NPS) as a precursor for the growth of silicon NWs. NPS has a much higher silicon content (92 mass %) than most other silicon precursors. It contains four Si–Si bonds, so high growth rates can be expected [40]. Additionally the molecule contains no chlorine or other potentially contaminating atoms. At room temperature it is a liquid with a reasonable vapor pressure of 20 mbar [41]. In this work, we compare the growth of silicon NWs from NPS using three kinds of gold catalysts: Firstly, sputtered gold films without and with annealing, and secondly, preformed gold nanoparticles chemisorbed wet-chemically onto suitable substrates. Additionally, an unusual gold precursor, “liquid bright gold”, is spin coated onto a substrate and activated by an annealing step. We demonstrate how the different nature of the gold catalyst as well as the deposition temperature (375 versus 650 °C) changes the outcome of the growth. In addition, we will demonstrate that the “liquid bright gold” can be patterned by irradiation with UV light, which in turn results in localized deposition of the silicon NWs.

Results and Discussion

Sputtered gold films as catalyst

The first series of experiments was performed with Si[111] and borosilicate glass substrates. Borosilicate glass was used in this case to prove that the silicon in the grown nanowires originated from the precursor and not from the substrate. A uniform, thin layer of gold was sputtered onto the substrates with a sputtering time of one minute, corresponding to a thickness of about 10 nm. After transfer of these substrates into a tube reactor, NPS was carried into the reactor by a stream of argon.

At a reaction temperature of 375 °C silicon NWs formed within a typical reaction time of 1 h. SEM images of the NWs show a thickness of 1 µm and varying length of up to several 100 µm (Figure 1, left and center).

The NWs do not grow evenly but are buckled in multiple directions, which presumably indicates that the catalytically active gold nanoparticles are of irregular shape and thus excrete the silicon nanowires in different directions. Nevertheless, several single NWs growing in a straight fashion over several hundreds of micrometers on the surface of the NW layer could be observed. The surfaces of the formed NWs are covered with smaller structures indicating that the NWs may still contain

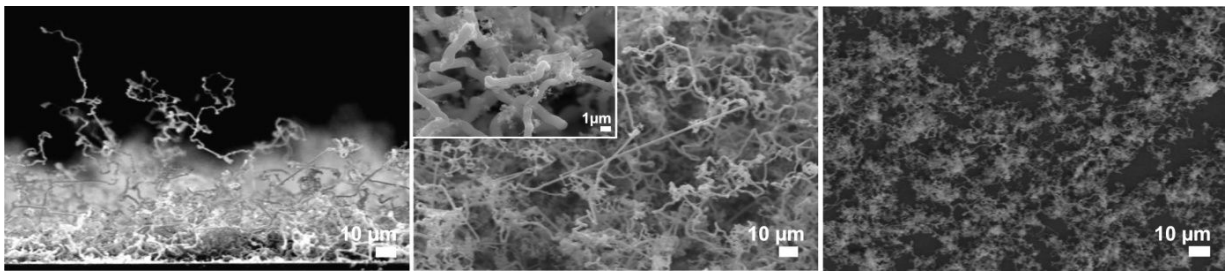

Figure 1: SEM images of NWs grown on gold-sputtered Si[111] exposed to NPS vapor at 375 °C for 1 h (left: side view; center: top view) and 30 min (right: top view). In the insert of the center view, the smaller, branching structures on the NWs become visible.

gold atoms, which catalyze the "branching" (Figure 1, insert in center image). Shortening the reaction time to 30 min resulted in a loosely packed layer of shorter NWs (Figure 1, right). Backscattered-electron images and EDX mapping of the NWs show that their bases as well as their bodies basically consist of pure silicon, whereas their tips are enriched with gold (Figure 2). These findings support the suggested VLS mechanism.

To learn about the structure of the NWs, additional analysis by TEM was carried out. The TEM measurements confirm the buckled structure as well as the branched surface of the NWs (Figure 3, center). The HRTEM measurements show that the NWs are crystalline. The lattice constant of 3.2 Å, which can be seen in the fast Fourier transformed (FFT) image and the selected-area electron diffraction (SAED) pattern, as well as the hexagonal pattern visible in the latter indicate the presence of the cubic Si lattice.

The influence of the gas flow on the nanowire deposition was investigated by varying it between 0.1 and 1.0 L/min. In all cases NW growth was observed. At the lower flow limit, the length and diameter of the individual NWs resembled those of the NWs in the previously mentioned experiments; however,

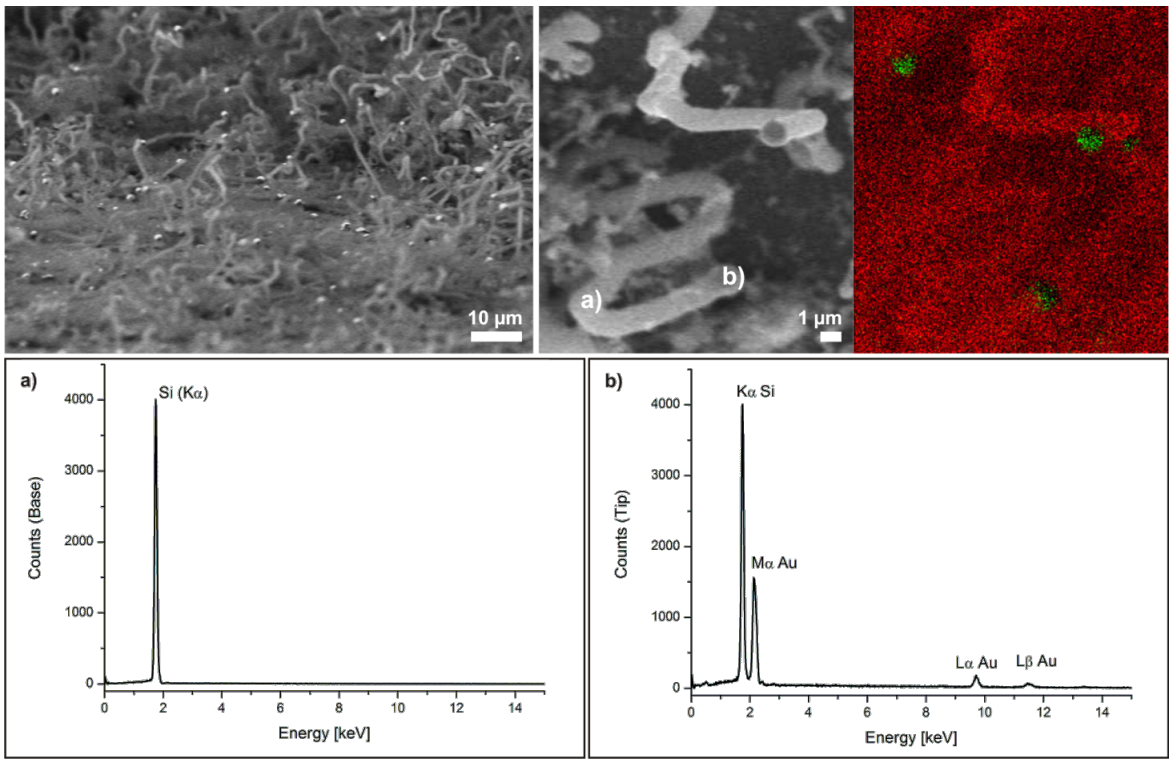

Figure 2: Analysis of NWs grown on gold-sputtered Si[111] for 1 h at 375 °C. Top left: Backscattered-electron image. The bright spots at the tips indicate the presence of a high-*z* material (gold). Top right: Composite EDX mapping image, green = gold, red = silicon. Bottom: EDX spectra obtained (a) at the base, (b) at the tip of the NWs.

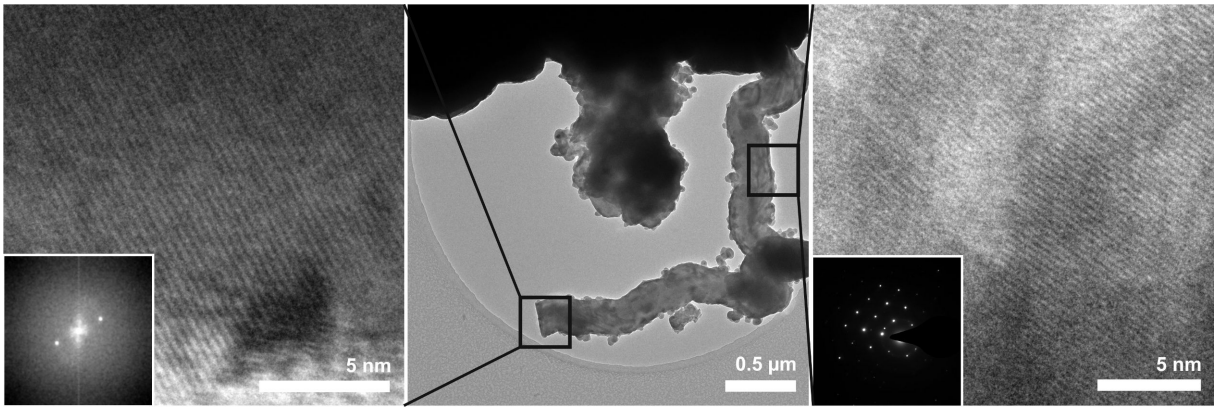

Figure 3: TEM images of NWs grown on gold-sputtered Si[111] for 1 h at 375 °C. The FFT of the HRTEM image and the SAED pattern indicate the crystallinity of the Si NWs.

the substrate was not completely covered with NWs but rather showed only sparsely distributed, small NW islands. These results were similar to the ones obtained with a shortened reaction time and can in both cases be explained by the relatively small amount of precursor being carried into the system. At the upper limit of the gas flow, the NWs grew efficiently, covering most of the substrate. Nevertheless, a large amount of precursor seemed to pass through the system without the formation of Si, since at the exit valve, a white insoluble material formed in copious amounts. On account of these results, all other experiments were carried out with an argon flow that lay well between 1.0 and 0.1 L/min.

The reaction was repeated at 650 °C, but otherwise under the same conditions. SEM measurements of the formed NWs showed similarly shaped growth patterns as for the NWs formed at 375 °C (Figure 4). However, with diameters of about 650 nm, the NWs were slightly thinner than in the previous experiments. One possible reason for this could be that at temperatures as high as 650 °C the sputtered gold layer disrupts to form smaller particles, enhancing the NW growth. Raising of the reaction temperature to as high as 900 °C resulted in the deposition of amorphous silicon throughout the reactor.

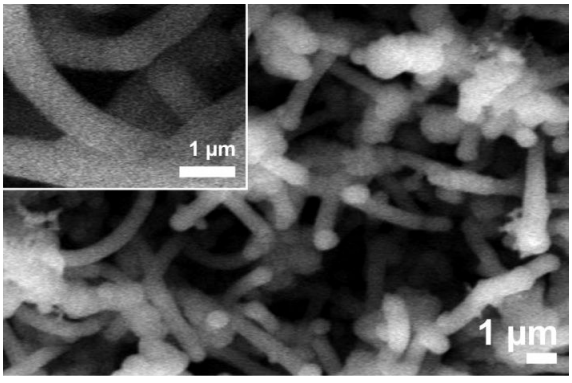

Figure 4: SEM images of NWs grown on gold-sputtered Si[111] by exposure to NPS vapor for 1 h at 650 °C.

Sputtering and in situ formation of nanoparticles by dewetting

To produce more uniform layers of low diameter NWs, the sputtered Au layers were transformed into nanoparticles before the Si deposition. The amount of gold on the substrate surface was controlled by varying the sputtering time to obtain differently sized gold nanoparticles. Sputtering times were 30 s (sample 1), 1 min (sample 2) and 2 min (sample 3). By means of AFM measurements, we determined the deposition rate to be about 10 nm/min.

Upon heating these films to 375 °C no obvious changes occurred, while at 650 °C nanostructures formed within 1 h as a result of a dewetting process [28]. As visible in the SEM images (Figure 5), the size and shape of the nanostructures formed on the three kinds of samples varied considerably. While on samples 1 and 2 separate nanoparticles with diameters of 30–100 nm (sample 1) and 170–300 nm (sample 2) were found, sample 3 rather showed a network of gold after annealing (Figure 5, right).

When these substrates were treated with NPS vapor for 1 h at 650 °C (treatment “a”), the resulting NWs on the three samples also differed in their shapes and diameters. On sample 1a, a dense layer of long NWs with diameters varying between 100 and 200 nm could be observed (Figure 6, left). Again, the NWs were buckled, as in the case of nonannealed Au layers. Additionally, bulkier structures and a few thicker NWs could be observed on the substrate surface. The NWs on sample 2a grew in a more straight fashion with a diameter of 600–700 nm

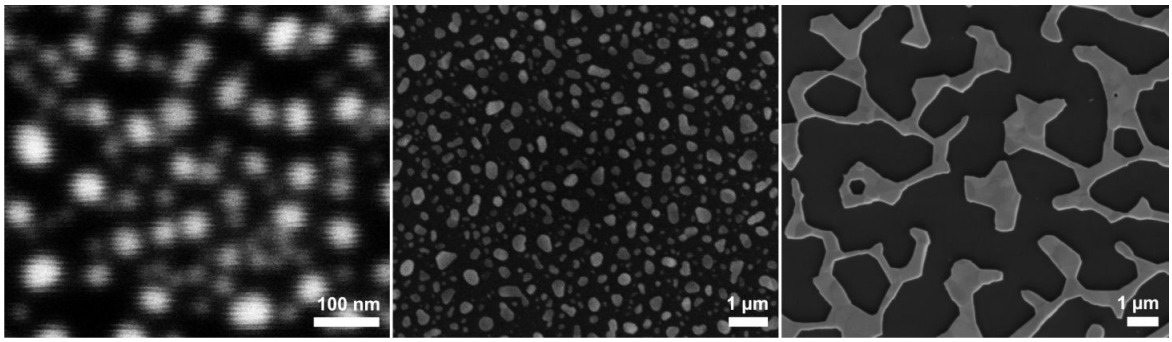

Figure 5: SEM image of gold nanoparticles formed on the native oxide surface of Si[111] after annealing of Au films deposited by sputtering for different lengths of time (left: 30 s; center: 1 min; right: 2 min). The annealing was performed at 650 °C for 1 h.

(Figure 6, center). In both cases the diameters of all NWs were more than twice the size of the nanoparticles. The NWs on sample 3a, on which no nanoparticles had been formed during the annealing step, were even bulkier than the ones on the other samples, with a diameter of around 800 nm or more (Figure 6, right). Remarkably, these NWs showed significant branching.

Since NW growth was achieved at temperatures as low as 375 °C on sputtered surfaces, the NW growth was repeated at this temperature for 1 h (treatment ”b”) by using again gold films previously annealed at 650 °C for 1 h, as described above. SEM measurements showed the growth of NWs with a diameter of 60–100 nm on sample 1b (Figure 7, left). The NWs have a lot of kinks and are clustered together forming a dense layer on the substrate. On sample 2b, the NWs can be seen more clearly (Figure 7, center). Their buckled growth resembles the NW formation on nonannealed substrates, while their diameter is somewhat smaller, between 300 and 500 nm. On sample 3b, the

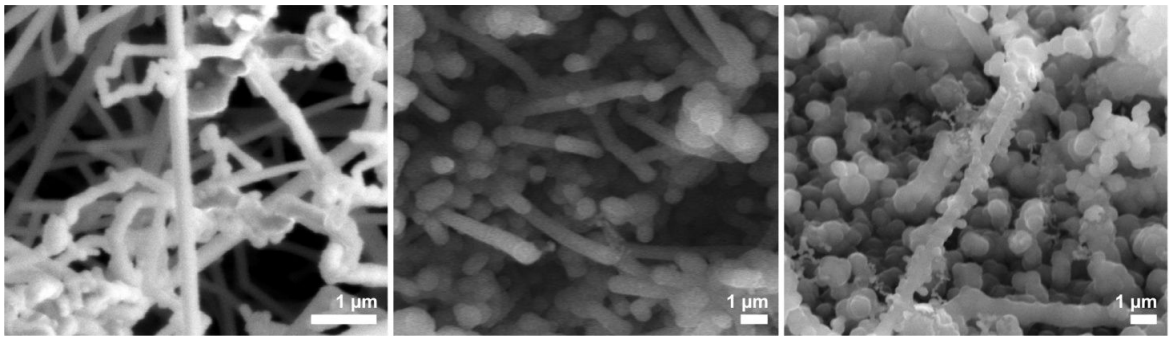

Figure 6: SEM image of NWs grown at 650 °C for 1 h on Si[111] surfaces with annealed gold films (left: sample 1a; center: sample 2a; right: sample 3a).

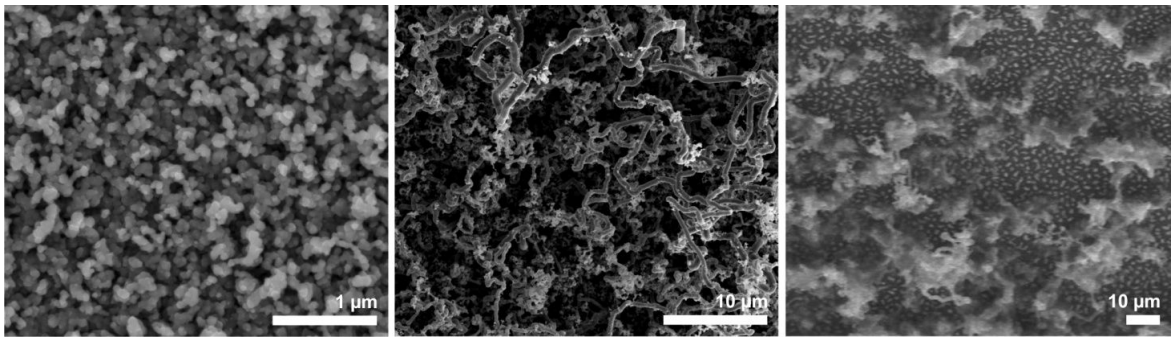

Figure 7: SEM image of NWs grown at 375 °C for 1 h, on annealed gold films of different sputtering times (left: sample 1b; center: sample 2b; right: sample 3b).

networked structure of the annealed gold layer is basically maintained. Structures with a size of several micrometers formed on the surface of the substrate. On top of those formations, agglomerated NWs with a diameter of 1 µm started to grow. In between these structures, the formation of particles with a size of around 500 nm could be observed. These particles contained silicon and a high amount of gold, as determined by EDX measurements. No NW growth could be observed from these particles (Figure 7, right). At both temperatures, the diameter of the NWs exceeded the diameters of the catalytically active nanoparticles. Nevertheless, when the growth was performed at 375 °C, the diameter of the NWs was significantly smaller than the diameter of the NWs grown at 650 °C (Table 1).

We assume that the nanoparticles become larger by taking up the silicon atoms from the precursor, which results in thicker nanowires. At higher temperatures, the alloy can take up more silicon, resulting in even bigger nanoparticles, further increasing the diameter of the extruded NWs.

Deposition of preformed nanoparticles from solution

To decrease the diameter of the NWs, gold nanoparticles with a size of 60 nm were synthesized by following standard protocols [42] and deposited from solution onto Si[111] substrates. For this, the native oxide layer of the silicon wafers was modified by a monolayer of 3-aminopropyl-terminated siloxane [43], the amino groups of which are able to coordinate to the Au nanoparticles. The chemisorption of the nanoparticles proceeded by simple immersion into the respective solution and resulted in surfaces that were evenly, but not closely decorated by the nanoparticles (Figure 8). The average distance between two nanoparticles could be estimated to be about 1 µm.

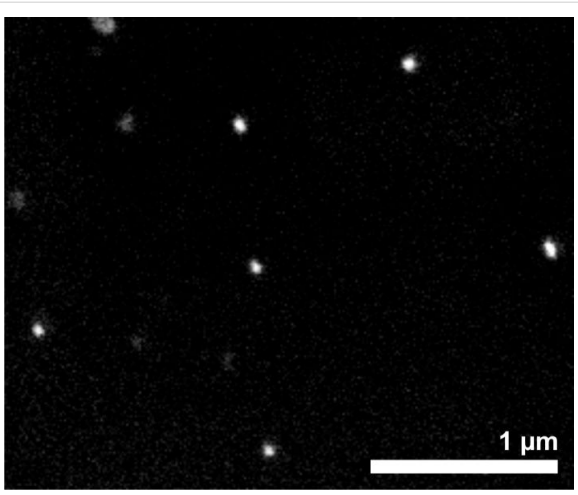

Figure 8: SEM image of the chemisorbed gold nanoparticles on the aminopropylated Si[111] surface.

Using these surfaces without further treatment, no NW growth was observed below 650 °C. At this temperature, NWs with a diameter of less than 100 nm and a length of up to 10 µm formed on the silicon surface (Figure 9, left). We assumed that at this temperature, the organic stabilizers thermally decomposed, making the surface of the nanoparticles accessible for the precursor. To cross-check this hypothesis, we used an alternative, but established protocol [44], i.e., the removal of organic material by a treatment with H_2 plasma prior to NW deposition. Indeed, after this treatment, the formation of NWs with a diameter of 60 nm and a length of up to 10 µm could be observed already at reaction temperatures of 375 °C (Figure 9, right). Due to the relatively large distance between the nanoparticles, the NWs did not form a dense carpet on the substrate, as was the case with the sputtered substrates. The buckling of the NWs even when growing far apart demonstrates that the buckling does not arise from contact/steric hindrance within the more densely packed NW layers. While the images of the two different methods look quite similar at first sight, it should be mentioned that the pretreatment with H_2 plasma and the low temperature seems to avoid the formation of the silicon nanoparticles that can be found in between the NWs on the sample formed at 650 °C.

Nanoparticles from “liquid bright gold” as precursor

One alternative method for the deposition of thin gold films to surfaces is the use of “liquid bright gold”, also called “porcelain gold” or “gold ink”. This material, which is formed by

Table 1: Size distribution of the NWs obtained at different temperatures, grown on sputtered gold films of different thickness that had been annealed at 650 °C before the NW formation.

sample	sputtering time	nanoparticles	NWs at 375 °C	NWs at 650 °C
1	30 sec	30–100 nm	60–100 nm	100–200 nm
2	1 min	170–300 nm	300–500 nm	600–700 nm
3	2 min	—	1000 nm	>800 nm

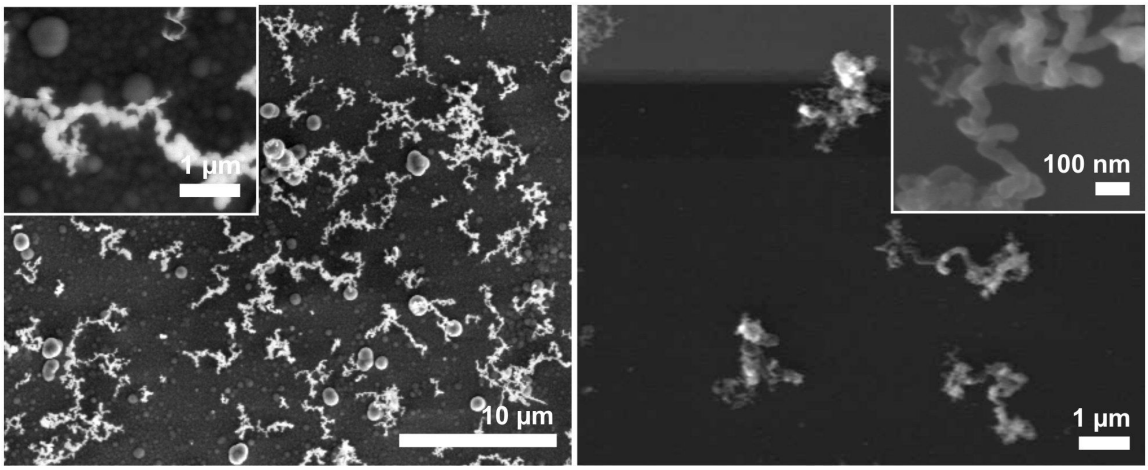

Figure 9: SEM image of NWs grown from nanoparticles at 650 °C without prior treatment (left) and at 375 °C after H_2-plasma treatment for 40 min (right). Observe that at the lower temperature no round Si particles could be found on the sample.

heating gold dust with sulfur and terpenes, was commonly used in the manufacturing and refinement process of porcelain [45]. When the tar-like material is painted onto ceramic surfaces, it can be converted to gold films by simple heating in air. Today it is typically applied by screen printing for the decoration of porcelain and glassware [46].

To obtain thin gold films, commercial Screen Printing Bright-gold 14603 (Surcotech) was diluted with dichloromethane and spin coated onto the native oxide layer of a Si[111] substrate. At 7000 rpm a dense coating was achieved in the form of a sticky film. Annealing of this film at 650 °C for 1 h in the presence of air resulted in dense but inhomogeneous gold particle coverage. Those particles partially resembled the nanoparticle assemblies obtained from the annealing of the sputtered gold films, although their size and shape distribution was much wider (Figure 10, right). Many disruptions as well as areas with more aggregated particles could be found on the substrate surface, which is presumably due to inhomogeneous drying/decomposition of the films during its thermolysis (Figure 10, left and center).

Again, NW growth was achieved by treatment with NPS at different deposition temperatures. At 375 °C NW growth could be observed, but the NWs were less densely packed than in the sputtered cases. In the background small particles could be found, which contained larger amounts of gold as shown by EDX measurements. The NWs were thin with many kinks, growing on the substrate in an insular mode (Figure 11, left). At 650 °C and a deposition time of 1 h the observed NWs seemed to grow in a straighter fashion with a length of several 100 µm and a diameter of around 150 nm. Additionally, smaller-scaled NWs growing in a buckled way could be observed on the substrate (Figure 11, right).

The polymeric nature of “liquid bright gold” offers opportunities for patterning and hence controlling the growth areas of the NWs. One well-established method for the patterned deposition

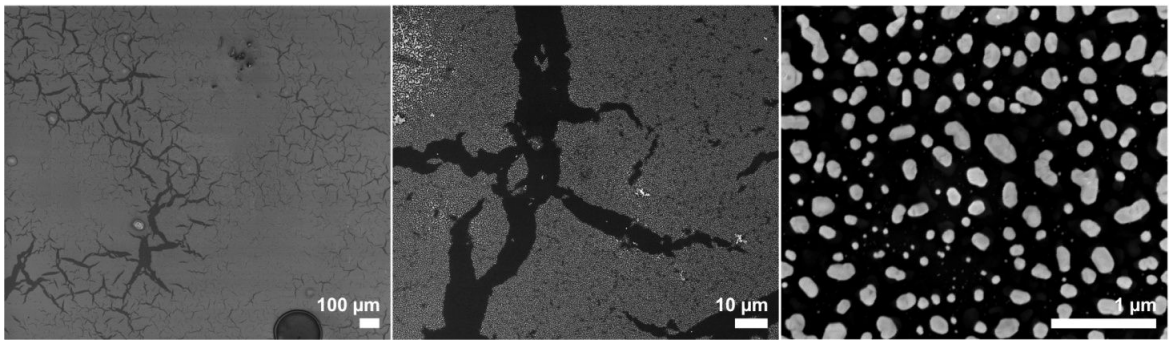

Figure 10: SEM images with different magnifications of a spin coated film of “liquid bright gold” on Si[111] after annealing at 650 °C for 1 h.

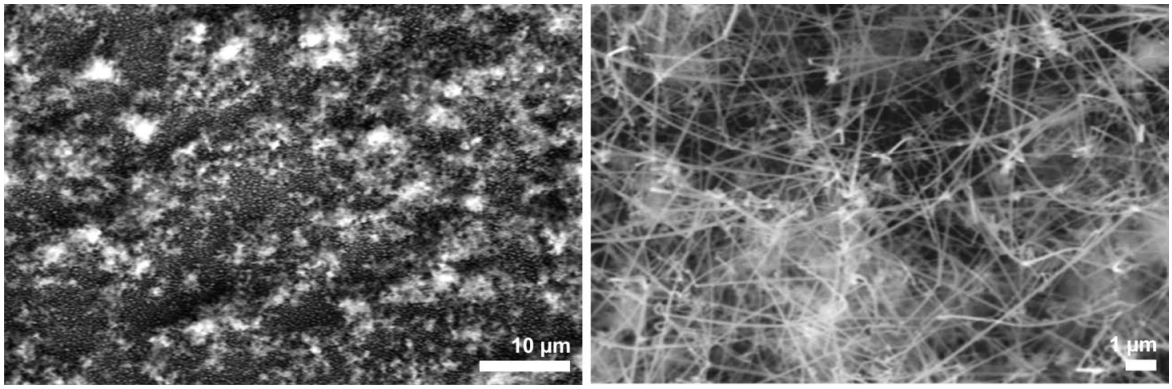

Figure 11: SEM image of Si NWs obtained from spin-coated "liquid bright gold" films after annealing at 650 °C, followed by treatment with NPS at 375 °C (left) and 650 °C (right) for 1 h each.

of polymer films is microcontact printing [47], which is generally considered advantageous since it is an "additive" method. In this particular case the need for dichloromethane or a similar solvent makes this process unsuitable due to the well-known swelling of the stamp material with these solvents [48]. We figured that the gold in these resins might be reducible to the elemental state by irradiation and devised, therefore, a scheme similar to the well-established photolithographic process, which by definition is a "subtractive" one. When a spin-coated layer of the "liquid bright gold" was illuminated with a mercury-vapor lamp through a mask consisting of a metal pattern on a planar quartz substrate, no visible changes took place in the polymer layer. Nevertheless, after washing with dichloromethane, the nonirradiated areas were dissolved, while the irradiated parts of the "liquid bright gold" persisted, reproducing the pattern of the mask (Figure 12, left). Obviously cross-linking occurs during the irradiation, decreasing the solubility of this material (negative photoresist). Annealing of this patterned film for one hour in the presence of air, as described above, left a thin but visible layer of gold with the same pattern (Figure 12, center). The gold-patterned substrates were placed into the reactor and treated with NPS for 1 h at 650 °C (Figure 12, right) and 375 °C. NW growth could be observed in both cases; however, the coverage of the substrate at 375 °C turned out to be not dense enough to form a satisfying pattern (Figure 13).

At a reaction temperature of 650 °C the pattern was much more pronounced. SEM images of the substrate showed that long NWs grew within the previously irradiated areas, similar to those in Figure 11, right. These NWs have a diameter of around 800 nm and grow in a straight fashion over several micrometers (Figure 14). Although the borders of the pattern were relatively sharp, a zone about 100 µm wide could be observed in which the NW growth differed from inner parts of the NW-covered areas. The NWs at the border zone had a diameter of up to 2 µm and grew longer than on the rest of the pattern (Figure 14, left, insert). It remains unclear, why these zones of different morphology are formed in the first place. Currently, investigations are under way to understand this peculiar behavior.

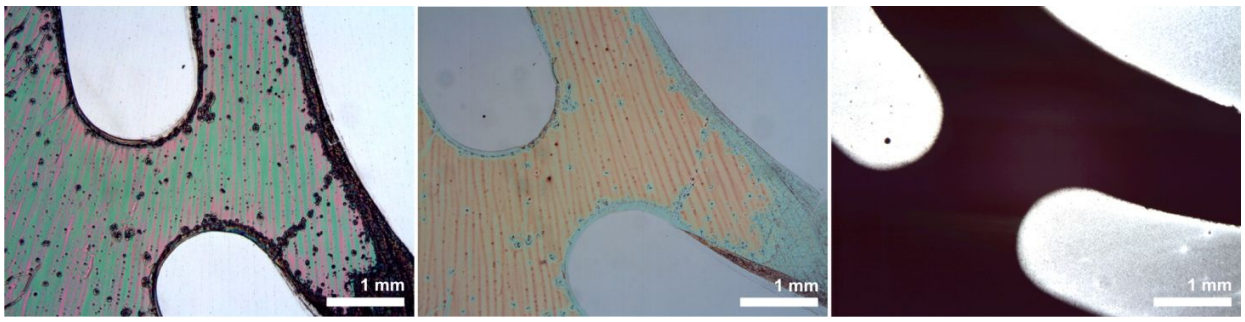

Figure 12: Optical microscopy images of the different steps of the irradiation-induced pattern formation. Left: The "liquid bright gold" film after UV irradiation and washing with dichloromethane. Center: The same area after annealing at 650 °C. Right: The pattern is reproduced after 1 h of treatment with NPS at 650 °C. The bright areas are due to the high reflectivity of the uncovered Si substrate.

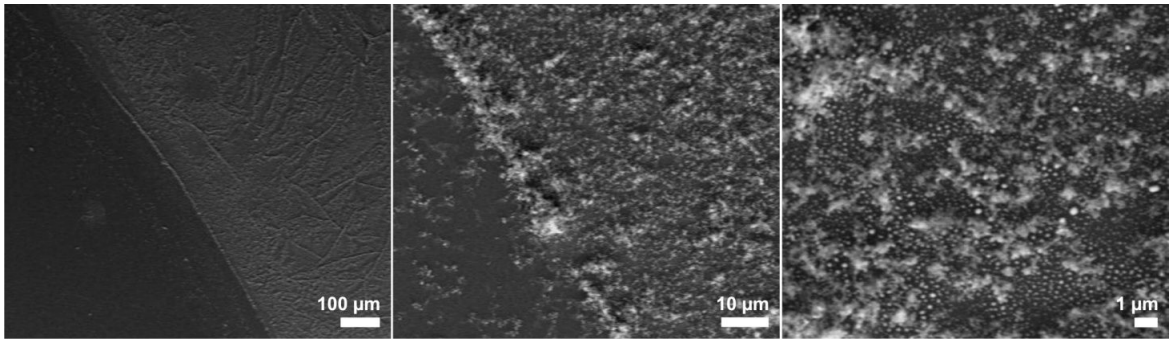

Figure 13: SEM images (different magnifications) of Si NWs obtained from UV-patterned spin-coated "liquid bright gold" films after annealing at 650 °C, followed by treatment with NPS at 375 °C for 1 h.

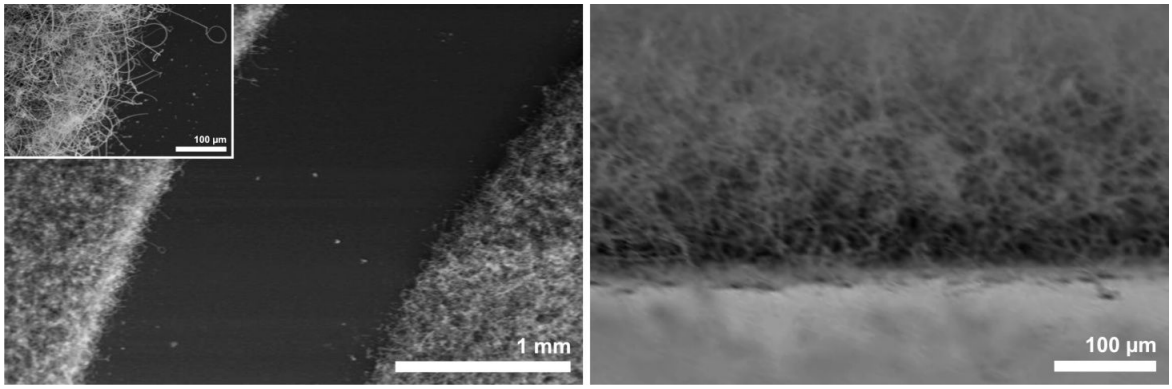

Figure 14: SEM image of the border region of a Si NW pattern obtained from UV-patterned "liquid bright gold" films after annealing at 650 °C, followed by treatment with NPS at 650 °C. Left: Top view, right: Side view.

Conclusion

In this project, we demonstrated that silicon NWs can be reliably prepared from the silicon-rich precursor neopentasilane ($Si(SiH_3)_4$) using gold as catalyst. It could be demonstrated clearly that the formation of the NWs proceeds by the VLS mechanism, in which an Au/Si alloy forms that upon further exposure to the precursor starts excreting the excess silicon in the form of nanowires. The diameter of the nanowires depends on the size of the Au/Si droplets, which in turn can be determined by the size of the employed gold nanoparticles. As a rule of thumb, the diameter of the NWs deposited at 375 °C is about 1.5 times larger than the diameter of the nanoparticles; at 650 °C this factor amounts to ≈2.5, presumably due to the higher solubility of silicon in the Au/Si alloy at higher temperatures.

Following this trend, the thinnest NWs were obtained by using preformed nanoparticles, which became deposited at the substrate surface by chemical means. The fact that the resulting, spatially separated NWs are buckled demonstrates that the shape is not influenced by steric effects but rather by irregularities of the nanoparticles themselves. Furthermore, the nanoparticles had to be deprotected (either by H_2 plasma treatment or thermal decomposition) to achieve the NW formation. No clear trends could be observed yet regarding the length and the shape (straight/buckled) of the NWs.

In extension of this, a rather classical method for the deposition of decorative gold films was modified for the deposition of gold nanoparticles. Upon annealing of spin-coated films of "liquid bright gold" at 650 °C, dense layers of nanoparticles can be easily formed, which serve as efficient catalysts for Si NW production. An interesting extension of this approach is that these films can be cross-linked by UV irradiation, permitting their lateral patterning. These patterns are maintained during the annealing and the Si deposition steps, so that spatially localized Si NW formation can be achieved.

We believe that the combination of using neopentasilane, as a convenient-to-handle Si precursor, with the different possibilities of gold nanoparticle deposition provides a powerful tool for the fabrication of Si NWs for different applications, such as

sensing or photovoltaics. Future work will not only go deeper into determining the guiding principles of NW formation but also in studying the optical and electronic properties of these interesting materials.

Experimental

All substrates were cleaned with freshly prepared Caro's acid (consisting of 3 parts of H_2SO_4 and 1 part of 30% H_2O_2) prior to use. After washing with copious amounts of demineralized water, they were dried in a stream of nitrogen.

Sputtering was carried out for 30 s, 1 min or 2 min by using a Sputter coater S150B from Edwards with argon as the collision gas. For the formation of nanoparticles, the substrates were annealed at 650 °C for 1 h in air. Citrate-stabilized gold nanoparticles were synthesized by the method of Frens [42]. SEM measurements as well as UV–vis spectra [49] indicated a size distribution of around 60 nm. To attach the nanoparticles to the surface, the Si substrates were treated for 2 h with a solution of 10% 3-aminopropyltriethoxysilane in toluene at 100 °C [43]. After washing and sonication of the substrates with ethanol, the nanoparticles were brought to the surface by immersing the aminopropylated substrates into the nanoparticle solution for 90 min. After drying of the substrates in a stream of nitrogen, one group of samples was treated with H_2 plasma for 45 min, while the other group experienced no further treatment.

For the "liquid bright gold" films, 10% solutions of Screen Printing Bright Gold 14603 (Surcotech) in dichloromethane were filtered (0.2 µm) and spin-coated onto the Si wafers at 7000 rpm. To pattern these films, they were irradiated through a mask (a patterned gold film on a quartz plate), which was placed into direct contact with the film. The best results were obtained after 3 h with a medium-pressure mercury-vapor lamp (25 W). To develop the pattern, the films were purged with dichloromethane. Patterned as well as uniform films were then annealed at 650 °C for 1 h in the presence of air to obtain the Au nanoparticle deposits.

NPS was synthesized by following a literature procedure [50]. For the formation of the Si NWs, the substrates were placed in a quartz glass tube (3 cm diameter), which was heated in a tube furnace to the appropriate temperature, in a stream of argon regulated by a pressure control valve. For the deposition, the NPS vapor was carried into the reactor by an argon stream at about 0.5 L/min, by simply bubbling the gas through the liquid while it was kept at 0 °C. The deposition took place at 375 and 650 °C for a typical reaction time of 1 h. Substrates were analyzed by SEM/EDX (Atomica/Amray, 1920 ECO and FEI Nova Nanolab 600), TEM (FEI Tecnai Spirit) and light microscopy (Reichert, Univar) measurements.

Acknowledgements

We want to thank Thalia Vavaleskou and Doris Ceglarek for the SEM and EDX measurements. Financial support by the Beilstein-Institut, Frankfurt/Main, Germany within the research collaboration NanoBiC is gratefully acknowledged.

References

1. Wind, S. J.; Appenzeller, J.; Martel, R.; Derycke, V.; Avouris, P. *Appl. Phys. Lett.* **2002,** *80,* 3817–3819. doi:10.1063/1.1480877
2. Cui, Y.; Lieber, C. M. *Science* **2001,** *291,* 851–853. doi:10.1126/science.291.5505.851
3. Li, Z.; Chen, Y.; Li, X.; Kamins, T. I.; Nauka, K.; Williams, R. S. *Nano Lett.* **2004,** *4,* 245–247. doi:10.1021/nl034958e
4. Cui, Y.; Wei, Q.; Park, H.; Lieber, C. M. *Science* **2001,** *293,* 1289–1292. doi:10.1126/science.1062711
5. Cui, Y.; Zhong, Z.; Wang, D.; Wang, W. U.; Lieber, C. M. *Nano Lett.* **2003,** *3,* 149–152. doi:10.1021/nl025875l
6. Duan, X.; Huang, Y.; Cui, Y.; Wang, J.; Lieber, C. M. *Nature* **2001,** *409,* 66–69. doi:10.1038/35051047
7. Baxter, J. B.; Aydil, E. S. *Appl. Phys. Lett.* **2005,** *86,* 053114. doi:10.1063/1.1861510
8. Qi, P.; Wong, W. S.; Zhao, H.; Wang, D. *Appl. Phys. Lett.* **2008,** *93,* 163101. doi:10.1063/1.2999591
9. Pan, H.; Lim, S.; Poh, C.; Sun, H.; Wu, X.; Feng, Y.; Lin, J. *Nanotechnology* **2005,** *16,* 417–421. doi:10.1088/0957-4484/16/4/014
10. Schubert, L.; Werner, P.; Zakharov, N. D.; Gerth, G.; Kolb, F. M.; Long, L.; Gösele, U.; Tan, T. Y. *Appl. Phys. Lett.* **2004,** *84,* 4968–4970. doi:10.1063/1.1762701
11. Wang, N.; Tang, Y. H.; Zhang, Y. F.; Lee, C. S.; Lee, S. T. *Phys. Rev. B* **1998,** *58,* R16024–R16026. doi:10.1103/PhysRevB.58.R16024
12. Hwang, N. M.; Cheong, W. S.; Yoon, D. Y.; Kim, D.-Y. *J. Cryst. Growth* **2000,** *218,* 33–39. doi:10.1016/S0022-0248(00)00543-1
13. Wagner, R. S.; Ellis, W. C. *Appl. Phys. Lett.* **1964,** *4,* 89–90. doi:10.1063/1.1753975
14. Cui, Y.; Lauhon, L. J.; Gudiksen, M. S.; Wang, J.; Lieber, C. M. *Appl. Phys. Lett.* **2001,** *78,* 2214–2216. doi:10.1063/1.1363692
15. Shao, M.; Ma, D. D. D.; Lee, S.-T. *Eur. J. Inorg. Chem.* **2010,** 4264–4278. doi:10.1002/ejic.201000634
16. Liu, Z. Q.; Zhou, W. Y.; Sun, L. F.; Tang, D. S.; Zou, X. P.; Li, Y. B.; Wang, C. Y.; Wang, G.; Xie, S. S. *Chem. Phys. Lett.* **2001,** *341,* 523–528. doi:10.1016/S0009-2614(01)00513-9
17. Yao, Y.; Fan, S. *Mater. Lett.* **2007,** *61,* 177–181. doi:10.1016/j.matlet.2006.04.045
18. Gu, Q.; Dang, H.; Cao, J.; Zhao, J.; Fan, S. *Appl. Phys. Lett.* **2000,** *76,* 3020–3021. doi:10.1063/1.126565
19. Alet, P.-J.; Yu, L.; Patriarche, G.; Palacin, S.; Cabarrocas, P. R. *J. Mater. Chem.* **2008,** *18,* 5187–5189. doi:10.1039/b813046a
20. Kolb, F. M.; Hofmeister, H.; Scholz, R.; Zacharias, M.; Gösele, U.; Ma, D. D.; Lee, S.-T. *J. Electrochem. Soc.* **2004,** *151,* G472–G475. doi:10.1149/1.1759365
21. Zeng, X. B.; Xu, Y. Y.; Hu, Z. H.; Diao, H. W.; Wang, Y. Q.; Kong, G. L.; Liao, X. B. *J. Cryst. Growth* **2003,** *247,* 13–16. doi:10.1016/S0022-0248(02)01901-2
22. Bandaru, P. R.; Pichanusakorn, P. *Semicond. Sci. Technol.* **2010,** *25,* 024003. doi:10.1088/0268-1242/25/2/024003
23. Ghosh, S. K.; Pal, T. *Chem. Rev.* **2007,** *107,* 4797–4862. doi:10.1021/cr0680282

24. Glass, R.; Möller, M.; Spatz, J. P. *Nanotechnology* **2003,** *14,* 1153–1160. doi:10.1088/0957-4484/14/10/314
25. Taue, S.; Nishida, K.; Sakaue, H.; Takahagi, T. *E-J. Surf. Sci. Nanotechnol.* **2007,** *5,* 74–79. doi:10.1380/ejssnt.2007.74
26. Colli, A.; Hofmann, S.; Fasoli, A.; Farrari, A. C.; Ducati, C.; Dunin-Borkowski, R. E.; Robertson, J. *Appl. Phys. A* **2006,** *85,* 247–253. doi:10.1007/s00339-006-3708-8
27. Mbenkum, B. N.; Schneider, A. S.; Schütz, G.; Xu, C.; Richter, G.; van Aken, P. A.; Majer, G.; Spatz, J. P. *ACS Nano* **2010,** *4,* 1805–1812. doi:10.1021/nn900969y
28. He, J.-Y.; Lu, J.-X.; Dai, N.; Zhu, D.-M. *J. Mater. Sci.* **2012,** *47,* 668–676. doi:10.1007/s10853-011-5837-5
29. Pillai, S.; Catchpole, K. R.; Trupke, T.; Green, M. A. *J. Appl. Phys.* **2007,** *101,* 093105. doi:10.1063/1.2734885
30. Ozaki, N.; Ohno, Y.; Takeda, S. *Appl. Phys. Lett.* **1998,** *73,* 3700–3702. doi:10.1063/1.122868
31. Schmidt, V.; Wittemann, J. V.; Senz, S.; Gösele, U. *Adv. Mater.* **2009,** *21,* 2681–2702. doi:10.1002/adma.200803754
32. Hochbaum, A. I.; Fan, R.; He, R.; Yang, P. *Nano Lett.* **2005,** *5,* 457–460. doi:10.1021/nl047990x
33. Emeléus, H. J.; Steward, K. *J. Chem. Soc.* **1935,** 1182–1189. doi:10.1039/JR9350001182
34. Explosive Silicon Gas Casts Shadow on Solar Power Industry. Scientific American, 2010; http://www.scientificamerican.com/article.cfm?id=explosive-gas-silane-used-to-make-photovoltaics (accessed July 10, 2012).
35. Bloem, J.; Claassen, W. A. P.; Valkenburg, W. G. J. N. *J. Cryst. Growth* **2001,** *57,* 177–184. doi:10.1016/0022-0248(82)90264-0
36. Molnar, W.; Lugstein, A.; Pongratz, P.; Auner, N.; Bauch, C.; Bertagnolli, E. *Nano Lett.* **2010,** *10,* 3957–3961. doi:10.1021/nl101744q
37. Park, W. I.; Zheng, G.; Jiang, X.; Tian, B.; Lieber, C. M. *Nano Lett.* **2008,** *8,* 3004–3009. doi:10.1021/nl802063q
38. Roenigk, K. F.; Jensen, K. F.; Carr, R. W. *J. Phys. Chem.* **1987,** *91,* 5732–5739. doi:10.1021/j100306a043
39. Walsh, R. *Acc. Chem. Res.* **1981,** *14,* 246–252. doi:10.1021/ar00068a004
40. Chung, K. H.; Yao, N.; Benziger, J.; Sturm, J. C.; Singh, K. K.; Carlson, D.; Kuppurao, S. *Appl. Phys. Lett.* **2008,** *92,* 113506. doi:10.1063/1.2897325
41. Chung, K. H. Silicon-Based Epitaxy by Chemical Vapor Deposition Using Novel Precursor Neopentasilane. Ph.D. Thesis, Princeton University, 2010; pp 13–14.
42. Frens, G. *Nature (London), Phys. Sci.* **1973,** *241,* 20–22.
43. Aureau, D.; Varin, Y.; Roodenko, K.; Seitz, O.; Pluchery, O.; Chabal, Y. J. *J. Phys. Chem. C* **2010,** *114,* 14180–14186. doi:10.1021/jp104183m
44. Raiber, K.; Terfort, A.; Benndorf, C.; Krings, N.; Strehblow, H.-H. *Surf. Sci.* **2005,** *595,* 56–63. doi:10.1016/j.susc.2005.07.038
45. Hunt, L. B. *Gold Bull.* **1979,** *12,* 116–127. doi:10.1007/BF03215112
46. Tumanov, S. G. *Glass Ceram.* **1961,** *18,* 297–301. doi:10.1007/BF00668523
47. Xia, Y.; Whitesides, G. M. *Annu. Rev. Mater. Sci.* **1998,** *28,* 153–184. doi:10.1146/annurev.matsci.28.1.153
48. Lee, J. N.; Park, C.; Whitesides, G. M. *Anal. Chem.* **2003,** *75,* 6544–6554. doi:10.1021/ac0346712
49. Haiss, W.; Thanh, N. T. K.; Aveyard, J.; Fernig, D. G. *Anal. Chem.* **2007,** *79,* 4215–4221. doi:10.1021/ac0702084
50. Winhold, M.; Schwalb, C. H.; Porrati, F.; Sachser, R.; Frangakis, A. S.; Kämpken, B.; Terfort, A.; Auner, N.; Huth, M. *ACS Nano* **2011,** *5,* 9675–9681. doi:10.1021/nn203134a

License and Terms

Beilstein Journal of Nanotechnology

Spontaneous dissociation of $Co_2(CO)_8$ and autocatalytic growth of Co on SiO_2: A combined experimental and theoretical investigation

Kaliappan Muthukumar[1], Harald O. Jeschke[1], Roser Valentí[*1], Evgeniya Begun[2], Johannes Schwenk[2,3], Fabrizio Porrati[2] and Michael Huth[*2]

Full Research Paper

Open Access

Address:
[1]Institut für Theoretische Physik, Goethe-Universität, Max-von-Laue-Straße 1, 60438 Frankfurt am Main, Germany, [2]Physikalisches Institut, Goethe-Universität, Max-von-Laue-Straße 1, 60438 Frankfurt am Main, Germany and [3]present address: Empa, CH-8600 Dübendorf, Switzerland

Email:
Roser Valentí[*] - valenti@itp.uni-frankfurt.de; Michael Huth[*] - michael.huth@physik.uni-frankfurt.de

* Corresponding author

Keywords:
$Co_2(CO)_8$; deposition; dissociation; EBID; FEBID; precursor; radiation-induced nanostructures

Beilstein J. Nanotechnol. **2012,** *3,* 546–555.
doi:10.3762/bjnano.3.63

Received: 09 May 2012
Accepted: 02 July 2012
Published: 25 July 2012

This artice is part of the Thematic Series "Radiation-induced nanostructures: Formation processes and applications".

Associate Editor: J. J. Schneider

Abstract

We present experimental results and theoretical simulations of the adsorption behavior of the metal–organic precursor $Co_2(CO)_8$ on SiO_2 surfaces after application of two different pretreatment steps, namely by air plasma cleaning or a focused electron beam pre-irradiation. We observe a spontaneous dissociation of the precursor molecules as well as autodeposition of cobalt on the pretreated SiO_2 surfaces. We also find that the differences in metal content and relative stability of these deposits depend on the pretreatment conditions of the substrate. Transport measurements of these deposits are also presented. We are led to assume that the degree of passivation of the SiO_2 surface by hydroxyl groups is an important controlling factor in the dissociation process. Our calculations of various slab settings, using dispersion-corrected density functional theory, support this assumption. We observe physisorption of the precursor molecule on a fully hydroxylated SiO_2 surface (untreated surface) and chemisorption on a partially hydroxylated SiO_2 surface (pretreated surface) with a spontaneous dissociation of the precursor molecule. In view of these calculations, we discuss the origin of this dissociation and the subsequent autocatalysis.

Introduction

In recent years, focused electron beam induced deposition (FEBID) has emerged as a versatile, high-resolution technique for nanostructure fabrication in contrast to the more conventional nanolithographic techniques. In FEBID, a previously adsorbed precursor gas is dissociated in the focus of an electron beam. The nonvolatile part of the dissociation products remains as a deposit whose shape and position can be accurately controlled by the lateral positioning of the electron beam in an electron microscope [1-5]. Mostly gaseous, e.g., $W(CO)_6$, $Fe(CO)_5$, and $CH_3C_5H_5Pt(CH_3)_3$ [6-9], but also liquid organometallic precursors (chloroplatinic acid) [10] are used to deposit metals or metal composites on selected regions of the substrates. Deposits with a wide spectrum of properties and composition can be consequently obtained due to the availability of suitable precursors [1,2]. $Co_2(CO)_8$ has been recently used as a precursor molecule in FEBID to obtain granular deposits with differing compositions of cobalt [11]. Electronic and physical properties, such as grain size and metal content of these deposits, depend strongly on the deposition and pretreatment conditions of the substrate. By regulating these conditions, deposits of desired size and different Co content can be fabricated [12-15]. For example, granular Co-nanostructures suitable for micro Hall sensing devices [16] were thus obtained. Very recently this precursor has also been used in combination with the precursor $CH_3C_5H_5Pt(CH_3)_3$ to fabricate nanogranular CoPt-C structures with CoPt nanocrystallites having the $L1_0$ crystal structure with hard-magnetic properties [17]. Also, it has been shown that, under well-controlled conditions, Co line structures with a width down to 30 nm are feasible [18,19]. These findings make FEBID with the Co-precursor particularly attractive for the fabrication of micromagnetic structures in the sub-100 nm regime, relevant for studies of the domain wall dynamics [20], the Barkhausen effect in single-domain-wall structures [21] and dipolar coupling effects [22]. While several experimental studies based on infrared spectroscopy [23-26] and theoretical [27-30] studies on $Co_2(CO)_8$ are available in the literature, an issue that remains unclear so far is the possible tendency of this precursor to spontaneously dissociate on SiO_2 surfaces, as well as to autocatalytically grow by spontaneous decomposition on existing Co clusters. Similar features have been reported to be exhibited by $Fe(CO)_5$ [31,32]. In order to evaluate the previous effects in the FEBID process, it is mandatory to acquire an in-depth knowledge of the interactions between the precursor molecule $Co_2(CO)_8$ and SiO_2 surfaces, representing the different pretreatment conditions of the substrate [33].

In the present work, we report on experimental results of Co deposition by spontaneous dissociation of the precursor $Co_2(CO)_8$ on untreated and two differently pretreated SiO_2 surfaces (by an air plasma cleaning process and a pregrowth electron irradiation of selected areas). To our knowledge, no systematic theoretical studies with in-depth DFT calculations on $Co_2(CO)_8$ adsorbed on different SiO_2 surfaces are available. Therefore, we extent the study using density functional theory (DFT) calculations on slabs representing the various SiO_2 surface conditions, and we aim to relate the observations to the plasma and electron irradiation conditions prevailing in FEBID experiments.

Experimental

Cobalt growth and imaging experiments were carried out at room temperature in a dual-beam scanning electron microscope (FEI Nova NanoLab 600) with a Schottky electron emitter. A plasma source using ambient air at a chamber pressure of 1×10^{-4} to 5×10^{-4} mbar was used for the surface-activation experiment (GV10x Downstream Asher, ibss Group). Electron pregrowth irradiation experiments were carried out at 5 kV beam voltage and 1.6 nA beam current. Si(100) (p-doped) substrates with thermal oxide layers of 50 nm up to 285 nm were used. Before use, the substrates were chemically cleaned by acetone, isopropanol and distilled water in an ultrasound bath. In the plasma activation experiments the silica sample surface (285 nm oxide layer) was exposed to the plasma discharge for 75 min after the scanning electron microscope (SEM) chamber had been evacuated to its base pressure of about 5×10^{-6} mbar. After the plasma treatment the chamber was again evacuated to base pressure and Co-precursor flux was admitted to the chamber by opening the valve of a home-made gas injection system for 30 min, causing a pressure increase to 3×10^{-5} mbar, which dropped within ten minutes to about 6×10^{-6} mbar. The gas injection system employs a stainless-steel precursor capsule with a fine-dosage valve. The precursor temperature was set by the ambient conditions to 27 °C. From the known precursor temperature and associated vapor pressure, as well as the geometry of our gas injection system we can roughly estimate the maximum molecular flux at the substrate surface to be 1.4×10^{17} cm^{-2} s^{-1} following [34].

In the second series of experiments the untreated silica surface was pregrowth irradiated with a focused electron beam, which was moved in a raster fashion (dwell time 100 µs, pitch 20 nm) for 30 min over a rectangular region of 3.7×1.0 µm^2 bridging the gap between two prepatterned Cr/Au electrodes. The background pressure during the irradiation process was 6×10^{-6} mbar. Within the 30 min irradiation time about two thousand passes of the rectangular pattern were performed, amounting to an overall dose of 0.78 µC/µm^2. After this treatment the Co-precursor was admitted to the SEM chamber and the current between the electrodes was measured at a fixed bias

voltage of 10 mV as a function of time (see below in Figure 3b). By this method the formation of a conducting path between the metallic electrode can be conveniently followed and gives a first indication of the spontaneous formation of a deposit. After about 20 min the injection was stopped, and the SEM chamber was flushed with dry nitrogen and evacuated again for image acquisition.

Computational details

We performed spin-polarized density functional theory (DFT) calculations within the generalized gradient approximation in the parametrization of Perdew, Burke and Ernzerhof (PBE) [35,36]. Corrections for long-range van der Waals interactions [37,38] were included in all calculations. We worked with a kinetic energy cut-off of 400 eV and relaxed all the ions with the conjugate gradient scheme until the forces were less than 0.01 eV/Å. In order to reproduce the experimental settings, untreated SiO_2 surfaces were described in terms of fully hydroxylated substrates, while pretreated SiO_2 surfaces were described in terms of partially hydroxylated substrates [39-41]. Our (fully and partially hydroxylated) SiO_2 substrates consist of four layers of (3 × 3) supercells of β-cristobalite primitive unit cells. We calculated total energy differences ΔE for substrates, precursor molecules, and the complex of the substrate with adsorbed precursor molecules, as reported previously [9,33] using the projector augmented wave method [42,43] as implemented in the Vienna Ab-initio Simulation Package (VASP) [44-46]. In the geometry optimizations for the molecule and the substrate models the Brillouin zone was sampled at the Γ point only. In addition, to analyze the molecular orbitals, we employed Turbomole 6.0 [47,48] to optimize the $Co_2(CO)_8$ molecule with triple-zeta valence plus polarization basis sets with the PBE functional using the resolution-of-the-identity (RI) approximation. The Bader charge partition analysis was performed by using the code of Henkelman et al. to determine the charges of individual atoms [49,50].

Results and Discussion

Formation of Co from $Co_2(CO)_8$ on pretreated SiO_2 surfaces

In Figure 1a we present an optical micrograph of a spontaneous dissociation product obtained on the plasma pretreated SiO_2 surface. A Co-rich layer of varying thickness has been formed, whose lateral shape clearly depicts the precursor flux profile imposed by the gas injection needle. This profile appears in Figure 1b and is in excellent agreement with simulations of the precursor flux presented in [34]. It should be stressed that no such spontaneous growth was observed on the untreated SiO_2 surface after 30 min exposure to the Co-precursor. Only for extended exposure times (30 min or longer) do we find evidence of the tendency for spontaneous dissociation also on the

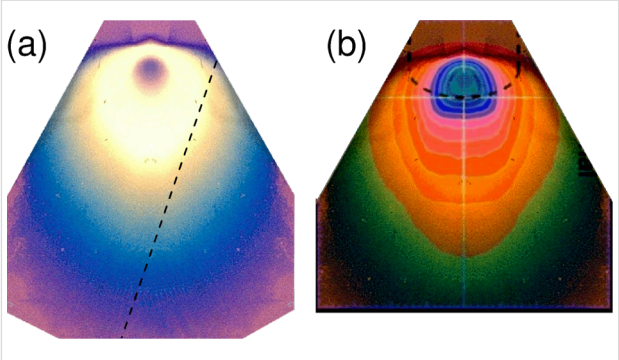

Figure 1: (a) Optical micrograph of the Co dissociation product on the plasma-activated silica surface. The deposit mimics the flux profile set by the gas injection needle. The dashed line represents the rightmost substrate edge. The deposit profile to the right of the dashed line was complemented by image processing from the left side for ease of comparison. (b) Overlay of the calculated precursor flux profile from [34] (contour lines) with the isotropically scaled optical microsocope image of the deposit profile shown in (a).

untreated surfaces. At this stage we are led to assume that the untreated SiO_2 surface, usually hydroxylated after chemical cleaning as performed by us, shows a weak tendency to induce spontaneous dissociation of the Co-precursor. Partial or full removal of the hydroxyl surface passivation layer leads to an increased driving force for dissociation. This will be discussed in more detail in the the next section in which we present results obtained in the framework of DFT calculations concerning the adsorption behavior and stability of the Co-precursor on the SiO_2 surface under different hydroxylation conditions.

In a follow-up experiment, we analyzed the influence of a metallic surface, as provided by Cr/Au (20 nm/80 nm) contact structures, on this spontaneous dissociation process (see Figure 2). Inspection of the surface at various positions on the SiO_2 surface and the Au/Cr contact structures, and after 30 min plasma treatment and 10 min precursor flux exposure reveals clear differences. In regions of maximum precursor flux (see position A in Figure 2) we observe slight differences in the morphology of the formed Co clusters on the electrodes as compared to the growth on the SiO_2 surface. In particular, a reduced average Co grain size and grain density on the Au electrodes is observed. In regions of low precursor flux, only small islands of the dissociation product are visible on the Au contacts, whereas the SiO_2 surface is mostly covered (see region D and E in Figure 2). Evidently, the surface state of the plasma-pretreated SiO_2 surface provides a stronger driving force for the spontaneous precursor dissociation.

We now turn to the results obtained on the SiO_2 surface with selected regions that were pretreated by electron irradiation. In Figure 3a we show the SEM micrograph of a Co-containing deposit obtained in a region in which the electron beam was

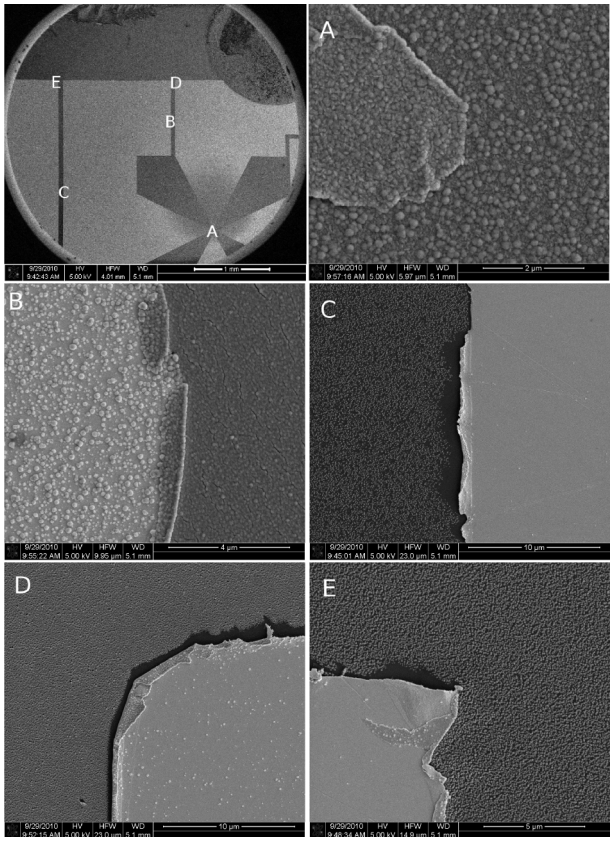

Figure 2: SEM images of Co deposited on the plasma-pretreated silicon oxide and gold. The picture on the top left is an overview of a SiO_2 surface prepatterned with Cr/Au contact structures. The labeling A–E indicates regions of different precursor flux, which was centered at A. The gas injection capillary is visible on the upper right. Gold surfaces appear as bright regions, SiO_2 surfaces as dark regions. Selected area SEM images are represented in images A–E.

rastered over a rectangular area of the SiO_2 surface for 10 min before admission of the precursor for 20 min. As is evident from the figure, a deposit between the Au electrodes was formed, whose outline represents a slightly blurry replica of the previously activated region. According to our Monte Carlo simulations using CASINO V2.42 [51] the extent of the blurred region corresponds roughly to the range of the backscattered electrons. Additional islands of the spontaneous dissociation products are visible away from the pretreated region. The density of these islands drops off to zero over a length scale of about 1 μm.

An energy dispersive X-ray (EDX) analysis of the dissociation products obtained by the plasma activation and pregrowth electron irradiation treatment reveals a Co content of approximately 95 and 76%, respectively. In subsequent resistivity measurements we found a room temperature resistivity of 223 and 480 μΩ·cm, respectively. This is about a factor of 5 larger than the room temperature resistivity found for FEBID-grown Co nanowires employing the same precursor [52,53]. A larger degree of grain boundary scattering in the spontaneously formed deposit, as well as a possibly higher carbon content may be the cause for this enhanced resistivity. We also performed temperature-dependent resistivity measurements (Figure 4a) as well as Hall effect measurements (Figure 4b) for the sample grown on the plasma-activated silica. The samples grown under pre-irradiation conditions are unstable under thermal stress and could not be measured below room temperature. The temperature-dependent resistivity shows a typical metallic behavior as expected for a dirty metal. From the Hall measurement we deduced the saturation magnetization, as indicated in Figure 4b, following established procedures, as detailed in [54].

Structure and bonding of $Co_2(CO)_8$ on SiO_2 surfaces

Structure of the $Co_2(CO)_8$ molecule

The structure of $Co_2(CO)_8$ has been well studied and found to have a distorted $Fe_2(CO)_9$ structure with one bridge carbonyl

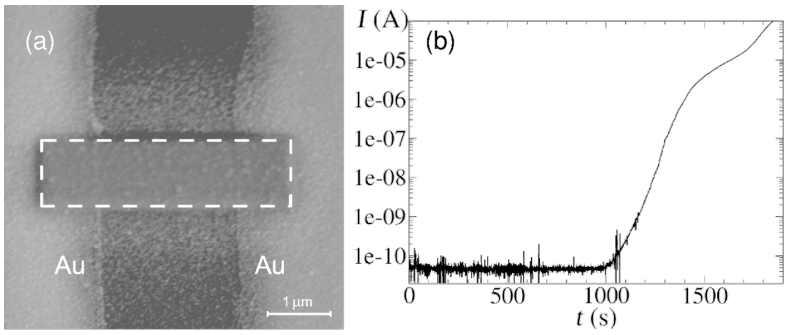

Figure 3: (a) SEM micrograph of Co deposit formed after electron pre-irradiation of the rectangular area depicted by the dashed contour. (b) Time-dependence of the current flow between the Au electrodes at fixed bias voltage (10 mV) as the Co deposit forms spontaneously. The current increase after closing the valve of the gas injector (1200 s) indicates that residual precursor molecules in the SEM vacuum chamber are continuously dissociated resulting in a further increase of the thickness of the Co layer. After exposure of the sample to air the layer thickness was determined by atomic force microscopy and found to be approximately 50 nm.

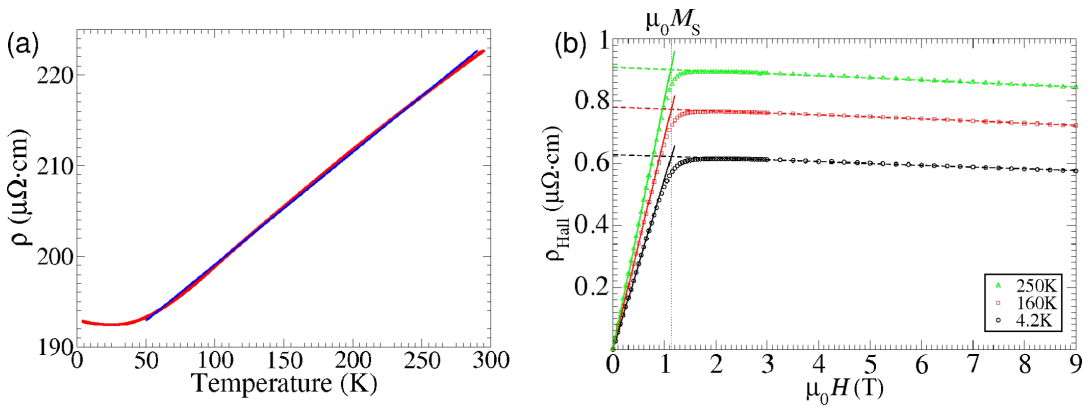

Figure 4: (a) Temperature dependence of resistivity of Co deposit grown on the plasma-activated SiO_2 surfaces. The lateral shape of the deposit for resistivity and Hall effect measurements was defined by a lift-off procedure of a photolithographically defined resist pattern on which the plasma-activated growth had been performed. The deposit height was determined as 55 nm by atomic force microscopy. Blue line: linear fit between 50 and 290 K. (b) Hall resistivity as function of magnetic field, measured at different temperatures as indicated. The saturation magnetization is denoted as $\mu_0 M_S$.

less. Sumner et al. reported a C_s symmetric structure resembling the C_{2v} symmetry (Figure 5a), which was analyzed by DFT calculations [27]. Less stable D_{2d} and D_{3d} isomers that do not have the bridging ligands have also been observed in solution [55-57]. The structural parameters obtained from our DFT studies, such as the distance between the two cobalt atoms (2.52 Å) and the distance to the bridging (1.95 Å) and terminal ligands (1.81 Å) from the metal atom, match the reported values well [58]. Further, we find the D_{3d} symmetric structure to be less stable by 6.9 kcal/mol with respect to the C_{2v} isomer compared to the reported value of 5.8 kcal/mol [27]. Electronic-structure analysis indicates that the highest occupied orbital (HOMO) is dominated by Co 3d orbitals (Figure 5c), and the lowest unoccupied orbital (LUMO) has a significant contribution from the 2p orbitals (Figure 5d) of the carbonyls.

Bonding of $Co_2(CO)_8$ molecules on SiO_2 surfaces

In general, the interaction of metal carbonyls with hydroxylated oxidic surfaces occurs through the coordination of the basic oxygen of the metal carbonyls with the weakly acidic surface hydroxyls. In this study, we consider fully (FOH) and partially hydroxylated (POH) SiO_2 surfaces that directly represent the untreated and pretreated surfaces. For the POH-SiO_2 surfaces three different cases that differ in the degree of hydroxylation,

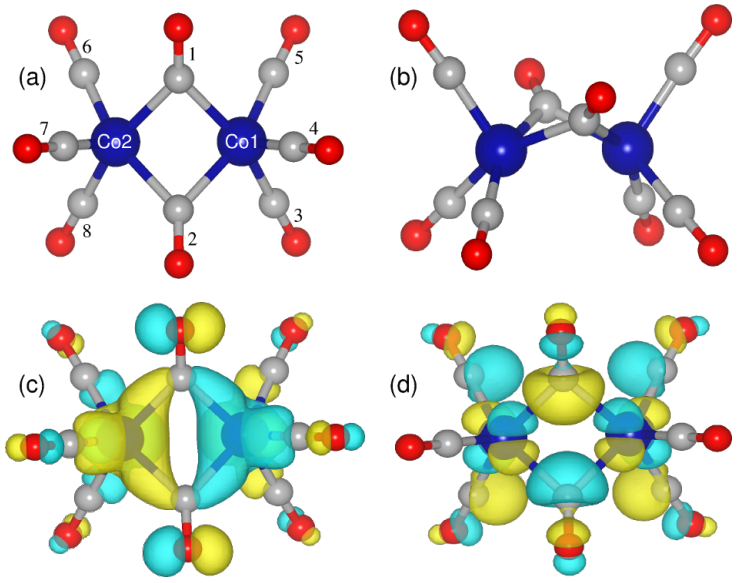

Figure 5: (a) Top and (b) side view of DFT optimized structure of $Co_2(CO)_8$ and its frontier orbitals (c) HOMO and (d) LUMO. Blue, red and grey spheres represent cobalt, oxygen and carbon atoms respectively.

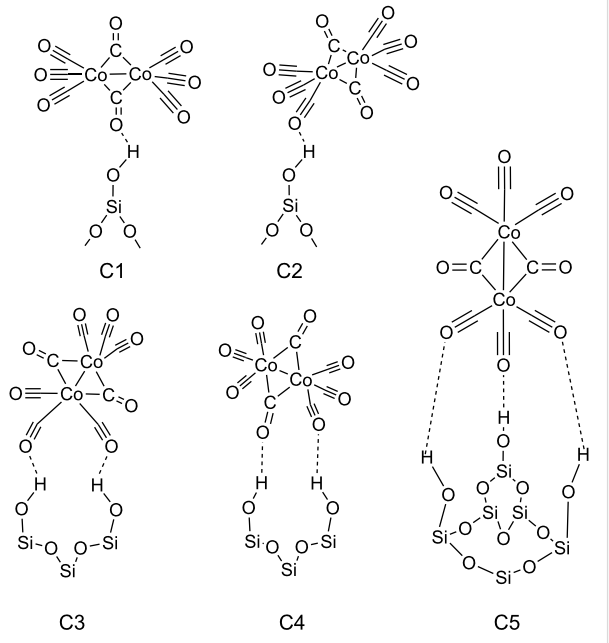

Figure 6: Schematic representation of the starting configurations with possible $Co_2(CO)_8$ orientations, considered in this study, on FOH-SiO_2 surfaces. In POH-SiO_2 surfaces some of the OH groups are partially removed in order to simulate the pretreated surfaces.

corresponding to an OH vacancy concentration of 11, 22 and 33%, were considered depending upon the orientation of $Co_2(CO)_8$ on the surface [33]. In order to have the most stable bonding configuration of $Co_2(CO)_8$ on these FOH-SiO_2 and POH-SiO_2 surfaces, five different orientations (C1 to C5 as shown in Figure 6) were considered. These orientations take into account the possible ways in which the precursor molecule can adsorb on the surface.

The calculated adsorption energies for the different configurations of $Co_2(CO)_8$ on FOH-SiO_2 surfaces range from −0.26 to −0.76 eV (Table 1) illustrating that the precursor molecule

Table 1: Calculated adsorption energies (in eV) of $Co_2(CO)_8$ on SiO_2 surfaces. Configurations marked with an asterisk change as a result of geometry optimization and are discussed in the text.

configuration	FOH-SiO_2	POH-SiO_2
C1	−0.34	−1.69
C2	−0.26	−0.78
C3	−0.47	−2.46*
C4	−0.76*	−3.54*
C5	−0.36	−1.12

binds weakly on these surfaces. Bonding through one of the basic bridging ligands (C1) is preferred compared to bonding with one of the terminal ligands of the molecule (C2). However, an interesting result was obtained when relaxations were started with the C4 configuration, in which case the molecule rearranges in such a way that two of its bridging and terminal ligands are oriented towards the surface (Figure 7a), with distances to the surface of 2.08–2.39 Å. The obtained distances agree well with the recently reported hydrogen-bonding distance of tungsten carbonyls with the SiO_2 substrate [33]. This configuration turns out to be the most stable configuration. The difference in adsorption energy between the C4 configuration and the rest of the configurations ranges between 0.3–0.5 eV. These differences may be small under typical FEBID conditions, in particular if local beam heating has to be taken into account. In this case the molecule is expected to possess random orientations on the fully hydroxylated surface. For the pretreated SiO_2 surfaces a preferential precursor orientation is expected. It was suggested that the weak interaction between the metal carbonyls and the surface OH groups weakens bonding in the molecule [59]. This is not supported by our calculations, which show negligible changes in the Co–Co and Co–CO bonds of the precursor $Co_2(CO)_8$ on the order of 0.01–0.02 Å.

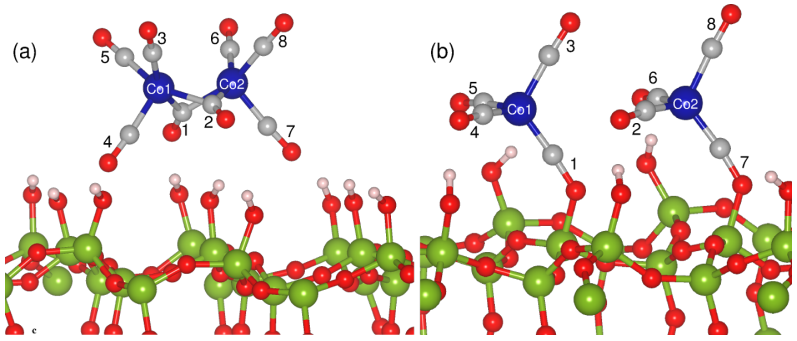

Figure 7: (a) Most stable structure of $Co_2(CO)_8$ on the (a) FOH-SiO_2 and (b) POH-SiO_2 surfaces. The molecule dissociates on the POH surfaces into two $Co(CO)_4$ ions bonding to a terminal Si of the surface. Green, blue, red and grey spheres represent silicon, cobalt, oxygen and carbon atoms, respectively.

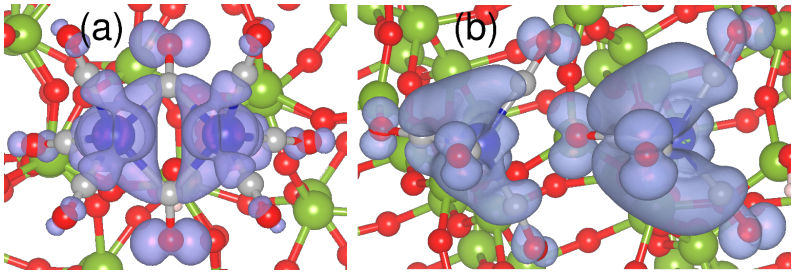

Figure 8: Band decomposed charge density for the valence band maximum for $Co_2(CO)_8$ on the (a) FOH-SiO_2 and (b) POH-SiO_2 surfaces.

In the case of POH-SiO_2 surfaces, adsorption energies are on the order of −0.78 to −3.54 eV indicating that the molecule is bound strongly to these surfaces. The least stable configuration is C2, in which one of the terminal ligands is bonded to the surface Si atoms. The most stable case, with an adsorption energy of −3.54 eV, is obtained when relaxations are started with C4, in which one bridging and one terminal ligand are involved in bonding to the surface. The most interesting observation in this case, is that the $Co_2(CO)_8$ dissociates spontaneously into two $Co(CO)_4$ molecules during geometry optimization (see Figure 7b). This dissociation has also been observed when the molecule interacts with the POH-SiO_2 surface with two terminal ligands (C3), and has not been observed when the molecule binds either with one bridging or one terminal oxygen (C1, C2). Although one may expect a fragmentation of a Co–C bond to be similar to the W–C bond breaking in $W(CO)_6$ [33], the dissociation of $Co_2(CO)_8$ occurs by breaking of the Co–Co bonds. We will discuss this process in the next section.

The above results are in agreement with our experimental observations that the precursor molecules dissociate much more easily on the pretreated surfaces, as discussed in the previous section. In earlier experiments it was found that the decomposition of $Co_2(CO)_8$ depends on the different number of surface hydroxyls on the SiO_2 substrates [23,60]. Although our calculations confirm that the molecule behaves differently on FOH-SiO_2 and POH-SiO_2 surfaces, we would like to note that the dissociation also depends on the orientation of the molecules. For example, on the POH-SiO_2 surface the dissociation is observed only in two cases, i.e, when $Co_2(CO)_8$ is oriented in such a way that it bonds through one terminal and one bridging ligand, and when it is bonded through two terminal ligands. In particular, we did not observe any dissociation in C1, which has been believed to be the prominent mode of interaction with the weakly acidic hydroxylated surfaces in previous studies [59,61]. However, our results have been obtained by relaxing the initially prepared configurations to $T = 0$ directly; further studies on the thermal stability of $Co_2(CO)_8$ on POH-SiO_2 in C1, C2, and C5 configurations are required. Moreover, the calculated charge density for the highest occupied valence band of $Co_2(CO)_8$ adsorbed on FOH-SiO_2 and POH-SiO_2 confirms that the molecule retains its character on FOH-SiO_2 (compare Figure 5c and Figure 8a), but is strongly altered on the POH-SiO_2 surfaces (compare Figure 5c and Figure 8b).

Discussion on the dissociation and autocatalytic deposition of $Co_2(CO)_8$ precursor on SiO_2 surface

In view of the results presented in the previous section, we will discuss here the possible reasons for dissociation and autocatalytic deposition of $Co_2(CO)_8$ molecules on SiO_2 surfaces. The bridging CO ligands of $Co_2(CO)_8$ possess, in the free molecule, relatively higher electron density compared to the terminal ligands (Table 2, second column) and therefore are expected to be the ligands that preferentially interact with the dehydroxylated Si sites on the POH-SiO_2 surface. Our results illustrate that, while the adsorption through the bridging ligands is essential, the terminal ligands are also involved in bonding to both FOH-SiO_2 and POH-SiO_2 surfaces. Let us focus now on the dissociation process of $Co_2(CO)_8$ on the POH-SiO_2 surface,

Table 2: Calculated Bader charges for $Co_2(CO)_8$ in units of electrons in the gas phase and for the adsorbate on SiO_2 surfaces. The numbers in parenthesis identify the CO ligand as shown in Figure 5a and Figure 7. Values indicated by an asterisk correspond to the total charge of the $Co(CO)_4$ fragments

case	gas-phase	FOH-SiO_2	POH-SiO_2
CO(1)	−0.29	−0.24	−0.78
CO(2)	−0.29	−0.26	−0.24
CO(3)	−0.14	−0.09	−0.16
CO(4)	−0.14	−0.11	−0.22
CO(5)	−0.15	−0.06	−0.21
CO(6)	−0.15	−0.10	−0.23
CO(7)	−0.15	−0.12	−0.76
CO(8)	−0.16	−0.10	–0.15
Co1	+0.74	+0.55	+0.54
Co2	+0.74	+0.55	+0.54
total	+0.01	+0.02	(−0.83/−0.84)*

resulting in the formation of $Co(CO)_4$ subcarbonyl motifs. The interaction between the CO ligands of the molecule precursor and the dehydroxylated Si sites of the surface alters the electronic distribution on the precursor molecule as well as its geometry. The changes in the electronic distribution are verified by the computed Bader charges on the CO ligands (Table 2, second and fourth columns) as well as on the Co atoms, in which the charge changes from +0.74 electrons in the free molecule to +0.54 electrons upon adsorption. This electronic change is accompanied by a structural change. The bond between C and O in the bridging CO ligand weakens (it elongates from 1.16 Å in the free molecule to 1.25 Å in the adsorbate) and the Co–C bond strengthens (it shortens from 1.95 Å in the free molecule to 1.66 Å in the adsorbate). Further, the bond angle (Co–C=O) in the bridging ligands changes from 140 to 174°. In addition, the surface Si atoms acquire a more positive character (the charge increases from +2.35 to +3.2 electrons) illustrating that this transfer of nearly one electron each from the two terminal Si sites on to the $Co_2(CO)_8$ molecule plays a crucial role in the fragmentation process. This accumulation of additional electron density on the individual Co atoms should weaken the bonding between the two Co atoms in the precursor. These effects, such as the strong bond (Si–CO) formation followed by the electronic redistribution in the precursor molecule, are further assisted by the interaction of the terminal carbonyl (see C4 in Figure 6) with the surface sites, which cleaves the molecules into two $Co(CO)_4$ fragments.

In contrast, $Co_2(CO)_8$ binds weakly on the FOH-SiO_2 surface compared to POH-SiO_2 (see Table 1) and it retains a similar character to that of the free molecule (compare Figure 5a and Figure 8a). Analysis of the charges on the CO ligands (Table 2, second and third columns) confirm this observation. Nevertheless, the formation of hydrogen bonds with surface hydroxyls leads to some charge redistribution within the adsorbed molecule, resulting in a reduction of positive charge from +0.74 to +0.55 on Co. Also, we find minimal differences in structural parameters (on the order of 0.01 Å).

The above observations illustrate the fact that the weak interaction between molecule and surface will not cause dissociation of the precursor. However, we would like to note that we have observed spontaneous dissociation of $Co_2(CO)_8$ in our experiments after extended exposure of the precursor flux (30 min or more). The spontaneous dissociation under long-time exposure is likely just a sign of the instability of the molecule which dissociates under CO release over the intermediate $Co_4(CO)_{12}$ at 52 °C. At lower temperature some degree of this dissociation will already be observable, in particular if there is no stabilizing CO atmosphere, such as is the case in a SEM vacuum chamber. (Moreover, the reduced neighbor coordination of the adsorbed molecules as compared to the bulk solid may speed up the dissociation process.)

In summary, our calculations confirm that $Co_2(CO)_8$ decomposes upon its interaction with POH-SiO_2 surfaces, illustrating what may be the first step occurring in this deposition process. Furthermore, $Co_2(CO)_8$ molecules possess the capability to deposit autocatalytically as a result of spontaneous dissociation. At present it is unclear how to rationalize this autocatalysis, and a detailed study based on molecular dynamic simulations is in progress but beyond the scope of the present work. We expect that the total charge on the fragmented species of $Co_2(CO)_8$ is among the important factors that cause autocatalytic deposition. In our calculations, these fragments possess a net charge of −0.84 electrons. This charge is expected to play a similar role as the surface Si atoms on the POH-SiO_2 surface, namely, it activates the approaching molecule and triggers the autocatalytic process. This indeed accounts for the fact that, in our experimental observations, the deposition occurs immediately on the pretreated surface, on which the fragments are formed as soon as the precursor flux is in contact with the POH-SiO_2 surface, and with a slight delay on the FOH-SiO_2 surface. However, this needs to be confirmed with theoretical simulations and remains as an open question that will be addressed in our future studies.

Conclusion

We report here the deposition of Co from the precursor $Co_2(CO)_8$ on two different pretreated SiO_2 surfaces, and our results provide an in-depth understanding of preliminary interactions and evidence for the spontaneous dissociation. Our observations suggest an activation of silica surfaces, which is also effective, although to a lesser degree, on Au layers. In view of the fact that no such spontaneous dissociation effects on Si substrates with a very thin native oxide layer have been reported in previous works [13,18], we are led to assume that this surface activation process depends on both a modified surface termination and trapped charges. Presently it is not clear whether the activation process observed on silica layers under ultrahigh vacuum conditions in conjunction with the precursor $Fe(CO)_5$ [31] is also at work here. Further, we have also performed DFT calculations for this deposition process considering various slab settings, and we find that the extent of surface hydroxylation and the orientation of the precursor plays a vital role in the dissociation and the formation of the nanocomposites. The so-formed sub-carbonyl motifs during the FEBID process may be the true precursor for the Co-rich nanocomposite formation.

Acknowledgements

The authors would like to thank M. U. Schmidt and M. A. Señaris-Rodríguez for useful discussions and gratefully acknowledge financial support by the Beilstein-Institut,

Frankfurt/Main, Germany, within the research collaboration NanoBiC as well as by the Alliance Program of the Helmholtz Association (HA216/EMMI). The generous allotment of computer time by CSC-Frankfurt and LOEWE-CSC is gratefully acknowledged.

References

1. Utke, I.; Hoffmann, P.; Melngailis, J. *J. Vac. Sci. Technol., B* **2008,** *26,* 1197–1276. doi:10.1116/1.2955728
2. Wnuk, J. D.; Rosenberg, S. G.; Gorham, J. M.; van Dorp, W. F.; Hagen, C. W.; Fairbrother, D. H. *Surf. Sci.* **2011,** *605,* 257–266. doi:10.1016/j.susc.2010.10.035
3. Utke, I.; Gölzhäuser, A. *Angew. Chem., Int. Ed.* **2010,** *49,* 9328–9330. doi:10.1002/anie.201002677
4. Randolph, S. J.; Fowlkes, J. D.; Rack, P. D. *Crit. Rev. Solid State Mater. Sci.* **2006,** *31,* 55–89. doi:10.1080/10408430600930438
5. Silvis-Cividjian, N.; Hagen, C. W.; Kruit, P. *J. Appl. Phys.* **2005,** *98,* 084905. doi:10.1063/1.2085307
6. Porrati, F.; Sachser, R.; Huth, M. *Nanotechnology* **2009,** *20,* 195301. doi:10.1088/0957-4484/20/19/195301
7. Porrati, F.; Sachser, R.; Schwalb, C. H.; Frangakis, A. S.; Huth, M. *J. Appl. Phys.* **2011,** *109,* 063715. doi:10.1063/1.3559773
8. Huth, M.; Klingenberger, D.; Grimm, C.; Porrati, F.; Sachser, R. *New J. Phys.* **2009,** *11,* 033032. doi:10.1088/1367-2630/11/3/033032
9. Shen, J.; Muthukumar, K.; Jeschke, H. O.; Valentí, R. *New J. Phys.* submitted.
10. Donev, E. U.; Hastings, J. T. *Nano Lett.* **2009,** *9,* 2715–2718. doi:10.1021/nl9012216
11. Botman, A.; Mulders, J. J. L.; Hagen, C. W. *Nanotechnology* **2009,** *20,* 372001. doi:10.1088/0957-4484/20/37/372001
12. Lau, Y. M.; Chee, P. C.; Thong, J. T. L.; Ng, V. *J. Vac. Sci. Technol., A* **2002,** *20,* 1295–1302. doi:10.1116/1.1481040
13. Fernández-Pacheco, A.; De Teresa, J. M.; Szkudlarek, A.; Córdoba, R.; Ibarra, M. R.; Petit, D.; O'Brien, L.; Zeng, H. T.; Lewis, E. R.; Read, D. E.; Cowburn, R. P. *Nanotechnology* **2009,** *20,* 475704. doi:10.1088/0957-4484/20/47/475704
14. Bernau, L.; Gabureac, M.; Erni, R.; Utke, I. *Angew. Chem., Int. Ed.* **2010,** *49,* 8880–8884. doi:10.1002/anie.201004220
15. Utke, I.; Bret, T.; Laub, D.; Buffat, P.; Scandella, L.; Hoffmann, P. *Microelectron. Eng.* **2004,** *73–74,* 553–558. doi:10.1016/j.mee.2004.02.084
16. Gabureac, M.; Bernau, L.; Utke, I.; Boero, G. *Nanotechnology* **2010,** *21,* 115503. doi:10.1088/0957-4484/21/11/115503
17. Porrati, F.; Begun, E.; Winhold, M.; Schwalb, C. H.; Sachser, R.; Frangakis, A. S.; Huth, M. *Nanotechnology* **2012,** *23,* 185702. doi:10.1088/0957-4484/23/18/185702
18. Serrano-Ramón, L.; Córdoba, R.; Rodrírguez, L. A.; Magén, C.; Snoeck, E.; Gatel, C.; Serrano, I.; Ibarra, M. R.; De Teresa, J. M. *ACS Nano* **2011,** *5,* 7781–7787. doi:10.1021/nn201517r
19. Nikulina, E.; Idigoras, O.; Vavassori, P.; Chuvilin, A.; Berger, A. *Appl. Phys. Lett.* **2012,** *100,* 142401. doi:10.1063/1.3701153
20. Fernández-Pacheco, A.; De Teresa, J. M.; Córdoba, R.; Ibarra, M. R.; Petit, D.; Read, D. E.; O'Brien, L.; Lewis, E. R.; Zeng, H. T.; Cowburn, R. P. *Appl. Phys. Lett.* **2009,** *94,* 192509. doi:10.1063/1.3139068
21. Das, P.; Porrati, F.; Wirth, S.; Bajpai, A.; Huth, M.; Ohno, Y.; Ohno, H.; Müller, J. *Appl. Phys. Lett.* **2010,** *97,* 042507. doi:10.1063/1.3467870
22. Porrati, F.; Huth, M. *Appl. Phys. Lett.* **2004,** *85,* 3157–3159. doi:10.1063/1.1805697
23. Suvanto, S.; Pakkanen, T. A.; Backman, L. *Appl. Catal., A: Gen.* **1999,** *177,* 25–36. doi:10.1016/S0926-860X(98)00253-1
24. Schneider, R. L.; Howe, R. F.; Watters, K. L. *Inorg. Chem.* **1984,** *23,* 4593–4599. doi:10.1021/ic00194a038
25. Rao, K. M.; Spoto, G.; Guglielminotti, E.; Zecchina, A. *J. Chem. Soc., Faraday Trans. 1* **1988,** *84,* 2195–2207. doi:10.1039/F19888402195
26. Rao, K.; Spoto, G.; Zecchina, A. *J. Catal.* **1988,** *113,* 466–474. doi:10.1016/0021-9517(88)90272-2
27. Aullón, G.; Alvarez, S. *Eur. J. Inorg. Chem.* **2001,** 3031–3038. doi:10.1002/1099-0682(200112)2001:12<3031::AID-EJIC3031>3.0.CO;2-D
28. Suvanto, S.; Hirva, P.; Pakkanen, T. *Surf. Sci.* **2000,** *465,* 277–285. doi:10.1016/S0039-6028(00)00713-5
29. Barckholtz, T. A.; Bursten, B. E. *J. Organomet. Chem.* **2000,** *596,* 212–220. doi:10.1016/S0022-328X(99)00696-8
30. Ryeng, H.; Gropen, O.; Swang, O. *J. Phys. Chem. A* **1997,** *101,* 8956–8958. doi:10.1021/jp9728565
31. Walz, M.-M.; Schirmer, M.; Vollnhals, F.; Lukasczyk, T.; Steinrück, H.-P.; Marbach, H. *Angew. Chem., Int. Ed.* **2010,** *49,* 4669–4673. doi:10.1002/anie.201001308 *Angew. Chem.*, **2010,** *122,* 4774–4778. doi:10.1002/ange.201001308
32. Hochleitner, G.; Wanzenboeck, H. D.; Bertagnolli, E. *J. Vac. Sci. Technol., B* **2008,** *26,* 939–944. doi:10.1116/1.2907781
33. Muthukumar, K.; Opahle, I.; Shen, J.; Jeschke, H. O.; Valentí, R. *Phys. Rev. B* **2011,** *84,* 205442. doi:10.1103/PhysRevB.84.205442
34. Friedli, V.; Utke, I. *J. Phys. D: Appl. Phys.* **2009,** *42,* 125305. doi:10.1088/0022-3727/42/12/125305
35. Perdew, J. P.; Burke, K.; Ernzerhof, M. *Phys. Rev. Lett.* **1996,** *77,* 3865–3868. doi:10.1103/PhysRevLett.77.3865
36. Perdew, J. P.; Burke, K.; Ernzerhof, M. *Phys. Rev. Lett.* **1997,** *78,* 1396. doi:10.1103/PhysRevLett.78.1396
37. Grimme, S. *J. Comput. Chem.* **2006,** *27,* 1787–1799. doi:10.1002/jcc.20495
38. Wu, X.; Vargas, M. C.; Nayak, S.; Lotrich, V.; Scoles, G. *J. Chem. Phys.* **2001,** *115,* 8748–8757. doi:10.1063/1.1412004
39. Mens, A. J. M.; Gijzeman, O. L. J. *Appl. Surf. Sci.* **1996,** *99,* 133–143. doi:10.1016/0169-4332(95)00603-6
40. Idriss, H.; Barteau, M. A. *Catal. Lett.* **1994,** *26,* 123–139. doi:10.1007/BF00824038
41. Göpel, W.; Anderson, J. A.; Frankel, D.; Jaehnig, M.; Phillips, K.; Schäfer, J. A.; Rocker, G. *Surf. Sci.* **1984,** *139,* 333–346. doi:10.1016/0039-6028(84)90054-2
42. Kresse, G.; Joubert, D. *Phys. Rev. B* **1999,** *59,* 1758–1775. doi:10.1103/PhysRevB.59.1758
43. Blöchl, P. E. *Phys. Rev. B* **1994,** *50,* 17953–17979. doi:10.1103/PhysRevB.50.17953
44. Kresse, G.; Furthmüller, J. *Comput. Mater. Sci.* **1996,** *6,* 15–50. doi:10.1016/0927-0256(96)00008-0
45. Kresse, G.; Hafner, J. *Phys. Rev. B* **1993,** *47,* 558–561. doi:10.1103/PhysRevB.47.558
46. Kresse, G.; Hafner, J. *Phys. Rev. B* **1994,** *49,* 14251–14269. doi:10.1103/PhysRevB.49.14251
47. Treutler, O.; Ahlrichs, R. *J. Chem. Phys.* **1995,** *102,* 346–354. doi:10.1063/1.469408
48. Eichkorn, K.; Weigend, F.; Treutler, O.; Ahlrichs, R. *Theor. Chem. Acc.* **1997,** *97,* 119–124.

49. Bader, R. F. W. *Atoms in Molecules: A Quantum Theory;* Oxford University Press: Oxford, 1990.
50. Henkelman, G.; Arnaldsson, A.; Jónsson, H. *Comput. Mater. Sci.* **2006,** *36,* 354–360. doi:10.1016/j.commatsci.2005.04.010
51. *CASINO,* v2.42; University of Sherbrooke: Quebec, Canada, 2002.
52. Fernández-Pacheco, A.; De Teresa, J. M.; Córdoba, R.; Ibarra, M. R. *J. Phys. D: Appl. Phys.* **2009,** *42,* 055005. doi:10.1088/0022-3727/42/5/055005
53. Belova, L. M.; Dahlberg, E. D.; Riazanova, A.; Mulders, J. J. L.; Christophersen, C.; Eckert, J. *Nanotechnology* **2011,** *22,* 145305. doi:10.1088/0957-4484/22/14/145305
54. Porrati, F.; Sachser, R.; Walz, M.-M.; Vollnhals, F.; Steinrück, H.-P.; Marbach, H.; Huth, M. *J. Phys. D: Appl. Phys.* **2011,** *44,* 425001. doi:10.1088/0022-3727/44/42/425001
55. Bor, G. *Spectrochim. Acta* **1963,** *19,* 2065–2073. doi:10.1016/0371-1951(63)80226-X
56. Noack, K. *Helv. Chim. Acta* **1964,** *47,* 1064–1067. doi:10.1002/hlca.19640470417
57. Bor, G.; Dietler, U. K.; Noack, K. *J. Chem. Soc., Chem. Commun.* **1976,** 914–916. doi:10.1039/C39760000914
58. Sumner, G. G.; Klug, H. P.; Alexander, L. E. *Acta Crystallogr.* **1964,** *17,* 7327–7342. doi:10.1107/S0365110X64001803
59. Zecchina, A.; Aréan, C. O. *Catal. Rev.* **1993,** *35,* 261–317. doi:10.1080/01614949308014607
60. Zhuravlev, L. T. *Colloids Surf., A* **1993,** *74,* 71–90. doi:10.1016/0927-7757(93)80399-Y
61. Rao, K. M.; Spoto, G.; Guglielminotti, E.; Zecchina, A. *J. Chem. Soc., Faraday Trans. 1* **1988,** *84,* 2195–2207. doi:10.1039/F19888402195

License and Terms

Beilstein Journal of Nanotechnology

Nanolesions induced by heavy ions in human tissues: Experimental and theoretical studies

Marcus Bleicher[1,2], Lucas Burigo[1,2], Marco Durante[*1,3,4], Maren Herrlitz[1,3,4], Michael Krämer[3], Igor Mishustin[1,5], Iris Müller[3], Francesco Natale[1,3], Igor Pshenichnov[1,6], Stefan Schramm[1,7], Gisela Taucher-Scholz[3] and Cathrin Wälzlein[1,3,4]

Full Research Paper

Open Access

Address:
[1]Frankfurt Institute for Advanced Studies (FIAS), Ruth-Moufang-Str. 1, 60438 Frankfurt am Main, Germany, [2]Institut für Theoretische Physik, Johann Wolfgang Goethe-Universität, Max-von-Laue-Str. 1, 60438 Frankfurt am Main, Germany, [3]GSI Helmholtzzentrum für Schwerionenforschung GmbH, Planckstr. 1, 64291 Darmstadt, Germany, [4]Technische Universität Darmstadt, Institut für Festkörperphysik, Hochschulstr. 8, 64289 Darmstadt, Germany, [5]National Research Center "Kurchatov Institute", 1, Akademika Kurchatova pl., Moscow, 123182, Russia, [6]Institute for Nuclear Research, Russian Academy of Sciences, 7a, 60th October Anniversary prospect, Moscow 117312, Russia and [7]Center for Scientific Computing, Johann Wolfgang Goethe-Universität, Max-von-Laue-Str. 1, 60438 Frankfurt am Main, Germany

Email:
Marco Durante* - M.Durante@gsi.de

* Corresponding author

Keywords:
DNA repair; heavy ions; microdosimetry; Monte Carlo simulations; nanolesions; radiation-induced nanostructures

Beilstein J. Nanotechnol. **2012,** *3,* 556–563.
doi:10.3762/bjnano.3.64

Received: 30 March 2012
Accepted: 24 May 2012
Published: 25 July 2012

This article is part of the Thematic Series "Radiation-induced nanostructures: Formation processes and applications ".

Guest Editor: M. Huth

Abstract

The biological effects of energetic heavy ions are attracting increasing interest for their applications in cancer therapy and protection against space radiation. The cascade of events leading to cell death or late effects starts from stochastic energy deposition on the nanometer scale and the corresponding lesions in biological molecules, primarily DNA. We have developed experimental techniques to visualize DNA nanolesions induced by heavy ions. Nanolesions appear in cells as “streaks” which can be visualized by using different DNA repair markers. We have studied the kinetics of repair of these “streaks” also with respect to the chromatin conformation. Initial steps in the modeling of the energy deposition patterns at the micrometer and nanometer scale were made with MCHIT and TRAX models, respectively.

Introduction

In a low-dose field of γ-rays, such as that normally experienced on Earth due to background radiation, each human cell is traversed by very few electrons, which hence produce little damage. However, for energetic heavy ions, the situation is different. A low dose, such as the one experienced in a manned mission to the International Space Station or the Moon [1], corresponds to only a few tracks, but each track can affect a whole tissue or organ, and each cell that is found in the path of the ion. The central part of the track, where most of the energy is deposited, has a radial extension of only a few nanometers, while a lower energy is deposited at a larger distance by energetic δ-rays. Thus, each heavy ion will produce a nanochannel in neighboring cells in a tissue or organ, a situation that makes the concept of low dose itself flawed. Although the concept of a "microlesion" induced by heavy ions in space was already acknowledged long ago [2], there is a lack of experimental models for testing the hypothesis that they represent a distinct, unique type of damage at the tissue level. Moreover, Monte Carlo codes should be able to simulate the damage at the micrometer and even nanometer level, basing on the stochastic energy deposition pattern. One problem associated with the formation of nanolesions is the nonuniform structure of the target, i.e., of the cell nucleus [3]. In fact, the compact heterochromatin provides a different environment compared to the transcriptionally competent euchromatin, and it had been proposed that heterochromatin was "refractory" to repair proteins [4]. We have investigated in detail the structure of nanolesions, their formation and movement in the cell nucleus, using live cell microscopy and immunohistochemistry. Stimulated by the differences in repair kinetics and movement of the tracks in eu- and heterochromatin, we have further analyzed the histone modifications (particularly acetylation) along heavy-ion nanolesions. We have also started a full-genome deep-sequencing approach to correlate the microscopy data with the cellular response. In principle, the nanolesion structure can be predicted by accurate Monte Carlo simulations of the energy deposition by the projectile and of the target structure. We used the Monte Carlo model for heavy-ion therapy (MCHIT) code [5] to simulate the energy deposition to micrometer-sized objects, e.g., cell nuclei, and compared the results to microdosimetric spectra previously measured [6]. To further describe the nanometer region, the GSI track structure Monte Carlo code TRAX [7], whose purpose is to properly describe the creation and transport of low energy electrons, has been extended to describe inhomogeneous targets.

Results and Discussion

Nanolesions in different regions of the chromatin

Physics obviously predicts that streaks produced by heavy ions in the DNA should be linear. However, using a double-strand break (DSB)-specific marker (phosphorylated histone γH2AX), we found "bending" of the streaks when cells were fixed for 30 min or more after irradiation [8] (Figure 1). Reconstruction of the track dynamics by using live-cell imaging (Supporting Information File 1) and the heavy-ion microbeam (Figure 2)

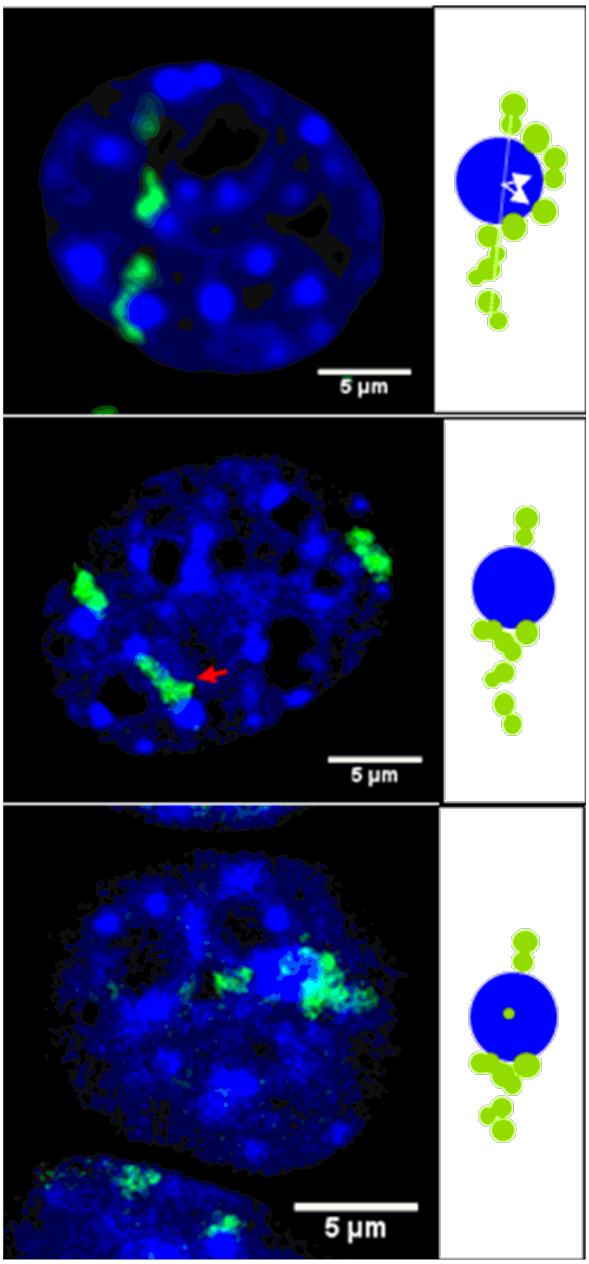

Figure 1: Bending of linear ion-induced γH2AX streaks indicates chromatin density-dependent damage relocation. Three types of γH2AX patterns, each shown in a mouse embryo fibroblast nucleus and as a schematic drawing, were observed at ion-hit chromo centers: bent streaks (upper panel), interrupted streaks (middle panel) and internal signals (lower panel). Modified from [8].

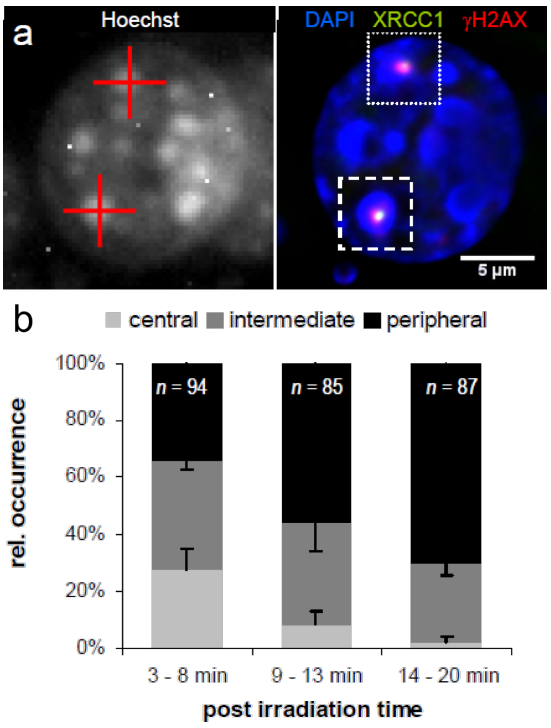

Figure 2: Relocation dynamics of damage sites centrally induced within heterochromatic chromo centers. (a) The mouse embryo fibroblast (MEF) nucleus was irradiated with single sulfur ions and immunostained 5 min after irradiation. H2AX is phosphorylated and the repair protein XRCC1 accumulates at heterochromatic DSBs directly after single-ion irradiation. The left-hand image shows the aimed targeting of chromo centers (red crosses) for single-ion irradiation by using Hoechst 33342 (grey scale) as a marker in the nuclei of living MEF cells. The right-hand image shows the same nucleus after fixation at 5 min after irradiation. DNA-damage-induced foci of the repair factor XRCC1 (green) and γH2AX (red) are clearly visualized at the sites of ion traversal. Both proteins colocalize within each of the targeted chromo centers (blue: DAPI DNA staining). (b) Analysis of the time-dependent localization of XRCC1 and γH2AX radiation-induced foci. Relative frequencies of each position are given for the indicated post-irradiation intervals and (n), the total number of ion-hit chromo centers from three independent experiments, is indicated. Error bars represent the SEM. Figure adapted from [8].

showed that DNA-DSBs are indeed formed within heterochromatin, but they are relocated to euchromatin and the repair kinetics are slower than for euchromatic lesions [8]. These results in mammalian cells have also been observed at the Lawrence Berkeley Laboratory in *Drosophila* [9], thus suggesting that the lesion relocation from hetero- to euchromatin is a universal phenomenon.

Conformational changes in chromatin

The results described above point to a large-scale chromatin decondensation at sites of nanometric DNA lesions. This observation shifted our attention from the analysis of "DNA nanolesions" to a more general concept of "chromatin nanolesions". Histone modifications, especially histone acetylation at defined lysine residues, play a major role in changing the density of chromatin. To explain the local decompaction of heterochromatic regions that takes place at sites of DNA damage [8], we investigated the acetylation of different histone residues that may be involved in this process. We investigated the histone residues H4K16 as well as H3K56. It is known that these residues play a role in the DNA damage response after irradiation by X-rays and UV-lasers [10,11]. In a limited fraction of cells, we measured H4K16ac streaks after exposure to heavy ions (white arrow in Figure 3) that are clearly distinguishable from the H4K16ac signal in the whole nucleus [12].

An accumulation of H3K56ac was not observed. These findings suggest that H4K16ac may also play a role in the damage response after irradiation with heavy ions. Since it is known that acetylation of H4K16 changes chromatin to a more open conformation it has to be elucidated whether H4K16 acetylation is involved in decompaction of DNA at damage sites. However, not all of the cells presented visible H4K16ac streaks, and the effect was observed only with very heavy Au ions. At the fluence used in our experiments ($3 \cdot 10^6$ Au-ions/cm^2) we measured an average of three streaks/cell by using DNA repair

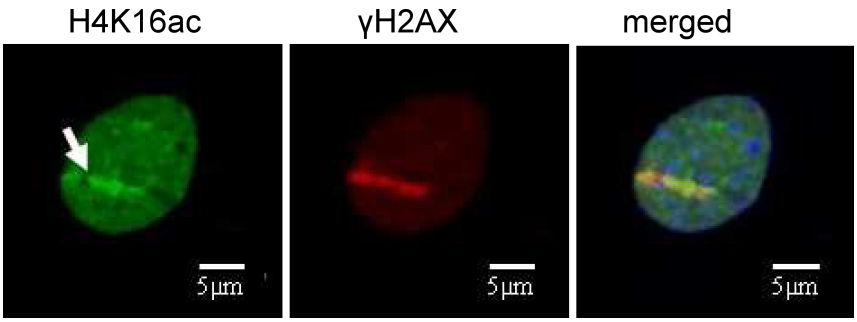

Figure 3: Accumulation of H4K16ac in mouse embryonic fibroblasts. Cells were irradiated with Au ions (energy: 8 MeV/n, linear energy transfer (LET): 13000 keV/µm; fluence: $3 \cdot 10^6$ ions/cm^2) at a low angle and fixed after 1 h. H4K16ac (green) is increased at damage sites. DNA damage is shown by γH2AX staining (red). DNA is counterstained with ToPro3 (blue). From [12] – Copyright: GSI Helmholtzzentrum für Schwerionenforschung GmbH.

markers, and therefore less than 5% of the cells should have no streaks according to Poisson statistics. Moreover, experiments with lighter ions did not produce clear signals. Further experiments are underway to clarify these issues.

Genome-wide screening of the chromatin nanolesions

Alternatively to observation by microscope, the distribution of DNA nanolesions can be investigated with the novel ChIP-Seq technology [13], which allows the mapping of DNA-protein interactions sequence-wise and genome-wide. We used ChIPSeq to provide a genome-scale sequence-based map of the γH2AX signature induced by ionizing radiation. Compaction state of chromatin domains was characterized by multiparametric analysis (e.g., GC content), and the distribution of radiation-induced γH2AX along such chromatin domains was investigated. This complex study is still underway, but preliminary results (Figure 4) suggest that γH2AX is positively correlated to the GC content. Such a feature would indicate that a less compact state (high GC content) could be a more favorable environment for γH2AX spreading than highly compact heterochromatin [14].

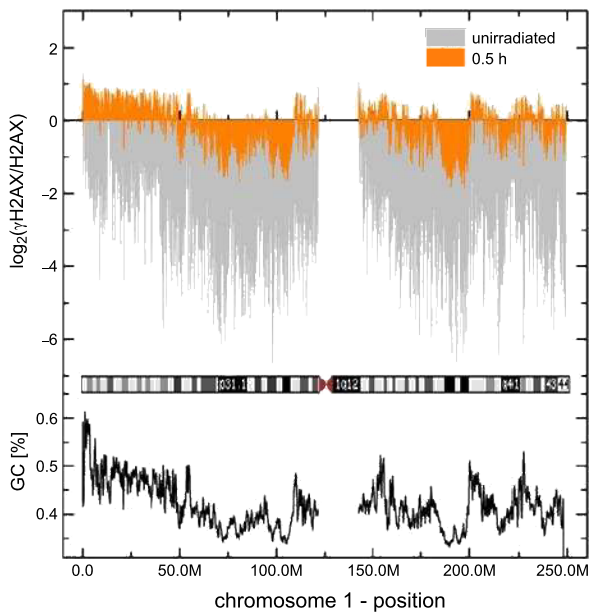

Figure 4: The phosphorylated H2AX distribution after radiation is correlated with the GC base content (a genomic feature associated with high gene content) of the transcriptionally competent and relaxed chromatin (euchromatin). The chromosome 1 profile is shown in the cartoon, with dark bands corresponding to heterochromatin and light bands to euchromatin (from chromosome G-banding). Preliminary ChIP-Seq data show that the γH2AX signature (orange) is enriched in high-GC-content DNA sequences (black line, below) and dark chromosomal bands (e.g., p31.1, q41), corresponding to a very low GC content are underrepresented. From [14] – Copyright: GSI Helmholtzzentrum für Schwerionenforschung GmbH.

MCHIT simulations of microdosimetry distributions

The Monte Carlo method is a convenient technique to account for the interactions of beam nuclei and all secondary particles with tissues. The MCHIT [5] based on the Geant4 toolkit was created in the Frankfurt Institute for Advanced Studies (FIAS) to study the propagation of therapeutic beams in extended media. MCHIT calculates the spatial distribution of energy deposited in a tissue-like phantom, taking into account the fragmentation of beam nuclei.

A practical way to investigate energy deposition to objects equivalent to living cells consists of measurements with detectors called tissue-equivalent proportional counters (TEPC). Typically a TEPC is designed as a low-pressure gas chamber a few millimeters in size. The energy ε delivered to the small sensitive volume in a single event fluctuates due to the stochastic nature of particle propagation in media. Microdosimetry measurements provide the probability distributions for lineal energy defined as $y = \varepsilon/\langle l \rangle$, where $\langle l \rangle$ is the mean chord length of the sensitive volume of the detector. The distributions of lineal energy (microdosimetric spectra) are directly related to the biological effects of radiation.

The MCHIT model was used to simulate microdosimetry measurements at GSI [6]. In this experiment the microdosimetry $yd(y)$ spectra (see [6] for their definition) were collected on the beam axis, as well as off-axis, inside a water phantom, irradiated by a narrow 300 A MeV ^{12}C beam. Simulation results for four TEPC positions inside the phantom are shown in Figure 5. Two of the four measurements (marked as "0 cm") were performed on the beam axis and the other two at 10 cm radius at the beam entrance to the water phantom ("plateau") and at the depth of the Bragg peak ("peak").

It is known that secondary particles of various charges and velocities can eventually contribute with similar lineal energy values. Therefore, the considered $yd(y)$-distribution is built as a sum of contributions from various secondary particles representing a multicomponent radiation field around the primary beam. The contributions of various fragments to the spectra are shown separately in Figure 6 for a TEPC located at the Bragg peak on the beam axis. The peak in the distribution at $y \approx 131$ keV/μm is due to the primary carbon nuclei while the second broad peak at $y \approx 25$ keV/μm is caused by projectile fragments produced in fragmentation reactions. The MCHIT model reproduces the general shape of $yd(y)$ distributions at all four TEPC positions in the phantom (Figure 5). However, it underestimates the spectra for TEPCs located far from the beam axis. This problem is apparently related to an underestimation of yields of light fragments produced by primary nuclei in the phantom. The contributions to $yd(y)$ distributions from second-

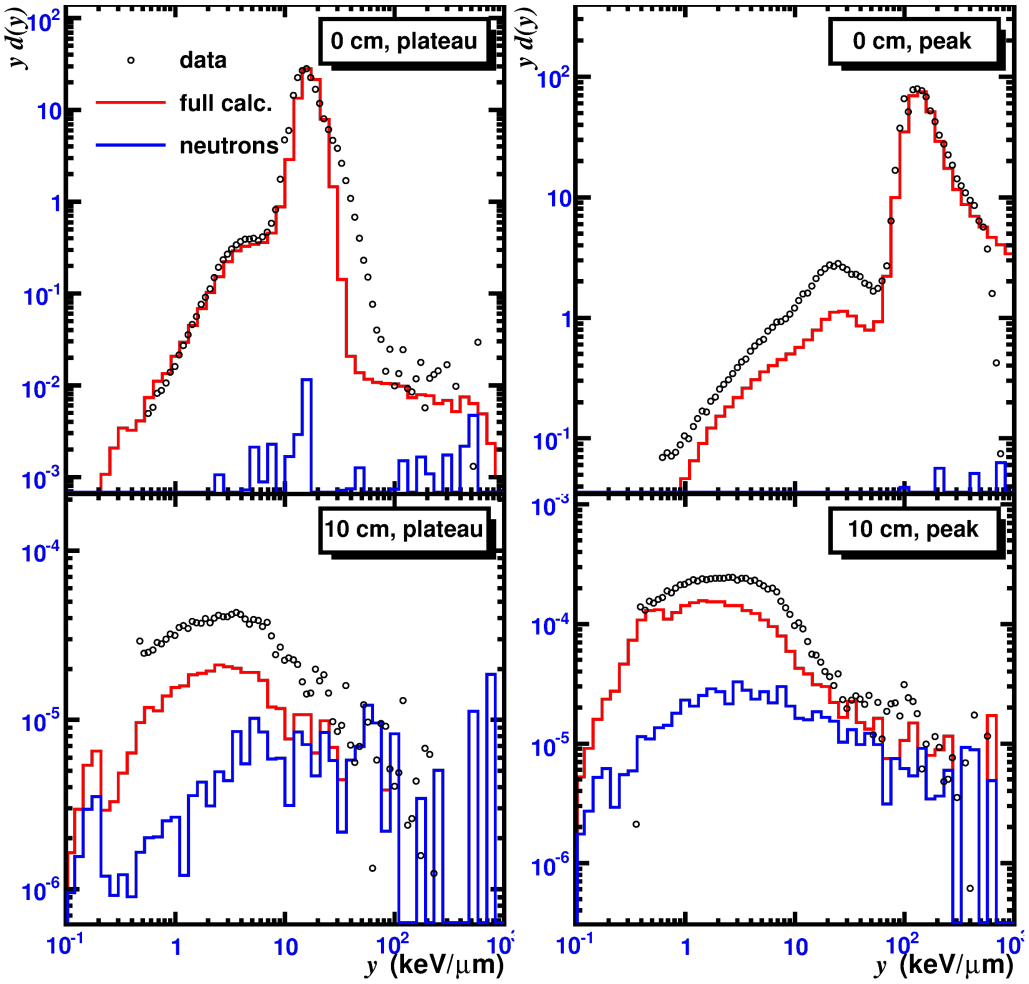

Figure 5: Microdosimetric spectra in a water phantom irradiated by 300 A MeV ^{12}C nuclei. Upper (red) histograms are the total spectra calculated with MCHIT, the lower (blue) histograms show the neutron contributions. Data points from [6].

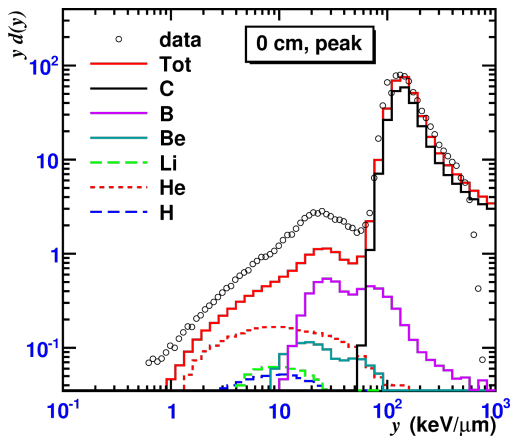

Figure 6: Contribution of various fragments to the microdosimetry spectra measured on the beam axis in the Bragg peak region in a water phantom irradiated by 300 A MeV ^{12}C nuclei. Histograms represent MCHIT calculations. Data points from [6].

ary neutrons are also shown in Figure 5 for the considered TEPC positions. The neutron contribution increases with the distance from the beam axis. At the TEPC positions far from the beam (at 10 cm radius) the total contribution from neutrons amounts to ≈50% at the plateau and to ≈25% at the Bragg peak depth. More details on microdosimetry simulations with the MCHIT model, in particular on specific physics models used in calculations, can be found elsewhere [15].

Extensions of the TRAX code

The elevated radiobiological effectiveness of heavy ions can be attributed to the largely inhomogeneous damage deposition on the micro- or even nanometer level when compared to sparsely ionizing reference radiation with the same macroscopic dose deposition. Whereas photons or electrons show an almost uniform distribution of interaction events, even on this small-scale level, the dose deposition caused by ions is centered on the track core and falls off as $1/r^2$. Thus, towards the ion-track

core, local doses deposited by ions can reach values up to kilo- or even megagrays for the heaviest ions. On the other hand, biological endpoints important for radiotherapy, such as tumor cell killing and healthy tissue damage, follow the well-known and well-proven linear-quadratic dose dependence. This means that high doses, as they occur in the ion track core, contribute disproportionally to the radiobiological effect. Thus this part of the radial dose distribution will contribute most to the radiation action. Unfortunately the ion track core is also the least known region in this scenario. Available models usually cut off and renormalize the radial dose at distances of the order of ten nanometers to avoid the mathematical divergence at $r = 0$, which is justified by reasonable results, but somewhat unsatisfying from the physical point of view. Experimental data are almost nonexistent in this region, even in gases, let alone in condensed phase.

To improve on this situation, at least from the computational side, we apply our simulation code TRAX [7], constantly developed at GSI over several years. It uses the single interaction Monte Carlo method, rather than a condensed random walk, to describe radiation action at the lowest possible level. When inspecting the nanoscale, however, not only the usual ionization and excitation events, but also elastic scattering of the primary ion, which is often neglected, may play a role. Therefore we have included this interaction in the simulation to evaluate its influence on the nanoscale damage distribution. Screened Rutherford cross sections according to Berger [16] were used to account for the elastic scattering of ions. The correct implementation of this additional interaction in the code was benchmarked against experimental results. Gottschalk et al. [17] have measured the angular distribution of 158.6 MeV protons incident on several different target materials and thicknesses. The TRAX simulations including elastic ion scattering showed good agreement with these experimental results, as can be seen in Figure 7.

Additionally the simulations were compared to Highland's formula [18], which is a parameterized approximation of the Molière theory. The implementation of elastic ion scattering is an important step towards a complete description of the relevant physical effects that contribute to the energy deposition on the nanoscale. However, further extensions of the code may be necessary to account for all important physical effects. Figure 8 shows that the elastic scattering of the primary ions has an effect on the nanometer scale. Energy deposition events, such as excitation and ionization, which are caused by the primary ions, no longer occur only at $r = 0$. The positions are shifted on the nanometer scale. This reduces the calculated radial dose at $r = 0$ (not shown in the figure) and increases the calculated radial dose at radii within the scattering radius of the primary ions.

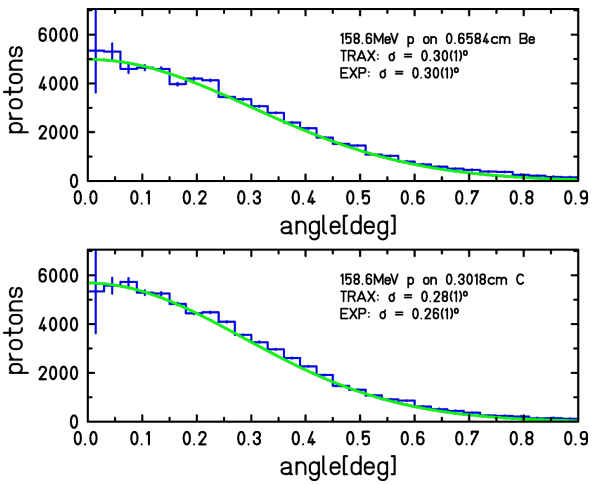

Figure 7: Simulated angular distributions of 158.6 MeV protons incident on 0.66 cm beryllium (upper picture) and 0.30 cm carbon (lower picture) with TRAX. The binning of the histogram in the TRAX simulation is 0.03 degrees. In the case of the beryllium target, fitting a Gaussian distribution to the simulated data resulted in a Gaussian width of (0.30 ± 0.01)° which is exactly the same result as experimentally determined in [17]. Highland's formula [18] led to a width of 0.27°. In the case of carbon, the fit to the TRAX results resulted in a Gaussian width of (0.28 ± 0.01)°, while Gottschalk et al. [17] determined this width to be (0.26 ± 0.01)°. Highland's formula [18] resulted in 0.24° for the carbon target.

Conclusion

We have developed experimental techniques to visualize nanolesions in human tissues and to analyze these lesions genome-wide. In our approach, nanolesions are induced by very heavy ions and studied by the recruitment of repair proteins and the epigenetic changes in the chromatin surrounding the damaged DNA molecule. We concluded that the structure of the nanolesions depends strongly on the target structure, where the target is not only DNA, but the protein-nucleic acid complex (chromatin). Monte Carlo codes MCHIT and TRAX can elegantly reproduce the measured [6,17] energy deposition patterns following the passage of energetic heavy ions. However, further efforts are required to improve the MCHIT model accuracy in calculating spectra far from the beam axis and to extend TRAX to complex inhomogeneous targets. Novel target simulations will be necessary to simulate the observed formation and dynamics of nanolesions in tissues. Further extensions of the MCHIT and TRAX code will be necessary to obtain a satisfactory description of energy deposition and track behavior at the nanometer scale in realistic targets.

Experimental

Detailed experimental methods for immunohistochemistry and live-cell imaging in our laboratories are described elsewhere [8,12]. We have recently installed a 405 nm laser for photoacti-

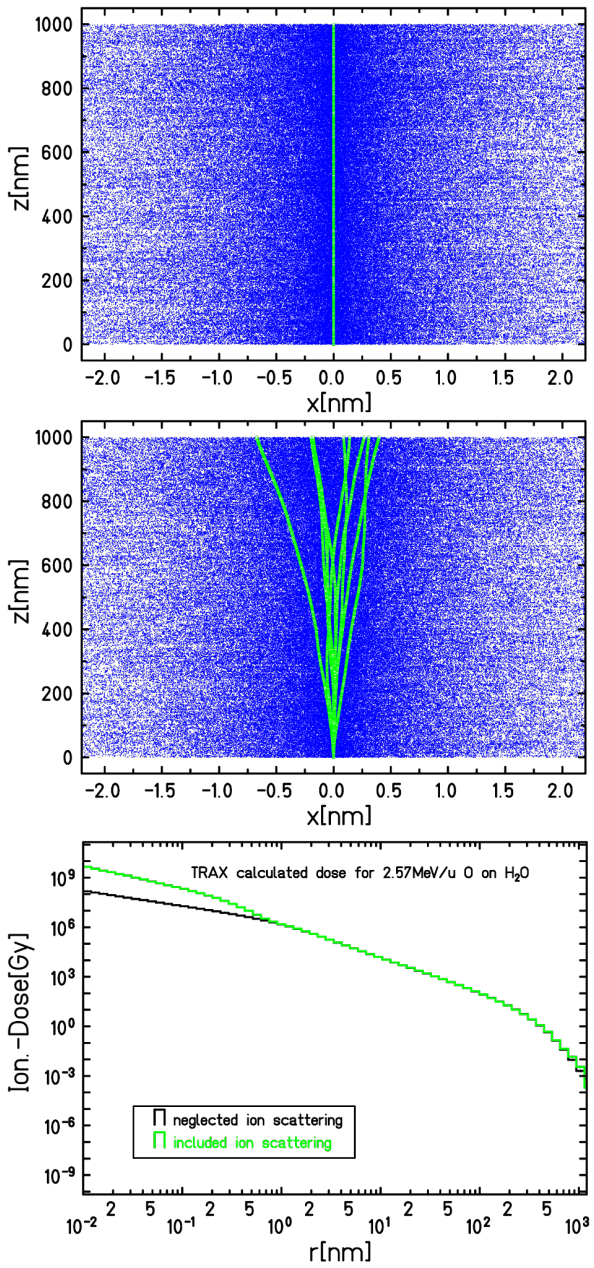

Figure 8: In the upper picture, the tracks of 10 individual oxygen ions with a primary energy of 2.57 MeV/u, incident on water, are shown while the elastic scattering of ions is neglected. They all travel straight through the medium. The blue spots indicate the interaction positions of the secondary electrons. In the central picture the same plot is shown including the elastic scattering of ions. The angular deflection over a travelling length of 1 µm can be seen. On the nanometer scale, the shift of ionization and excitation events of the primary ions is noticeable. The resulting radial dose with and without elastic ion scattering is shown in the lower picture. It can be seen that the radial dose differs in the area that is equal to the radius of the elastic scattering of ions. The deflection of the primary ions leads to a natural "diffusion" of the radial dose.

vation studies [19]. The experimental setup is based on a Leica IRE2 inverted microscope equipped with LED light sources and a climate chamber for controlling of the temperature, humidity and CO_2 concentration, for long-term live-cell observations. Image acquisition is done by a Hamamatsu C7190 EB-CCD camera. Photobleaching of GFP-tagged H2B in living HeLa cells by the 405 laser is demonstrated in Figure 9. By turning and panning of the laser circle, the logo of the Beilstein-Institut was visualized by pseudocoloring of the bleached regions. Details of the microdosimetry measurements are given in [6]. We simulated with MCHIT the TEPC model LET-1/2, Far West Technology at a gas pressure of 120 mbar, equivalent to 2.7 µm tissue.

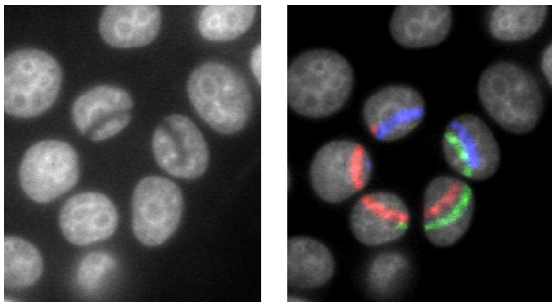

Figure 9: Living HeLa cells expressing histone H2B tagged to GFP were photobleached. Bleaching within a region of three sectors of a circle depletes fluorescence from the bleached region. Colors of the three regions were adjusted with ImageJ and the different channels were merged. From [19] – Copyright: GSI Helmholtzzentrum für Schwerionenforschung GmbH.

Supporting Information

Supporting Information File 1

The animation in Supporting Information File 1 shows a real time observation of the recruitment of GFP-XRCC1 to two charged particle tracks traversing the nucleus of a living MEF cell during high energy (1 GeV/n) uranium irradiation. From these 3-D image stacks, movies were generated by making maximum projections of the fluorescence intensity using Image J (http://rsb.info.nih.gov/ij/). Red color indicates Cherry-tagged HP1α (marking chromocenters), green color GFP-XRCC1. Total imaging time: 9.5 min. Shot noise (due to neutron scattering) indicates the irradiation time points. Please note the fast GFP-XRCC1 recruitment along tracks, disappearance of euchromatic foci (green) and the prolonged retention of heterochromatic GFP-XRCC1 (yellow, overlapping HP1α) in the left radiation track. [http://www.beilstein-journals.org/bjnano/content/supplementary/2190-4286-3-64-S1.avi]

Supporting Information File 2

Supporting Information File 2 is a high resolution animation showing real time GFP-XRCC1 recruitment to the high energy uranium ion track traversing a single MEF chromocenter (red, marked by Cherry-HP1α). Note the billowing motion of the damaged domain (XRCC1, green; appears yellow due to HP1α overlap in heterochromatin) and a drift toward the chromocenter periphery.
[http://www.beilstein-journals.org/bjnano/content/supplementary/2190-4286-3-64-S2.avi]

Acknowledgements

This work was supported by the Beilstein-Institut, Frankfurt am Main, Germany (NanoBiC collaboration).

References

1. Durante, M.; Cucinotta, F. A. *Rev. Mod. Phys.* **2011,** *83,* 1245–1281. doi:10.1103/RevModPhys.83.1245
2. Todd, P. *Adv. Space Res.* **1983,** *3,* 187–194. doi:10.1016/0273-1177(83)90189-8
3. Jakob, B.; Durante, M. *Radiat. Res.* **2012,** *177,* 524–532. doi:10.1667/RR2452.1
4. Kim, J.-A.; Kruhlak, M.; Dotiwala, F.; Nussenzweig, A.; Haber, J. E. *J. Cell Biol.* **2007,** *178,* 209–218. doi:10.1083/jcb.200612031
5. Pshenichnov, I.; Botvina, A.; Mishustin, I.; Greiner, W. *Nucl. Instrum. Methods Phys. Res., Sect. B* **2010,** *268,* 604–615. doi:10.1016/j.nimb.2009.12.023
6. Martino, G.; Durante, M.; Schardt, D. *Phys. Med. Biol.* **2010,** *55,* 3441–3449. doi:10.1088/0031-9155/55/12/011
7. Krämer, M.; Durante, M. *Eur. Phys. J. D* **2010,** *60,* 195–202. doi:10.1140/epjd/e2010-00077-8
8. Jakob, B.; Splinter, J.; Conrad, S.; Voss, K.-O.; Zink, D.; Durante, M.; Löbrich, M.; Taucher-Scholz, G. *Nucleic Acids Res.* **2011,** *39,* 6489–6499. doi:10.1093/nar/gkr230
9. Chiolo, I.; Minoda, A.; Colmenares, S. U.; Polyzos, A.; Costes, S. V.; Karpen, G. H. *Cell* **2011,** *144,* 732–744. doi:10.1016/j.cell.2011.02.012
10. Miller, K. M.; Tjeertes, J. V.; Coates, J.; Legube, G.; Polo, S. E.; Britton, S.; Jackson, S. P. *Nat. Struct. Mol. Biol.* **2010,** *17,* 1144–1151. doi:10.1038/nsmb.1899
11. Li, X.; Corsa, C. A. S.; Pan, P. W.; Wu, L.; Ferguson, D.; Yu, X.; Min, J.; Dou, Y. *Mol. Cell. Biol.* **2010,** *30,* 5335–5347. doi:10.1128/MCB.00350-10
12. Herrlitz, M.; Müller, I.; Liefke, A. L.; Becker, G.; Durante, M.; Taucher-Scholz, G. *GSI Scientific Report* **2012,** *60,* 1448.
13. Iacovoni, J. S.; Caron, P.; Lassadi, I.; Nicolas, E.; Massip, L.; Trouche, D.; Legube, G. *EMBO J.* **2010,** *29,* 1446–1457. doi:10.1038/emboj.2010.38
14. Natale, F.; Rapp, A.; Durante, M.; Taucher-Scholz, G.; Cardoso, M. C. *GSI Scientific Report* **2012,** *84,* 1542.
15. Burigo, L.; Pshenichnov, I.; Mishustin, I.; Bleicher, M., *Microdosimetry of radiation fields from therapeutic ^{12}C beams in water: a study with Geant4 toolkit,* in preparation.
16. Berger, M. J. *Methods Comput. Phys.* **1963,** *1,* 135.
17. Gottschalk, B.; Koehler, A. M.; Schneider, R. J.; Sisterson, J. M.; Wagner, M. S. *Nucl. Instrum. Methods Phys. Res., Sect. B* **1993,** *74,* 467–490. doi:10.1016/0168-583X(93)95944-Z
18. Highland, V. L. *Nucl. Instrum. Methods* **1975,** *129,* 497–499. doi:10.1016/0029-554X(75)90743-0
19. Khan, R.; Herrlitz, M.; Jakob, B.; Durante, M.; Taucher-Scholz, G. *GSI Scientific Report* **2012,** *75,* 1490.

License and Terms

Beilstein Journal of Nanotechnology

Synthesis and electrical characterization of intrinsic and in situ doped Si nanowires using a novel precursor

Wolfgang Molnar[1], Alois Lugstein[*1], Tomasz Wojcik[2], Peter Pongratz[2], Norbert Auner[3,4], Christian Bauch[3,4] and Emmerich Bertagnolli[1]

Full Research Paper

Open Access

Address:
[1]Institute of Solid State Electronics, TU-Wien, Floragasse 7, A-1040 Vienna, Austria, [2]Institute of Solid State Physics, TU-Wien, Wiedner Hauptstrasse 8/052, A-1040 Vienna, Austria, [3]Spawnt Research GmbH, Entwicklungszentrum Wolfen, Kunstseidenstrasse 6, D-06766 Bitterfeld-Wolfen and [4]Johann Wolfgang von Goethe-University, Max-von-Laue-Strasse 7, D-60438 Frankfurt am Main, Germany

Email:
Alois Lugstein[*] - alois.lugstein@tuwien.ac.at

* Corresponding author

Keywords:
chemical vapour deposition; field-effect transistor; oligosilanes; radiation-induced nanostructures; silicon nanowires; vapor–liquid–solid mechanism

Beilstein J. Nanotechnol. **2012,** *3,* 564–569.
doi:10.3762/bjnano.3.65

Received: 30 March 2012
Accepted: 11 May 2012
Published: 31 July 2012

This article is part of the Thematic Series "Radiation-induced nanostructures: Formation processes and applications".

Guest Editor: M. Huth

Abstract

Perchlorinated polysilanes were synthesized by polymerization of tetrachlorosilane under cold plasma conditions with hydrogen as a reducing agent. Subsequent selective cleavage of the resulting polymer yielded oligochlorosilanes Si_nCl_{2n+2} (n = 2, 3) from which the octachlorotrisilane (n = 3, Cl_8Si_3, OCTS) was used as a novel precursor for the synthesis of single-crystalline Si nanowires (NW) by the well-established vapor–liquid–solid (VLS) mechanism. By adding doping agents, specifically BBr_3 and PCl_3, we achieved highly p- and n-type doped Si-NWs by means of atmospheric-pressure chemical vapor deposition (APCVD). These as grown NWs were investigated by means of scanning electron microscopy (SEM) and transmission electron microscopy (TEM), as well as electrical measurements of the NWs integrated in four-terminal and back-gated MOSFET modules. The intrinsic NWs appeared to be highly crystalline, with a preferred growth direction of [111] and a specific resistivity of ρ = 6 kΩ·cm. The doped NWs appeared to be [112] oriented with a specific resistivity of ρ = 198 mΩ·cm for p-type Si-NWs and ρ = 2.7 mΩ·cm for n-doped Si-NWs, revealing excellent dopant activation.

Introduction

As potential building blocks for nanoelectronics [1,2], biochemical sensors [3,4], light-emitting devices with extremely low power consumption, and solar cells [5], nanotubes [6] and NWs [7] have drawn a lot of interest during the last two decades. To tune the NWs for their respective applications, their electrical and optical properties, which strongly depend on the

diameter [8] as well as the crystallographic orientation [9] and defect structure [10] of the NW, must be carefully adjusted. Several synthesis techniques have proven suitable to achieve NWs with tailored properties, namely chemical vapor deposition (CVD) [11], metal–organic CVD [12], molecular-beam epitaxy [13] and laser ablation techniques [14]. In this work we focus on the well-established VLS growth mechanism [15,16], which has shown remarkable potential in the fabrication of straight, crystalline, nanometre-sized wires. During VLS growth a Si precursor is introduced, which is cracked and dissolved into the catalytic liquid phase. Generally Au is used as the catalyst on Si substrates, forming a liquid alloy with a eutectic temperature of 364 °C, which, upon supersaturation, nucleates the growth of a Si-NW.

In previous work [17] we investigated the crucial importance of substrate preparation in the case of Au-catalysed NWs grown by the VLS mechanism. Removal of silicon oxide shortly before catalyst deposition proved to be decisive for achieving epitaxy and crystallinity. The oxide on top of a Si substrate can also be removed during growth by using $SiCl_4$ as a precursor. Gaseous HCl, a byproduct of $SiCl_4$ decomposition in the presence of H_2, etches the native oxide, providing a clean substrate surface for epitaxial NW growth. The same effect can be utilized by intentionally adding HCl to the growth atmosphere [18]. For such VLS grown NW dopants can be introduced either through particular catalyst particles, such as In [19], Al [20] or Ga [21], which become partly incorporated into the NW during growth and thus work as p-type dopants themselves, or by adding a small amount of dopant intentionally to the Au catalyst particle [22]. Much more common and effective is to add a gaseous dopant, such as PH_3, B_2H_6 or $B(CH_3)_3$, to the precursor gas feed during growth. Thus, for example, p–i–n^+-type doped Si-NW heterostructures with a resistivity of a few mΩ·cm have been achieved [20]. Unfortunately, such in situ doping can negatively affect the actual growth process. B_2H_6 for example triggers the formation of an amorphous Si shell [23], whereas PH_3 reduces the growth rate and completely inhibits NW growth at higher PH_3 partial pressures [24]. Furthermore, the doping often appears to be radially inhomogeneous and diameter dependent [25]. In this paper we discuss the electric properties of Si-NWs grown with Si_3Cl_8 [26] as well as peculiarities of the in situ doped NW synthesis using this precursor in combination with BBr_3 or PCl_3.

Experimental

For the synthesis of perchlorinated polysilanes an industrial microwave device (MX 4000, Muegge Electronics GmbH), connected to a rectangular waveguide that leads into a reaction chamber, was used. The reactor itself consisted of a quartz-glass tube, inserted into the microwave cavity, with the axis of the waveguide being perpendicularly aligned to the reaction tube. Prior to use, the reaction apparatus was carefully dried by heating in vacuum. A gaseous mixture of 40 mL (59.2 g) of $SiCl_4$ and 17 L of H_2 was introduced into the reaction chamber and the pressure was carefully adjusted to 2 mbar. By powering a solid-state Tesla transformer, a glow discharge (10 W) of about 12 cm in length was generated. Then, pulsed microwave radiation was used to initiate plasma filling of the whole reaction tube at a length of 8 cm. The microwave pulse duration was set to 1 ms at 4 kW followed by a pause of 59 ms, resulting in an average power level of 67 W. The gas mixture was consumed within 200 min and a white-brown waxy solid (22 g) was deposited on the tube walls. This polymeric material was dissolved in a small amount of $SiCl_4$ and isolated from the reactor. Cryoscopic investigations showed the molecular weight of the polymer to be around 1700 g/mol, which proves the formation of a perchlorinated polysilane $(SiCl_2)_n$ and/or of Si_nCl_{2n+2}, with an average chain length of about $n = 17$ for $(SiCl_2)_n$ or $n = 16$ for Si_nCl_{2n+2}. Moreover the molar ratio of Si/Cl was found to be 1:2 by titration after Mohr [27]. Similar to the process described in the literature [28], 50 g of the perchlorinated polysilane were dissolved in 500 mL of $SiCl_4$ and placed in a 1 L flask equipped with a reflux condenser, a stirrer and a gas inlet. The reflux condenser was connected with a cooling trap (−20 °C). Dry chlorine gas was slowly passed through the reaction solution at the reflux temperature of $SiCl_4$ (~57 °C). The reflux temperature was slowly raised but kept below the boiling point of Si_2Cl_6, whereupon most of the $SiCl_4$ was distilled off. After 10 h the slightly yellow solution was distilled at normal pressure to separate $SiCl_4$, Si_2Cl_6 (T_B = 145 °C/760 mmHg, 25 g), and Si_3Cl_8 (T_B = 215 °C/760 mmHg, 16 g). Higher oligosilanes remained in the distillation residue and were not isolated. For characterization of the precursor compounds, Si_2Cl_6 and Si_3Cl_8 were identified by their characteristic ^{29}Si NMR chemical shifts (Si_2Cl_6, δ = −6.4 ppm; Si_3Cl_8, δ = −3.7 (-$SiCl_3$), −7.4 ppm (-$SiCl_2$-)) [29,30] and by GC–MS measurements. Trace analysis was performed by ICP–MS measurements. For the preparation of the doped samples, BBr_3 and PCl_3 were added to the oligosilanes in very small quantities (100 ppm). After distillation the doped oligosilanes were directly used for NW growth in an APCVD system.

The main components of the APCVD growth chamber are a horizontal tube furnace with three individually controlled heating zones, a quartz tube connected to a gas feed, and a pumping unit. To supply the furnace with gaseous OCTS precursor a saturator was utilized with He as the feed gas. A more detailed description of the growth apparatus is given in [30]. As substrates, pieces of Si (111) were cleaned with acetone, rinsed with propan-2-ol and blown dry with N_2. The

native oxide was removed by buffered hydrofluoric acid (BHF; HF/NH_4F 7:1) resulting in a hydrogen-terminated Si surface. Au colloids (80 nm) in propan-2-ol were then dropped onto the substrate and after evaporation of the solvent and an additional dip in BHF, the samples were immediately introduced into the APCVD system. The reactor was evacuated and purged with He, three times, to remove any traces of air. Thereafter the temperature was ramped up with the samples still outside of the heated zone, under a flow of 100 sccm of He. When the furnace reached the final growth temperature the sample holder was transferred into the growth region with the aid of a magnetic specimen-transport system, enabling accurate and fast placement of the samples at desired temperatures without breaking the vacuum. It turned out that annealing of the samples for 30 min at 800 °C prior to growth improved epitaxy considerably. After this pre-annealing, OCTS was introduced into the growth atmosphere with a partial pressure of ~0.03 mbar by routing the He through the saturator. Taking into account the temperature gradient of the furnace, process temperatures from 900 to 400 °C in steps of 100 °C were investigated simultaneously within the same growth sequence, which gave the most direct and reliable information about the influence of the growth temperature [30]. After the standard growth duration of 60 min, the sample holder was pulled out of the heating zone with the magnetic specimen-transport system, enabling a very fast cool down of the samples, which still remained in the growth atmosphere. Finally, the precursor gas flow was stopped, and the quartz tube was purged with He for a further 5 min before the sample was removed from the APCVD system.

For contacting the NWs, 200 × 200 μm^2 Au pads were structured on a highly doped Si (100) wafer, capped with 80 nm Al_2O_3, by photolithography and lift-off techniques. VLS-grown Si-NWs were then removed from their growth substrates by ultrasonication in propan-2-ol. Subsequently the NWs were randomly distributed by dropping the suspension onto the above mentioned Si(100) wafer with prepatterned Au pads. Finally the NWs were connected to the prepatterned Au pads by electron beam lithography, Ni sputter deposition and lift-off techniques.

Results and Discussion

Single-crystalline and epitaxial Si-NWs were grown by using OCTS as a precursor and Au colloids at a growth temperature of 700 °C, with a pre-annealing of the samples at 800 °C for 30 min. The thus synthesized NWs, shown in Figure 1a, were 4 to 10 µm long and 80 to 100 nm thick.

Based on such an optimized NW synthesis procedure, we added BBr_3 to the OCTS precursor expecting the formation of p-type doped Si-NWs. However, the addition of BBr_3 strongly affects the growth behaviour. Notably, effective growth of B-doped Si-NWs with OCTS and BBr_3 requires a reduction of the growth temperature and the addition of H_2. Remarkably, the addition of H_2 during the growth of intrinsic NWs causes significant etching under the given experimental conditions [30]. However, adding 10 sccm of H_2 for the synthesis of p-type doped NWs yielded epitaxial, 10 to 20 µm long and 80 to 150 nm thick Si-NWs at a growth temperature of 600 °C (Figure 1b). NWs were observed in large quantity down to temperatures of 400 °C, but epitaxy deteriorated with decreasing temperature. To achieve n-type Si-NWs, PCl_3 was added to OCTS. Again effective NW growth required the addition of H_2 to the growth atmosphere and a higher growth temperature of at least 800 °C. Furthermore, to achieve epitaxial NW growth, the colloids were replaced by a 2 nm thick sputter-deposited Au layer. Epitaxial NWs about 60 nm to 150 nm in diameter and up to 30 µm long are shown in Figure 1c.

Summarizing the synthesis results, one has to note that even small amounts (ppm) of the doping agent change the growth

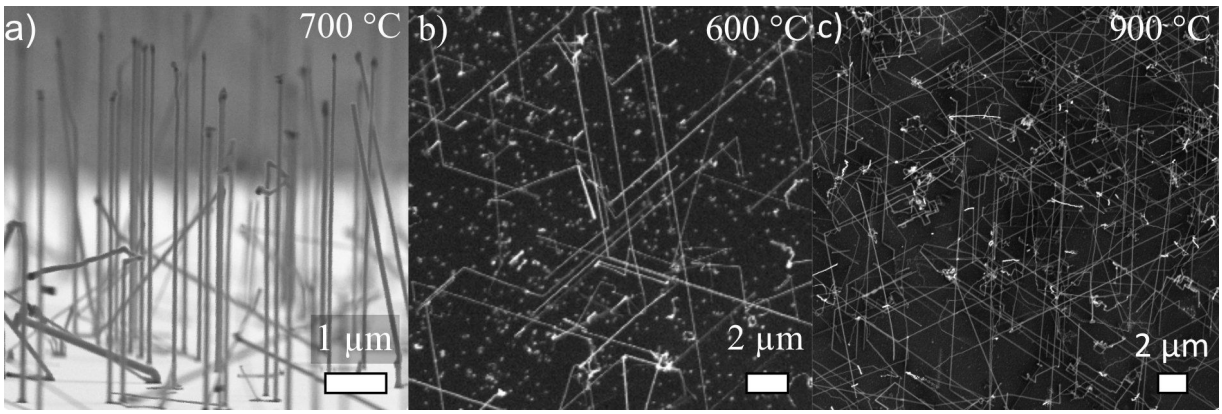

Figure 1: (a) tilted-view SEM image of Au-catalysed NWs grown at 700 °C with OCTS, (b) top-view SEM image of boron-doped Si-NWs grown at 600 °C, (c) SEM image of phosphorus-doped NWs grown at 900 °C.

behaviour considerably. For pure OCTS we achieved effective Si-NWs growth in the temperature regime from 600 to 900 °C without any H_2, though with varying quality. With the addition of BBr_3, NWs growth was restricted to the temperature regime between 400 and 600 °C, although this required the addition of H_2 to the growth atmosphere. Briand et al. [31] also reported lower growth temperatures when adding B_2H_6 to SiH_4, as boron promotes the decomposition of the precursor and therefore increases the growth rate. With PCl_3 as the dopant, at least 800 °C, 20 sccm H_2, and a 2 nm layer of Au were needed to produce epitaxial NWs in considerable quantity. For a more detailed view of the morphology of the intrinsic and doped Si-NWs we performed HRTEM investigations. The TEM image in Figure 2a shows a slightly tapered, intrinsic Si-NW with a catalytic particle atop. The HRTEM micrograph of the crystalline core in Figure 2b shows clearly the Si(111) atomic planes (separation 3.14 Å) perpendicular to the NW axis. The reciprocal lattice peaks in the diffraction pattern (inset in Figure 2b) prove that the growth axis is [111], and previous work on Si-NWs grown with SiH_4 revealed, vertical {112} facets [32]. The NWs are usually free of dislocations and stacking faults and are covered by a very thin oxide layer.

As already mentioned above, the addition of B_2H_6 requires the modification of growth parameters, such as temperature and feed-gas composition, to achieve effective NW growth. Moreover the addition of the dopant species, and thus the expected insertion of B into the lattice of the Si-NW, also influences the morphology and crystal orientation. Nevertheless, they have comparable diameters to those of the intrinsic NWs grown with pure OCTS. The growth orientation of the p-type doped NWs appears to be [112], as shown in the HRTEM image and the respective diffraction pattern (Figure 2c,d). Stacking faults run along the entire NW from the base to the top, and the crystalline core is enwrapped by an amorphous shell. A similar amorphous shell was also observed by Lauhon et al. [33] on addition of B_2H_6 to the growth atmosphere with the SiH_4 precursor. The images in Figure 2e and Figure 2f show that also PCl_3 affects NW growth by changing the growth direction. Such epitaxial NWs grow preferentially along the [112] direction, like their B-doped counterparts. The NWs themselves are rod-like, exhibit good crystallinity, and feature no observable defects or stacking faults.

To test the activation of the dopants in the NWs, electrical characterization was performed with back-gated Schottky-barrier NW-FETs and four-point measurement modules. The results of the four-point measurements and the back-gated measurements are illustrated in Figure 3. The four-point measurements of nominally intrinsic NWs grown with pure OCTS revealed a resistivity of about 5.9 kΩ·cm. This is in accordance with the

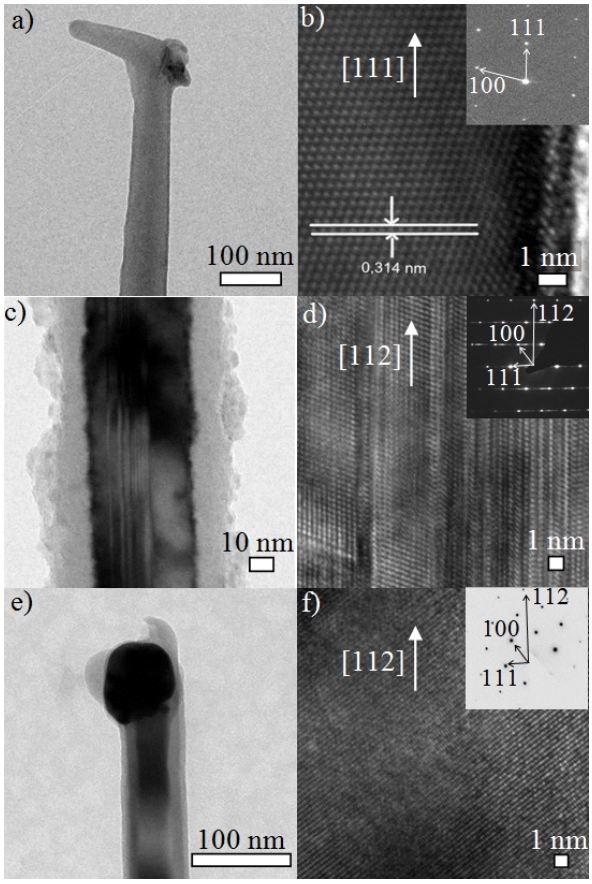

Figure 2: TEM images (a), (c) and (e) show impressions of intrinsic, B-doped and P-doped NWs respectively. Analogously (b), (d) and (f) represent the respective HRTEM images with diffraction images in the inset.

results of Heath et al. [34], who reported a specific resistivity of intrinsic NWs, grown with SiH_4 as a precursor, of about 1 kΩ·cm. Back-gated measurements revealed an unintentionally p-type doping leading to a threshold voltage of −4.5 V (Figure 3 inset). Such p-type behaviour is observed for most intrinsic VLS-grown Si-NWs and can be attributed to hole accumulation at the surface due to trapped negative surface charge, although contributions from impurities such as Au and O cannot be excluded completely [35].

For the as grown intentionally p-doped NWs, we determined a resistivity of about 862 Ω·cm. This rather high resistivity arose from the immense amorphous shell (see Figure 2c) wrapped around a highly crystalline core. Thus, in the case of the intentionally B-doped NWs, an annealing step at 470 °C for 2 min was required to achieve reliable contacts. Subsequent measurements revealed a specific resistivity of 198 mΩ·cm (Figure 3), which corresponds to an active dopant concentration of 10^{17} cm^{-3} in bulk Si. A similar behaviour was also reported by

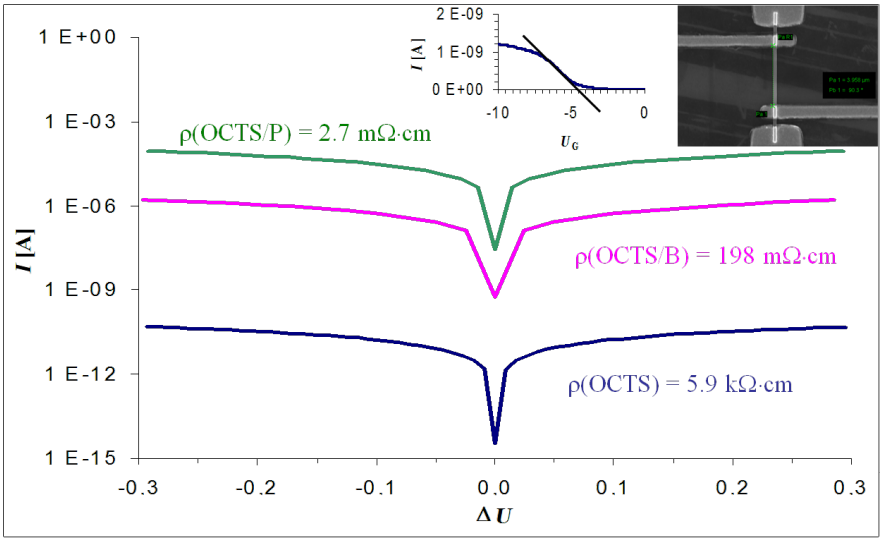

Figure 3: Semilogarithmic *I*/*V* plot of intrinsic, p- and n-type NWs. The calculated specific resistivity values are shown next to the respective curves. The transfer characteristic of the intrinsic NW integrated into a back-gated Schottky-barrier NW-FET and a SEM image of a four-point setup is shown in the inset.

Lauhon et al. [35]. The p-type doped NWs showed a high resistivity in the kΩ·cm regime, which can be reduced upon annealing to a few mΩ·cm as a result of complete crystallisation. Adding PCl_3 to the growth atmosphere results in n-type Si-NWs with a resistivity of 2.7 mΩ·cm, corresponding to an active P concentration of 3×10^{19} cm^{-3} in bulk Si. Remarkably this is more than six orders of magnitude lower than the resistivity of the intrinsic NWs in this work. Due to the high doping level we observed no channel modulation in response to the gate voltage for the doped NWs integrated in back-gated FETs.

Conclusion

In conclusion, OCTS appeared to be a favourable precursor for VLS synthesis of intrinsic as well as in situ doped NWs. However, the addition of BBr_3 and PCl_3 as doping agents requires a careful tuning of the growth parameters. NWs synthesized with pure OCTS exhibit a growth orientation of [111], while the doped NWs appear to be predominantly [112] oriented. Finally the electrical characterisation revealed a resistivity of 5.9 kΩ·cm for intrinsic Si-NWs, which appeared to be unintentionally p-type doped and 198 mΩ·cm and 2.7 mΩ·cm for the B- and P-doped NWs, respectively. This proves that the electronic properties of Si-NWs grown with OCTS as Si precursor can be tuned according to the desired applications. Also the growth orientation can be controlled, which may prove useful for device integration. Therefore OCTS-grown NWs represent promising new alternatives in the upcoming fields of nanoelectronics, optics, thermoelectronics and sensor devices [36].

References

1. Duan, X.; Huang, Y.; Lieber, C. M. *Nano Lett.* **2002,** *2,* 487–490. doi:10.1021/nl025532n
2. Javey, A.; Nam, S.; Friedman, R. S.; Yan, H.; Lieber, C. M. *Nano Lett.* **2007,** *7,* 773–777. doi:10.1021/nl063056l
3. Cui, Y.; Lieber, C. M. *Science* **2001,** *291,* 851–853. doi:10.1126/science.291.5505.851
4. Zheng, G.; Patolsky, F.; Cui, Y.; Wang, W. U.; Lieber, C. M. *Nat. Biotechnol.* **2005,** *23,* 1294–1301. doi:10.1038/nbt1138
5. Pettersson, H.; Trägårdh, J.; Persson, A. I.; Landin, L.; Hessman, D.; Samuelson, L. *Nano Lett.* **2006,** *6,* 229–232. doi:10.1021/nl052170l
6. Martel, R.; Derycke, V.; Lavoie, C.; Appenzeller, J.; Chan, K. K.; Tersoff, J.; Avouris, P. *Phys. Rev. Lett.* **2001,** *87,* 256805. doi:10.1103/PhysRevLett.87.256805
7. Duan, X.; Huang, Y.; Cui, Y.; Wang, J.; Lieber, C. M. *Nature* **2001,** *409,* 66–69. doi:10.1038/35051047
8. Brus, L. *J. Phys. Chem.* **1994,** *98,* 3575–3581. doi:10.1021/j100065a007
9. Yorikawa, H.; Uchida, H.; Muramatsu, S. *J. Appl. Phys.* **1996,** *79,* 3619. doi:10.1063/1.361416
10. Mozos, J. L.; Machado, E.; Hernandez, E.; Ordejon, P. *Int. J. Nanotechnol.* **2005,** *2,* 114–128.
11. Wagner, R. S.; Ellis, W. C. *Appl. Phys. Lett.* **1964,** *4,* 89. doi:10.1063/1.1753975
12. Arakawa, Y. *Solid-State Electron.* **1994,** *37,* 523–528. doi:10.1016/0038-1101(94)90238-0
13. Martelli, F.; Piccin, M.; Bais, G.; Jabeen, F.; Ambrosini, S.; Rubini, S.; Franciosi, A. *Nanotechnology* **2007,** *18,* 125603. doi:10.1088/0957-4484/18/12/125603
14. Wang, N.; Tang, Y. H.; Zhang, Y. F.; Lee, C. S.; Lee, S. T. *Phys. Rev. B* **1998,** *58,* R16024–R16026. doi:10.1103/PhysRevB.58.R16024
15. Levitt, A. P., Ed. *Whisker Technology;* Wiley-Interscience: New York, 1970.

16. Givargizov, E. I. *J. Cryst. Growth* **1975,** *31,* 20–30. doi:10.1016/0022-0248(75)90105-0
17. Lugstein, A.; Hyun, Y. J.; Steinmair, M.; Dielacher, B.; Hauer, G.; Bertagnolli, E. *Nanotechnology* **2008,** *19,* 485606. doi:10.1088/0957-4484/19/48/485606
18. Sharma, S.; Kamins, T. I.; Stanley Williams, R. *J. Cryst. Growth* **2004,** *267,* 613–618. doi:10.1016/j.jcrysgro.2004.04.042
19. Iacopi, F.; Vereecken, P. M.; Schaekers, M.; Caymax, M.; Moelans, N.; Blanpain, B.; Richard, O.; Detavernier, C.; Griffiths, H. *Nanotechnology* **2007,** *18,* 505307. doi:10.1088/0957-4484/18/50/505307
20. Björk, M. T.; Knoch, J.; Schmidt, H.; Riel, H.; Riess, W. *Appl. Phys. Lett.* **2008,** *92,* 193504. doi:10.1063/1.2928227
21. Sharma, S.; Sunkara, M. K. *Nanotechnology* **2004,** *15,* 130. doi:10.1088/0957-4484/15/1/025
22. Schmidt, V.; Riel, H.; Senz, S.; Karg, S.; Riess, W.; Gösele, U. *Small* **2006,** *2,* 85–88. doi:10.1002/smll.200500181
23. Lew, K.-K.; Pan, L.; Bogart, T. E.; Dilts, S. M.; Dickey, E. C.; Redwing, J. M.; Wang, Y.; Cabassi, M.; Mayer, T. S.; Novak, S. W. *Appl. Phys. Lett.* **2004,** *85,* 3101. doi:10.1063/1.1792800
24. Schmid, H.; Björk, M. T.; Knoch, J.; Karg, S.; Riel, H.; Riess, W. *Nano Lett.* **2009,** *9,* 173–177. doi:10.1021/nl802739v
25. Xie, P.; Hu, Y.; Fang, Y.; Huang, J.; Lieber, C. M. *Proc. Natl. Acad. Sci. U. S. A.* **2009,** *106,* 15254–15258. doi:10.1073/pnas.0906943106
26. Molnar, W.; Lugstein, A.; Pongratz, P.; Auner, N.; Bauch, C.; Bertagnolli, E. *Nano Lett.* **2010,** *10,* 3957–3961. doi:10.1021/nl101744q
27. Jander, G.; Blasius, E. *Einführung in das anorganisch-chemische Praktikum;* S. Hirtzel Verlag: Stuttgart, 1995.
28. Schmeisser, M.; Voss, P. *Z. Anorg. Allg. Chem.* **1964,** *334,* 50–56. doi:10.1002/zaac.19643340108
29. Sharp, K. G.; Sutor, P. A.; Williams, E. A.; Cargioli, J. D.; Farrar, T. C.; Ishibitsu, K. *J. Am. Chem. Soc.* **1976,** *98,* 1977–1979. doi:10.1021/ja00423a062
30. Marsmann, H. C.; Raml, W.; Hengge, E. *Z. Naturforsch.* **1980,** *35b,* 35–37.
31. Briand, D.; Sarret, M.; Kis-Sion, K.; Mohammed-Brahim, T.; Duverneuil, P. *Semicond. Sci. Technol.* **1999,** *14,* 173–180. doi:10.1088/0268-1242/14/2/012
32. Lugstein, A.; Andrews, A. M.; Steinmair, M.; Hyun, Y.-J.; Bertagnolli, E.; Weil, M.; Pongratz, P.; Schramböck, M.; Roch, T.; Strasser, G. *Nanotechnology* **2007,** *18,* 355306. doi:10.1088/0957-4484/18/35/355306
33. Lauhon, L. J.; Gudiksen, M. S.; Wang, D.; Lieber, C. M. *Nature* **2002,** *420,* 57–61. doi:10.1038/nature01141
34. Yu, J.-Y.; Chung, S.-W.; Heath, J. R. *J. Phys. Chem. B* **2000,** *104,* 11864–11870. doi:10.1021/jp002595q
35. Zhang, S.; Hemesath, E. R.; Perea, D. E.; Wijaya, E.; Lensch-Falk, J. L.; Lauhon, L. J. *Nano Lett.* **2009,** *9,* 3268–3274. doi:10.1021/nl901548u
36. Sarkar, J.; Khan, G. G.; Basumallick, A. *Bull. Mater. Sci.* **2007,** *30,* 271–290. doi:10.1007/s12034-007-0047-0

License and Terms

Beilstein Journal of Nanotechnology

The oriented and patterned growth of fluorescent metal–organic frameworks onto functionalized surfaces

Jinliang Zhuang, Jasmin Friedel and Andreas Terfort*

Full Research Paper

Open Access

Address:
Institute for Inorganic and Analytical Chemistry, University of Frankfurt, Max-von-Laue-Str. 7, D-60438 Frankfurt, Germany

Email:
Andreas Terfort* - aterfort@chemie.uni-frankfurt.de

* Corresponding author

Keywords:
electron-beam lithography; irradiation-promoted exchange reaction; microcontact printing; radiation-induced nanostructure; self-assembled monolayer; surface-attached metal–organic framework

Beilstein J. Nanotechnol. **2012,** *3,* 570–578.
doi:10.3762/bjnano.3.66

Received: 31 March 2012
Accepted: 13 June 2012
Published: 02 August 2012

This article is part of the Thematic Series "Radiation-induced nanostructures: Formation processes and applications".

Guest Editor: M. Huth

Abstract

A metal–organic framework (MOF) material, $[Zn_2(adc)_2(dabco)]$ (adc = anthracene-9,10-dicarboxylate, dabco = 1,4-diazabicyclo[2.2.2]-octane), the fluorescence of which depends on the loading of its nanopores, was synthesized in two forms: as free-flowing nanocrystals with different shapes and as surface-attached MOFs (SURMOFs). For the latter, we used self-assembled monolayers (SAMs) bearing functional groups, such as carboxylate and pyridyl groups, capable of coordinating to the constituents of the MOF. It could be demonstrated that this directed coordination also orients the nanocrystals deposited at the surface. Using two different patterning methods, i.e., microcontact printing and electron-beam lithography, the lateral distribution of the functional groups could be determined in such a way that the highly localized deposition of the SURMOF films became possible.

Introduction

Metal–organic frameworks (MOFs) are a fascinating class of organic–inorganic hybrid materials with nanometer-sized pores. The size and density of the pores renders these materials with extraordinary large free volumes and inner surfaces, which are accessible by guest molecules. Based on this, MOFs have already demonstrated their potential for gas storage/separation [1], heterogeneous catalysis [2], molecular recognition [3], and sensing [4]. Some of these applications, such as gas storage, require the bulk preparation of the materials, what is typically performed by solvothermal synthesis at high temperatures [5,6]. For more sensitive materials, the interdiffusion method, in which the initially separated reactants slowly diffuse towards each other, is also often used [6-8]. Both procedures have the advantage that relatively large crystals can be obtained, which may be suitable for single crystal X-ray diffraction. For many other applications, such as sensing, these crystals often are too large, since the path lengths for the guest molecules within the nanochannels become too long for a fast response.

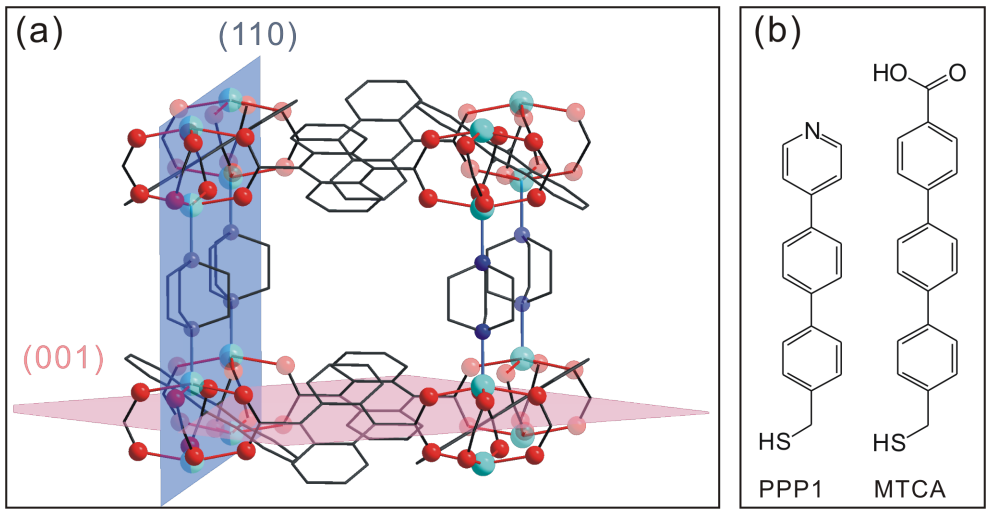

Figure 1: (a) The crystallographic cell of [$Zn_2(adc)_2(dabco)$]. The directionality of the attachment of carboxylate and monodentate Lewis bases (dabco/pyridine) determines the two crystallographic planes given in the scheme. (b) SAM-forming molecules used in this study.

Thus, nanoscale MOFs have attracted great attention for sensing purposes, but also for bioimaging and biomedical applications, such as nitric oxide (NO) storage and drug delivery [9]. Several strategies have been developed to obtain control over the size and morphology of the MOF crystals, such as microwave heating [10,11], ultrasonic synthesis [12,13], microemulsions [14,15], or solvent-triggered precipitation [16,17]. Nanoscale MOFs with various morphologies, (e.g., nanospheres [16,18-20], nanocubes [21], nanorods [14,22], nanowheels [23], and hierarchical spheres [22]) have been synthesized [24].

For sensoric applications in particular, the nanoscale MOF should be immobilized at specific locations on surfaces rather than being a free-flowing powder, to facilitate the read-out of their response. Thus, the spatially and morphologically controlled growth of MOFs, in the form of small crystals or films on specific surfaces, gains significant importance [25-27]. Several methods have been developed to control the growth of such surface-attached MOFs (so-called SURMOFs) on various substrates [28-35]. To adjust the surface chemistry of such substrates, self-assembled monolayers (SAMs) are a powerful tool due to the flexibility regarding the functional groups that they expose, which in turn permit a remarkable control over the growth of SURMOFs. In particular, by using a step-wise layer-by-layer procedure, it has been demonstrated that SAMs cannot only control the spatial deposition of MOF films, but also determine the crystallographic orientation within the films [25,29,31].

MOFs based on large π-conjugated molecules are expected to be useful optical materials, e.g., as sensors, photocatalysts, or electroluminescent devices [36,37]. In this paper, we describe a rapid route to synthesize photoluminescent MOF nanocrystals at room temperature, and the growth of highly orientated and patterned SURMOFs by using SAMs as a template. We have chosen anthracene-9,10-dicarboxylate (adc) as an organic linker to grow a tetragonal MOF, [$Zn_2(adc)_2(dabco)$] (dabco = 1,4-diazabicyclo[2.2.2]-octane), since anthracene-based compounds show interesting luminescent properties, such as photoluminescence and electroluminescence [36,38,39]. In order to obtain highly orientated SURMOFs, we used two SAMs of very high structural quality: The COOH-terminated SAM was formed from 4′-(mercaptomethyl)-terphenyl-4-carboxylic acid (MTCA, see Figure 1b) [40] and the monodentate Lewis base one was formed from (4′-(pyridin-4-yl)-[1,1′-biphenyl]-4-yl)methanethiol (PPP1, see Figure 1b) [41]. Similar to other M_2L_2P (M = Cu, Zn; L = benzene-1,4-dicarboxylate (bdc), tetrafluorobenzene-1,4-dicarboxylate (F_4bdc), naphthalene-1,4-dicarboxylate (ndc); P = dabco, 4,4′-bipyridine (bipy)) type SURMOFs [42], two different principal growth directions are expected on MTCA and PPP1 surfaces, which correspond to the directionality of the attachment, either of carboxylate ([110] direction) or of pyridyl groups ([001] direction) to the [$Zn_2(adc)_2(dabco)$] crystallographic cell (Figure 1a).

Results and Discussion

Synthesis of [$Zn_2(adc)_2$dabco] nanocrystals at room temperature

For reference purposes, bulk [$Zn_2(adc)_2(dabco)$] crystals were synthesized in accordance to the literature procedure [36]. This procedure was then varied to explore the possibility of nanocrystal fabrication. Thus various concentrations and ratios of the

precursors were used to evaluate the influence on the crystal size and appearance. Figure 2 depicts $[Zn_2(adc)_2(dabco)]$ crystals obtained under three different conditions. When an equimolar solution of $Zn(NO_3)_2$ and H_2adc ("Zn–adc", 50 mM each in *N*,*N*-dimethylformamide) was mixed with a 50 mM solution of dabco in methanol, cuboid crystals with a size of 200–500 nm became visible in scanning electron microscopy (SEM) images (Figure 2a).

However, when the concentration of dabco in methanol was reduced to 25 mM, brick-like $[Zn_2(adc)_2(dabco)]$ crystals of 1–2 µm were obtained. By maintaining the ratio of Zn/dabco at 2/1 but reducing the concentrations of both precursors to 25 mM (Zn–adc) and 12.5 mM (dabco), respectively, the morphology of the crystals varied again and we obtained plate-like nanocrystals with a size of 300 nm, as shown in Figure 2c. Powder X-ray diffraction (PXRD) studies showed that all the nanocrystals of $[Zn_2(adc)_2(dabco)]$ are crystalline and of the same polymorph as described in the literature [36], confirmed by the good agreement of the determined diffractograms with the one simulated from reported crystallographic data (Figure 3a, lowest trace) [36].

Since the distances between the anthracene moieties in the $[Zn_2(adc)_2(dabco)]$ framework are large enough to preclude electronic interactions, the absorption and emission spectra should resemble those of molecularly dispersed anthracene, e.g., in solutions. Thus a blue fluorescence would be expected. Instead, as can be seen in the right column of Figure 2, all the nanocrystals show green fluorescence when exposed to UV light. The respective fluorescence spectrum was determined to be quite broad with a maximum at 475 nm (Figure 3b, green curve). According to Tanaka et al. [36] this shift results from the interaction of electron-donor molecules with the anthracene units, and can be used to detect certain analytes, such as *N*-methylaniline or *N*,*N*-dimethylaniline. In our case the *N*,*N*-dimethylformamide (DMF), which was used as a solvent, interacted with the anthracene π-system of the host and caused the observed red shift. This could be easily demonstrated by removing the solvent from the framework by heating under vacuum, which changed the fluorescence of the material to blue

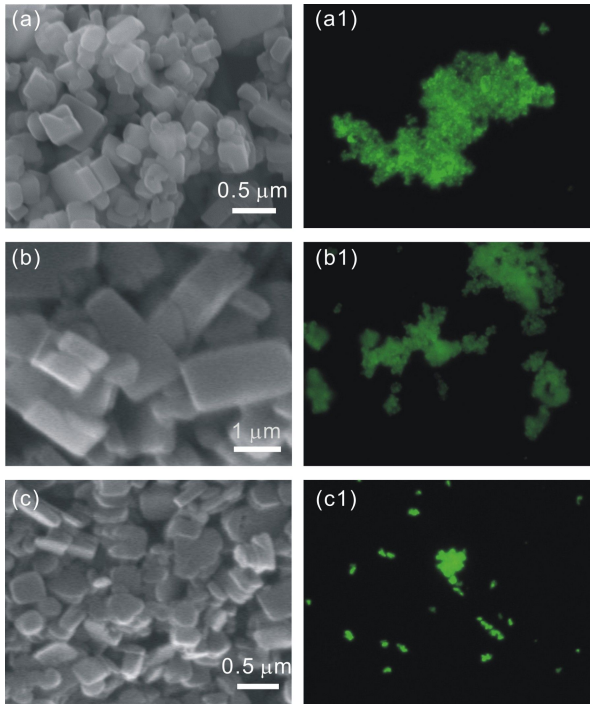

Figure 2: SEM images (a–c) and epifluorescence images (a1–c1) of Zn-MOF nanocrystals synthesized at various concentrations and ratios of the precursors at room temperature. (a) 50 mM of Zn–adc and 50 mM of dabco; (b) 50 mM of Zn–adc and 25 mM of dabco; (c) 25 mM of Zn–adc and 12.5 mM of dabco.

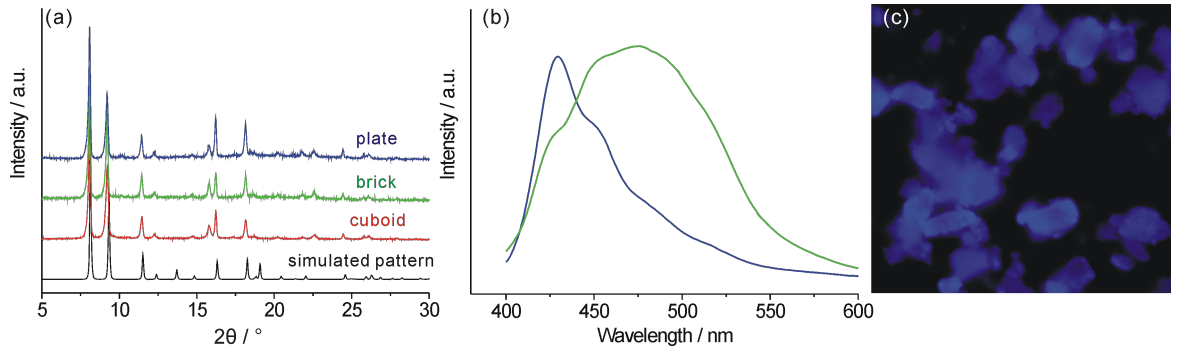

Figure 3: (a) Powder diffractograms of the nanocrystalline products (cuboid (50 mM Zn–adc/50 mM dabco); brick-like (50 mM Zn–adc/25 mM dabco), and plate-like (25 mM Zn–adc/12.5 mM dabco)) in comparison with the one simulated from $[Zn_2(adc)_2(dabco)]$ single-crystal data. The minor differences between the powder XRD patterns and the simulated one may result from different guests in the MOF pores. (b) Solid-state emission spectra of as-synthesized $[Zn_2(adc)_2(dabco)]$ nanocrystals (loaded with solvent molecules such as DMF, green curve) and in the dried bulk form (blue curve). (c) Fluorescence image of a DMF-free sample. Excitation wavelength was 365 nm.

(Figure 3c). The respective solid-state emission spectrum of the solvent-free [Zn_2(adc)$_2$(dabco)] crystals (Figure 3b, blue) displays an emission maximum at 429 nm with a vibrational band at 453 nm, similar to the emission from monomeric anthracene [36,43]. This behaviour shall be used as a sensoric principle in future projects.

Controlled growth of [Zn_2(adc)$_2$dabco] on SAM-functionalized surfaces

As mentioned before, many applications rely on the attachment of the active materials to surfaces [25,26,44]. For the formation of SURMOFs, several strategies exist, such as direct growth/deposition from solvothermal mother solutions [28,30], electrochemical deposition [33], gel-layer deposition [35], spin-coating deposition from a precursor solution [17,45], Langmuir–Blodgett based layer-by-layer method [34,46], and direct step-wise layer-by-layer growth [29,31,44,47,48]. Of these, the latter method is particular suitable, since it is easily performed and provides very good control over the amount of material being deposited. For this deposition technique, essentially the substrate is alternately exposed to a solution containing the metal source and a solution containing the organic linker(s), with purging steps in between. In our case, a solution of zinc acetate in ethanol (1 mM) acted as the metal source, and the ligands were deposited from an equimolar H_2adc/dabco mixture (0.1 mM each, also in ethanol). When a MTCA-functionalized substrate was used for the deposition at 15 °C, after 45 cycles, uniform plate-like [Zn_2(adc)$_2$(dabco)] nanocrystals with high density on the gold surface could be observed in the SEM and atomic force microscopy (AFM) images (Figure 4).

The thickness and the height of the nanoplates could be estimated from these images and the AFM cross-sectional profile to be around 75 nm and 230 nm, respectively. More interestingly, the nanoplate crystals show a highly vertical alignment at the MTCA surface hinting at a preferred crystallographic orientation. Out-of-plane surface X-ray diffraction (SXRD, Figure 4c) supports this assumption, since only two diffraction peaks at 2θ = 8.1 and 16.2° were observed, which can be assigned to the reflections of the (110) and (220) planes according to the powder XRD pattern of [Zn_2(adc)$_2$(dabco)]. The [110] orientation of the SURMOF is in agreement with the expectation deducible from the crystal structure: The surface carboxylate groups replace, e.g., the leftmost carboxyl groups in Figure 1a, directing the (110) plane (blue) parallel to the substrate surface.

In contrast, the growth of [Zn_2(adc)$_2$(dabco)] on a SAM with monodentate Lewis base headgroups capable of coordinating to the apical sites of the Zn_2 units should lead to a [001] orientated SURMOF, in analogy to the observations made for the isoreticular [Cu_2(ndc)$_2$dabco] SURMOF [42]. To test this, we

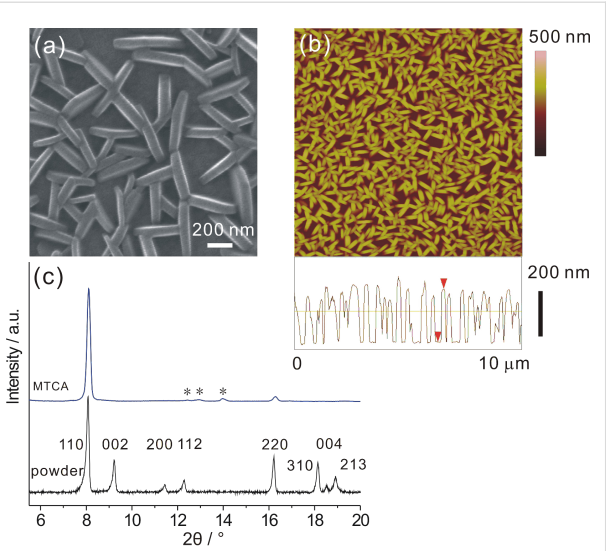

Figure 4: Characterization of [Zn_2(adc)$_2$(dabco)] grown on a MTCA surface at 15 °C after 45 cycles by using the layer-by-layer deposition method. (a) High-magnification SEM image; (b) AFM image and cross-sectional profile; (c) XRD patterns of SURMOF and powder sample. The asterisks denote signals from the background.

employed the pyridine-terminated PPP1 SAM as a substrate. Again plate-like nanocrystals with a thickness of about 60 nm formed after 45 cycles, as shown in Figure 5a. However, this time the nanoplates were lying on the PPP1 surface. That this morphological change is in fact correlated to a different crystallographic orientation can be clearly seen from the SXRD pattern: Only the diffraction peak corresponding to the (002) planes at 2θ = 9.2° became visible, revealing that in this case the SURMOF was oriented along the [001] direction.

It is noteworthy that the deposition temperature is a crucial factor to achieve a completely orientated SURMOF growth. Thus, for the MTCA surface, the perfect [110] orientation was obtained at 15 °C, while on the PPP1 SAM a complete [001] orientation could only be attained at 60 °C. This temperature effect is now under investigation and is not part of the current work.

Fabrication of patterned [Zn_2(adc)$_2$dabco] films by microcontact printing and electron-beam lithography techniques

SAMs cannot only control the crystallographic orientation of SURMOFs, as has been demonstrated above, but in combination with micro/nanofabrication techniques also the lateral control of SURMOF growth is possible, opening valuable opportunities, e.g., for MOF sensor development. Here, we wish to present two different approaches to pattern SAMs, which have been used for the localized growth of SURMOFs. As described in Figure 6, the substrates became patterned with two

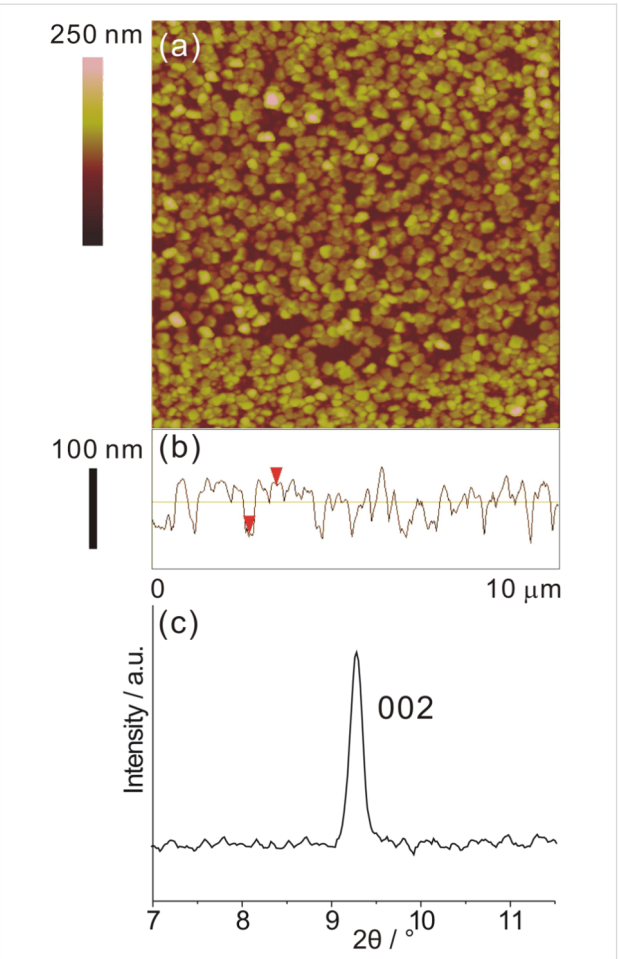

Figure 5: [$Zn_2(adc)_2(dabco)$] grown on a PPP1 surface at 60 °C after 45 cycles. (a) AFM image; (b) cross-sectional profile; (c) SXRD pattern of the range in which the (110) and the (002) reflections are expected.

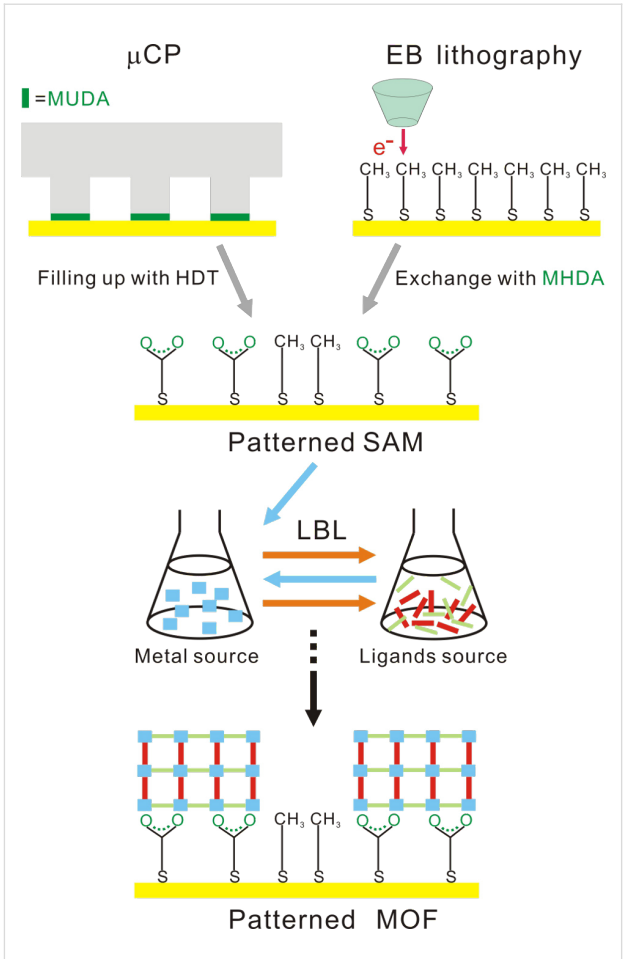

Figure 6: SAMs can be either patterned by µCP (top row, left) or by EB lithography (top row, right) before the layer-by-layer deposition of [$Zn_2(adc)_2(dabco)$] (bottom).

different functional SAMs, one of which could promote the nucleation (such as a –COOH group), while the other inhibits the nucleation (such as a $–CH_3$ group).

One of the methods to create a patterned SAMs is microcontact printing (µCP) [49]. For this, a microstructured polydimethylsiloxane (PDMS) stamp was inked with 11-mercaptoundecanoic acid (MUDA) to transfer a pattern of 3 µm squares to the Au surface. The area surrounding the MUDA patterned parts was filled with 1-hexadecanethiol (HDT) by simple immersion in its ethanolic solution. Due to the chemical properties of –COOH and $–CH_3$, we could expect that the growth of [$Zn_2(adc)_2(dabco)$] would be restricted to the –COOH functionalized areas. As the fluorescence-microscopy image given in Figure 7a demonstrates, the growth of [$Zn_2(adc)_2(dabco)$] on such a patterned surface occurs indeed selectively on the MUDA-functionalized surface (square areas), while the HDT surface shows remarkable inhibition of [$Zn_2(adc)_2(dabco)$] nucleation.

The AFM measurement (Figure 7b,c) shows more details of the SURMOF pattern. In contrast to the nonpatterned MTCA surface, the [$Zn_2(adc)_2(dabco)$] nanocrystals completely cover the MUDA areas, forming a closed, thin film. The average thickness of these films estimated from AFM cross section is about 55 nm after 45 cycles. We believe that the difference in the morphology of [$Zn_2(adc)_2(dabco)$] nanocrystals on both carboxylate (MTCA versus MUDA) terminated surfaces results from the inferior order quality of the MUDA films [40], which causes multiple nucleation sites, from which smaller, but more densely packed MOF crystals grow.

Based on the observation that the exchange reaction of alkanethiol SAMs upon immersion into another ω-substituted alkanethiol solution can be significantly enhanced by electron irradiation, a new patterning technique was developed by Zharnikov et al. [50-54]. Thus, our second strategy to fabricate a patterned SAM was the combination of this irradiation-promoted exchange reaction (IPER) with electron-beam litho-

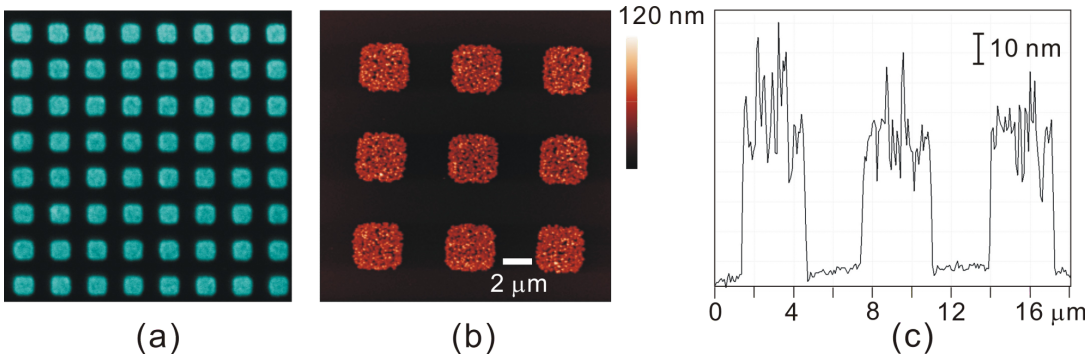

Figure 7: [$Zn_2(adc)_2(dabco)$] patterns grown on MUDA/HDT surfaces (square areas: MUDA, remaining area: HDT) structured by μCP: (a) Epifluorescence image (b) AFM image and (c) AFM cross-sectional profile.

graphy (EB lithography). The primary advantage of EB lithography is that the fabricated features can be in the nanometer regime. Figure 6 (upper right) illustrates the process: Starting from a HDT SAM as the primary matrix, disordering and fragmentation occur within the electron-beam-exposed areas, significantly enhancing the exchange rate during the following immersion into the 16-mercaptohexadecanoic acid (MHDA) solution. These carboxyl-terminated areas then acted as nucleation sites for the growth of the SURMOF, again by the layer-by-layer method. As shown in the optical micrograph in Figure 8a, the irradiated areas indeed became covered with [$Zn_2(adc)_2(dabco)$].

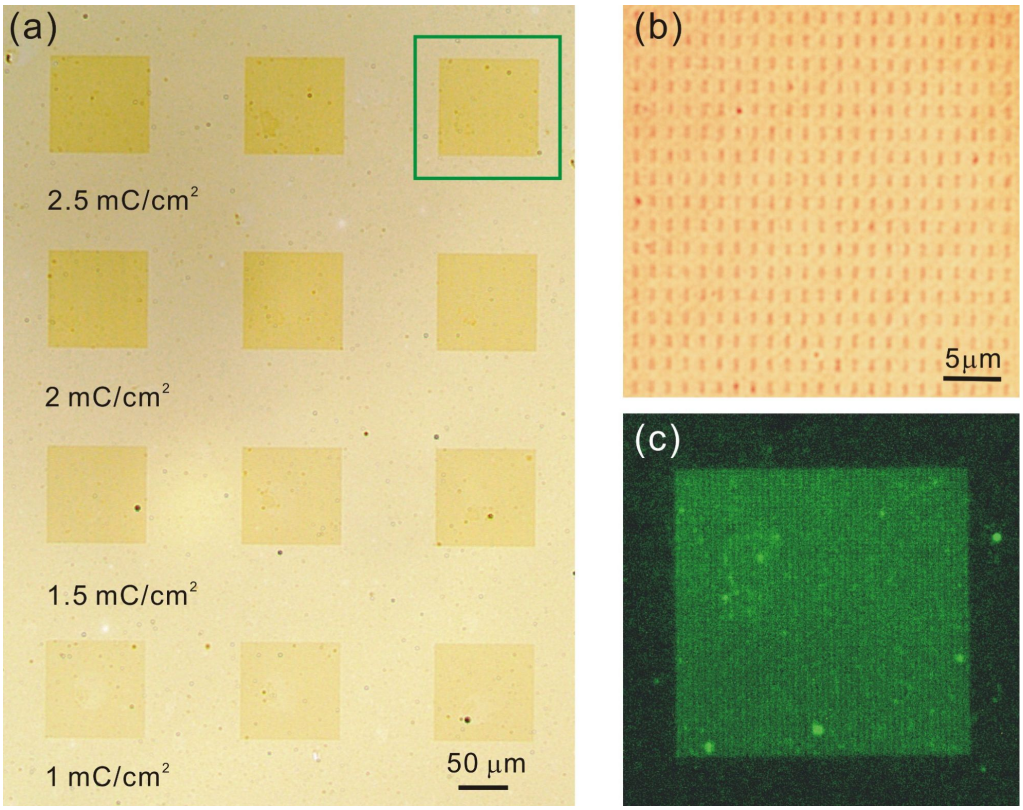

Figure 8: Patterned deposition of [$Zn_2(adc)_2(dabco)$] by using the irradiation-promoted exchange reaction (IPER) to modify the surface chemistry of the SAM. (a) Square arrays of rectangles (1 × 0.3 μm^2) were written into the HDT SAM by using different area doses (increasing from bottom to top), followed by exchange with MHDA, before the layer-by-layer growth of the MOF was performed. (b) Close-up of one of the arrays (area dose: 2.5 mC/cm^2) showing the small rectangular deposits of [$Zn_2(adc)_2(dabco)$]. (c) Epifluorescence image (excitation wavelength 475 nm) of the region marked by the green square in (a).

We also observed that with increasing area dose, the growth of $[Zn_2(adc)_2(dabco)]$ became more pronounced. Obviously with higher doses, more MHDA molecules become exchanged into the HDT matrix, thus promoting the $[Zn_2(adc)_2(dabco)]$ nucleation. The close-up image shows the well-defined rectangles (1×0.3 μm^2) where EB irradiation was performed. Again, the fluorescence microscopy image (Figure 8c) supports the notion that the darker areas in Figure 8a are in fact arrays of rectangles formed by the $[Zn_2(adc)_2(dabco)]$ MOF.

Conclusion

Fluorescent, porous materials, the photoluminescent properties of which are sensitive to certain molecular guests, are promising sensor materials. Nevertheless, their application typically requires some kind of directed immobilization, either regarding their crystallographic orientation, which also determines the orientation and accessibility of their pores, or their lateral distribution, which is a necessity for the fabrication of, e.g., sensor arrays. In this project, we demonstrated the feasibility of self-assembled monolayers for both purposes, since these monolayers are able to interact strongly with the building blocks of the MOFs. In conjunction with the recently established layer-by-layer deposition method, this directed interaction also orients the building blocks during the MOF formation, resulting in well-oriented SURMOF surfaces. When the functional headgroups of the SAM constituents are not distributed evenly over the surface, but are instead patterned, they also direct the location of SURMOF deposition. Two different methods have been employed for the patterning, namely microcontact printing and electron-beam lithography. We demonstrated that both methods provide the possibility to grow SURMOF arrays selectively with micrometer resolution or better. In continuation of this project, we will explore how the orientation of the SURMOFs and their patterning influence the response (selectivity and kinetics) to different analytes.

Experimental

Synthesis of anthracene-9,10-dicarboxylic acid (H_2adc)

The synthesis of 9,10-anthracenedicarboxylic acid mainly followed the procedure described in the literature [55]. *n*-Butyllithium (22.5 mmol, 1.44 g) was added under nitrogen to a suspension of 9,10-dibromoanthracene (7.5 mmol, 2.50 g) in absolute diethyl ether (30 mL). The reaction mixture was stirred for 20 min and a colour change from yellow to dark yellow indicated the formation of the dilithium compound. Dry ice (approximately 10 g) was added to the mixture and stirred until the excess evaporated. After the addition of water (100 mL) and diethyl ether (75 mL), the aqueous phase was separated. Diluted sulfuric acid (H_2SO_4, 3%, 40 mL) was added and an immediate precipitation of yellow crystals was observed. The crude product was collected by filtration and washed with cold water, and then dried overnight in an oven. Recrystallization in diluted ethanol (10%) could not completely remove the impurities (mainly 9-anthracenecarboxylic acid). Therefore, the crude product was purified by gradient sublimation at 250 °C at a pressure of 10^{-5} mbar. ^{1}H NMR (DMSO-d_6, 300 MHz) δ 7.66–7.72 (m, 4H), 8.04–8.10 (m, 4H), 14.14 (br, 2H). Anal. calcd for C, 72.10; H, 3.75; found C, 72.00; H, 4.00.

Synthesis of bulk $[Zn_2(adc)_2(dabco)]$ as a reference material

$[Zn_2(adc)_2(dabco)]$ crystals were prepared according to the literature procedure [36]. $Zn(NO_3)_2{\cdot}6H_2O$ (0.30 g, 1 mmol) and H_2adc (0.27 g, 1 mmol) were dissolved in DMF (5 mL). A solution of dabco (0.06 g, 0.5 mmol) in MeOH (5 mL) was added to the mixture under stirring for 12 h at room temperature. The white precipitate formed was filtered off. The resulting clear solution was heated to 120 °C for 2 d. The colourless crystals were collected and washed with DMF, MeOH and dried in an oven.

Synthesis of $[Zn_2(adc)_2(dabco)]$ nanocrystals

In contrast to the bulk synthesis, no heating was applied. For example, 5 mL of a DMF solution of an equimolar mixture of $Zn(NO_3)_2{\cdot}6H_2O$ and H_2adc, respectively, ("Zn-adc", 50 mM or 25 mM each) was mixed with 5 mL of a 50 mM solution of dabco in methanol under stirring for 15 min at room temperature. Within a few minutes, the mixture turned to a suspension. The precipitate was collected by centrifugation and washed with methanol twice. Finally, the precipitate was dried under vacuum. Yield: 0.13 g. By changing the concentration of the precursor solutions, the other nanocrystal samples were synthesized. The yield for Zn–adc/dabco = 25 mM:25 mM was 0.05 g and for Zn–adc/dabco = 25 mM:12.5 mM was 6 mg.

SAM-functionalized substrates

The Au substrates were manufactured by electron-beam evaporation of 5 nm of Cr and 100 nm of Au onto four-inch Si wafers with (100) orientation. Whenever these films could not be used immediately, they were cleaned prior to use by immersion into a 10 mM 1-hexadecanethiol (HDT, Aldrich) solution in ethanol for 2 h followed by a 2 min treatment in H_2 plasma [56]. The clean gold substrates were immersed either in a 0.1 mM (4'-(pyridin-4-yl)-[1,1-biphenyl]-4-yl)methanethiol (PPP1, synthesized according to [57]) or 0.1 mM 4'-(mercaptomethyl)-terphenyl-4-carboxylic acid (MTCA, synthesized according to [40]) solution in ethanol for 24 h.

Microcontact printing

Patterned SAMs were fabricated by microcontact printing (μCP) using PDMS stamps, which were cast from a master

fabricated by photolithography. The pattern consisted of an array of 3 μm protruding squares with a distance of 3 μm. The stamps were inked with 11-mercaptoundecanoic acid (MUDA, 3 mM solutions in ethanol) and brought into contact with the Au surface for 20 s. The resulting patterned Au substrates were immersed in HDT solution (10 mM in ethanol) for 5 min, and then washed with ethanol followed by drying in a stream of N_2.

Electron-beam lithography

The cleaned Au substrate was immersed into a 10 mM 1-hexadecanethiol (HDT, Aldrich) solution in ethanol for 4 h. After being rinsed with ethanol, and dried with N_2, the sample was ready for e-beam writing. The sample was e-beam patterned by a JEOL JSM-7001F scanning electron microscope, equipped with a XENOS XeDraw2 lithography system. The beam current was 200 pA and the acceleration voltage 15 kV. Area doses were varied between 0.1 and 2.5 mC/cm^2.

Layer-by-layer growth of $[Zn_2(adc)_2(dabco)]$ on SAM-functionalized surfaces

Layer-by-layer deposition was performed in a custom-made, temperature-controllable glass cell. The functionalized substrates were alternately immersed into a zinc acetate dihydrate solution in ethanol (1 mM) for 20 min and in an equimolar H_2adc/dabco mixture (0.1 mM each) for 40 min. Between each step, the substrate was purged with fresh ethanol for 5 min twice.

Characterization

SEM images were recorded on a JEOL JSM 7001F scanning electron microscope. Powder X-ray diffraction patterns were collected between 2θ = 2 and 90°, on a STOE theta/theta diffractometer by using Cu $K\alpha_1$ (1.5418 Å) radiation and a linear position-sensitive detector. The surface X-ray diffraction (SXRD) measurements were performed in theta/theta mode, with a step width of 0.02°, and a scan rate of 100 s per step for thin-film samples. AFM measurements were performed on a NanoScope Dimension^{TM} 3100 atomic force microscope in tapping mode. FT-IR spectra were recorded with a NICOLET 6700 Fourier transform infrared reflection–absorption spectrometer. For bulk substances a diamond ATR cell was used; for thin films on reflective substrates (gold) a modified smart SAGA unit providing an incidence angle of 80° was utilized. SAMs of perdeuterated hexadecanethiol ($C_{16}D_{33}SH$) on gold were used as background samples for the thin-film FT-IR measurement. Photoluminescence spectra were recorded on a PerkinElmer LS 50B fluorescence spectrometer. Epifluorescence images were recorded on an Olympus BX51 fluorescence system. Laser scanning confocal microscopy (LSCM) was carried out on a Zeiss LSM 510 META microscope.

Acknowledgements

We gratefully acknowledge financial support by the Beilstein-Institut, Frankfurt/Main, Germany, within the research collaboration NanoBiC. We thank Dr. L. Fink, Frankfurt, for the help with the acquisition of the PXRD data and Dr. T. Henning (Mikro-/Nanolabor, Gießen) for assisting with the SE microscopy. The generous gift of gold granules by Aurubis, Hamburg, is gratefully acknowledged.

References

1. Murray, L. J.; Dincă, M.; Long, J. R. *Chem. Soc. Rev.* **2009,** *38,* 1294–1314. doi:10.1039/b802256a
2. Lee, J.; Farha, O. K.; Roberts, J.; Scheidt, K. A.; Nguyen, S. T.; Hupp, J. T. *Chem. Soc. Rev.* **2009,** *38,* 1450–1459. doi:10.1039/b807080f
3. Chen, X.-D.; Wan, C.-Q.; Sung, H. H.-Y.; Williams, I. D.; Mak, T. C. W. *Chem.–Eur. J.* **2009,** *15,* 6518–6528. doi:10.1002/chem.200900010
4. Kitagawa, S.; Kitaura, R.; Noro, S.-i. *Angew. Chem., Int. Ed.* **2004,** *43,* 2334–2375. doi:10.1002/anie.200300610
5. Livage, C.; Egger, C.; Férey, G. *Chem. Mater.* **1999,** *11,* 1546–1550. doi:10.1021/cm980781r
6. Rosseinsky, M. J. *Microporous Mesoporous Mater.* **2004,** *73,* 15–30. doi:10.1016/j.micromeso.2003.05.001
7. Li, H.; Eddaoudi, M.; O'Keeffe, M.; Yaghi, O. M. *Nature* **1999,** *402,* 276–279. doi:10.1038/46248
8. Maspoch, D.; Ruiz-Molina, D.; Wurst, K.; Domingo, N.; Cavallini, M.; Biscarini, F.; Tejada, J.; Rovira, C.; Veciana, J. *Nat. Mater.* **2003,** *2,* 190–195. doi:10.1038/nmat834
9. Keskin, S.; Kızılel, S. *Ind. Eng. Chem. Res.* **2011,** *50,* 1799–1812. doi:10.1021/ie101312k
10. Ni, Z.; Masel, R. I. *J. Am. Chem. Soc.* **2006,** *128,* 12394–12395. doi:10.1021/ja0635231
11. Jhung, S. H.; Lee, J.-H.; Yoon, J. W.; Serre, C.; Férey, G.; Chang, J.-S. *Adv. Mater.* **2007,** *19,* 121–124. doi:10.1002/adma.200601604
12. Qiu, L.-G.; Li, Z.-Q.; Wu, Y.; Wang, W.; Xu, T.; Jiang, X. *Chem. Commun.* **2008,** 3642–3644. doi:10.1039/b804126a
13. Li, Z.-Q.; Qiu, L.-G.; Xu, T.; Wu, Y.; Wang, W.; Wu, Z.-Y.; Jiang, X. *Mater. Lett.* **2009,** *63,* 78–80. doi:10.1016/j.matlet.2008.09.010
14. Taylor, K. M. L.; Jin, A.; Lin, W. *Angew. Chem., Int. Ed.* **2008,** *47,* 7722–7725. doi:10.1002/anie.200802911
15. Rieter, W. J.; Taylor, K. M. L.; An, H.; Lin, W.; Lin, W. *J. Am. Chem. Soc.* **2006,** *128,* 9024–9025. doi:10.1021/ja0627444
16. Spokoyny, A. M.; Kim, D.; Sumrein, A.; Mirkin, C. A. *Chem. Soc. Rev.* **2009,** *38,* 1218–1227. doi:10.1039/b807085g
17. Zhuang, J.-L.; Ceglarek, D.; Pethuraj, S.; Terfort, A. *Adv. Funct. Mater.* **2011,** *21,* 1442–1447. doi:10.1002/adfm.201002529
18. Sun, X.; Dong, S.; Wang, E. *J. Am. Chem. Soc.* **2005,** *127,* 13102–13103. doi:10.1021/ja0534809
19. Imaz, I.; Hernando, J.; Ruiz-Molina, D.; Maspoch, D. *Angew. Chem., Int. Ed.* **2009,** *48,* 2325–2329. doi:10.1002/anie.200804255
20. Imaz, I.; Maspoch, D.; Rodríguez-Blanco, C.; Pérez-Falcón, J. M.; Campo, J.; Ruiz-Molina, D. *Angew. Chem., Int. Ed.* **2008,** *47,* 1857–1860. doi:10.1002/anie.200705263
21. Tsuruoka, T.; Furukawa, S.; Takashima, Y.; Yoshida, K.; Isoda, S.; Kitagawa, S. *Angew. Chem., Int. Ed.* **2009,** *48,* 4739–4743. doi:10.1002/anie.200901177

22. Zhuang, J.-L.; Lommel, K.; Ceglarek, D.; Andrusenko, I.; Kolb, U.; Maracke, S.; Sazama, U.; Fröba, M.; Terfort, A. *Chem. Mater.* **2011,** *23,* 5366–5374. doi:10.1021/cm2021092
23. Lu, W.; Chui, S. S.-Y.; Ng, K.-M.; Che, C.-M. *Angew. Chem., Int. Ed.* **2008,** *47,* 4568–4572. doi:10.1002/anie.200704450
24. Carné, A.; Carbonell, C.; Imaz, I.; Maspoch, D. *Chem. Soc. Rev.* **2011,** *40,* 291–305. doi:10.1039/c0cs00042f
25. Shekhah, O.; Liu, J.; Fischer, R. A.; Wöll, C. *Chem. Soc. Rev.* **2011,** *40,* 1081–1106. doi:10.1039/c0cs00147c
26. Li, Y.-S.; Bux, H.; Feldhoff, A.; Li, G.-L.; Yang, W.-S.; Caro, J. *Adv. Mater.* **2010,** *22,* 3322–3326. doi:10.1002/adma.201000857
27. Kreno, L. E.; Leong, K.; Farha, O. K.; Allendorf, M.; Van Duyne, R. P.; Hupp, J. T. *Chem. Rev.* **2012,** *112,* 1105–1125. doi:10.1021/cr200324t
28. Hermes, S.; Schröder, F.; Chelmowski, R.; Wöll, C.; Fischer, R. A. *J. Am. Chem. Soc.* **2005,** *127,* 13744–13745. doi:10.1021/ja053523l
29. Shekhah, O.; Wang, H.; Kowarik, S.; Schreiber, F.; Paulus, M.; Tolan, M.; Sternemann, C.; Evers, F.; Zacher, D.; Fischer, R. A.; Wöll, C. *J. Am. Chem. Soc.* **2007,** *129,* 15118–15119. doi:10.1021/ja076210u
30. Biemmi, E.; Scherb, C.; Bein, T. *J. Am. Chem. Soc.* **2007,** *129,* 8054–8055. doi:10.1021/ja0701208
31. Shekhah, O.; Wang, H.; Paradinas, M.; Ocal, C.; Schüpbach, B.; Terfort, A.; Zacher, D.; Fischer, R. A.; Wöll, C. *Nat. Mater.* **2009,** *8,* 481–484. doi:10.1038/nmat2445
32. Demessence, A.; Horcajada, P.; Serre, C.; Boissière, C.; Grosso, D.; Sanchez, C.; Férey, G. *Chem. Commun.* **2009,** 7149–7151. doi:10.1039/b915011k
33. Ameloot, R.; Stappers, L.; Fransaer, J.; Alaerts, L.; Sels, B. F.; De Vos, D. E. *Chem. Mater.* **2009,** *21,* 2580–2582. doi:10.1021/cm900069f
34. Makiura, R.; Motoyama, S.; Umemura, Y.; Yamanaka, H.; Sakata, O.; Kitagawa, H. *Nat. Mater.* **2010,** *9,* 565–571. doi:10.1038/nmat2769
35. Schoedel, A.; Scherb, C.; Bein, T. *Angew. Chem., Int. Ed.* **2010,** *49,* 7225–7228. doi:10.1002/anie.201001684
36. Tanaka, D.; Horike, S.; Kitagawa, S.; Ohba, M.; Hasegawa, M.; Ozawa, Y.; Toriumi, K. *Chem. Commun.* **2007,** 3142–3144. doi:10.1039/b707947h
37. Cui, Y.; Yue, Y.; Qian, G.; Chen, B. *Chem. Rev.* **2012,** *112,* 1126–1162. doi:10.1021/cr200101d
38. Wang, J.-J.; Liu, C.-S.; Hu, T.-L.; Chang, Z.; Li, C.-Y.; Yan, L.-F.; Chen, P.-Q.; Bu, X.-H.; Wu, Q.; Zhao, L.-J.; Wang, Z.; Zhang, X.-Z. *CrystEngComm* **2008,** *10,* 681–692. doi:10.1039/b710209g
39. Kim, Y. H.; Shin, D. C.; Kim, S.-H.; Ko, C.-H.; Yu, H.-S.; Chae, Y.-S.; Kwon, S. K. *Adv. Mater.* **2001,** *13,* 1690–1693. doi:10.1002/1521-4095(200111)13:22<1690::AID-ADMA1690>3.0.CO;2-K
40. Himmel, H.-J.; Terfort, A.; Wöll, C. *J. Am. Chem. Soc.* **1998,** *120,* 12069–12074. doi:10.1021/ja981872s
41. Liu, J.; Schüpbach, B.; Bashir, A.; Shekhah, O.; Nefedov, A.; Kind, M.; Terfort, A.; Wöll, C. *Phys. Chem. Chem. Phys.* **2010,** *12,* 4459–4472. doi:10.1039/b924246p
42. Zacher, D.; Yusenko, K.; Bétard, A.; Henke, S.; Molon, M.; Ladnorg, T.; Shekhah, O.; Schüpbach, B.; de los Arcos, T.; Krasnopolski, M.; Meilikhov, M.; Winter, J.; Terfort, A.; Wöll, C.; Fischer, R. A. *Chem.–Eur. J.* **2011,** *17,* 1448–1455. doi:10.1002/chem.201002381
43. Mizobe, Y.; Miyata, M.; Hisaki, I.; Hasegawa, Y.; Tohnai, N. *Org. Lett.* **2006,** *8,* 4295–4298. doi:10.1021/ol0616440
44. Zacher, D.; Shekhah, O.; Wöll, C.; Fischer, R. A. *Chem. Soc. Rev.* **2009,** *38,* 1418–1429. doi:10.1039/b805038b
45. Ameloot, R.; Gobechiya, E.; Uji-i, H.; Martens, J. A.; Hofkens, J.; Alaerts, L.; Sels, B. F.; De Vos, D. E. *Adv. Mater.* **2010,** *22,* 2685–2688. doi:10.1002/adma.200903867
46. Motoyama, S.; Makiura, R.; Sakata, O.; Kitagawa, H. *J. Am. Chem. Soc.* **2011,** *133,* 5640–5643. doi:10.1021/ja110720f
47. Shekhah, O.; Wang, H.; Zacher, D.; Fischer, R. A.; Wöll, C. *Angew. Chem., Int. Ed.* **2009,** *48,* 5038–5041. doi:10.1002/anie.200900378
48. Bétard, A.; Fischer, R. A. *Chem. Rev.* **2012,** *112,* 1055–1083. doi:10.1021/cr200167v
49. Xia, Y.; Whitesides, G. M. *Annu. Rev. Mater. Sci.* **1998,** *28,* 153–184. doi:10.1146/annurev.matsci.28.1.153
50. Ballav, N.; Shaporenko, A.; Krakert, S.; Terfort, A.; Zarnikov, M. *J. Phys. Chem. C* **2007,** *111,* 7772–7782. doi:10.1021/jp0700635
51. Ballav, N.; Terfort, A.; Zharnikov, M. *Langmuir* **2009,** *25,* 9189–9196. doi:10.1021/la9007476
52. Ballav, N.; Thomas, H.; Winkler, T.; Terfort, A.; Zharnikov, M. *Angew. Chem., Int. Ed.* **2009,** *48,* 5833–5836. doi:10.1002/anie.200900950
53. Ballav, N.; Shaporenko, A.; Terfort, A.; Zharnikov, M. *Adv. Mater.* **2007,** *19,* 998–1000. doi:10.1002/adma.200602168
54. Zhao, J. L.; Terfort, A.; Zharnikov, M. *J. Phys. Chem. C* **2011,** *115,* 14058–14066. doi:10.1021/jp202758e
55. Herrmann, U.; Tümmler, B.; Maass, G.; Mew, P. K. T.; Vögtle, F. *Biochemistry* **1984,** *23,* 4059–4067. doi:10.1021/bi00313a008
56. Raiber, K.; Terfort, A.; Benndorf, C.; Krings, N.; Strehblow, H.-H. *Surf. Sci.* **2005,** *595,* 56–63. doi:10.1016/j.susc.2005.07.038
57. Schüpbach, B.; Terfort, A. *Org. Biomol. Chem.* **2010,** *8,* 3552–3562. doi:10.1039/C003795H

License and Terms

Beilstein Journal of Nanotechnology

Focused electron beam induced deposition: A perspective

Michael Huth*[1], Fabrizio Porrati[1], Christian Schwalb[1], Marcel Winhold[1], Roland Sachser[1], Maja Dukic[2], Jonathan Adams[2] and Georg Fantner[2]

Review

Open Access

Address:
[1]Physikalisches Institut, Max-von-Laue-Str. 1, Goethe-Universität, 60438 Frankfurt am Main, Germany and [2]Institute of Bioengineering, EPFL, STI IBI-STI LBNI, BM 3109 (Bâtiment BM), Station 17, CH-1015 Lausanne, Switzerland

Email:
Michael Huth* - michael.huth@physik.uni-frankfurt.de

* Corresponding author

Keywords:
atomic force microscopy; binary systems; electron beam induced deposition; granular metals; micro Hall magnetometry; radiation-induced nanostructures; strain sensing

Beilstein J. Nanotechnol. **2012,** *3,* 597–619.
doi:10.3762/bjnano.3.70

Received: 08 June 2012
Accepted: 19 July 2012
Published: 29 August 2012

This article is part of the Thematic Series "Radiation-induced nanostructures: Formation processes and applications".

Associate Editor: A. Gölzhäuser

Abstract

Background: Focused electron beam induced deposition (FEBID) is a direct-writing technique with nanometer resolution, which has received strongly increasing attention within the last decade. In FEBID a precursor previously adsorbed on a substrate surface is dissociated in the focus of an electron beam. After 20 years of continuous development FEBID has reached a stage at which this technique is now particularly attractive for several areas in both, basic and applied research. The present topical review addresses selected examples that highlight this development in the areas of charge-transport regimes in nanogranular metals close to an insulator-to-metal transition, the use of these materials for strain- and magnetic-field sensing, and the prospect of extending FEBID to multicomponent systems, such as binary alloys and intermetallic compounds with cooperative ground states.

Results: After a brief introduction to the technique, recent work concerning FEBID of Pt–Si alloys and (hard-magnetic) Co–Pt intermetallic compounds on the nanometer scale is reviewed. The growth process in the presence of two precursors, whose flux is independently controlled, is analyzed within a continuum model of FEBID that employs rate equations. Predictions are made for the tunability of the composition of the Co–Pt system by simply changing the dwell time of the electron beam during the writing process. The charge-transport regimes of nanogranular metals are reviewed next with a focus on recent theoretical advancements in the field. As a case study the transport properties of Pt–C nanogranular FEBID structures are discussed. It is shown that by means of a post-growth electron-irradiation treatment the electronic intergrain-coupling strength can be continuously tuned over a wide range. This provides unique access to the transport properties of this material close to the insulator-to-metal transition. In the last part of the review, recent developments in mechanical strain-sensing and the detection of small, inhomogeneous magnetic fields by employing nanogranular FEBID structures are highlighted.

Conclusion: FEBID has now reached a state of maturity that allows a shift of the focus towards the development of new application fields, be it in basic research or applied. This is shown for selected examples in the present review. At the same time, when seen from a broader perspective, FEBID still has to live up to the original idea of providing a tool for electron-controlled chemistry on the nanometer scale. This has to be understood in the sense that, by providing a suitable environment during the FEBID process, the outcome of the electron-induced reactions can be steered in a controlled way towards yielding the desired composition of the products. The development of a FEBID-specialized surface chemistry is mostly still in its infancy. Next to application development, it is this aspect that will likely be a guiding light for the future development of the field of focused electron beam induced deposition.

Review

Introduction

Focused electron beam induced deposition (FEBID) is receiving strongly increasing attention as a direct-writing technique for nanostructures due to its great versatility. In FEBID a previously adsorbed molecular precursor is dissociated in the focus of an electron beam provided by a scanning or transmission electron microscope (SEM/TEM). By and large, the focal area diameter of the electron beam, convoluted by the surface-leaving secondary electrons, determines the lateral resolution of this method. Resolutions better than 3 nm in SEMs [1] and even below 1 nm in TEMs [2] have been shown to be feasible. Due to this excellent resolution, FEBID, with the extension of focused electron beam induced etching (FEBIE), is now the de facto standard in mask repair for the 193 nm node [3]. It also holds great promise for circuit editing. Several reviews have been published in recent years [4,5] discussing various aspects of FEBID, or focused electron beam induced processing (FEBIP), the most comprehensive of which is the excellent article by Utke, Hoffmann and Melngailis [6]. These reviews mainly cover the principles of gas-assisted deposition and etching with electrons, provide a summary of modeling approaches to FEBIP, and give some details of the various characterization techniques for FEBID structures. Application fields in research are discussed with a strong view to potential uses in industry.

In this review, some very recent developments in FEBID-based research are presented. In this context we limit the presentation to an interrelated group of topics covering the importance of granular metals obtained from FEBID for basic research in correlation physics, as well as the potential for application of these granular metals in magnetic and strain sensing. Furthermore, the extensibility of FEBID to the preparation of binary metals is discussed with a prospect of directly writing a wider range of magnetic or superconducting structures on the nanometer scale. After a very brief discourse of the FEBID process presented in the next section, the modeling of FEBID on the basis of rate equations is discussed with a view to more than one precursor being present during the process. This leads on to the third section, which presents some recent results on the preparation and characterization of binary FEBID structures, with special focus on magnetism and superconductivity. The following section reviews the particular advantages that FEBID structures provide in resolving long-standing issues in the physics of nanogranular metals close to the metal–insulator transition. The implications of the nanogranular microstructure, often obtained in FEBID, for sensor applications are subsequently presented. Nanogranular structures, i.e., structures that contain metal nanocrystallites embedded in a dielectric matrix, have special properties that make them particularly suitable for magnetic-field- and strain-sensing applications. The conclusion will present our views on the challenges that FEBID will have to face in the near to midterm future.

FEBID: Brief review of the fundamentals

FEBID in a nutshell: The FEBID process is based on the electron-induced dissociation of a molecular precursor previously adsorbed on a substrate surface and constantly replenished by a gas-supply system. In most instances the gas-supply or gas-injection system consists of a precursor reservoir that can be heated or cooled, and which is coupled to a fine capillary with a typical diameter of 0.5 mm. The open end of the capillary can be brought into close proximity to the substrate surface on which the electron beam is focused.

Technical parameters: The main parameters that govern the writing process are the primary-beam energy E and beam current I, the time for which the electron beam is held constant on a particular point on the surface, the dwell time t_D, the distance between neighboring dwell points, the pitch p, and the number of loops for which the writing pattern is repeated, n_L. Further important parameters are the replenishment time, t_r, i.e., the time period for which the writing is paused between two successive loops, and the geometry of the writing path, i.e., zig-zag, meander or spiral, to list the most commonly used. Figure 1 gives a graphical overview of the FEBID process.

Precursor chemistry: Suitable precursors for the FEBID process, which mostly takes place with the precursor and sub-

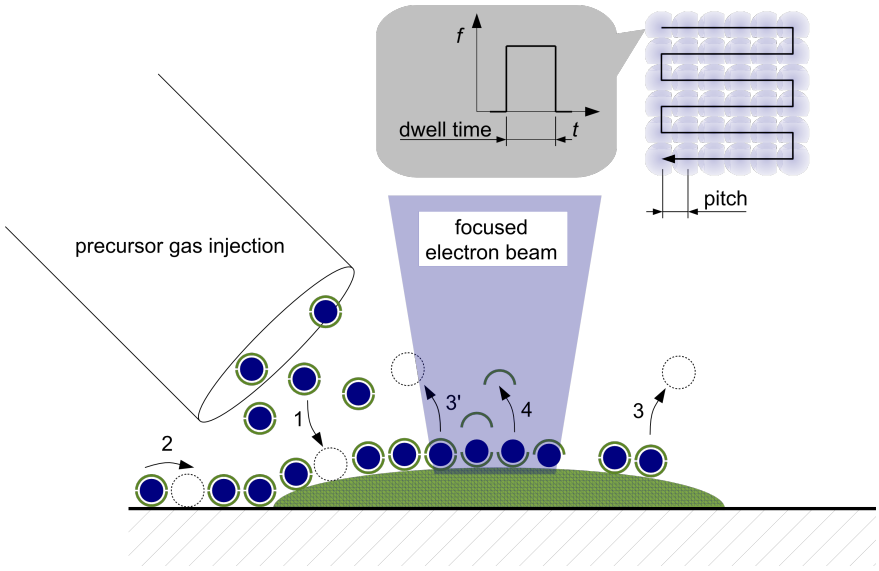

Figure 1: Illustration of FEBID. Precursor molecules (here: organometallic complex; blue: metal, green: organic ligands) are supplied by a gas-injection system and physisorb (1) on the surface. Surface diffusion (2), thermally induced desorption (3) and electron-stimulated desorption (3') take place. Within the focus of the electron beam, adsorbed precursor molecules are (partly) dissociated followed by desorption of volatile organic ligands (4). Upper right: For pattern definition the electron beam is moved in a raster fashion (here: serpentine) over the surface and settles on each dwell point for a specified dwell time. After one raster sequence is completed the process is repeated until a predefined number of repeated loops is reached.

strate temperature close to room temperature, need to have sufficiently high vapor pressures in the temperature range of about 270 K to 320 K. A typical vapor pressure would be 10^{-2} to 10 mbar for organometallic precursors, but this can only serve as a very crude guideline. A very detailed account on FEBID precursors and their properties can be found in Utke et al. [6], ordered according to the respective type of organic ligand. Quite generally speaking, once supplied to the substrate a precursor must have a sufficiently long residence time τ on the surface, typically lasting microseconds to milliseconds. Otherwise, at typical energy-dependent dissociation cross sections $\sigma(E)$ of 10^{-3} to 10^{-2} nm^2 in the energy range below 500 eV for metal–organic precursors, the deposition yield would be too small. On the other hand, the volatile organic dissociation products should readily desorb to prevent their usually undesired inclusion in the deposit. Depending on the targeted functionality of the FEBID structure, several different precursor classes are employed, such as alkanes, silanes, metal halogens, carbonyls, phosphines, acetylacetonates and so forth. In the following the focus is on organometallic precursors. Popular representatives for the transition metals are carbonyls, such as $W(CO)_6$ or $Co_2(CO)_8$, but also more complex precursors, such as $Me_3Pt(IV)CpMe$. For details the reader is referred to Utke et al. [6]. With a view to the following sections silane-based precursors, such as neo-pentasilane Si_5H_{12}, are also of interest. The chemical-bond structure is highly relevant for the details of the electron-induced dissociation process, which is discussed next.

Electron-induced dissociation: Many different electron–molecule interaction processes are relevant for FEBID. They can be summarized as shown in Table 1.

Table 1: Electron–molecule interaction processes relevant for FEBID according to [3]. Rotational excitations are not explicitly included. E_i: initial kinetic energy of electron, E_r: residual kinetic energy of electron after process.

	process type
$e^-(E_i) + AB \rightarrow AB + e^-(E_i)$	elastic scattering
$e^-(E_i) + AB \rightarrow AB(v) + e^-(E_r)$	vibrational excitation (VE)
$e^-(E_i) + AB \rightarrow AB^* + e^-(E_r)$	electronic excitation (EE)
$e^- + AB \rightarrow A^\bullet + B^-$	dissociative electron attachment (DEA)
$e^- + AB \rightarrow A^\bullet + B^\bullet + e^-$	neutral dissociation (ND)
$e^- + AB \rightarrow A^\bullet + B^+ + 2e^-$	dissociative ionization (DI)
$e^- + AB \rightarrow A^- + B^+ + e^-$	bipolar dissociation / ion pair formation (BD)

Depending on the energy range, various different specialized instruments have to be applied to acquire absolute energy-dependent cross sections for these processes. For FEBID the relevant energy range is 1 meV (slowed-down secondary electrons) up to the keV regime (typical primary electron regime, forward and backscattered electrons). As a consequence, complete cross section data sets are very rare, and this is in particular the case for precursors commonly used in FEBID. In particular, one has to keep in mind that dissociation cross sections obtained on precursor molecules in the gas phase do not necessarily provide a suitable basis for a quantitative description of precursors in an adsorbed state. The coupling to the substrate provides additional relaxation channels for both electronic and vibronic excitations. As an additional complexity, one has to note that several relevant cross sections, such as those of transient molecules produced in FEBID, are very hard to measure or may even be inaccessible to quantification. Therefore, theoretical advancements in calculating reliable energy-dependent cross sections are of special importance. At the present stage it is fair to say that for none of the precursors commonly used in FEBID is a full set of data of energy-dependent cross sections available, although some energy-dependent data for a few precursors can be found in the literature [3,6]. The reader is referred to Utke et al. [3] for a detailed account on the fundamentals of the interactions of electrons with molecules relevant for FEBID.

As a consequence of the lack of reliable energy-dependent cross-section data, in all attempts at modeling FEBID effectively, energy-integrated dissociation cross sections are used. These can be self-consistently obtained from the modeling approach, by comparison with the experimentally determined deposition yields. An additional important aspect is that previously deposited material is constantly irradiated as the deposition progresses since the electrons typically penetrate at least 100 nm into the grown structures at the often-employed primary energy of 5 keV. Nondissociated precursor fragments, which have been embedded in the deposit during the FEBID process, can thus become subject to post-growth dissociation. As a matter of fact, post-growth irradiation can be advantageously used for fine-tuning the electronic transport properties of FEBID structures, and this will be discussed in the context of nanogranular structures later in this review. In any case, the energy spectrum of the electrons that can take part in the FEBID process is important and will be briefly reviewed in the following paragraph.

Spectrum of relevant electrons: Assuming an aberration-free primary electron beam with proper astigmatic correction, the radial flux distribution impinging on a plane surface has the shape of a Gaussian

$$f(r) = \frac{I/e}{2\pi a^2} \exp\left(-\frac{r^2}{2a^2}\right) \quad (1)$$

where $f(r)$ defines the radial flux per unit time and area, and a is the standard deviation. As a possible measure of the focal diameter of the beam, the full width at half maximum (FWHM) can be used, which amounts to $2a\sqrt{2\ln 2} \approx 2.36a$. These primary electrons are subject to interactions with the precursor molecules but also with the underlying substrate. They generate secondary electrons, which are produced by inelastic collisions with the weakly bound valence electrons in the substrate or previously grown deposit. In general, the spectrum of secondary electrons depends on the properties of the substrate material and is characterized by a maximum in the low-energy region from 1 to 10 eV, followed by a tail to higher energies that roughly decreases with the third power of E.

An idealized spectral shape was suggested by Chung and Everhart [7], which does in fact provide a reasonable description of the higher-energy tail:

$$f_{SE}(E) \propto \frac{E}{(E+\Phi)^4} \quad (2)$$

with the work function Φ. For FEBID, in particular with a view to the microstructure of the typically obtained inhomogeneous deposits, which then act as a "growing substrate", the spectrum of secondary electrons is a priori unknown. Considering the fact that the radial density distribution of the surface-leaving electrons is very important for FEBID, in particular since the dissociation cross sections tend to be larger at low energies, Monte Carlo simulations, describing in detail the electron transport in the substrate and deposit, provide important insights [8,9]. For the purpose of the present review it suffices to state that it is mainly the lateral range of the surface-leaving secondary electrons that limits the resolution of FEBID. Nevertheless, sub-3 nm resolution is achievable in high-resolution SEMs for small-aspect-ratio structures [2]. The electron flux used in the FEBID modeling approach presented in the next section effectively incorporates the contribution of secondary electrons. The influence of forward-scattered electrons is important for high-aspect-ratio FEBID structures and can be properly accounted for in Monte Carlo simulations [8,9].

Deposit microstructure: The microstructure of materials obtained by FEBID falls into the three categories amorphous, nanogranular or nanocomposite and polycrystalline. Depending on the microstructure the physical properties vary substantially, e.g., with regard to electrical transport, magnetism or the

mechanical strength. Since the local growth rates can be very high, reaching tens to hundreds of nanometers per second, growth proceeds far from equilibrium and is mainly kinetically controlled. A qualitative understanding of the processes resulting in these microstructure classes can be gained from modeling the evolution of phase boundaries in solids at the nanoscale. The formation of a nanogranular microstructure in particular can be understood in the framework of Cahn–Hilliard-like equations applied to such aspects as spinodal decomposition or nucleation [10]. At this point a similarity to the microstructure formation processes in the growth of diamond-like carbon (DLC) films with metal additives can be stated [11]. A distinct difference between FEBID and DLC thin-film research is of course that, in most instances, attempts are made to tune the FEBID process such that carbon inclusion in the deposit can be avoided, whereas in DLC thin-films the carbon component is essential with regard to the desired mechanical or electrical properties. Nevertheless, considering the substantial amount of literature devoted to DLC research, much can be learned concerning the microstructure formation processes. In FEBID it can be observed that organometallic precursors with metal atoms having a tendency to carbide formation result mainly in amorphous deposits, whereas precursors with metals that are immiscible with carbon tend to yield nanogranular structures, i.e., they form metallic nanocrystallites embedded in an amorphous, carbonaceous matrix. In DLC thin-film growth, which is mostly done by reactive sputtering in a mixed Ar and acetylene gas atmosphere from a metallic target, analogous observations are made with regard to the microstructure depending on the miscibility of the target metal with carbon. The granular microstructure is most interesting for basic research on nanogranular metals as artificial nanosolids, in particular if the electronic coupling strength between the metallic grains can be tuned through the insulator-to-metal transition. The exact nature of this transition in three spatial dimensions is not known yet [12]. Also with regard to sensor applications nanogranular materials prepared by FEBID hold great promise. These aspects will be discussed in later chapters of this review. For selected precursors, such as $Co_2(CO)_8$ [13], $Fe(CO)_5$ [14,15] and also $AuClPF_3$ [16], polycrystalline deposits can be obtained with only small carbon impurity contributions.

So far the complexity of the beam-induced chemical reaction pathways is too large to allow us to develop a detailed understanding of the microscopic formation processes that result in a particular microstructure and elemental composition. Very few surface-science-oriented experiments that try to get an understanding of the deposition process on the molecular level have been performed under well-controlled conditions, such as ultra-high vacuum. A recent brief overview of this research can be found in Wnuk et al. [17]. Also, initial steps in the analysis, by theoretical means, of the adsorption process of commonly used precursors on thermally grown SiO_2 surfaces, often employed in FEBID, have only recently been taken within a density functional approach including van der Waals corrections [18-20].

FEBID modeling

To date no attempts have been made to realistically simulate the nanostructure formation process during FEBID. This must remain a goal for the future. What has been achieved is the modeling of process rates and the simulation of growth geometries. Process rate calculations are almost solely based on continuum models that rely on differential equations for the rate of change of adsorbates relevant for the FEBID process. This will be the focus of this section, with particular emphasis on employing this approach to multicomponent scenarios relevant for the formation of binary FEBID structures, i.e., structures grown in the presence of two different precursor species. The modeling of growth geometries is mainly done by Monte Carlo approaches and allows for integrating the simulation of the electron–solid interaction processes with the surface-based dissociation rates at the cost of a substantially larger numerical complexity [21].

Single precursor species continuum model of FEBID

The single precursor species continuum model of FEBID assumes a weak precursor–substrate interaction of the van der Waals type and relies on a Langmuir adsorption description neglecting possible interactions between the adsorbed precursor molecules. The surface coverage is assumed to be limited to one monolayer, such that the maximum fractional coverage n/n_{ML} is 1, where n_{ML} stands for the full area density of a complete precursor monolayer and n for the temporally and spatially dependent precursor adsorbate density. The fraction of surface sites that is available for adsorption is therefore $1 - n/n_{ML}$. The model also includes surface diffusion, with diffusion constant D, and an average residence time τ for the precursor molecules before desorption. It furthermore takes into account the electron-induced dissociation leading to a reduction of the adsorbate density assuming an energy-integrated dissociation cross section σ. The electron flux profile $f(r)$ at the sample surface is taken to be radially symmetric and can be obtained from Monte Carlo simulations of the electron–solid interaction. Under these conditions the radially symmetric rate equation reads [22]

$$\frac{\partial n(r,t)}{\partial t} = \underbrace{sJ\left(1-\frac{n(r,t)}{n_{ML}}\right)}_{\text{adsorption}} - \underbrace{\frac{n(r,t)}{\tau}}_{\text{desorption}} \underbrace{-\sigma f(r) n(r,t)}_{\text{dissociation}} + \underbrace{D\left(\frac{\partial^2 n(r,t)}{\partial r^2} + \frac{1}{r}\frac{\partial n(r,t)}{\partial r}\right)}_{\text{diffusion}} \quad (3)$$

where J is the precursor flux modified by the sticking coefficient s. The local growth rate $R(r)$ of the deposit, assuming the volume V for the nonvolatile dissociation product of an individual precursor molecule, is then obtained from

$$R = \frac{V\sigma f(r)}{t_D}\int_0^{t_D} n(r,t)\mathrm{d}t \tag{4}$$

with t_D denoting the beam dwell time.

Valuable insight can be obtained from the analytical solution of the rate equation, if the diffusion term is neglected. Depending on the diffusion constant this is a good approximation for short dwell times. Taking $f = f(r = 0)$ as the electron flux at the beam center one obtains, after direct integration

$$n(t) = \left(n_r - n_d\right)\mathrm{e}^{-k_d t} + n_d \tag{5}$$

and consequently

$$R = V\sigma f\left[\left(n_r - n_d\right)\frac{1-\mathrm{e}^{-k_d t_D}}{k_d t_D} + n_d\right] \tag{6}$$

with the depletion rate k_d defined as

$$k_d = \frac{sJ}{n_{ML}} + \frac{1}{\tau} + \sigma f \tag{7}$$

and the depleted adsorbate density $n_d = sJ/k_d$. The initial adsorbate density $n(t = 0)$ was set to the adsorbate density after long times n_r in the absence of the dissociation term. It is defined by the replenishment rate k_r given by

$$k_r = \frac{sJ}{n_{ML}} + \frac{1}{\tau} \tag{8}$$

via the relation $n_r = sJ/k_r$.

The important result obtained from this analysis is the generic shape of the deposit growth rate R as a function of the dwell time t_D, as is shown in Figure 2. For the calculation, the a priori unknown model parameters σ and τ are needed. These can in fact be obtained from fitting of the dwell-time-dependent growth rates for different precursor flux settings J by using Equation 6, as e.g., detailed in Utke et al. [6]. Here parameters for the precursor $Me_3Pt(IV)CpMe$ have been used, as given in the figure caption.

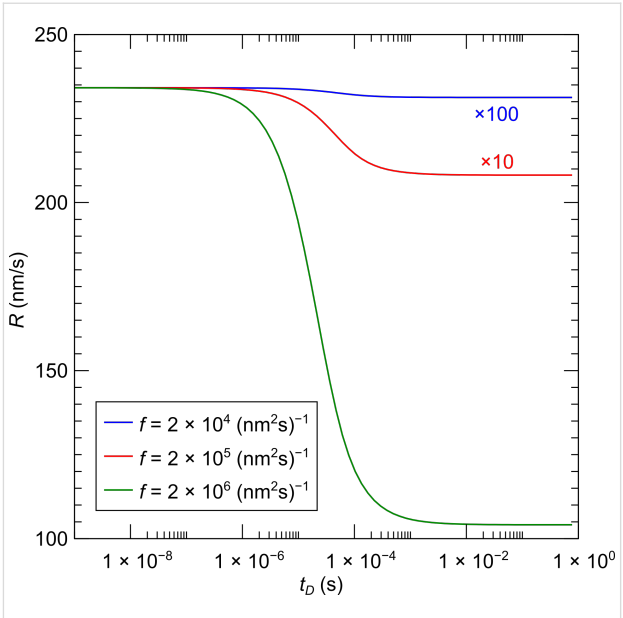

Figure 2: Single-species growth rate calculated for the precursor $Me_3Pt(IV)CpMe$ assuming three different electron-flux values as indicated. The flux values correspond to beam currents of approximately 0.1, 1 and 10 nA with a beam diameter of 20 nm. The model parameters $\sigma = 2.2 \times 10^{-2}$ nm^2 [23] and $\tau = 29$ µs [24] were used. The effective precursor flux was set to $sJ = 1.5 \times 10^3$ (nm^{2}s)$^{-1}$.

Apparently the growth rate is proportional to the electron flux for very short dwell times, which is termed as the *reaction-rate-limited* (RRL) regime. For longer dwell times the precursor adsorbate becomes depleted as a consequence of the dissociation rate exceeding the replenishment rate. The resulting growth regime is *mass-transport-limited* (MTL). Since the characteristic dwell time for which, at a given precursor and electron flux, the crossover between the growth regimes takes place is precursor specific, an interesting FEBID-specific observation can be made with regard to using two (or more) adsorbate species. In this case, conditions can in principle be found under which, by varying the dwell time alone, the growth regimes for the precursors can be made to differ. As a consequence, under otherwise constant conditions the dwell time can be used as the decisive parameter to appreciably change the material composition. Firstly, this is of relevance in finding optimum process conditions for preventing the undesired inclusion of impurity adsorbates from the residual gas. In this case the residual gas adsorbate would act as a second precursor. Secondly, for the preparation of binary FEBID structures by using two or more functional precursors, a recipe for the fine-tuning of the material composition by variation of the dwell time can be devised. In the next subsection the continuum model will therefore be extended to a multicomponent variant.

Multicomponent extension of the continuum model

The extension of the model described above to the multicomponent case was first introduced by Lobo and Toth in order to describe simultaneous FEBID and focused electron beam induced etching (FEBIE) [25]. Etching can intentionally be induced by supplying a reactive precursor, such as XeF_2. Bernau et al. adapted this model to describe the deposition process in the presence of a functional precursor and a typical hydrocarbon contaminant from the residual gas [26]. For two precursors the rate equations read

$$\frac{\partial n_1}{\partial t} = s_1 J_1 \left(1 - \left[\frac{n_1}{\bar{n}_1} + \frac{n_2}{\bar{n}_2}\right]\right) - \frac{n_1}{\tau_1} - \sigma_1 f(r) n_1 + D_1 \left(\frac{\partial^2 n_1}{\partial r^2} + \frac{1}{r}\frac{\partial n_1}{\partial r}\right) \tag{9}$$

$$\frac{\partial n_2}{\partial t} = s_2 J_2 \left(1 - \left[\frac{n_1}{\bar{n}_1} + \frac{n_2}{\bar{n}_2}\right]\right) - \frac{n_2}{\tau_2} - \sigma_2 f(r) n_2 + D_2 \left(\frac{\partial^2 n_2}{\partial r^2} + \frac{1}{r}\frac{\partial n_2}{\partial r}\right) \tag{10}$$

$$\frac{\partial N}{\partial t} = \sigma_1 f(r) n_1 + \sigma_2 f(r) n_2 \tag{11}$$

which we consider in the following in a simplified form without the diffusion term and taking again $f(r = 0) = f$ as electron flux at the beam center

$$\frac{\partial n_1}{\partial t} = s_1 J_1 \left(1 - \left[\frac{n_1}{\bar{n}_1} + \frac{n_2}{\bar{n}_2}\right]\right) - \frac{n_1}{\tau_1} - \sigma_1 f n_1 \tag{12}$$

$$\frac{\partial n_2}{\partial t} = s_2 J_2 \left(1 - \left[\frac{n_1}{\bar{n}_1} + \frac{n_2}{\bar{n}_2}\right]\right) - \frac{n_2}{\tau_2} - \sigma_2 f n_2 \tag{13}$$

$$\frac{\partial N}{\partial t} = \sigma_1 f n_1 + \sigma_2 f n_2 \tag{14}$$

This system of coupled equations can be analytically solved and leads to

$$n_i(t) = n_{di} + e^{-\bar{k}_d}\left[\Delta n_i \cosh(\kappa t) + N_i \sinh(\kappa t)\right] \tag{15}$$

with $i = 1, 2$ using the following abbreviating definitions

$$n_{di} = \frac{\left(s_i J_i k_{dj} - s_j J_j k_{ci}\right)}{\left(k_{d1}k_{d2} - k_{c1}k_{c2}\right)}$$

$$n_{ri} = \frac{s_i J_i \tau_i n_{ML,1} n_{ML,2}}{\left(s_1 J_1 \tau_1 n_{ML,2} + s_2 J_2 \tau_2 n_{ML,1} + n_{ML,1} n_{ML,2}\right)}$$

$$\Delta n_i = n_{ri} - n_{di}$$

$$N_i = \left[\left(\bar{k}_d - k_{di}\right)\Delta n_i - k_{ci}\Delta n_j\right] / \kappa$$

$$k_{di} = s_i J_i / n_{ML,i} + 1/\tau_i + \sigma_i f$$

$$k_{ri} = s_i J_i / n_{ML,i} + 1/\tau_i$$

$$k_{ci} = s_i J_i / n_{ML,j}$$

$$\bar{k}_d = \left(k_{d1} + k_{d2}\right)/2$$

$$\kappa = \sqrt{\left(k_{d1} + k_{d2}\right)^2/4 + k_{c1}k_{c2}} \tag{16}$$

with $(i, j) = (1, 2)$ or $(i, j) = (2, 1)$, respectively. The initial conditions have again been set to the fully replenished state, i.e., $n_i(t = 0) = n_{ri}$.

An interesting piece of information to be obtained for these calculations is the expected yield ratio, that is the ratio of the dissociation rates per primary electron for the two precursors

$$Y_i = \frac{\sigma_i}{t_D}\int_0^{t_D} n_i(t)\mathrm{d}t \tag{17}$$

from which the yield ratio Y_1/Y_2 can be directly obtained.

We now briefly review the results obtained by Bernau et al. [26] who studied the inclusion rate of carbon from the residual gas component octanol, $C_8H_{17}OH$, which is often found in high-vacuum systems that are pumped by diffusion pumps. At a background pressure of 1×10^{-5} mbar they estimated the effective impingement rate of octanol on the substrate surface to be $J_2 = 1.6 \times 10^{15}$ $(cm^2s)^{-1}$. As the functional precursor, $Co_2(CO)_8$ was used at a flux of $J_1 = 1.5 \times 10^{17}$ $(cm^2s)^{-1}$ (see Figure 3 for molecular models of the precursors). In independent octanol-free calibration measurements, the elemental composition was found to be $Co_2C_{0.6}O_{0.4}$, i.e., a Co–Content of 66 atom %. Deposits from the residual gas contained carbon and oxygen in the ratio 8.5:1. The depositions were performed at a beam energy of 25 keV and a beam current of 1 nA. The FWHM of the electron beam was given as 70 nm, which translates to an electron flux of about 1.6×10^6 $(nm^2s)^{-1}$. The monolayer densi-

ties were estimated from the dimensions of the intact molecules to be $n_1 = 2.6\ \mathrm{nm}^{-2}$ ($Co_2(CO)_8$) and $n_2 = 3.4\ \mathrm{nm}^{-2}$ (octanol).

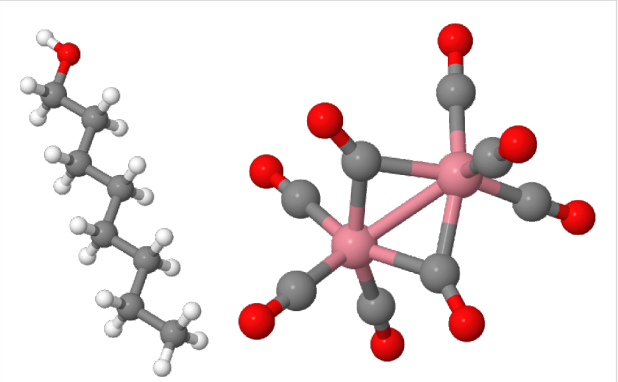

Figure 3: Molecular models of octanol (left) and $Co_2(CO)_8$ (right). Rendered using Jmol.

In order to determine the unknown quantities σ_i and τ_i, independent deposition experiments were performed under pure residual gas or quasi-pure $Co_2(CO)_8$ precursor conditions. The growth rate was in either case determined by measuring the height of the deposits by atomic force microscopy (AFM). From fitting of the obtained growth rates by using Equation 6 the following model parameters were obtained (see the supplementary information in Bernau et al. [26] for details): $\sigma_1 = 4.95 \times 10^{-3}\ \mathrm{nm}^2$, $\tau_1 = 720\ \mu\mathrm{s}$ and $\sigma_2 = 2.1\ \mathrm{nm}^2$, $\tau_2 = 190\ \mu\mathrm{s}$. Employing these model parameters the yield ratios Y_1/Y_2 were calculated as a function of the dwell time. The results of this calculation are reproduced in Figure 4 (inset). After the composition of the deposits under single-precursor conditions (see above) was properly taken into account, this translates into the composition variation as function of dwell time as shown in Figure 4, which turned out to be in excellent agreement with the experimental observations.

In the next section binary FEBID materials will be discussed and the continuum growth model analysis of this section will be applied to the case of the parallel use of $Co_2(CO)_8$ and $Me_3Pt(IV)CpMe$.

Binary FEBID structures

The parallel use of two (or more) precursors in FEBID provides access to a whole new class of functional nanostructures. FEBID structures with tailored cooperative ground states, such as superconductivity and magnetism, can be envisioned. However, one has to keep in mind that the local growth rates in FEBID are high and that the beam-induced chemistry is presently neither well-understood nor well-controlled in most cases of single-precursor usage, not to mention precursor mixtures. As a consequence, due to strong kinetic limitations

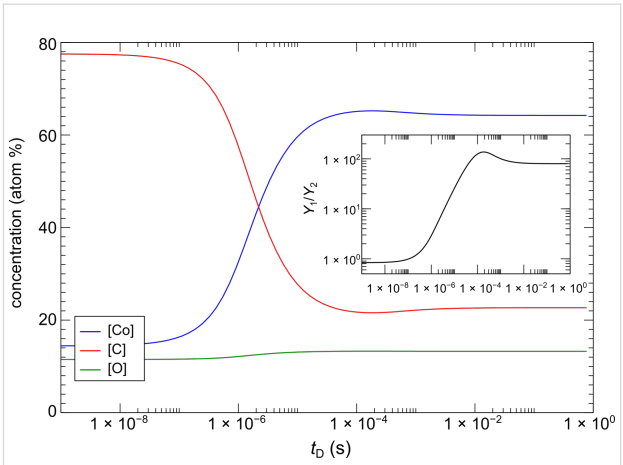

Figure 4: Simulation of concentration of different elements in FEBID structure under parallel use of $Co_2(CO)_8$ and octanol as precursors. The dissociation product of $Co_2(CO)_8$ is assumed to have the composition $Co_2C_{0.6}O_{0.4}$, whereas for the octanol the composition $C_{8.5}O_1$ is assumed. Inset: Dissociation yield ratio for $Co_2(CO)_8$ and octanol from solving Equation 14 and using Equation 17 (abscissa units as in main graph). See text for details.

(large growth rate, reduced diffusion in the presence of two precursor adsorbates) a strong inclination to the formation of amorphous material can be expected. Nevertheless, in the case of combining an organometallic precursor with metal species that exhibit large mixing enthalpies and tend to form either alloys and intermetallic compounds, or that are continuously mixable, a crystallized product may be expected even under rapid growth conditions, such as in FEBID.

In this section two examples of binary FEBID will be discussed. So far, very little work has been done in this field. Che et al. reported on FEBID of FePt nanopillar structures by using $Fe(CO)_5$ and $Me_3Pt(IV)CpMe$ as precursor gases in parallel [27]. The originally amorphous deposits were shown to crystallize into the $L1_0$ "face-centered tetragonal" structure of FePt after an in situ annealing step at 600 °C. The magnetic analysis was performed by using off-axis magnetic holography in a transmission electron microscope (TEM) and provided evidence for the hard-magnetic nature of the FePt nanorods. Unfortunately, very little details concerning the FEBID growth parameters and precursor flux conditions were provided in this report. In particular, the elemental compositions under different precursor mixing ratios were not given, therefore any comparisons with the continuum-growth-model approach from the previous section are not possible.

The next section reports on binary FEBID focused on the fabrication of Pt–Si structures by employing the precursors $Me_3Pt(IV)CpMe$ and neopentasilane (Si_5H_{12}), the latter one being used for the first time in FEBID experiments [28]. Metal-

silicides are highly relevant for metallization layers in integrated circuits. More importantly, the binary Pt–Si phase diagram shows several intermetallic phases, two of which are superconductors. It is thus worthwhile discussing the Pt–Si system in some more detail.

Pt–Si FEBID structures

As already alluded to in the last subsection the binary phase diagram of the Pt–Si system reveals two intermetallic compounds, which have a superconducting ground state. PtSi crystallizes in an orthorhombic structure with space group *Pnma*. Thin film studies on Pt layers on Si substrates show that PtSi forms at annealing temperatures above 600 °C via Si diffusion into the preformed Pt_2Si phase, which has a body-centered tetragonal unit cell (space group *I*4/*mmm*) [29]. PtSi thin films become superconducting below T_c = 0.56 K [30]. A second Pt–Si phase of relevance for the present discussion is Pt_2Si_3, which is metastable and was found to form by annealing PtSi thin films of typically 30 nm thickness after Xe^+ ion bombardment at 300 keV (integrated flux 1 × 10^{15} cm^{-2}) [31]. The annealing was done at 400 °C for different time periods. The crystal structure of this metastable phase was resolved to be hexagonal, belonging to the space group *P*6/*mmc* [31]. Annealing at elevated temperatures (550 °C and above) leads to the destruction of the hexagonal phase under formation of PtSi and excess Si. A rather sharp superconducting transition was found for Pt_2Si_3 with an onset at 4.2 K [31].

Experimental: We now turn to the results obtained in FEBID experiments by Winhold et al. employing $Me_3Pt(IV)CpMe$ and Si_5H_{12} as precursors (see Figure 5) supplied by two independent gas injection systems [28]. In this work the liquid and pyrophoric precursor Si_5H_{12} was used for the first time in FEBID as carbon-free source of Si. The experiments were performed in a dual-beam instrument (FIB/SEM, FEI Nova NanoLab 600) with a Schottky electron emitter. The beam voltage and current were 5 kV and 930 pA, respectively. The molecular flux ratio of the two precursor species was controlled by the distance of the Si_5H_{12} gas injection capillary to the substrate surface (p-doped Si(100) with 300 nm thermally grown oxide), as well as a fine-dosing valve to control the Si_5H_{12} molecular flux, keeping the $Me_3Pt(IV)CpMe$ molecular flux constant. Details concerning the absolute molecular flux values were not provided. The deposition parameters of 20 nm pitch and 1 µs dwell time were kept constant for all experiments. For the electronic transport measurements the structures were deposited between Au/Cr contacts previously defined by standard lithographic means. The temperature-dependent measurements were performed in a ^4He cryostat with variable temperature insert.

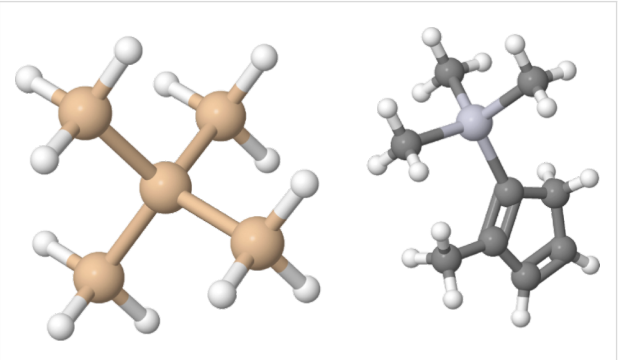

Figure 5: Molecular models of Si_5H_{12} (left) and $Me_3Pt(IV)CpMe$ (right). Rendered using Jmol.

In Figure 6 the results for the elemental composition of the deposits, as determined by energy dispersive X-ray analysis (EDX), are shown for nine samples. A priori it is not clear whether Si is preferentially included in the carbonaceous matrix or forms an alloy with Pt. From the EDX results several conclusions can be drawn, as was detailed in [28]. For low Si content a progressive decrease of the C content is observed accompanied by a parallel increase of Si and O. From this it may be concluded that Si is preferentially included in the C matrix and is partly oxidized in the presence of water and O_2 from the residual gases in the electron microscope at a background pressure of about 6 × 10^{-6} mbar. This parallel growth of Si and O content ceases when a Si/Pt ratio of about 1 is reached. It is speculated that a substantial part of the Si content of the samples is now bound to the Pt, forming amorphous Pt–Si alloy structures. This assumption is to some degree corroborated by the results of transmission electron microscopy (TEM) investigations which show a progression from nanocrystalline fcc Pt particles in a carbon matrix for Si-free deposits, towards an

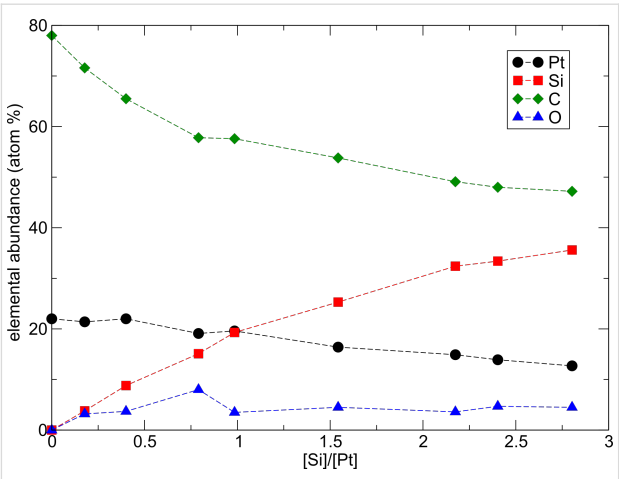

Figure 6: Elemental composition of various Pt–Si deposits as determined by EDX according to [28]. The data were taken after sample growth without a break of the vacuum.

amorphous structure of the granules. Since only a direct local probe, such as electron energy loss spectroscopy (EELS) in a TEM, would be able to unequivocally answer this question, we turn to some peculiarities observed in the transport-dependent conductivity of the FEBID samples.

Electronic transport properties: Figure 7 shows the resistivity as a function of the Si/Pt ratio of the as-grown samples. Apparently, the resistivity drops with increasing Si content reaching a well-defined minimum at a composition close to Pt_2Si_3. The temperature-dependent conductivity, which is shown in Figure 8, indicates for this composition and also for the composition PtSi a special form of thermally activated transport, which is commonly associated to a variable-range hopping (VRH) conductance mechanism in the presence of electronic correlation effects [12], namely

$$\sigma(T) = \sigma_0 \exp\left[-\left(T_0 / T\right)^a\right], \quad a = \frac{1}{2} \tag{18}$$

For all other samples either a VRH behavior in three dimensions (3-D) according to Mott (a = 1/4) [32] or some intermediate behavior is apparent.

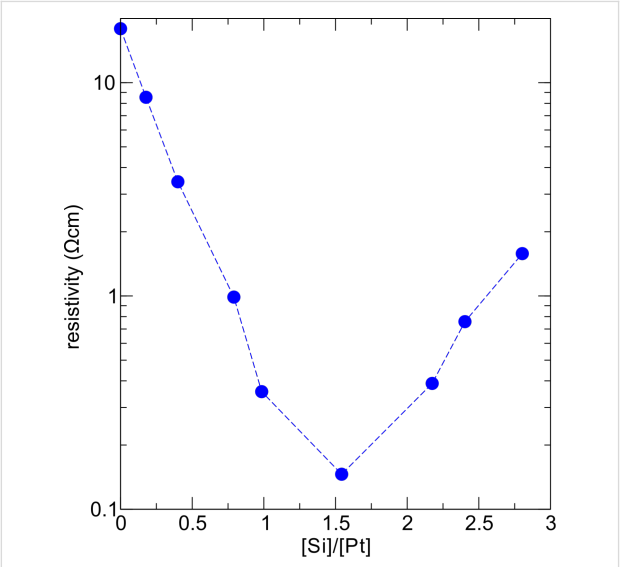

Figure 7: Dependence of the room temperature resistivity on the Si/Pt ratio in the FEBID samples according to [28].

The observed correlated VRH behavior observed for the samples with composition ratio [Si]/[Pt] = 1 and 3/2 indicates a granular electronic density of states of the FEBID samples. The minimal resistivity of the [Si]/[Pt] = 3/2 sample provides evidence that the intergranular tunnel-coupling strength is largest for this sample. On the other hand, from the TEM measurements no special microstructural feature, such as re-entrant

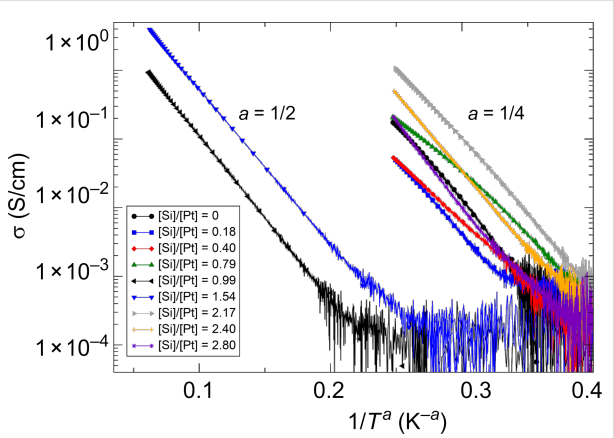

Figure 8: Temperature-dependent conductivity of the Pt–Si FEBID samples represented as ln σ vs T^{-a} to facilitate comparison with VRH models according to Mott (a = 1/4, three spatial dimensions) and for correlated VRH (a = 1/2). The data are taken from Winhold et al. [28].

crystallization of the granules, has been observed. It thus remains an unresolved issue, whether the granular electronic density of states is indeed indicative of the formation of an amorphous precursor of the metastable, hexagonal and superconducting Pt_2Si_3 phase. Unpublished results of one of us (M. W.) on the low-temperature resistance of FEBID samples with a composition close to [Si]/[Pt] = 3/2, which have been subjected to an extended post-growth electron irradiation treatment, show the onset of superconducting correlations below 4.2 K at large bias current. Future research will have to show whether this is the result of local crystallization towards the Pt_2Si_3-phase caused by the high dissipation levels under large current bias. For details concerning the electronic transport properties of nanogranular FEBID structures the reader is referred to the next section.

Co–Pt FEBID structures

As a second example of a binary FEBID experiment recent results on the Co–Pt system are reviewed [33]. The binary phase diagram of Co–Pt features several ferromagnetic intermetallic compounds. The most prominent of these is the $L1_0$ phase of CoPt, which has a face-centered tetragonal structure and is hard magnetic at room temperature [34]. Without any doubt FEBID holds great promise to become an important fabrication technique for magnetic nanostructures for micromagnetic studies, such as in the area of artificial spin-ice systems [35] or dipolar coupling effects [36]. Several interesting investigations on the growth and magnetic properties of Co–C deposits employing the precursor have been published in recent years [13,37-42]. Co–C deposits have also been used in recent experiments on the guided motion of vortices in the Shubnikov phase of epitaxial Nb thin films [43-46]. Two issues have to be considered here. Firstly, the precursor is relatively unstable and

dissociates, in particular under vacuum conditions, via the intermediate tetracobalt dodecarbonyl, into Co and carbon monoxide. Combined experimental and theoretical research has furthermore found clear indications that this precursor spontaneously dissociates on non-hydroxylated SiO_2 surfaces, i.e., on substrate surfaces often used in FEBID [20]. In this same research the catalytic decomposition of $Co_2(CO)_8$ on previously formed Co structures has also been experimentally demonstrated. Great care has therefore to be taken when this precursor in used. Secondly, FEBID structures from $Co_2(CO)_8$ can have a metal content of more than 95 atom % and show temperature-dependent transport properties reminiscent of dirty Co thin films in combination with soft-magnetic behavior at room temperature [13]. It would be desirable to also have access to hard-magnetic structures via the FEBID route. In this regard CoPt in the $L1_0$ phase represents an excellent choice.

Experimental: The experiments were performed in a dual-beam microscope with Schottky electron emitter (FIB/SEM, FEI Nova NanoLab 600) at 5 keV beam energy and 1.6 nA current. The writing parameters were 20 nm pitch and 1 µs dwell time. p-Doped Si (100) substrates with 200 nm of thermally grown oxide were used. The structures were deposited between Au/Cr contacts previously defined by standard lithographic means. The molecular flux ratios of the employed precursors $Co_2(CO)_8$ (at 28 °C) and $Me_3Pt(IV)CpMe$ (at 52 °C) were adjusted by varying the distance between the $Co_2(CO)_8$ injector's capillary exit and the substrate surface at a beam focus between 7 and 26 mm while keeping the $Me_3Pt(IV)CpMe$ injector's capillary exit at a fixed distance of 32 mm. No absolute values for the molecular flux were provided in [33]. The transport measurements were performed in a variable-temperature insert mounted in a ^4He cryostat with a superconducting solenoid. Two series of three samples were grown close to the 1:1 composition ratio of Co and Pt. One sample set was treated by post-growth electron irradiation by using the same beam parameters as in the deposition experiments. The elemental composition of the samples was determined by EDX. In Table 2 relevant information concerning the samples is compiled for ease of reference. For more details the reader is referred to [33].

Microstructural characterization: TEM investigations (FEI Tecnai F20 at 200 kV beam voltage) were performed on samples prepared in independent experiments on 30 nm thick carbon membranes. The sample composition for the as-grown sample as well as the sample for post-growth electron irradiation (dose 8.64 µC/µm^2) was tuned to that of sample B, i.e., close to a [Co]/[Pt]-ratio of 1. From bright-field imaging a nanogranular structure was deduced with Co–Pt grains embedded in an amorphous, carbonaceous matrix. Figure 9 shows the diffraction images of the as-grown and post-growth irradiated sample for comparison. Apparently, the diffraction contrast for the as-grown sample is weak, indicating a largely amorphous state of the Co–Pt grains. This changed appreciably after the postgrowth electron-irradiation treatment. A multitude of well-defined diffraction rings formed, which can be unequivocally attributed to the $L1_0$ intermetallic phase of CoPt, as detailed in Porrati et al. [33].

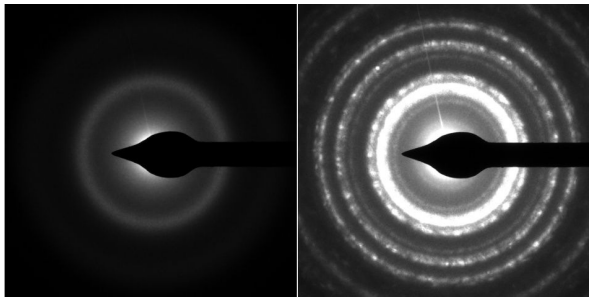

Figure 9: TEM electron diffraction pattern of samples on carbon membrane before (left) and after (right) postgrowth electron irradiation. The phase transformation from an amorphous to a crystalline state of the Co–Pt grains is apparent. See text for details. Images reproduced from Porrati et al. [33].

Table 2: Sample composition and $Co_2(CO)_8$ injector distance s_{Co} for Co–Pt samples. Samples A, B and C are as-grown. Samples A', B' and C' are subject to a post-growth electron-irradiated treatment with doses of 10.58, 7.02 and 14.24 µC/µm^2, respectively. For all depositions the $Me_3Pt(IV)CpMe$ injector's capillary distance to the substrate surface at the focus of the electron beam was kept constant at s_{Pt} = 32 mm. Table data reproduced from [33].

sample	[Co] (atom %)	[Pt] (atom %)	[C] (atom %)	[O] (atom %)	[Co]/[Pt]	s_{Co} (mm)
A	16.9	12.5	60.2	10.4	1.35	7
B	13.4	13.9	60.6	12.1	0.96	10
C	8.9	14.8	62.0	14.3	0.6	26
A'	21.3	16.5	40.2	22.0	1.29	7
B'	15.7	18.2	47.4	18.7	0.86	10
C'	13.5	22.4	37.7	26.4	0.6	26

Magnetic and transport properties: Selected results from the electronic transport measurements comprising the temperature-dependent conductivity and the magnetic field dependence of the Hall voltage are shown in Figure 10 for sample B (Figure 10a and Figure 10c) and B' (Figure 10b and Figure 10d). The as-grown sample exhibits a roughly linear temperature dependence of the conductivity down to about 12 K, which is followed by a quite sudden drop to a very small conductance level. The anomalous Hall effect, indicative of the Hall contribution proportional to the sample's magnetization, shows superparamagnetic behavior at room temperature. Data at low temperature could not be taken due to noise issues. From these observations, and in particular with regard to the sudden drop in conductance below 12 K, a glassy transition from a superparamagnetic state to a super-spin-glass [47] state may be assumed. However, further work on the low-temperature magnetic state of these deposits is needed before a definite statement can be made. More importantly, the conductivity of the postgrowth electron irradiated sample shows an increase by about two orders of magnitude. The conductivity levels off below 50 K and shows only a small residue of the conductance drop at 12 K. The Hall data indicate now a ferromagnetic state at room temperature with increasing coercive field as the sample is cooled to low temperatures. This indicates that the phase transformation from an amorphous to the ordered $L1_0$ phase is accompanied by a corresponding phase transition from a superparamagnetic to a moderately hard ferromagnetic state. The overall magnetic properties of these samples depend strongly on the magnetic intergrain interaction, which has tunnel-exchange and dipolar contributions. Since the coupling strength is tunable, as indicated by the strong increase of the conductivity after post-growth irradiation, FEBID of nano-granular Co–Pt systems provides a particularly elegant pathway to sample preparation for the study of different collective magnetic states.

Modeling within the multicomponent continuum scenario: We now turn to a more in-depth analysis of the composition of the deposits obtained from the parallel dissociation of the two precursors. The analysis is mainly based on the multicomponent continuum growth model of FEBID reviewed in the first section. Such an analysis has not been done so far and may provide some leads for future work on this binary system with regard to the fine-tuning of the elemental composition.

The compositional analysis from EDX measurements yields the relative fractions or concentrations [X] of the constituent elements in the deposits. From the continuum model analysis,

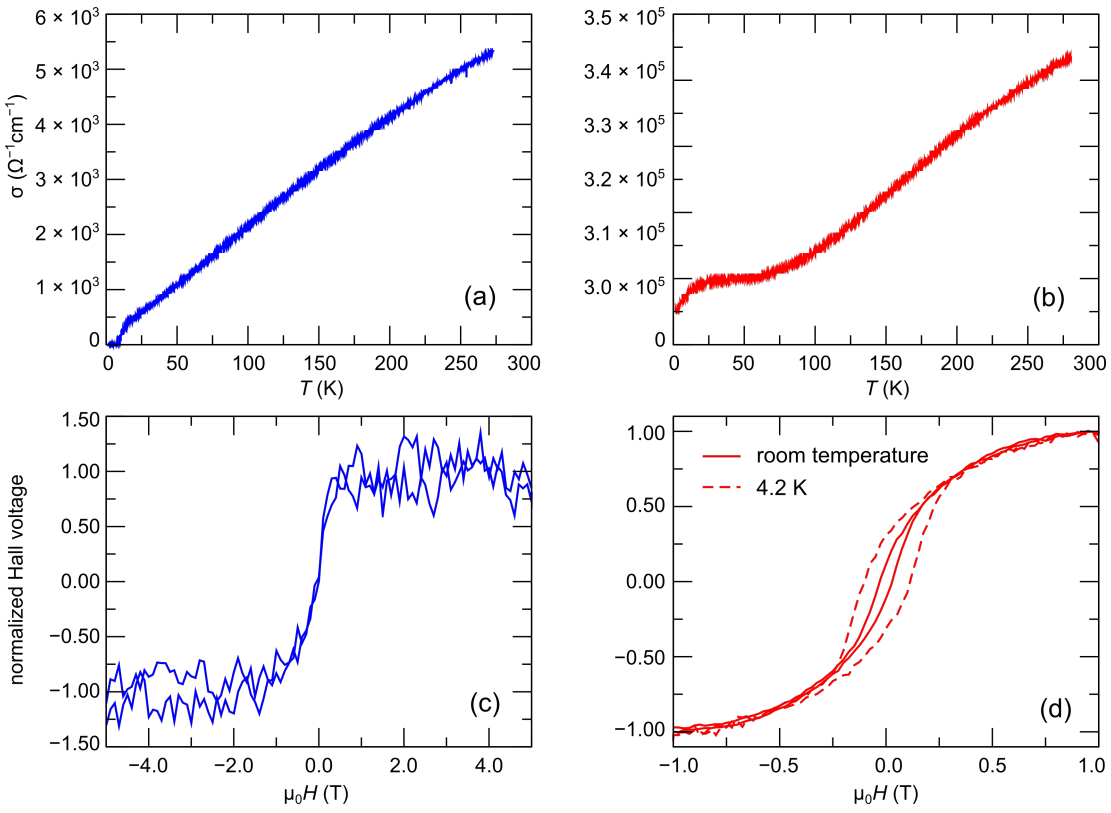

Figure 10: Temperature-dependent conductivity and Hall effect as a function of the applied magnetic field for samples B (a,c) and B' (b,d). The Hall data shown in (c) were taken at 228 K. Adapted from [33].

on the other hand, the individual yields Y_i of the nonvolatile dissociation products for each precursor, as given by Equation 17, are obtained. Within the model assumptions of noninteracting precursor fragments, i.e., under the assumption that no secondary chemical reactions are taking place between volatile dissociation fragments, the concentration ratios [X]/[Z] of two elements in the binary deposit can be calculated from the yields as follows

$$\frac{[\mathrm{X}]}{[\mathrm{Z}]} = \frac{Y_1[\mathrm{X}]_1 + Y_2[\mathrm{X}]_2}{Y_1[\mathrm{Z}]_1 + Y_2[\mathrm{Z}]_2} \tag{19}$$

where $[\mathrm{X}]_i$ and $[\mathrm{Z}]_i$ (i = 1, 2) represent the concentration of the respective elements in the nonvolatile dissociation products of each of the two precursors individually. In turn, this allows for determination of the yield ratios from the found elemental composition ratios

$$\frac{Y_1}{Y_2} = \frac{[\mathrm{X}]_2 - [\mathrm{Z}]_2 \dfrac{[\mathrm{X}]}{[\mathrm{Z}]}}{[\mathrm{Z}]_1 \dfrac{[\mathrm{X}]}{[\mathrm{Z}]} - [\mathrm{X}]_1} \tag{20}$$

In Table 3 the element concentrations of deposits formed from the individual precursors are compiled for the experimental conditions specified in Porrati et al. [33]. From these the yield ratio Y_1/Y_2 = 0.282 is obtained by using the elemental concentration ratio for sample B, [Co]/[Pt] = 0.96.

The expected elemental concentrations of C and O can now be predicted within the assumptions of the continuum model (index *cm*) by using Equation 19. One obtains $([\mathrm{C}]/[\mathrm{O}])_{cm}$ = 36.6 and $([\mathrm{C}] + [\mathrm{O}])/([\mathrm{Co}] + [\mathrm{Pt}])_{cm}$ = 1.97. From the experimentally determined elemental composition one derives [C]/[O] = 5.0 and ([C] + [O])/([Co] + [Pt]) = 2.66 (see data in Table 2). This allows directly for a qualitative assessment of the applicability of the continuum model for this binary system. The neglect of interfragment reactions in the model leads to an underestimate of the abundance of the nonmetallic precursor fragments in the deposits. Apparently, the parallel dissociation of the oxygen-free $Me_3Pt(IV)CpMe$ and oxygen-containing $Co_2(CO)_8$ precursor leads to an enhanced inclusion of oxygen. In parallel, the overall concentration of the nonmetallic components increases. It may be speculated that secondary reactions between the volatile precursor fragments, e.g., oligomerization, lead to the formation of less-volatile organic species, which are eventually included in the deposits. This simple analysis makes it quite clear that a more detailed understanding of the fragmentation and reaction pathways is needed for a thorough understanding of the process of deposit formation. In principle, the continuum model can be extended to include secondary reactions as long as the corresponding reaction rate parameters can be deduced from independent experiments. Future work on the development of a better understanding of the FEBID process will have to make use of surface-science techniques under well-controlled experimental conditions, in particular ultrahigh vacuum, to allow for a detailed analysis of the reaction mechanisms. For selected examples this has already started [17].

Although the predictive power of the multicomponent continuum model of FEBID is limited, it can nevertheless provide useful information with regard to the dependence of the sample composition of the dwell time at fixed molecular fluxes. To show this, the dependence of the yield ratio Y_1/Y_2 on the dwell time has been calculated by using Equation 15 and Equation 17 with the $Co_2(CO)_8$ precursor parameters introduced in the first section for a reduced molecular flux value of 75 $(\mathrm{nm^2 s})^{-1}$ owing to the larger capillary distance of 10 mm. The electron flux was set to 1.6×10^6 $(\mathrm{nm^2 s})^{-1}$. The model parameters for $Me_3Pt(IV)CpMe$ were extracted from the literature, namely $\sigma_2 = 2.2 \times 10^{-2}$ nm^2 [23], τ_2 = 29 µs [24] and $\bar{n}_2$ = 2.0 nm^{-2} [24]. The precursor flux for $Me_3Pt(IV)CpMe$ was set to 54 $(\mathrm{nm^2 s})^{-1}$ so that the calculated yield ratio corresponded to the value of 0.283 derived for sample B previously. Figure 11 shows that the yield ratio can be tuned to a large degree by simply changing the dwell time. In particular, within the dwell time range of 1 µs to 10 ms the yield ratio can be changed by a factor of three. This should allow for a very fine tuning of the [Co] versus [Pt] concentration in FEBID experiments at otherwise fixed deposition conditions. An analogous behavior is expected for other binary systems.

Nanogranular FEBID structures

On a very general level FEBID structures can be classified as disordered electronic materials. In between the extreme cases of fully amorphous deposits and polycrystalline structures with

Table 3: Composition of nonvolatile dissociation products from the individual precursors $Co_2(CO)_8$ and $Me_3Pt(IV)CpMe$ on Si/SiO_2 substrates at 5 keV beam energy, 1.6 nA beam current (measured at Faraday cup), 20 nm pitch and 1 µs dwell time.

	$[\mathrm{Co}]_i$	$[\mathrm{Pt}]_i$	$[\mathrm{C}]_i$	$[\mathrm{O}]_i$
dissociation product precursor 1: $Co_2(CO)_8$	0.75	0.0	0.17	0.08
dissociation product precursor 2: $Me_3Pt(IV)CpMe$	0.0	0.22	0.78	0.0

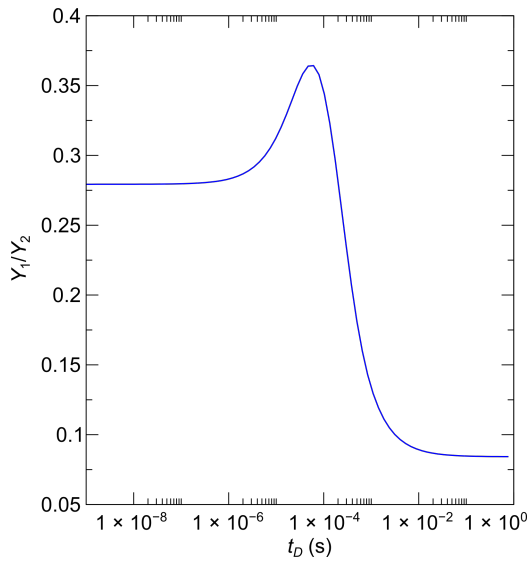

Figure 11: Dependence of the yield ratio for the precursors $Co_2(CO)_8$ and $Me_3Pt(IV)CpMe$ on the dwell time within the multicomponent continuum model of FEBID. See text for details.

some degree of defects falls the class of nanogranular systems. They consist of nanocrystallites embedded into a carbon-rich dielectric matrix, which are subject to an intergranular electronic coupling due to a finite tunneling probability between the crystallites or grains. The binary systems Pt–Si and Pt–Co discussed previously fall into this class. For nanogranular materials the semiclassical approach of Boltzmann transport theory is not applicable since disorder does not simply cause scattering but must be included in the theoretical analysis from the beginning. A recent theoretical review on the electronic transport properties of granular metals can be found in [12].

The electrical transport within the metallic grains can be considered diffusive due to intragrain and surface scattering. Despite this scattering there is a well-defined and important intragrain energy scale, which is the mean spacing δ between the one-electron levels close to the chemical potential of the grain. It is given by $\delta = 1/N_F V$, where $V \propto r^3$ is the grain volume (r: grain radius) and N_F denotes the density of states at the chemical potential. For typical grain sizes in FEBID structures with a diameter of a few nanometers, δ/k_B (k_B: Boltzmann constant) is of the order of 1 K for metallic grains with a density of states on the order of 1 $(\text{eVnm}^3)^{-1}$. From this rough estimate, one can directly conclude that quantum size effects due to the discrete energy levels can only become relevant at very low temperatures.

The electronic (transport) properties of granular metals depend sensitively on the average tunnel conductance G between neighboring grains, which is commonly expressed as the dimensionless quantity $g = G/(2e^2/h)$, i.e., normalized to the conductance quantum. Metallic behavior will be observed, if g surpasses a critical coupling strength $g_c \approx 1$. Samples with $g < g_c$ show insulating behavior, i.e., zero conductance as $T \rightarrow 0$. The notion *metallic* does not necessarily imply a positive temperature coefficient of the resistance but merely means a finite conductivity as T approaches 0. The formal condition for a material to qualify as a granular metal is that the intergrain coupling strength g is much smaller than the normalized conductance g_0 inside a grain.

Due to the tunnel-coupling between the grains the one-electron energy levels at the chemical potential are broadened. This effect is expressed by the broadening parameter $\Gamma = g\delta$. Another important parameter is the single-grain Coulomb charging energy $E_C = e^2/2C$ where $C \propto r$ is the capacitance of the grain. E_C is equal to the change in electrostatic energy of the grain when one electron is added or removed. For insulating samples charge transport is suppressed at low temperatures due to this charging energy. The average level spacing δ can become larger than the charging energy only for very small grains. For FEBID samples, however, typical grain sizes are in the range of several nanometers, and the assumption $E_C >> \delta$ is well justified.

Transport theory of granular metals

A detailed review of the theory necessary to describe the transport properties of granular metals goes far beyond the present review, and the reader is referred to Beloborodov et al. [12]. Nevertheless, a short account is given to provide a framework for the following discussion of the experimental findings on nanogranular FEBID structures prepared by using the precursor $Me_3Pt(IV)CpMe$.

Neglecting spin, which is of no relevance for nonmagnetic granular metals, the Hamiltonian has three components:

$$\mathcal{H} = \mathcal{H}_0 + \mathcal{H}_t + \mathcal{H}_C \tag{21}$$

where $\mathcal{H}_0$ comprises the intragrain kinetic and potential energies

$$\mathcal{H}_0 = \int \psi^*(\vec{r}) \left(-\frac{\hbar^2}{2m}\nabla^2 + U(\vec{r}) \right) \psi(\vec{r})\, \mathrm{d}^3 r \tag{22}$$

and $\psi(\vec{r})$ denotes the field operator representing the electron field. $\mathcal{H}_t$ describes the tunneling between the grains

$$\mathcal{H}_t = \sum_{i,j;\alpha,\beta} t_{ij} \psi^+_{i\alpha} \psi_{j\beta} \tag{23}$$

with (α, β) indexing the internal energy levels of the coupled grains with indices (i, j). The Coulomb charging energy is expressed through the capacitive coupling C_{ij} between the grains

$$\mathcal{H}_C = \frac{e^2}{2}\sum_{i,j}\mathcal{N}_i C_{ij}^{-1}\mathcal{N}_j \tag{24}$$

$\mathcal{N}_i$ denotes the electron number operator as the difference from the charge neutral state with N electrons per grain

$$\mathcal{N}_i = \int \psi^+(\vec{r}_i)\psi(\vec{r}_i)\,\mathrm{d}^3 r_i - N \tag{25}$$

By means of field-theoretical methods (bosonization techniques, perturbation theory in the strong-coupling regime $g \geq 1$), and under the assumption of a regular lattice of identical grains in one, two or three spatial dimensions (d = 1,2,3), the following results for the temperature-dependent conductivity are obtained.

In the *metallic state* a universal logarithmic conductivity correction is obtained that saturates for $k_\mathrm{B}T < \Gamma$. For $k_\mathrm{B}T < \Gamma$ a dimension-dependent higher-order correction indicates the development of a coherent transport regime, which is denoted as a granular Fermi liquid [48]

$$\sigma = \sigma_0\left(1 + \frac{\delta\sigma_1}{\sigma_0} + \frac{\delta\sigma_2}{\sigma_0}\right) \tag{26}$$

with

$$\frac{\delta\sigma_1}{\sigma_0} = -\frac{1}{6\pi g}\ln\left[\frac{gE_C}{\max(k_\mathrm{B}T,\Gamma)}\right] \tag{27}$$

and

$$\frac{\delta\sigma_2}{\sigma_0} \approx \frac{1.83}{12\pi^2 g}\sqrt{k_\mathrm{B}T/\Gamma} \tag{28}$$

The expressions are here only given for the case d = 3, as this is of relevance for the analysis of the transport properties of FEBID structures prepared so far.

In the *insulating regime* the theory predicts a hard energy gap $\Delta_M = \mathcal{O}(E_C)$ resulting in an Arrhenius-like conductivity

$$\sigma(T) = \sigma_0' \exp\left[-\frac{\Delta_M}{k_\mathrm{B}T}\right] \tag{29}$$

However, the experimental findings for granular metals in the insulating regime indicate a different activated behavior of the form

$$\sigma(T) = \sigma_0' \exp\left[-\left(\frac{T_0}{T}\right)^{1/2}\right] \tag{30}$$

which we denote as *correlated VRH*. Beloborodov et al. [49] provided a theoretical explanation by observing that inelastic (at higher temperature) and elastic (at low temperature) cotunneling of electrons through many grains, in conjunction with random chemical potential fluctuations in the grains, caused by charged impurities in the matrix and at surfaces, will smear out the hard energy gap and lead to the observed correlated VRH.

The results of this theoretical analysis can be conveniently compiled into a phase diagram of the transport regimes of granular metals [48], which is shown in Figure 12.

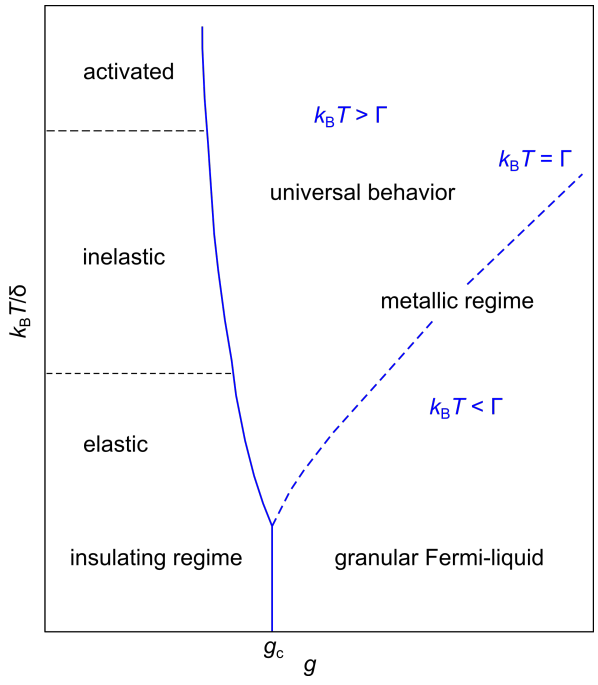

Figure 12: Phase diagram of the transport regimes of granular metals. In the insulating regime for $g < g_c$ thermally activated transport is observed of the Arrhenius type at elevated temperatures, which crosses over to correlated VRH due to inelastic or elastic cotunneling in the presence of potential disorder in the grains. In the metallic regime for $g > g_c$ a universal logarithmic correction for $k_\mathrm{B}T > \Gamma$ is expected, which saturates at lower temperature as coherent transport develops (granular Fermi liquid). Adapted from [48].

Tunable granular metals prepared by FEBID

Initial experiments addressing in particular the transport properties on the metallic side of the insulator-to-metal transition of FEBID structures were performed on the W–C–O-system prepared from the precursor $W(CO)_6$ [50]. In this case, the metal content was increased by carefully tuning the beam parameters. Since changes of the metal content are in general associated with corresponding changes in the microstructure, the interpretation of transport properties is not simple. Recent experimental findings in the transport properties of Pt–C FEBID structures prepared with the precursor $Me_3Pt(IV)CpMe$ allow for a particularly elegant way of testing the theoretical predictions presented in the previous subsection. In experiments on optimizing Pt–C FEBID structures for strain-sensor element applications (see next section) it was found that a strong increase of the conductivity by up to four orders of magnitude can be obtained by post-growth electron irradiation of the deposits [51]. Subsequent work identified the dominant reason for this apparent increase of the intergrain tunnel-coupling strength g to be caused by a microstructural change of the prevailing hybridization state of the C atoms in the matrix from amorphous carbon to nanocrystalline graphite [52]. This conclusion was drawn from the observed peak shifts and changes of the spectral weight of C-specific vibrational eigenmodes in Raman spectra of deposits that were subject to different post-growth electron irradiation doses. In follow-up work an optimized post-growth irradiation protocol was described that leads to an equally strong conductivity increase for shorter irradiation times [53]. In this subsection the focus is on the analysis of the temperature-dependent conductivity of these Pt–C deposits, which cover the full range from insulating to metallic behavior, i.e., $g \ll 1$ to $g > g_c \approx 1$.

Experimental details: The experiments were performed in a dual-beam microscope (FEI Nova NanoLab 600) with Schottky emitter. The precursor $Me_3Pt(IV)CpMe$ was heated to a temperature of 52 °C. A series of samples with a lateral size of 5×1 μm^2 were prepared between prefabricated Au/Cr electrodes under identical conditions of 5 keV, 1.6 nA (measured at Faraday cup), 20 nm pitch and 1 μs dwell time on a p-doped Si (100) substrate with 100 nm thermally grown oxide held at room temperature. In the as-grown state the samples had a thickness of 80 nm. After growth, the samples were subjected to a post-growth electron irradiation treatment of different duration employing the same beam parameters as used for the deposition. During the irradiation treatment the sample height showed a rapid drop by approximately 20% within the first 20 min. This was followed by a gradual thickness reduction over several 100 min down to approximately 55% of the original thickness for the samples subject to a long-term irradiation treatment [52]. This apparent volume loss is thought to be caused by the dissociation of residual precursor fragments embedded in the deposits during growth [53] and the partial loss of carbon due to electron-stimulated reaction with residual water to carbon monoxide [52].

Temperature-dependent conductivity: Figure 13 shows an overview of the temperature-dependent conductivity of the

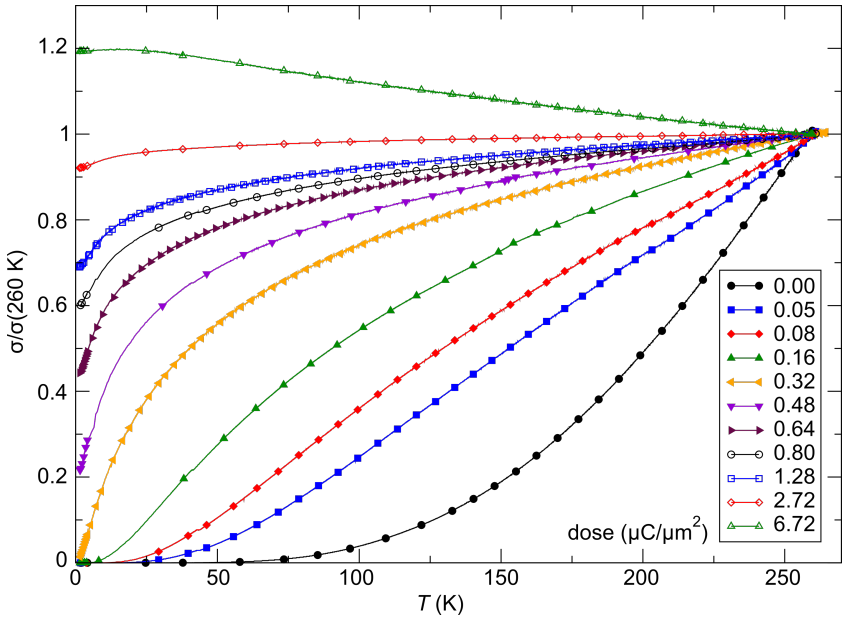

Figure 13: Temperature-dependent conductivity of Pt–C FEBID structures that have been exposed to different post-growth electron irradiation doses as indicated. See text for details. Adapted from [52].

samples exposed to different irradiation times as indicated. It is directly apparent that the Pt–C system can be finely tuned through a insulator-to-metal transition. The highly reproducible growth characteristic represents one particular advantage of this system. This ensures that under nominally identical conditions samples of very similar transport properties can be obtained. The irradiation-induced increase of the conductivity of up to four orders of magnitude as specified in Porrati et al. [52] is not apparent from the normalized representation.

Further analysis reveals that the as-grown sample shows correlated variable-range hopping according to Equation 30 over the complete measured temperature range. The same holds true for samples subject to small irradiation doses in the low-temperature region. As room temperature is approached a deviation from correlated VRH is observed, which may indicate the expected cross-over to simple Arrhenius behavior. However, further temperature-dependent measurements above room temperature are needed to clarify this point. Figure 14a shows this thermally activated behavior for two samples. Furthermore, Figure 14 depicts two different representations of the data for samples on the metallic side of the insulator-to-metal transition referring to the predicted behavior according to Equation 27 (Figure 14b) and Equation 28 (Figure 14c). The predicted universal logarithmic temperature dependence is fulfilled over a large temperature range from room temperature down to about 15 K [54]. Below this temperature deviations occur that could be indicative of the onset of coherent transport as expected for a granular Fermi-liquid (see Figure 14c). However, this latter part needs more thorough investigation at even lower temperatures.

Pt–C structures grown by FEBID provide a particularly valuable example of a nanogranular metal in which the intergrain tunnel coupling strength g can be tuned over a wide range so that the insulator-to-metal transition can be approached and passed with excellent control. In [54] a simple graphical analysis was introduced that allows for a quantitative determination of the coupling strength of samples that follow the universal logarithmic dependence on the metallic side. g-values between 0.25 and 3 were found with increasing irradiation dose.

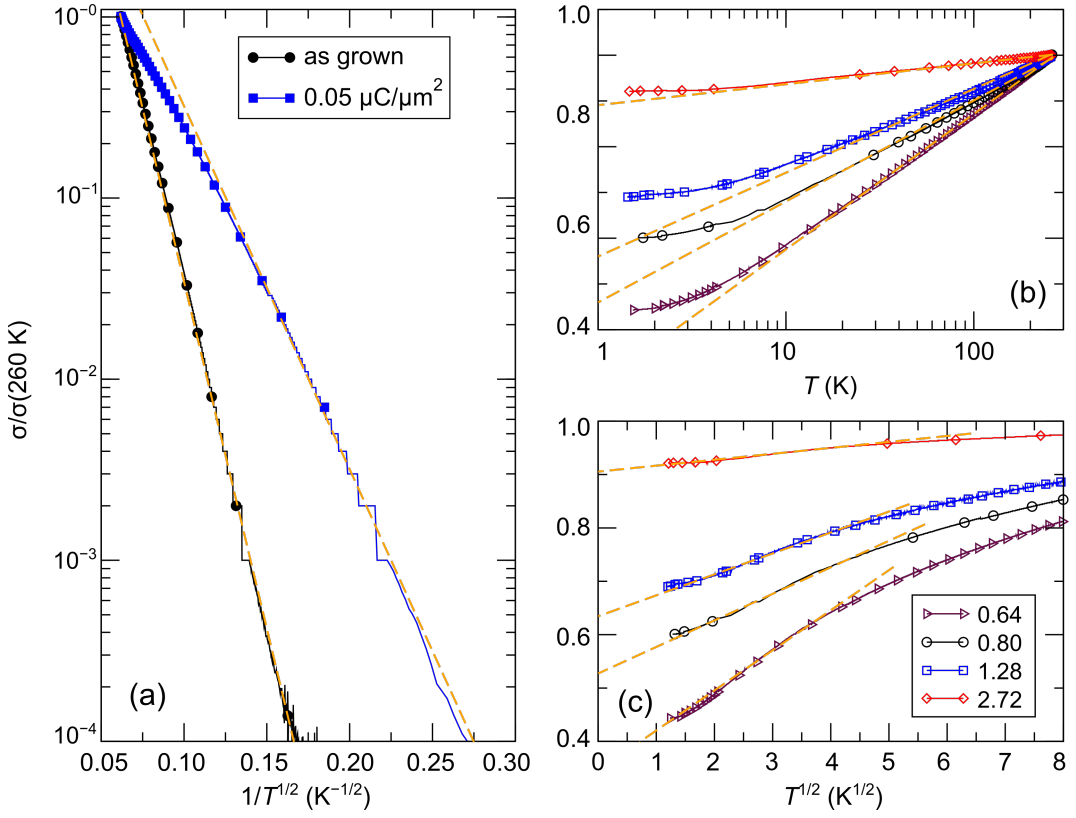

Figure 14: Temperature-dependent conductivity of Pt–C FEBID structures that have been exposed to different post-growth electron irradiation doses as indicated. (a) As-grown briefly irradiated samples show thermally activated behavior following the correlated VRH scenario. (b) Long-term irradiated samples reveal a logarithmic temperature dependence of the conductivity in accordance with Equation 27. Saturation of this behavior is observed below about 15 K. (c) Samples in the metallic regime at low temperature show indications for a crossover to a $\sqrt{T}$ -dependence of the conductivity. The straight dashed orange lines in the plots are meant to facilitate a judgement of the quality of the temperature dependence of the conductivity as predicted by theory. See text for details. Adapted from [54].

Several follow-up investigations are at hand to address important aspects for granular metals. The behavior for metallic samples needs to be followed to the sub-Kelvin regime with high data fidelity to check whether the indicated granular-Fermi-liquid behavior is indeed observable. One has to keep in mind that the theoretical model neglects disorder effects which are, of course, present in the samples. It would be desirable to extend these investigations to higher-order transport coefficients, such as the Seebeck effect [55] and also galvanomagnetic quantities (Hall resistance, magnetoresistance) for which also theoretical predictions are available and await experimental verification. With regard to the influence of disorder on the electronic properties of nanogranular metals, studies on artificial granular lattices would be particularly interesting. Initial steps in this regard have been taken in two recent investigations on two-dimensional granular dot-lattices prepared by using the precursor $W(CO)_6$ [56,57]. In these experiments a pitch-controlled insulator-to-metal transition was observed. Samples with large pitch (40 nm) clearly showed Arrhenius-like behavior at low-temperatures and indicated the presence of a hard energy gap consistent with the expected Coulomb-blockade energy of the individual nanodots [56]. At this stage it can only be speculated that the dot-size of about 20 nm and the minimum pitch of 20 nm realized in these experiments is too large to allow cotunneling. As a consequence, the expected correlated VRH behavior was not found. Nevertheless, the FEBID technique provides the capability to prepare nanodot lattices in the sub-10 nm regime, which would allow for a thorough comparison of the transport characteristics of disordered and ordered nanogranular metals.

Nano-granular FEBID sensors

The final section is devoted to the application of FEBID materials for sensor applications, which take particular advantage of the nanogranular microstructure. The applications addressed here are the detection of mechanical strain and magnetic fields employing highly miniaturized FEBID sensor elements.

Strain sensing with nanogranular metals

Physical principles of strain sensing with granular metals: The concept of strain sensing with granular metals is based on the observation that charge transport is realized via thermally assisted tunnel processes for which the tunneling probability decays exponentially with the intergrain distance. Several techniques for the preparation of granular strain sensors have been established in recent years. The most active areas of research are based on diamond-like carbon (DLC) films with metal inclusions [58] and, since very recently, FEBID-based sensor elements [51]. Although conceptually simple, a theoretical framework with predictive power concerning promising sensor-optimization strategies for this material class has been only recently suggested by one of us [59] and shall be in part very briefly reviewed here.

The strain-dependence of the conductivity or resistivity follows from the derivative

$$\frac{\Delta\sigma}{\sigma} = -\frac{\Delta\rho}{\rho} = \frac{1}{\sigma}\frac{\partial\sigma}{\partial g}\Delta g \tag{31}$$

with ρ and σ denoting the (temperature-dependent) resistivity and conductivity, respectively. Employing the expressions for the temperature-dependent conductivity regimes presented in the last section, the respective derivations can be done algebraically. With a view to the largest sensor response, i.e., the largest strain-resistance effect expressed via the gauge factor κ

$$\kappa = \frac{\Delta\rho}{\varepsilon\rho} \quad \text{and} \quad \varepsilon = \frac{\Delta s}{s} \tag{32}$$

with s as the peripheral intergrain spacing, the Arrhenius regime can be identified as the most promising [59]. However, the dependence of the hard energy gap Δ_M (see Equation 29) on the coupling strength g is not readily apparent. Theory predicts an exponential functional dependence in the intermediate coupling regime ($gz \approx 1$, z: number of nearest-neighbor grains) as the metallic regime is approached [12]

$$\Delta_M \approx E_C \exp\left[-\pi g z\right] \tag{33}$$

From this dependence and Equation 29 the following derivative can be readily obtained

$$\frac{\Delta\sigma}{\sigma} = \frac{\pi g z E_C}{k_B T}\exp[-\pi g z]\frac{\Delta g}{g} \tag{34}$$

In order to draw a link to the experimentally observed quantity $\Delta\rho/\rho(\varepsilon)$ the exponential dependence of the intergrain coupling strength g on the intergrain distance s has to be explicitly introduced

$$g = g_0' \exp[-2s/\lambda] \tag{35}$$

where g_0' subsumes material-dependent details of the tunnel barrier and λ is the attenuation length of the wave function. The latter coincides with the range for inelastic cotunneling

$$\xi_{in}(T) = \frac{2D}{\ln(\bar{E}^2/16\pi c_{in} g (k_B T)^2)} \tag{36}$$

with the boundary condition $1/4 \le c_{in} \le 1$ and here $c_{in} = 1$, if only the short-range part of the Coulomb interaction is important. D denotes the average grain diameter. $\bar{E}$ is a measure of the average Coulomb blockade energy of an individual grain and lies within the range $E_C/2 \le \bar{E} \le E_C$. The relative change of the coupling strength can now be expressed by the relative change of the grain distance

$$\frac{\Delta g}{g} = -\frac{2s}{\xi_{el}}\varepsilon \tag{37}$$

such that the relative conductivity change according to Equation 34 is now fully expressed as a function of the relative length change ε with s as a parameter that can be obtained from a suitable relationship between s and the metal volume fraction f, which depends on the details of the microstructure of the granular metal. In [59] a regular and dense packing of monodisperse spheres (fcc/hcp-like packing) is assumed, which leads to

$$s = D\left[\left(\frac{\pi}{3\sqrt{2}f}\right)^{1/3} - 1\right] \tag{38}$$

with $z = 12$ nearest neighbors. In this case $f = 0.7405$ for $s \to 0$.

With increasing metal content the effective dielectric constant of the granular metal ε_r starts to deviate from that of the insulating matrix. To some degree this can be taken into account by employing an effective-medium theory, such as the Maxwell–Garnett approximation [59]

$$\frac{\varepsilon_r}{\varepsilon_i} = \frac{\varepsilon_m(1+2f)+2\varepsilon_i(1-f)}{\varepsilon_m(1-f)+\varepsilon_i(2+f)} \tag{39}$$

in which ε_m and ε_i denote the dielectric constant of the metal and dielectric matrix, respectively.

In Figure 15 the result of a model calculation in the intermediate coupling Arrhenius regime is shown for three different temperatures. From these calculations a gauge factor of about 10 can be expected at room temperature. This has to be corrected for purely geometric effects caused by the reduction of the sample's cross section, and its length increase under tensile strain, which leads to an additional strain-resistance effect that adds to the intrinsic gauge factor. The resulting gauge factor then amounts to about 12, which was indeed found in experiments on Pt–C FEBID fabricated strain sensors as is shown in the following subsection. For strain sensors operating in the Arrhenius regime an enhancement of the gauge factor can be expected for smaller grain size and small dielectric constants of the matrix material, as detailed by Huth [59]. Depending on the transport regime, other gauge factors result. In particular, within the metallic regime the intrinsic gauge factor is close to 0 and thus not relevant for applications.

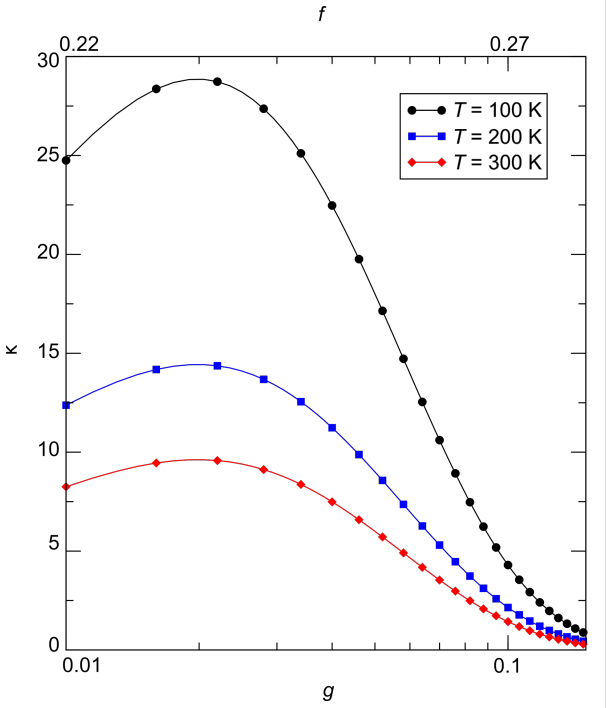

Figure 15: Calculated gauge factor κ as a function of intergrain coupling strength (bottom axis) and metal volume fraction (upper axis) at selected temperatures for the Arrhenius regime at intermediate coupling. Fcc-like packing of Au nanoparticles of 5.5 nm diameter in a dielectric matrix was assumed. The model parameters $g_0' = 3.29$, $\varepsilon_i = 1.02$, $\varepsilon_m = -16400$ and $\bar{E} = E_C$ were used. For details see [59].

FEBID-based strain sensors: Nanogranular strain sensors fabricated by means of FEBID offer a very great potential for miniaturization. Also, they can be realized on many different materials (oxides, polymers, metals with an electrical insulation layer, etc.). In selected areas this is a clear advantage, which is demonstrated here by some recent and unpublished results obtained with regard to the development of microcantilever-based atomic force microscopy for biological applications.

The strain-resistance effect in FEBID-based sensor elements was shown for the Pt–C system in [51] for the first time. Initial results from the use of sensor elements on cantilevers for dynamic-mode AFM appear in Figure 16. The strain-resistance effect shown in the left part allows for imaging of the surface fine structure of a collagen fibril, which is a proteinaceous fiber and a major component of mammalian connective tissue, such as skin and tendons. As was shown in [51], the voltage noise of the resistive sensor elements follows a $1/f$ frequency dependence and reaches the noise floor at the level of the Johnson

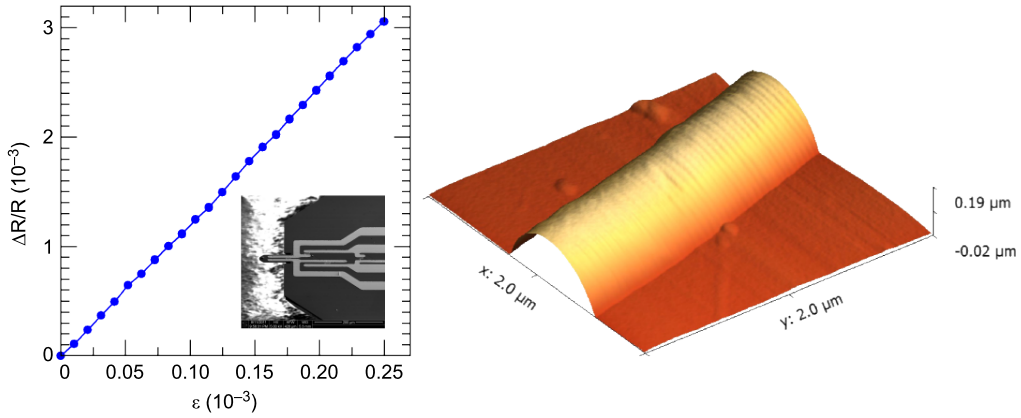

Figure 16: Left: Strain-resistance effect of a Pt–C nanogranular sensor element measured on a test cantilever (see inset). The sensor elements were prepared by FEBID employing the precursor $Me_3Pt(IV)CpMe$ at 5 keV beam energy, 1.6 nA beam current, 20 nm pitch and 1 µs dwell time. Within a full Wheatstone bridge each individual sensor element had a resistance of 51 kΩ. The Si (100) test cantilever had dimensions of 70 × 35 × 3 µm^3. Right: Exemplary AFM image of collagen fibril taken in noncontact mode at a resonance frequency of 420 kHz. The images were taken with an adapted MultiMode atomic force microscope with Nanoscope 3a controller at 0.2 Hz line rate.

noise at about 1 kHz. This frequency response is favorable for dynamic mode AFM applications. In the limit of highly miniaturized cantilevers, to be used in future high-speed AFM approaching line frequencies up to 1000 Hz, the sensor performance can be extrapolated to reach a deflection sensitivity of more than 200 µV/nm at a noise level of about 0.07 nm, for ultrasmall cantilevers with a size of 1 × 0.5 × 0.1 µm^3. For these cantilever structures, optical readout of the cantilever deflection is not an option anymore.

Micro Hall magnetometry with nanogranular metals

Hall effect in granular metals: The detection of spatially inhomogeneous magnetic fields, such as the dipolar stray fields obtained from magnetic beads for biological and medical applications or in magnetic media, relies on the availability of nanometer-sized magnetic sensor elements. Nanogranular metals with ferromagnetic grains can provide excellent detection sensitivity due to their large interfacial area per unit volume, which leads to a strong increase of the surface scattering rate and results in a strongly enhanced extraordinary Hall effect (EHE) as the insulator-to-metal transition is approached from the insulating side. More specifically, the Hall resistivity ρ_H in a ferromagnetic metal has contributions that stem from the Lorentz force acting on the charge carriers, i.e., the ordinary Hall effect (OHE), and the EHE, which is proportional to the spontaneous magnetization [60]

$$\rho_H = \rho_{OHE} + \rho_{EHE} = \mu_0 \left(R_0 H + R_S M_z \right) \qquad (40)$$

where H denotes the applied magnetic field aligned perpendicularly to the Hall device, M_z is the spontaneous magnetization in the field direction $\vec{e}_z$, R_0 and R_S are the ordinary and spontaneous Hall constants, respectively, and μ_0 is the magnetic permeability of the vacuum. In metals the OHE is negligible compared to the EHE, so that the saturation field of the magnetic response defines the upper limit of the working range of such a Hall device. The device yields a signal proportional to the local magnetization $M(H; x, y)_z$ averaged over the cross section of the nanostructured Hall sensing area. The sensitive dependence of the EHE on surface scattering is due to the relation between ρ_{EHE} and the longitudinal resistivity ρ with contributions from skew and side-jump scattering [60]

$$\rho_{EHE} = \gamma \rho_0 \rho_S + \gamma \rho_S^2 \qquad (41)$$

Here, ρ has been decomposed by using Matthiessen's rule in the spin-independent part ρ_0 and the magnetic part ρ_S.

FEBID-based Hall sensors: Submicrometer Hall devices prepared by FEBID employing the precursor $Co_2(CO)_8$ were first described by Boero and collaborators [38]. This work was later extended towards optimization of the Hall sensitivity by Gabureac et al. [39]. The devices in standard Hall-cross geometry had a thickness between a few tens up to a few hundreds of nanometers and widths between 200 and 500 nm. It was found that the room temperature $M_z(H)$ curves could be excellently described by a Langevin fit, indicating superparamagnetic behavior

$$M_z(H) = M_S L(x \equiv \mu_0 \mu H / k_B T) \text{ with } L(x) = \coth x - \frac{1}{x} \qquad (42)$$

µ denotes the averaged magnetic moment, which can be deduced by fitting the data according to Equation 40 with M_z

given by Equation 42. In the linear region of the $M_z(H)$ characteristics the supply-current-related field sensitivity $S_I = I^{-1}dV_H/d(\mu_0 H)$, with I denoting the bias current and V_H the Hall voltage, was found to be 0.15 Ω/T at 10 mA current for samples with about 65% Co content. This translated to a field-detection limit of 3 $\mu T/Hz^{1/2}$. The frequency-dependent voltage noise of the Hall device was found to follow a $1/f$ behavior hitting the thermal noise limit in the 100 kHz range for the largest bias currents.

The observed field detection limit of the Co–C Hall sensors is by a factor of about 100 worse than those which can be obtained with state-of-the-art InAsSb quantum-well structures [61]. However, the relevant quantity is the minimum detectable magnetic flux $\Phi_{min} = B_{min}A$ (A: sensing area) when considering the demands on a micro-Hall sensor, which is typically exposed to a highly inhomogeneous magnetic field distribution. It was found that for the Co–C Hall devices with the smallest width of about 100 nm this amounted to 4.5×10^{-6} Φ_0, with $\Phi_0 = h/2e$ the magnetic flux quantum, under optimal conditions which is about one order of magnitude better than what can be realized with semiconductor-quantum-well structures [39].

Conclusion

In this review a selected summary of recent developments in the use of FEBID-structures in basic and applied research has been presented. The addressed topics were fundamental questions relating to the nature of the charge transport in nanogranular metals close to the insulator-to-metal transition, the extension of FEBID to a multiprecursor technique for the direct nanostructure formation of granular alloys and intermetallic compounds, and finally to sensor applications, which benefit from this same granular structure. The authors consider these new developments as very promising for the development of the FEBID technique towards the fabrication of functional nanostructures, albeit the aspect of long-time stability of the transport properties certainly needs more attention [62]. On the other hand, when considering the development over the past two decades it can be stated that the holy grail of FEBID has been the identification of deposition protocols to obtain the purest metallic nanostructures possible. Presently, this has been achieved for a very limited group of precursors, e.g., $Co_2(CO)_8$ or $Fe(CO)_5$ (under UHV conditions) and not without problems, such as precursor instability or autocatalytic growth contributions, which limit the ultimately achievable resolution [63]. Nevertheless, the availability of FEBID processes for pure metallic structures would without any doubt render this technique the most versatile direct nanostructure fabrication technique in many fields of nanotechnology, be it in basic or applied research. Although this is certainly a valid argument, from a broader perspective FEBID holds the potential to become the basic technology of an electron-beam-induced and -controlled chemistry on the nanometer scale. The aspect of control is the critical issue in this regard. Very little research has been carried out concerning the details of the dissociation pathways for FEBID-relevant precursors, be it experimentally or theoretically [17,64]. This certainly needs to be intensified to provide the basis for the next step of controlling the dissociation process under electron impact, e.g., by providing supporting chemical agents that saturate free bonds of organic dissociation products, thus preventing their polymerization and keeping them sufficiently volatile to be eventually pumped away. There appears not to be a principle limitation in developing a specialized surface chemistry that is triggered by electrons but nevertheless can be controlled to a significant degree by supplying a suitable chemical environment aiming for an optimized product yield, e.g., a pure simple metal or alloy. From this perspective FEBID will have to move towards a better microscopic understanding of all relevant processes in a controlled environment, i.e., under UHV conditions and augmented by a selection of surface science analysis techniques. One may hope that results from research under these much better controlled conditions (see e.g., [65,66]) will also be helpful to optimize FEBID processes in the standard SEM environment where it is already today a most attractive technique for structure formation on the nanometer scale.

Acknowledgements

The authors acknowledge financial support by the European FP7 project “ALBICAN” under Grant No. 286146 and by the Beilstein-Institut, Frankfurt/Main, Germany within the research collaboration NanoBiC.

References

1. van Kouwen, L.; Botman, A.; Hagen, C. W. *Nano Lett.* **2009,** *9,* 2149–2152. doi:10.1021/nl900717r
2. van Dorp, W. F.; Hagen, C. W.; Crozier, P. A.; Kruit, P. *Nanotechnology* **2008,** *19,* 225305. doi:10.1088/0957-4484/19/22/225305
3. *Nanofabrication Using Focused Ion and Electron Beams;* Utke, I.; Moshkalev, S.; Russell, P., Eds.; Oxford University Press: Oxford, 2012.
4. Randolph, S. J.; Fowlkes, J. D.; Rack, P. D. *Crit. Rev. Solid State Mater. Sci.* **2006,** *31,* 55–89. doi:10.1080/10408430600930438
5. van Dorp, W. F.; Hagen, C. W. *J. Appl. Phys.* **2008,** *104,* 081301. doi:10.1063/1.2977587
6. Utke, I.; Hoffmann, P.; Melngailis, J. *J. Vac. Sci. Technol., B* **2008,** *26,* 1197. doi:10.1116/1.2955728
7. Chung, M. S.; Everhart, T. E. *J. Appl. Phys.* **1974,** *45,* 707–709. doi:10.1063/1.1663306
8. Liu, Z.-Q.; Mitsuishi, K.; Furuya, K. *Nanotechnology* **2006,** *17,* 3832–3837. doi:10.1088/0957-4484/17/15/038
9. Smith, D. A.; Fowlkes, J. D.; Rack, P. D. *Nanotechnology* **2007,** *18,* 265308. doi:10.1088/0957-4484/18/26/265308

10. Bray, A. J. *Adv. Phys.* **2002,** *51,* 481–587. doi:10.1080/00018730110117433
11. Tibrewala, A.; Peiner, E.; Bandorf, R.; Biehl, S.; Lüthje, H. *J. Micromech. Microeng.* **2007,** *17,* S77–S82. doi:10.1088/0960-1317/17/7/S03
12. Beloborodov, I. S.; Lopatin, A. V.; Vinokur, V. M.; Efetov, K. B. *Rev. Mod. Phys.* **2007,** *79,* 469–518. doi:10.1103/RevModPhys.79.469
13. Fernández-Pacheco, A.; De Teresa, J. M.; Córdoba, R.; Ibarra, M. R. *J. Phys. D: Appl. Phys.* **2009,** *42,* 055005. doi:10.1088/0022-3727/42/5/055005
14. Walz, M.-M.; Schirmer, M.; Vollnhals, F.; Lukasczyk, T.; Steinrück, H.-P.; Marbach, H. *Angew. Chem., Int. Ed.* **2010,** *49,* 4669–4673. doi:10.1002/anie.201001308
15. Porrati, F.; Sachser, R.; Walz, M.-M.; Vollnhals, F.; Steinrück, H.-P.; Marbach, H.; Huth, M. *J. Phys. D: Appl. Phys.* **2011,** *44,* 425001. doi:10.1088/0022-3727/44/42/425001
16. Utke, I.; Hoffmann, P.; Dwir, B.; Leifer, K.; Kapon, E.; Doppelt, P. *J. Vac. Sci. Technol., B* **2000,** *18,* 3168. doi:10.1116/1.1319690
17. Wnuk, J. D.; Rosenberg, S. G.; Gorham, J. M.; van Dorp, W. F.; Hagen, C. W.; Fairbrother, D. H. *Surf. Sci.* **2011,** *605,* 257–266. doi:10.1016/j.susc.2010.10.035
18. Muthukumar, K.; Opahle, I.; Shen, J.; Jeschke, H. O.; Valentí, R. *Phys. Rev. B* **2011,** *84,* 205442. doi:10.1103/PhysRevB.84.205442
19. Shen, J.; Muthukumar, K.; Jeschke, H. O.; Valentí, R. *arXiv:1203.4109v1 [cond-mat.mtrl-sci]* **2012**, 1–6.
20. Muthukumar, K.; Jeschke, H. O.; Valentí, R.; Begun, E.; Schwenk, J.; Porrati, F.; Huth, M. *Beilstein J. Nanotechnol.* **2012,** *3,* 546–555. doi:10.3762/bjnano.3.63
21. Fowlkes, J. D.; Rack, P. D. *ACS Nano* **2010,** *4,* 1619–1629. doi:10.1021/nn901363a
22. Friedli, V.; Utke, I. *J. Phys. D: Appl. Phys.* **2009,** *42,* 125305. doi:10.1088/0022-3727/42/12/125305
23. Wnuk, J. D.; Gorham, J. M.; Rosenberg, S. G.; van Dorp, W. F.; Madey, T. E.; Hagen, C. W.; Fairbrother, D. H. *J. Phys. Chem. C* **2009,** *113,* 2487–2496. doi:10.1021/jp807824c
24. Friedli, V.; Santschi, C.; Michler, J.; Hoffmann, P.; Utke, I. *Appl. Phys. Lett.* **2007,** *90,* 053106. doi:10.1063/1.2435611
25. Lobo, C. J.; Toth, M.; Wagner, R.; Thiel, B. L.; Lysaght, M. *Nanotechnology* **2008,** *19,* 025303. doi:10.1088/0957-4484/19/02/025303
26. Bernau, L.; Gabureac, M.; Erni, R.; Utke, I. *Angew. Chem., Int. Ed.* **2010,** *49,* 8880–8884. doi:10.1002/anie.201004220
27. Che, R. C.; Takeguchi, M.; Shimojo, M.; Zhang, W.; Furuya, K. *Appl. Phys. Lett.* **2005,** *87,* 223109. doi:10.1063/1.2136071
28. Winhold, M.; Schwalb, C. H.; Porrati, F.; Sachser, R.; Frangakis, A. S.; Kämpken, B.; Terfort, A.; Auner, N.; Huth, M. *ACS Nano* **2011,** *5,* 9675–9681. doi:10.1021/nn203134a
29. Bentmann, H.; Demkov, A. A.; Gregory, R.; Zollner, S. *Phys. Rev. B* **2008,** *78,* 205302. doi:10.1103/PhysRevB.78.205302
30. Baturina, T. I.; Horsell, D. W.; Islamov, D. R.; Drebushchak, I. V.; Tsaplin, Yu. A.; Babenko, A. A.; Kvon, Z. D.; Savchenko, A. K.; Plotnikov, A. E. *Phys. B (Amsterdam, Neth.)* **2003,** *329–333,* 1496–1497. doi:10.1016/S0921-4526(02)02631-5
31. Tsaur, B. Y.; Mayer, J. W.; Tu, K. N. *J. Appl. Phys.* **1980,** *51,* 5326–5333. doi:10.1063/1.327446
32. Mott, N. F. *J. Non-Cryst. Solids* **1968,** *1,* 1–17. doi:10.1016/0022-3093(68)90002-1
33. Porrati, F.; Begun, E.; Winhold, M.; Schwalb, C. H.; Sachser, R.; Frangakis, A. S.; Huth, M. *Nanotechnology* **2012,** *23,* 185702. doi:10.1088/0957-4484/23/18/185702
34. Jeong, S.; Hsu, Y.-N.; McHenry, M. E.; Laughlin, D. E. *J. Appl. Phys.* **2000,** *87,* 6950. doi:10.1063/1.372896
35. Wang, R. F.; Nisoli, C.; Freitas, R. S.; Li, J.; McConville, W.; Cooley, B. J.; Lund, M. S.; Samarth, N.; Leighton, C.; Crespi, V. H.; Schiffer, P. *Nature* **2006,** *439,* 303–306. doi:10.1038/nature04447
36. Porrati, F.; Huth, M. *Appl. Phys. Lett.* **2004,** *85,* 3157. doi:10.1063/1.1805697
37. Utke, I.; Hoffmann, P.; Berger, R.; Scandella, L. *Appl. Phys. Lett.* **2002,** *80,* 4792. doi:10.1063/1.1489097
38. Boero, G.; Utke, I.; Bret, T.; Quack, N.; Todorova, M.; Mouaziz, S.; Kejik, P.; Brugger, J.; Popovic, R. S.; Hoffmann, P. *Appl. Phys. Lett.* **2005,** *86,* 042503. doi:10.1063/1.1856134
39. Gabureac, M.; Bernau, L.; Utke, I.; Boero, G. *Nanotechnology* **2010,** *21,* 115503. doi:10.1088/0957-4484/21/11/115503
40. Belova, L. M.; Dahlberg, E. D.; Riazanova, A.; Mulders, J. J. L.; Christophersen, C.; Eckert, J. *Nanotechnology* **2011,** *22,* 145305. doi:10.1088/0957-4484/22/14/145305
41. Serrano-Ramón, L.; Córdoba, R.; Rodríguez, L. A.; Magén, C.; Snoeck, E.; Gatel, C.; Serrano, I.; Ibarra, M. R.; De Teresa, J. M. *ACS Nano* **2011,** *5,* 7781–7787. doi:10.1021/nn201517r
42. Nikulina, E.; Idigoras, O.; Vavassori, P.; Chuvilin, A.; Berger, A. *Appl. Phys. Lett.* **2012,** *100,* 142401. doi:10.1063/1.3701153
43. Soroka, O. K.; Shklovskij, V. A.; Huth, M. *Phys. Rev. B* **2007,** *76,* 014504. doi:10.1103/PhysRevB.76.014504
44. Dobrovolskiy, O. V.; Huth, M.; Shklovskij, V. A. *J. Supercond. Novel Magn.* **2010,** *24,* 375–380. doi:10.1007/s10948-010-1055-7
45. Dobrovolskiy, O. V.; Huth, M.; Shklovskij, V. A. *Supercond. Sci. Technol.* **2010,** *23,* 125014. doi:10.1088/0953-2048/23/12/125014
46. Dobrovolskiy, O. V.; Begun, E.; Huth, M.; Shklovskij, V. A.; Tsindlekht, M. I. *Phys. C (Amsterdam, Neth.)* **2011,** *471,* 449–452. doi:10.1016/j.physc.2011.05.245
47. Sahoo, S.; Petracic, O.; Binek, C.; Kleemann, W.; Sousa, J. B.; Cardoso, S.; Freitas, P. P. *Phys. Rev. B* **2002,** *65,* 134406. doi:10.1103/PhysRevB.65.134406
48. Beloborodov, I. S.; Lopatin, A. V.; Vinokur, V. M. *Phys. Rev. B* **2004,** *70,* 205120. doi:10.1103/PhysRevB.70.205120
49. Beloborodov, I. S.; Lopatin, A. V.; Vinokur, V. M. *Phys. Rev. B* **2005,** *72,* 125121. doi:10.1103/PhysRevB.72.125121
50. Huth, M.; Klingenberger, D.; Grimm, C.; Porrati, F.; Sachser, R. *New J. Phys.* **2009,** *11,* 033032. doi:10.1088/1367-2630/11/3/033032
51. Schwalb, C. H.; Grimm, C.; Baranowski, M.; Sachser, R.; Porrati, F.; Reith, H.; Das, P.; Müller, J.; Völklein, F.; Kaya, A.; Huth, M. *Sensors* **2010,** *10,* 9847–9856. doi:10.3390/s101109847
52. Porrati, F.; Sachser, R.; Schwalb, C. H.; Frangakis, A. S.; Huth, M. *J. Appl. Phys.* **2011,** *109,* 063715. doi:10.1063/1.3559773
53. Plank, H.; Kothleitner, G.; Hofer, F.; Michelitsch, S. G.; Gspan, C.; Hohenau, A.; Krenn, J. *J. Vac. Sci. Technol., B* **2011,** *29,* 051801. doi:10.1116/1.3622314
54. Sachser, R.; Porrati, F.; Schwalb, C. H.; Huth, M. *Phys. Rev. Lett.* **2011,** *107,* 206803. doi:10.1103/PhysRevLett.107.206803
55. Völklein, F.; Reith, H.; Schmitt, M. C.; Huth, M.; Rauber, M.; Neumann, R. *J. Electron. Mater.* **2009,** *39,* 1950–1956. doi:10.1007/s11664-009-1046-2
56. Sachser, R.; Porrati, F.; Huth, M. *Phys. Rev. B* **2009,** *80,* 195416. doi:10.1103/PhysRevB.80.195416
57. Porrati, F.; Sachser, R.; Strauss, M.; Andrusenko, I.; Gorelik, T.; Kolb, U.; Bayarjargal, L.; Winkler, B.; Huth, M. *Nanotechnology* **2010,** *21,* 375302. doi:10.1088/0957-4484/21/37/375302

58. Koppert, R.; Uhlig, S.; Schmid-Engel, H.; Göttel, D.; Probst, A.-C.; Schultes, G.; Werner, U. *Diamond Relat. Mater.* **2012,** *25,* 50–58. doi:10.1016/j.diamond.2012.01.031
59. Huth, M. *J. Appl. Phys.* **2010,** *107,* 113709. doi:10.1063/1.3443437
60. Nagaosa, N.; Onoda, S.; MacDonald, A. H.; Ong, N. P. *Rev. Mod. Phys.* **2010,** *82,* 1539–1592. doi:10.1103/RevModPhys.82.1539
61. Bando, M.; Ohashi, T.; Dede, M.; Akram, R.; Oral, A.; Park, S. Y.; Shibasaki, I.; Handa, H.; Sandhu, A. *J. Appl. Phys.* **2009,** *105,* 07E909. doi:10.1063/1.3074513
62. Porrati, F.; Sachser, R.; Huth, M. *Nanotechnology* **2009,** *20,* 195301. doi:10.1088/0957-4484/20/19/195301
63. Utke, I.; Gölzhäuser, A. *Angew. Chem., Int. Ed.* **2010,** *49,* 9328–9330. doi:10.1002/anie.201002677
64. Engmann, S.; Stano, M.; Matejčík, Š.; Ingólfsson, O. *Angew. Chem., Int. Ed.* **2011,** *50,* 9475–9477. doi:10.1002/anie.201103234
65. Lukasczyk, T.; Schirmer, M.; Steinrück, H.-P.; Marbach, H. *Langmuir* **2009,** *25,* 11930–11939. doi:10.1021/la901612u
66. Schirmer, M.; Walz, M.-M.; Vollnhals, F.; Lukasczyk, T.; Sandmann, A.; Chen, C.; Steinrück, H.-P.; Marbach, H. *Nanotechnology* **2011,** *22,* 085301. doi:10.1088/0957-4484/22/8/085301

License and Terms

Beilstein Journal of Nanotechnology

Characterization and properties of micro- and nanowires of controlled size, composition, and geometry fabricated by electrodeposition and ion-track technology

Maria Eugenia Toimil-Molares

Review

Open Access

Address:
Materials Research Department, GSI Helmholtz Centre for Heavy Ion Research, Planckstr. 1, 64291 Darmstadt, Germany

Email:
Maria Eugenia Toimil-Molares - m.e.toimilmolares@gsi.de

Keywords:
electrodeposition; etched ion-track membrane; finite-size effects; heavy ion irradiation; nanowire; radiation-induced nanostructures

Beilstein J. Nanotechnol. **2012,** *3,* 860–883.
doi:10.3762/bjnano.3.97

Received: 13 July 2012
Accepted: 19 November 2012
Published: 17 December 2012

This article is part of the Thematic Series "Radiation-induced nanostructures: Formation processes and applications".

Guest Editor: M. Huth

Abstract

The combination of electrodeposition and polymeric templates created by heavy-ion irradiation followed by chemical track etching provides a large variety of poly- and single-crystalline nanowires of controlled size, geometry, composition, and surface morphology. Recent results obtained by our group on the fabrication, characterization and size-dependent properties of nanowires synthesized by this technique are reviewed, including investigations on electrical resistivity, surface plasmon resonances, and thermal instability.

Introduction

During the past decade, nanowires have attracted an enormous interest due to a large variety of promising applications in areas such as nanoelectronics, biotechnology, magnetism, thermoelectrics, solar cells, and water splitting, among others [1-4]. Their reduced size, elongated geometry, and high surface-to-volume ratio turn nanowires into ideal elements for electrical and electrochemical systems [5,6]. In addition, nanowires are considered excellent model objects to study how fundamental physical properties (such as mechanical, optical, electronic, thermoelectrical and magnetic) depend on dimension, composition, geometry and crystallinity of the nanostructures [7-9]. The investigation of size effects requires methods to synthesize nanowires under controlled conditions and with tailored characteristics. Moreover, to characterize physical and chemical properties at the single-nanowire level requires appropriate techniques. In the two areas of fabrication and characterization,

great advances have been reported in recent years. Methods to fabricate nanowires include top-down approaches such as optical and electron-beam lithography, and focused ion beam. More commonly applied bottom-up approaches are, e.g., vapour–liquid–solid growth, sol–gel and other chemical methods [10,11]. This review focuses on the bottom-up template method, which provides nanowires of a great variety of materials, from metals to semiconductors, including polymers as well as inorganic and organic compounds [12]. The material of interest is synthesized in the channels or cavities of the given template. During growth, the nanostructures adopt the exact shape and size of the hosting channels [13]. The most commonly used templates are porous alumina [14], diblock-copolymers [15], and track-etched membranes. Electrochemical and electroless deposition, polymerisation reactions, sol–gel template synthesis, and high-pressure injection of a melted material are examples of available techniques suitable for filling the pores. The electrodeposition of 40 nm diameter metal nanowires (Sn, In, and Zn) in etched fission tracks in mica was reported by Possin et al. back in 1970 [16]. In 1984, Williams and Giordano employed the same method to synthesize nanowires with a diameter as small as 10 nm using mica templates [17]. Since then, a large variety of materials have been electrodeposited, mainly in polymeric etched ion-track membranes [18-24]. Advantages of the electrodeposition method include low fabrication cost, high deposition rates, and its suitability for filling low- and high-aspect-ratio pores and trenches [25]. The wires are grown from the bottom to the top, yielding homogeneous replication of channels with any given geometry [26]. All relevant parameters, such as wire diameter, wire density, geometry, material and crystallinity, can be adjusted, allowing systematic studies of finite- and quantum-size effects on wire properties relevant for various technological applications.

This paper reviews recent advances in the electrodeposition of metal, semimetal, and semiconductor nanowires in polymeric etched ion-track membranes. Particular focus is given to our current efforts to study the influence of size, morphology and crystallinity of nanowires on electrical, optical and thermal properties. In section 1, we discuss the processes involved in the fabrication of etched ion-track membranes and electrodeposition of nanowires. Section 2 includes results on the compositional and crystallographic characterization of nanowires of various materials including metals, semimetals and semiconductors. The different nanowire morphologies attained by deposition in etched ion-track membranes are summarized in section 3. Finally, in section 4, recent results obtained by our group on electrical, optical, and thermal size-effects of the electrodeposited nanowires are presented.

Review

1 Nanowire fabrication

1.1 Fabrication of etched ion-track membranes

In the past two decades, etched ion-track membranes have been widely used as templates for the creation of nanowires and nanotubes. Their fabrication involves two separate processing steps: (i) Irradiation of the template material with energetic heavy ions and creation of latent tracks; (ii) selective ion-track dissolution and formation of channels by chemical etching. Control over the irradiation and etching conditions enables the production of various membranes with channels of predefined geometries, sizes and aspect ratios.

1.1.1 Swift heavy-ion irradiation: Swift heavy-ion beams are provided at large accelerator facilities, such as the linear accelerator of GSI (Darmstadt, Germany), and the cyclotrons at GANIL (Caen, France), JINR (Dubna, Russia), and CICLONE (Louvain la Neuve, Belgium) and a few others outside Europe, for example in Lanzhou (China) and Brookhaven (USA). The UNILAC linear accelerator of GSI provides heavy ions (up to uranium) of specific energy up to 11.4 MeV per nucleon (MeV/u) corresponding to ≈15% of the velocity of light [27]. Ion beams of such high energy have a penetration range in polymers of about 120 μm. Given this large range, foil stacks (e.g., ten foils 12 μm thick, or four foils 30 μm thick) can be irradiated. Each ionic projectile induces electronic excitation and ionisation processes in a cylindrical zone along its trajectory. In polymers, chemical bonds are destroyed and small volatile fragments (e.g., H_2, CO, CO_2, hydrocarbons) easily outgas [28]. This damaged region is called the ion track and has a typical diameter of few nanometres.

By suitable adjustment of the ion beam and monitoring the flux (beam current), the applied ion fluence can be adjusted over a wide range, from exposure to a single ion (single track) up to more than 10^{12} ions/cm^2 (overlapping tracks) (Figure 1a). At the UNILAC beamline of the GSI facilities, irradiation with a broad homogenous beam is obtained by magnetic defocusing. Samples of up to several square centimetres in size can be exposed. The resulting ion tracks are stochastically distributed and oriented in parallel across the sample. Irradiation with one single ion requires monitoring of individual ions hitting the sample [29]. To achieve this, the sample is irradiated through a small circular aperture (diameter ≈ 200 μm) placed in front of a stack of foils. The ion beam is strongly defocused and adjusted in such a way that single projectiles pass through the aperture with a frequency of about 1 Hz. The ions are detected by a solid-state particle detector placed behind the sample. As soon as the detector has registered a single ion impact, the entire ion beam is deflected by an electrostatic chopper system. A schematic representation of the single-ion irradiation system is

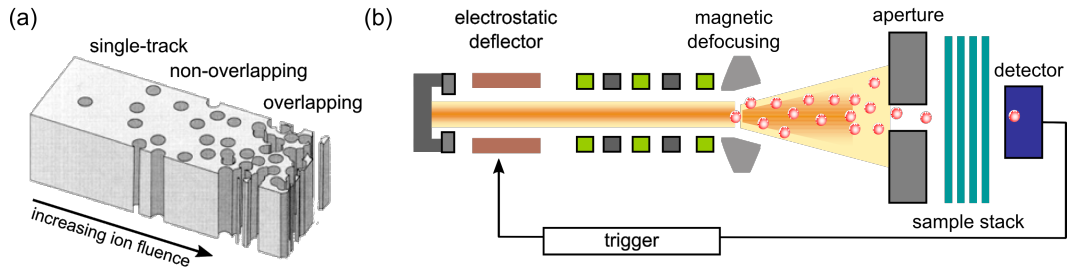

Figure 1: (a) Track-etched membrane illustrating the porosity regime available by means of ion-track technology: single channel, non-overlapping channels, and overlapping channels. (b) Schematic of single-ion irradiation setup.

presented in Figure 1b. This GSI single-ion irradiation facility is routinely used for the production of single-nanopore membranes [30-33] and the growth of single nanowires [34-36]. If required for specific applications, it is possible to create a preset regular ion-track arrangement by using a microprobe [37]. Materials commonly used as multi- and single-pore etched-ion-track membranes include polymers such as polyimide (PI), polyethylene terephthalate (PET) and polycarbonate (PC), and inorganic materials such as mica and glass.

The production of membranes with open channels requires selective dissolution of the latent tracks (cf. subsection 1.1.2). Selective track etching of channels with small size distributions requires continuous and homogeneous damage along the ion trajectory. Best results are achieved when the energy loss of the ions in the given material is above the so-called etching threshold [38]. Figure 2a presents the energy loss of light- and heavy-ion projectiles in polyimide. The different symbols denote cylindrical (full), discontinuous (crossed), and spherical (open) damage morphology with respective homogenous (full), inhomogeneous (crossed), and missing (open) selective track etching. Scanning electron microscopy (SEM) images in Figure 2b reveal how the etching of homogeneous tracks results in channels of uniform size (top) after etching tracks of homogeneous damage, whereas etching of inhomogeneous tracks leads to pores with a broad size distribution (bottom) [38]. Heavier projectiles (e.g., Au, Pb, Bi, U), produce tracks of more pronounced and continuous damage and are thus optimal for the production of porous membranes with small pore size distributions.

1.1.2. Chemical etching: In a suitable etching solution the ion tracks can be selectively dissolved and subsequently enlarged into channels [39]. For the successful fabrication of templates, the anisotropic dissolution rate along the ion track (V_t) must be higher than the dissolution rate of the undamaged bulk material (V_b). The material of choice together with the etching conditions (temperature, composition, and concentration of the etchant) determine the track-to-bulk etching ratio (V_t/V_b) and thus also the geometry of the channels. High V_t/V_b ratios result

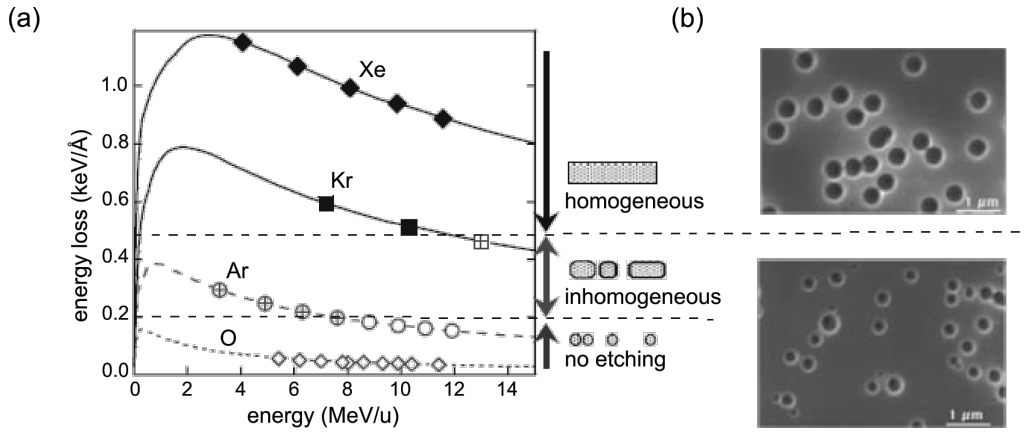

Figure 2: (a) Energy loss as a function of specific ion energy. The dashed lines separate the different regimes of track etching: homogenous (full symbols), inhomogeneous (crossed symbols), and absence of etching (open). (b) SEM images of uniform pores resulting from homogeneous tracks (top) and pores with broad size distribution due to inhomogeneous tracks (bottom). Adapted with permission from [38] – Copyright 1996 Elsevier.

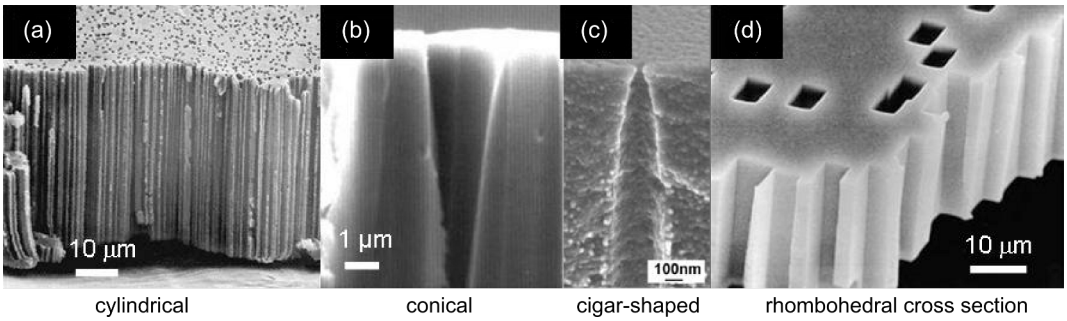

Figure 3: SEM images displaying the cross sections of the following membranes: (a) cylindrical channels in PI; (b) conical channels in PI; (c) cigar-shaped channels in PET, (d) cylindrical channels with rhombohedral cross section in mica. (a,b) Adapted with permission from [26] – Copyright 1996 Elsevier; (c) adapted with permission from [42] – Copyright 2007 IOP Publishing Ltd; (d) adapted with permission from [43] – Copyright 2012 American Physical Society.

in the formation of cylindrical channels (Figure 3a and Figure 3d), whereas low ratios result in conical (Figure 3b) or biconical channels. High etching selectivity is achieved in PI by using, e.g., sodium hypochlorite (NaOCl) [26], while tracks in PET and PC are preferentially etched in sodium hydroxide (NaOH) solutions [34,39]. Exposure of ion-irradiated polymers to UV light prior to etching increases V_t and leads to a narrower size distribution of the channels [40,41].

Symmetric etching of cylindrical channels is performed in a thermostated etching bath (Figure 4a). Stirring improves convection and provides a homogeneous temperature of the bath. Alternatively, chemical etching in both symmetric and asymmetric configuration can be performed in a two-compartment electrolytical cell at constant temperature (Figure 4b and Figure 4c). The irradiated foil is sealed between the two half-cells. Exposing the foil surfaces to different solutions (e.g., etching and neutralizing agents), allows one to adjust different conditions. By means of current measurements, the etching process is monitored online. A voltage U is applied between two gold electrodes immersed at each side of the foil and the current I is recorded with a picoammeter as a function of time. While the pore has not yet been etched through, the membrane acts as a very large resistance, and no current flows. As soon as the track is converted into an open channel, the electric current I starts to increase. The etching is continued and the current will increase as the pore diameter enlarges [31].

For the fabrication of cylindrical multi- or single pores in PC, the etching process is performed in a symmetric configuration by exposing the foil to concentrated NaOH solution on both membrane sides (Figure 4b) [34,44,45]. To obtain conical nanopores, one half-cell is filled with a suitable etchant while the other half-cell contains either water or an acidic stopping medium that neutralizes the etchant as soon as the pore opens. In both cases, further etching is extensively slowed down or entirely stopped (Figure 4c). In addition, by immersing the positive anode in the etching solution, the negative ions in the

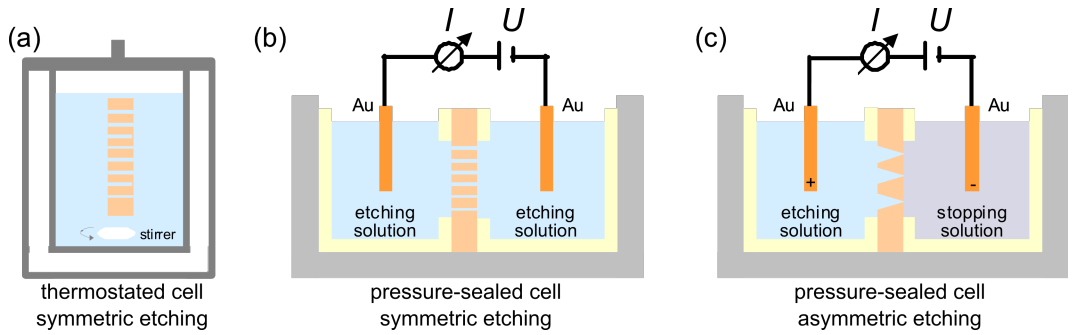

Figure 4: Schematic of etching equipment. Symmetric etching conditions leading to cylindrical channels in (a) thermostated cell and (b) pressure-sealed cell. (c) Asymmetric conditions leading to conical channels in pressure-sealed cell. Electric current measurements allow monitoring of the etching process.

etchant migrate away from the pore tip when the pore breaks through. This helps to create channels of reduced tip diameter [46].

Conical nanopores in PET, PC, and PI have been produced with different combinations of etching and stopping solutions. For example, conical channel geometries in PC and PET are typically achieved by using solutions of sodium hydroxide (various concentrations) for etching and a mixture of potassium chloride (KCl) and formic acid (HCOOH) for stopping [31,46]. Methanol can be added in different concentrations to the NaOH etchant to influence V_b. In the case of 30 µm thick PC foils, it was reported that with an increasing volume concentration of methanol from 0 to 80%, the cone half-angle increases from about 0.2 to about 3.6° [47]. In the case of PI, the etching is typically performed in sodium hypochlorite (NaOCl) solution with an initial pH value 12.6 and an active chlorine content of 13%, while KI acts as reducing agent for the OCl^- ions of the etchant [32,48]. The apex angle of the conical pores in PI becomes larger by increasing the pH of the NaOCl solution [26]. Channels with specific geometries other than cylindrical or conical, for example, cigar-shaped (Figure 3c), are fabricated by applying adequate surfactants [46,49]. Before further processing, the template is rinsed in purified water.

Compared to other available templates, such as di-block copolymer membranes or porous alumina, etched ion-track membranes offer the powerful possibility of controlling all important parameters of the synthesized nanostructures in an independent manner: (i) The irradiation fluence determines the preset density of parallelly oriented nanochannels; (ii) By tilting the samples in the ion beam, tilted channels can be produced yielding an interconnected nanochannel network; (iii) The polymer material of choice, together with the etching conditions, determine the geometry of the channels, e.g., cylindrical, conical, and biconical; (iv) Controlled by the etching time, uniform channels can be produced with diameters from about 10 nm to a few micrometres.

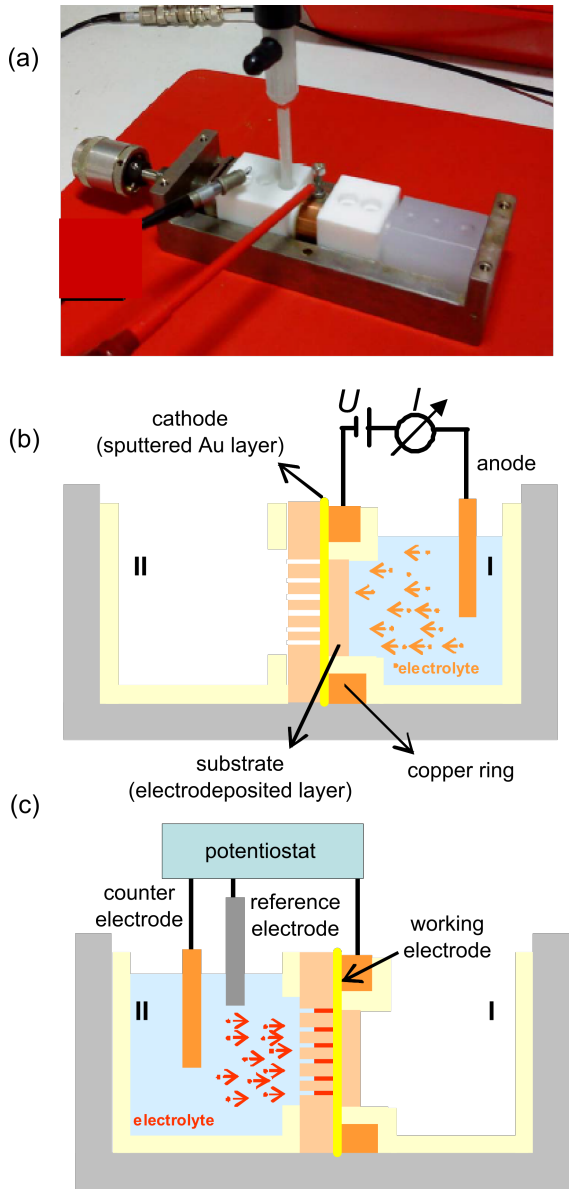

Figure 5: (a) Photograph of a pressure-sealed electrochemical cell. (b) Schematic for the electrodeposition of a conductive layer as substrate in a two-electrode configuration (cathode and anode). (c) Schematic for the growth of nanowire arrays by using three electrodes (working, counter, and reference electrode).

1.2 Electrodeposition of nanowires

This section presents the setting for nanowire electrodeposition, and discusses the electrochemical deposition processes as analysed by chronoamperometric monitoring.

1.2.1 Electrochemical cells: The photograph in Figure 5a shows our electrochemical cell, currently in use. The polymer foil is placed between two polytetrafluorethylene compartments, and is sealed by mechanical pressure. A good sealing is essential to avoid leak currents, an important requirement when growing single nanowires. Very small currents in the picoamp range must be recorded and analysed, as demonstrated during electrodeposition of nanowires, e.g., Cu and Bi, in single-nanopore membranes [35,36,50,51]. This pressure-sealed cell is also suitable for the growth of nanowire arrays of various materials [52-57]. Figure 5b and Figure 5c depict schematically the two deposition processes involved in the nanowire synthesis: substrate deposition and nanowire growth, respectively. First, one side of the track-etched polymer membrane is sputter coated with a thin (few ten nanometres) Au layer. The membrane is then mounted between the two cell compartments. The sputtered metal layer is in contact with a copper ring accessible

to external electronic equipment (voltage supply or potentiostat). In some cases, the thin conductive Au layer is reinforced electrochemically by a metal layer (e.g., Cu, Au) in a two electrode configuration (Figure 5b). After reinforcement, the electrolyte is removed from the first compartment (I) and the membrane is rinsed with distilled water. For the electrochemical deposition process, the specific electrolyte is introduced in the second compartment (II) and an adequate deposition potential is applied. At a preselected constant temperature, the nanowires then grow from the bottom-side (sputter-coated layer) to the top-side of the membrane (Figure 5c).

The wire synthesis can be performed by using a two- or a three-electrode arrangement, under potentiostatic or galvanostatic conditions. In the case of potentiostatic and pulsed deposition, the process is monitored by chronoamperometric current–time (*I*–*t*) curves. In the two-electrode arrangement the potential U_c is applied between cathode and anode. In the three-electrode arrangement, reference electrodes such as saturated silver/silver chloride (Ag/AgCl/sat. KCl) and saturated calomel electrodes (SCE) are currently employed. Larger thermostated cells have also been employed, e.g., for the growth of Cu and Bi_2Te_3 nanowires, to improve convection by magnetic stirring or to provide temperatures above or below ambient conditions [58,59].

1.2.2 Chronoamperometric monitoring: During the potentiostatic growth of nanowires, four different current regimes can be identified (Figure 6a): (1) A sharp decrease of the current at the beginning of the process attributed to the creation of the diffusion layer; (2) nanowire growth inside the channels with nearly constant current; (3) more or less sharp current increase when the material reaches the top side of the membrane and caps start to grow on top; and (4) if the process is continued, the caps grow further and eventually form a continuous layer. Current–time characteristics displaying these four distinct regions have been reported for the growth of Cu [52], Au [53], Bi [56], Pt [55], $Bi_{1-x}Sb_x$ [60], Bi_2Te_3 [58], and Ni nanowires among others. The integral of the *I*–*t* curves between the beginning of the deposition and the transition to zone 3 corresponds to the charge Q_{exp} applied during the growth process. Assuming complete pore filling, the expected total charge Q_{theo} is given by the Faraday law, namely $Q_{theo} = (z{\cdot}F{\cdot}m)/M$, with z being the number of electrons transferred per ion during the reaction, F the Faraday constant (96.485 $C{\cdot}mol^{-1}$), m the total mass and M the molar mass of the deposited substance. In the case of 100% efficient electrochemical reactions, the ratio Q_{exp}/Q_{theo} is an indicator of the homogeneity of the wire growth over the whole sample. $Q_{exp} < Q_{theo}$ indicates that deposition has not occurred in all channels simultaneously, and/or that the number density of the wires is lower than that of the channels. Monitoring the *I*–*t* curves during homogeneous growth allows us to stop the deposition after a given time to obtain nanowires of a predefined length. By this technique, wires of length between 1 and 60 µm were fabricated. Figure 6b shows representative chronoamperometric curves recorded during the potentiostatic growth of Cu nanowires in PC membranes (d_{pore} = 450 nm, 10^7 cm^{-2}) at 25 °C, in a solution consisting of 0.25 mol/L $CuSO_4{\cdot}5H_2O$ and 2 mol/L H_2SO_4, by applying different potentials ranging between −80 and −440 mV (versus Ag/AgCl/3 mol/L KCl provided with a Haber–Luggin capillary) [59].

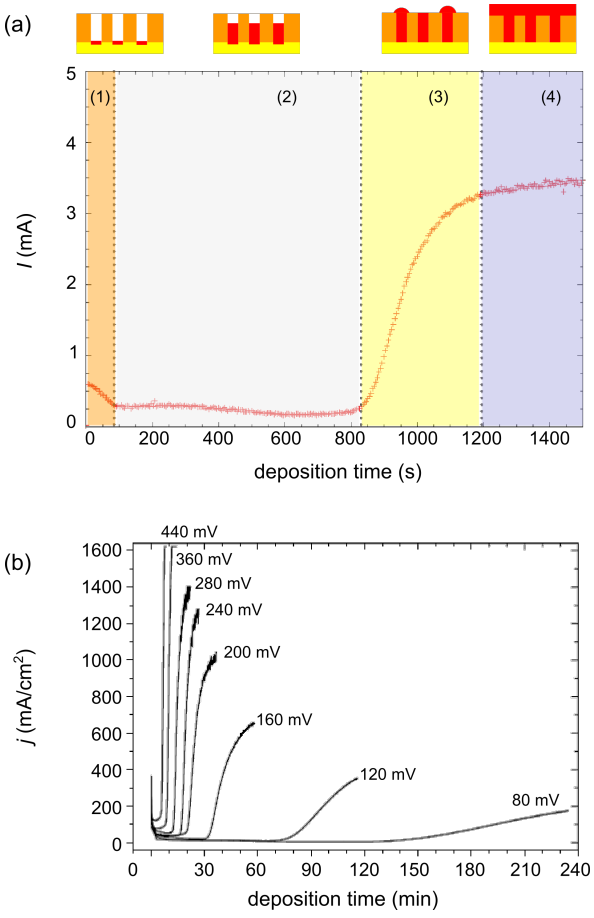

Figure 6: (a) Representative *I*–*t* curve and schematic of the four different deposition regimes. (b) Chronoamperometric curves recorded during growth of Cu nanowires in identical templates (30 µm thick PC, 10^7 channels/cm^2, pore diameter 450 nm) in a solution consisting of 0.25 mol/L $CuSO_4{\cdot}5H_2O$ and 2 mol/L H_2SO_4, by applying different potentials (versus Ag/AgCl/3 mol/L KCl provided with a Haber–Luggin capillary). Adapted with permission from [59] – Copyright 2003 The Electrochemical Society, Inc.

2 Composition and crystallinity of the nanowires

During electrochemical growth of nanowires, two mechanisms occur simultaneously inside the membrane channels: (i) nucleation of new grains and (ii) growth of existing nuclei. To

synthesize single-crystalline micro- or nanowires, the fabrication conditions should be chosen such that the second process dominates [61]. It should be noted, that other than on a macroelectrode surface, the wire deposition process occurs in a recessed electrode ensemble, and that the cathode surface is placed, at the beginning of the process, at the bottom of the channels and shifts to the opposite surface during the nanowire growth [59].

Control over the crystallinity is especially important when the size of the investigated nanostructures is comparable to characteristic length scales such as electron and phonon mean free paths and Fermi wavelength. For nanomaterials, phenomena such as electrical and thermal resistivity or magnetoresistance are known to depend strongly on their crystallinity and morphology [62-64]. Also the surface plasmon resonances show pronounced effects on size, material, and shape [65,66]. A detailed morphological and crystallographic characterization of the synthesized nanostructures is required (i) to understand how the synthesis parameters influence the resulting crystalline structure, and (ii) to investigate size-dependent nanowire properties relevant for different applications. The following sections present results from systematic studies of the influence of the growth parameters on the resulting crystallinity and morphology of nanowires of various materials.

2.1 Copper nanowires

Copper is an important material for the microelectronic industry due to its low resistivity and its low vulnerability to electromigration, a phenomenon that produces voids in wires and ultimately causes failure. Copper micro- and nanostructures in addition are synthesized for applications in solar cells, flat-panel displays, and sensorics. The most common approaches to synthesize copper micro- and nanostructures include electrodeposition, chemical vapour deposition, electroless deposition, and solution growth [67-69]. Among them, electrochemical deposition is most suitable for fabrication of nanostructures in trenches of small dimensions and/or high aspect ratios (length/diameter) [70].

Based on the above-described template technique, poly- and single-crystalline Cu nanowires with aspect ratios above 500 and diameters as small as 30 nm were synthesized by electrodeposition in PC etched ion-track membranes. A suitable electrolyte is, e.g., an aqueous solution containing 238 g/L $CuSO_4 \cdot 5H_2O$ and 21 g/L H_2SO_4 [52]. The high concentration of $CuSO_4$ guarantees a sufficiently large supply of ions inside the pores during the deposition. Addition of sulphuric acid increases the conductivity of the solution and lowers the cathode overvoltage. Electrodeposition is typically performed potentiostatically in a two-electrode arrangement by using a copper anode, at temperatures between 25 and 70 °C. By applying low overvoltages, side reactions, such as hydrogen evolution, are avoided. Figure 7 displays transmission electron microscopy (TEM) images of representative (a) single- and (b) polycrystalline Cu nanowires together with their respective selected-area electron diffraction (SAED) pattern. The single-crystalline Cu wire was deposited at 50 °C by applying a voltage of $U_c = -50$ mV. The wire exhibits cylindrical geometry with constant diameter and a smooth contour over the entire length. The polycrystalline wire was deposited at room temperature and at a larger negative potential. Its contour is clearly rougher, probably due to the higher growth rate. Increase of surface roughness with increasing deposition potential has also been observed in the case of Bi compound wires [58]. X-ray diffraction (XRD) performed on the single-crystalline nanowire arrays by using a four-circle diffractometer, revealed a preferred orientation of the (110) planes perpendicular to the wire axis [71].

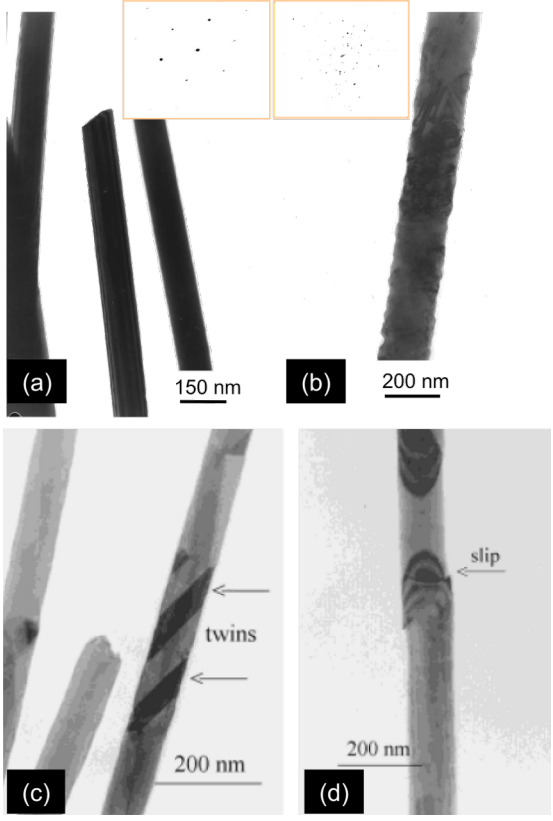

Figure 7: TEM images of representative Cu nanowires and lattice defects: (a) single-crystalline and (b) polycrystalline Cu wires together with their corresponding SAED patterns (insets). (c) 70 nm diameter single-crystalline wire with twin structures. (d) Slip in a 100 nm diameter Cu wire. (a,b) Adapted with permission from [71] – Copyright 2001 Elsevier and (c,d) adapted with permission from [52] – Copyright 2001 Wiley-VCH.

Recently, Duan et al. presented an exhaustive investigation of the preferred orientation of Cu nanowire arrays, demonstrating that their preferred crystallographic orientation can be adjusted along the [111], [100] or [110] directions by selecting specific parameters with respect to the sulphuric acid concentration in the electrolyte, the applied voltage, and the deposition temperature [72]. It was also reported that single-crystalline Cu microwires were grown under room-temperature conditions by using commercial baths and reverse-pulse plating in an ultrasonic bath in a two-electrode arrangement [73]. Copper nanowires were also synthesized in a three-electrode arrangement by using a SCE as reference electrode [59]. Cylindrical multilayered Cu/Cu_2O nanowires were electrochemically deposited from the self-oscillating Cu(II)-lactate system by using PC templates [74].

Figure 7c shows the TEM image of a twinned region, as frequently found in single-crystalline Cu wires. Twinning is a crystal defect characterized by the partial displacement relative to the matrix of a considerable number of neighbouring crystallographic planes [75,76] and is evident by the reduced brightness in Figure 7c. Twins can be created during the growth process but may also result from plastic deformation when handling the samples. Also slips are frequently observed, not only in Cu wires (Figure 7d) but also in other materials such as Au and Bi_2Te_3. Planar defects such as twinning or slips are expected to influence the electrical and thermal transport properties, as well as the mechanical stability of nanowires.

2.2 Gold nanowires

Numerous theoretical predictions and experiments have demonstrated that Au nanoparticles and nanowires are promising elements for sensoric, optical and biomedical applications. Of special interest are surface plasmon resonances (SPRs) of Au nanostructures, because electromagnetic radiation is confined to a volume of sub-wavelength dimensions. It is known that field enhancements due to SPRs are strongly dependent on size, geometry, and composition of the nanostructures [65,66].

Systematic studies were performed on the electrochemical template synthesis of Au-nanowires in a two-electrode configuration by using a sputtered Au film as initial cathode and a Au rod as anode. The investigations provided adequate growth conditions for both single- and polycrystalline wires with diameters between 20 and 100 nm [53,54]. Other than for copper, nanowires deposited by using the ammonium gold(I) sulfite electrolyte (gold content = 15 g/L, Metakem GmbH, Usingen, Germany), or the sodium disulfitoaurate(I) Imabrite 24 bath (gold content = 12.3 g/L, Schloetter Galvanotechnik, Geislingen/Steige, Germany) exhibit a polycrystalline structure independently of temperature and voltage. In contrast, wires grown in a solution of potassium dicyanoaurate(I) (Puramet 402 bath, gold content = 10 g/L, Doduco, Pforzheim, Germany) yield single crystals at temperatures between 50 and 65 °C under both direct-current and reverse-pulse deposition conditions. The resulting single-crystalline wires have a preferred [110] orientation.

Figure 8a shows a representative TEM image of a polycrystalline Au nanowire deposited with an ammonium gold(I) sulfite electrolyte, at 50 °C, by applying U_c = −500 mV between cathode and anode. Several zones of light and dark contrast reveal several grain boundaries along the wire axis. The TEM image in Figure 8c depicts a single-crystalline wire deposited with the cyanidic electrolyte at U_c = −900 mV and 60 °C, while the cell was immersed in an ultrasonic bath. The authors reported that the presence of ultrasound fields improved the convection in the pores and thus the homogeneity of the growth on the whole sample, leading to homogeneous wire arrays. The crystallinity of the different wires is confirmed by the respective SAED patterns (insets). Further, the XRD pattern of the polycrystalline wires indicates random orientation (Figure 8b), while single-crystalline wires have a preferred orientation of the (110) planes perpendicular to the wire axis (Figure 8d).

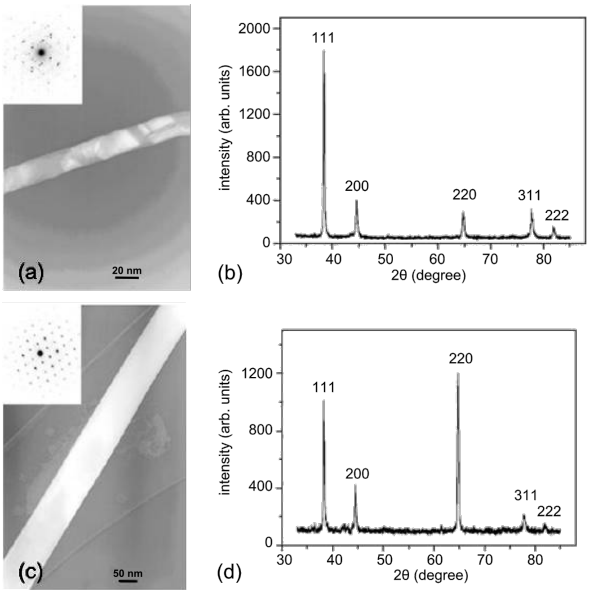

Figure 8: TEM images of representative (a) polycrystalline and (c) single-crystalline Au nanowires and (b,d) their corresponding XRD diffractograms measured on nanowire arrays deposited under the same conditions. Adapted with permission from [53] – Copyright 2006 IOP Publishing Ltd.

2.3 Nanowires from other metals

In the recent past, nanowires of a number of different metals have been synthesized, including Pt, Pb, Ni, Co, and Fe. Platinum is a noble metal with interesting nanowire applications in sensorics and catalysis.

Recently, the synthesis of Pt nanowires at 65 °C from an alkaline platinum bath (Platinum-OH, Metakem) in a two electrode arrangement by using a Pt rod as anode was reported by Rauber et al. [55]. Contrary to copper and gold, the crystallinity of nanowires of metals with high melting temperatures, such as Pt and Rh, is difficult to control through the deposition parameters (i.e., to control nucleation and surface diffusion processes at the cathode). TEM and XRD investigations revealed a fine-grained polycrystalline structure for all potentiostatic conditions applied. Multisegmented polycrystalline Pt nanowires with preset and controlled number of segments/interfaces were synthesized by pulse-reverse electrodeposition. The cathodic pulse was applied at a potential $U_c = -1.3$ V for different pulse durations ranging from $t_c = 1$ s to $t_c = 20$ s. The anodic pulse was invariably timed to $t_a = 1$ s at $U_a = 0.4$ V. In this process, the length of the segments is controlled by the duration of the cathodic pulse [55].

As demonstrated by Yi and Schwarzacher, single- and polycrystalline Pb nanowires of 50 nm diameter grow reproducibly in etched ion-track membranes for various pulse parameters. An interesting finding is that the superconducting transition temperature T_c depends on the crystallinity of the nanowires [78].

Magnetic nanowires were successfully grown from nickel [57], cobalt [79], and iron [80]. The growth of Fe-based nanowires with controllable size, aspect ratio, and magnetic anisotropy in $FeCl_3$ and $FeCl_2$ solutions was investigated by Song et al. They employed $FeCl_3$ and $FeCl_2$ solutions, studied the nanowire growth mechanism and provided real-time compositional and crystallographic information [80].

2.4 Bismuth and bismuth-compound nanowires

Due to its unique electronic properties, bismuth is a very interesting material to study the effect of finite- and quantum-size effects of nanostructures [9,81,82]. Characteristic length scales, such as the electron mean free path and Fermi wavelength are relatively large at room temperature, namely 100 and 40 nm, respectively [83,84]. Bulk Bi is a semimetal with a very small indirect band overlap, and its charge carrier density is low compared to conventional metals. Moreover, the electron effective mass is small (0.001–0.26) and depends on the crystalline orientation. Given these characteristics, size effects on Bi structures are expected at relatively large dimensions (≈100 nm). Also compound nanostructures of $Bi_{1-x}Sb_x$ and Bi_2Te_3 are being intensively investigated due to theoretical studies predicting a large enhancement of the thermoelectric efficiency, given by the so-called figure of merit ZT, $ZT = S^2 \cdot \sigma \cdot T/\kappa$, where S is the Seebeck coefficient, σ is the electrical conductivity, κ is the thermal conductivity and T is the temperature. The power factor ($S^2\sigma$) of these thermoelectric nanomaterials should increase due to quantum size effects and the thermal conductivity should decrease due to enhanced phonon surface scattering [85-88]. The thermoelectric properties of these Bi-compound materials are anisotropic and are extremely sensitive not only to composition and size, but also to the crystallographic orientation of the wires. During synthesis, it is thus important to control these three parameters simultaneously. To achieve a significant enlargement of the thermoelectric efficiency, the diameter of such nanowires should be below 30 nm.

Cornelius et al. fabricated pure Bi nanowires using an electrolyte consisting of 0.2 M $BiCl_3$, 0.3 M tartaric acid, 0.2 M NaCl, 1.3 M HCl, and 100 g/L glycerol, in most cases potentiostatically, but also using reverse-pulse deposition in a two-electrode arrangement [56]. The thin Au layer acted as cathode and a Bi rod as anode. XRD and TEM revealed that the nanowires deposited potentiostatically are <110> textured. At higher temperatures and smaller overpotentials, the texture increases. At $T = 60$ °C and low overpotentials (e.g., $U_c = -17$ mV), single-crystalline wires are produced (Figure 9a). In contrast, wires deposited with reverse pulses exhibit a <100> texture and are polycrystalline with grain sizes of ca. 0.5 µm (Figure 9b). Bi nanowires with other preferred orientations have been synthesized by other techniques, such as low-temperature solvothermal process and high-pressure injection in alumina [89,90].

Recently, Bi_2Te_3 nanowires with diameters from 150 nm down to 10 nm, and lengths of up to 60 µm, were potentiostatically grown by using a thermostated three-electrode setup with a thin sputtered Au layer acting as the cathode, a Pt counter electrode, and a SCE as the reference electrode [58]. The electrolyte consisted of an aqueous solution of bismuth nitrate pentahydrate, TeO_2, and nitric acid. As shown by means of XRD, TEM, SEM, and EDX (energy-dispersive X-ray analysis), the parameters involved in the electrodeposition process, T, U, and diameter, density, and length of the channels in the template, influence the morphology, crystallinity, and preferred crystallographic orientation of the wires in a complex manner. The Bi_2Te_3 nanowires have diameters and lengths interesting for both basic research on thermoelectric nanomaterials and development of thermoelectric devices. Figures 9c–e display SEM images of Bi_2Te_3 nanowires with average diameters (c) 14, (d) 19 and (e) 24 nm. The smallest Bi-compound wires synthesized so far had diameters as small as 9–10 nm (inset). To the

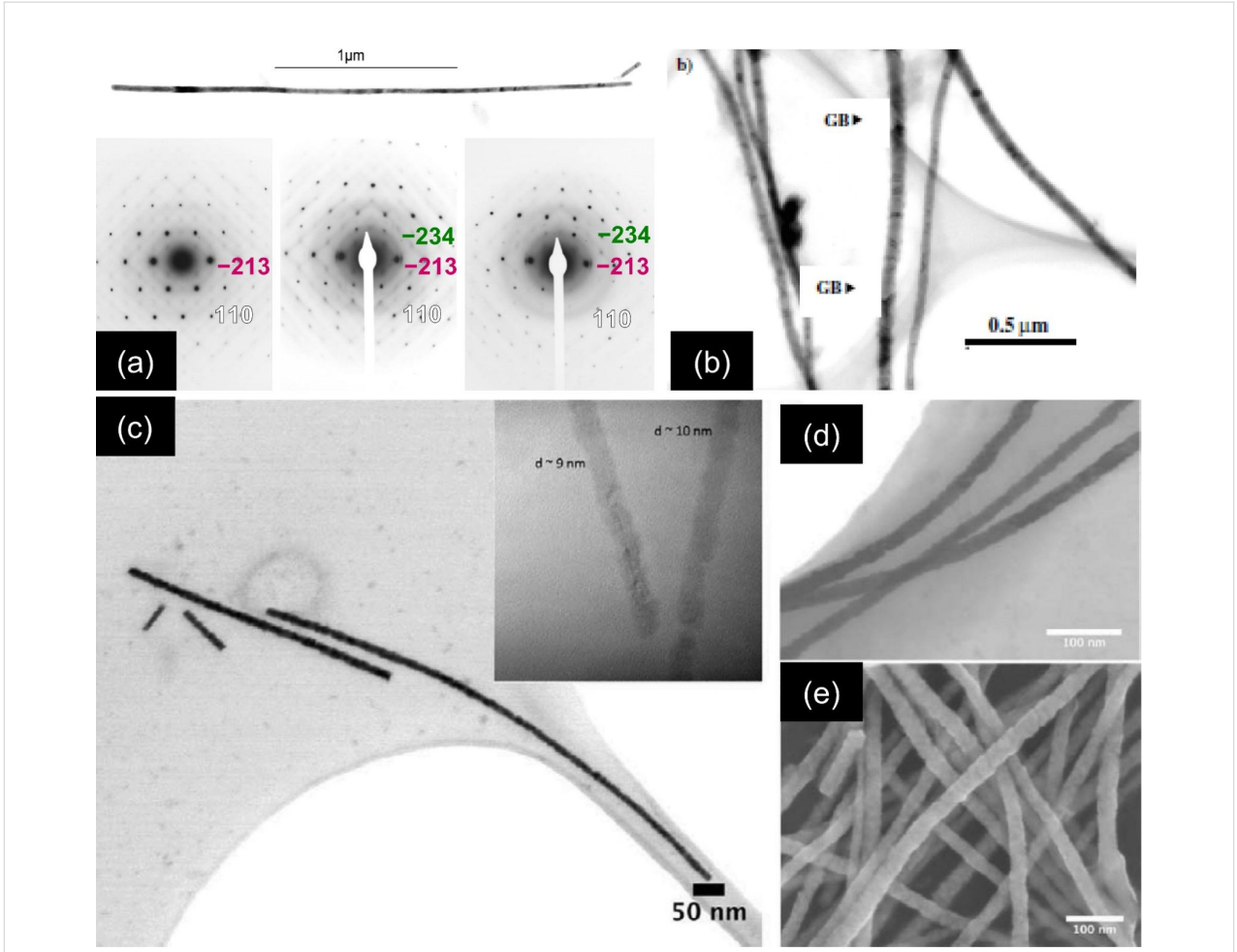

Figure 9: TEM images of Bi and Bi_2Te_3 nanowires: (a) individual single-crystalline Bi nanowire deposited under potentiostatic conditions together with SAED patterns from different wire positions and (b) several polycrystalline wires grown under pulsed conditions. Series of SEM images displaying Bi_2Te_3 nanowires with average diameters of (c) 14, (d) 19 and (e) 24 nm. The inset displays TEM images of sections with diameter 9–10 nm. (a,b) Adapted with permission from [56] – Copyright 2005 IOP Publishing Ltd and (c–e) adapted with permission from [58] – Copyright 2012 American Chemical Society.

best of our knowledge, with 14 nm average diameter, 10 µm length, and aspect ratios between 700 and 1000, these are presently the thinnest nanowires produced by electrodeposition in polymer membranes.

Polycrystalline $Bi_{1-x}Sb_x$ nanowires were successfully electrodeposited from an aqueous solution of $BiCl_3$ and $SbCl_3$, with simultaneous control over the diameter (between 20 and 200 nm), and varying Sb concentration ($0.05 \leq x \leq 0.4$). Coarse- and fine-tuning of the Sb concentration was achieved by selecting proper electrolyte composition and potential [60]. Figure 10 displays HRTEM images of 20−30 nm diameter nanowires deposited at $U = -200$ mV versus SCE and for different Sb concentrations in the electrolyte (c(Sb) = 0.01 (a), 0.02 (b), 0.03 (c), and 0.04 mol/L (d)), together with their respective EDX spectra (e). On average, the concentration of Sb in the wires was found to be $x = 0.07$, 0.18, 0.26, and 0.41, respectively. With increasing Sb concentration, the d-spacings belonging to the {012} lattice planes decrease, as evident by white lines in the HRTEM images (Figures 10a–d). XRD investigations on the preferred crystallographic orientation of Bi_2Te_3 and $Bi_{1-x}Sb_x$ nanowires grown in templates are described in references [58,60].

All experimental results reported so far clearly demonstrate that electrodeposition of thermoelectric nanowires in etched ion-track membranes enable the control of various wire parameters. It is particularly important to control the alloy composition and to obtain wire diameters as small as possible, because large enhancements in TE performance are expected when quantum size effects and enhanced phonon scattering come into play.

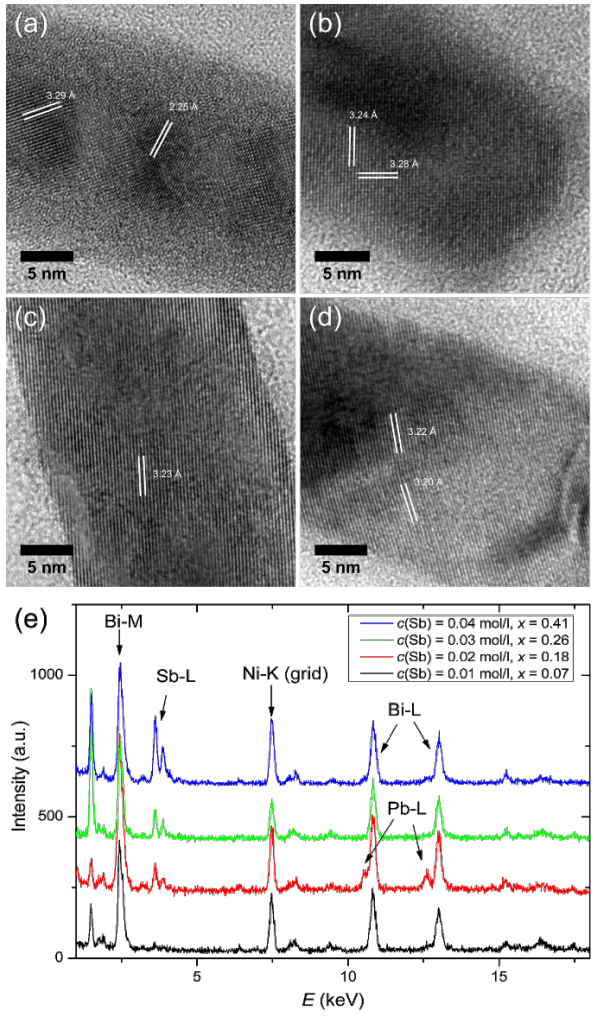

Figure 10: TEM images of $Bi_{1-x}Sb_x$ nanowires deposited at U = −200 mV versus SCE from electrolytes with Sb concentrations (c(Sb)) of (a) 0.01, (b) 0.02, (c) 0.03 and (d) 0.04 mol/L. (e) Corresponding EDX spectra, indicating the following Sb concentration in the wires x: 0.07, 0.18, 0.26 and 0.41. Adapted with permission from [60] – Copyright 2011 American Chemical Society.

2.5 Semiconductor nanowires

Semiconductor nanowires are excellent candidates to be functional elements in applications as diverse as optics, sensorics, and electronics, and energy applications such as thermoelectrics and hydrogen generation by water splitting [2-4,91]. In the past two decades, enormous progress has been achieved in the synthesizing and characterizing of semiconductor nanowires of controlled size and composition. Synthesis techniques include mostly vapour–liquid–solid growth, solution-phase, lithography, and electroless etching [2,10], while the template method in combination with electrodeposition of semiconductor nanowires (such as ZnO, Si, or ZnTe) has been rather limited.

Cylindrical ZnO nanowires have been electrochemically grown from aqueous solutions in the pores of both alumina and etched ion-track membranes with a rather limited range of diameters. Lai et al. reported the synthesis of ZnO nanowires using a $ZnSO_4$-based electrolyte at 22 °C, and a $Zn(NO_3)_2$-based solution at 70 °C [92]. Enculescu and co-authors reported the fabrication and optical characterization of ZnO wires with diameters between 80 nm and 1.5 µm, deposited in etched ion track membranes using a $Zn(NO_3)_2$-based electrolyte at 70 °C, with a Pt foil and a SCE electrode as counter and reference electrodes, respectively [93]. By appropriately tuning the composition of the electrolyte, they also synthesised doped ZnO nanowires. By using, for instance, an electrolyte containing $Zn(NO_3)$, $Co(NO_3)$, nitric acid, and polyvinylpyrrolidone (PVP) as an additive, 300 nm diameter $Zn_{1-x}Co_xO$ nanowires with x ranging from 0.01 to 0.05 were grown [94].

The synthesis and properties of semiconducting CdTe and CdS nanowires are being investigated for their potential in photodetector and photovoltaic applications. CdTe and CdS rods are mostly synthesized by chemical vapour deposition, and sol–gel processes. Electrodeposition of stoichiometric CdTe nanowires with diameters between 80 nm and 1 µm was reported by Enculescu et al. [95]. In addition to SEM, TEM, EDX, and XRD characterization, they also determined the band gap of nanowire arrays by reflection spectroscopy measurements [96]. Kum et al. reported the synthesis of ≈50 nm diameter CdTe wires and studied the influence of electrolyte, temperature, potential, and pH value on the composition and crystallinity of the nanowires [97]. They also demonstrated that as-deposited CdTe nanowires consist of nanocrystals with grain sizes up to 60 nm. Thermal annealing increases the wire resistivity and influences the grain size. The preparation of CdTe nanowire diodes with semiconductor homojunctions by using a single electrodeposition bath consisting of cadmium sulfate (0.02 M) and tellurium dioxide (1 mM) as sources of cadmium and tellurium ions, respectively, was described by Matei et al. [98]. The tellurium dioxide was dissolved in 50% concentrated sulfuric acid and the overall pH was adjusted to 2 with sodium hydroxide. Polyvinylpyrrolidone (1 g/L) was added as a wetting agent. A Pt foil and a SCE acted as counter and reference electrode, respectively. The potentiostatic electrodeposition of CdS nanowires by using an electrolyte solution containing $CdCl_2$ and thioacetamide, at 70 °C was reported by Mo et al. [99].

Finally, due to its availability, inertness, and compatibility with silicon-based technical processing, Si nanowires have a broad range of applications from sensorics, to biotechnology, photonics, IR-sensorics, and many others. Si wires have been prepared by a large variety of deposition techniques, including chemical vapour deposition, laser ablation, or thermal evapor-

ation. The first template-grown nanowires of amorphous Si were recently reported by using ionic liquids [100,101]. Ionic liquids have proved to be a good alternative electrolyte to fabricate materials such as Al, Ti, Si, or Ge, which cannot be electrodeposited in aqueous solvents [102]. Given the extreme versatility of etched ion-track membranes, future electrochemical growth of Si nanowires would allow tuning size parameters and provide interesting freestanding high-aspect ratio Si nano- or microstructures [103].

2.6 Segmented nanowires

Besides synthesizing single metal and semiconductor nanowires, electrodeposition also offers the possibility to grow segmented multimaterial nanowires. Combining various materials of interest can provide specific functionalities that are not present in the individual segments. Variations in composition along the length of the wire can, e.g., be used to incorporate electrical functionality, optical contrast, and/or desired surface chemistry [104]. Segmented Au/Pt nanowires were demonstrated to move autonomously when placed in a hydrogen peroxide solution [105]. Also, biofunctionalized nanowire bar codes were used for ss-DNA detection [106]. In addition, it is also of interest to grow metal segments on both sides of a semiconductor nanowire in order to provide electrical contacts.

To synthesize two-component multisegment nanowires, a single electrolyte bath containing the two ions of interest is employed. At less negative potentials, only the more noble metal is deposited, while at more negative potential, both metals are deposited. By keeping the concentration of the more noble metal in the electrolyte much lower than the concentration of the less noble metal, the less noble metal is mainly deposited containing a small fraction of the nobler one [64]. Alternatively, a two-bath sequential deposition can be employed. Multilayer nanowires were electrodeposited in etched ion-track membranes in the nineties to study the perpendicular-to-plane giant magnetoresistance (GMR) [64]. Multilayered nanowires reported so far include the following material combinations: Co/Cu, NiFe/Cu, CoNi/Cu, Ni/Cu, Ni/Au, AgPt, Co/Pt, and Fe/Cu [107-109]. In addition metal–semiconductor–metal junctions, such as Ni–ZnO–Ni and CdTe–Ni, were electrodeposited [110].

2.7 Cap morphology as an indication of wire crystallinity

When the grown nanowires reach the top side of the porous membrane, the deposition continues outside the pores forming so-called caps (Figure 6a, zone 3). The shape and morphology of the caps are a direct indication of the crystalline structure of the wires as shown for various materials (e.g., Cu, Au, Bi, Sb). Round caps are typically formed on top of polycrystalline wires (Figure 11a), while facetted caps grow on top of single-crystalline wires, or on wires consisting of large grains (Figure 11b–d). The facetted Au caps (Figure 11b) exhibit a cubic shape, revealing the cubic structure of the corresponding Au wires. In the case of Cu (Figure 11c), the caps often exhibit a five-fold symmetry. Such morphology is ascribed to multiple twinned crystals consisting of five deformed tetrahedral subunits. The morphology of the facetted Bi caps (Figure 11d) also reveals twinning.

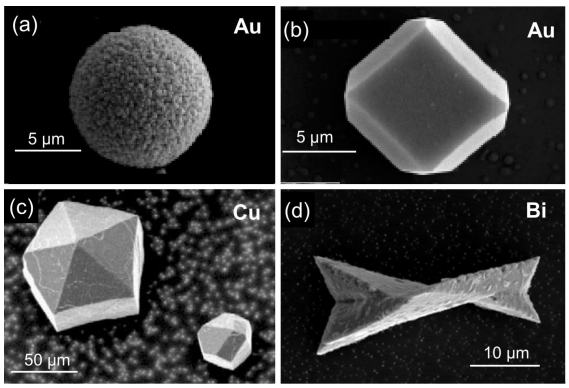

Figure 11: SEM images revealing the characteristic morphology of various metallic caps: (a) polycrystalline Au, (b) single-crystalline Au, (c) twinned Cu and (d) twinned Bi. (a,b) Adapted with permission from [54] – Copyright Springer Verlag 2006; (c) adapted with permission from [71] – Copyright 2005 Elsevier Science Ltd.; (d) adapted with permission from [56] – Copyright 2005 IOP Publishing Ltd.

3 Nanowire morphology

The morphology of nanowires, including their geometry, size, and surface contour, is primarily determined by the shape of the hosting channels. The production of templates with swift heavy-ion beams in combination with track etching enables us to control several template parameters such as well-defined channel shape and channel geometry, with the diameter adjustable between a few nanometres up to micrometres, membrane thickness up to 100 µm, and aspect ratios up to 1000. In addition, by varying the fabrication steps in a controlled manner, novel structures can be synthesized, such as pores with conical geometry or channels with smooth or rough inner walls. By exposing the samples to the ion beam under various tilting angles, nanochannel networks with controlled density and interconnection degree are possible. Figure 12 displays a selection of wire morphologies and wire arrangements recently obtained by ion-track technology at GSI: (a,b) rough nanowires; (c) conical nanowires [111]; and (d) nanowire networks.

3.1 Surface roughness

Smooth cylindrical nanowires are suitable for many applications, including sensing of electrical or optical signals. However, in some cases an increased surface roughness is of interest. Hochbaum et al. and Boukai et al. recently reported

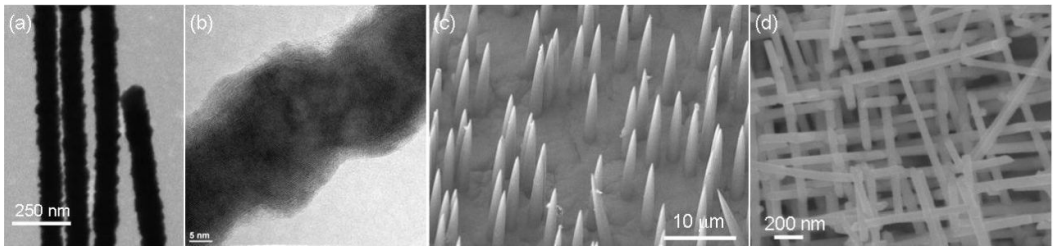

Figure 12: (a) SEM and (b) TEM images displaying the rough contour of Sb nanowires electrodeposited in PET membranes. (c) Array of free-standing conical Cu nanowires. (d) Network of interconnected Sb nanowires. Adapted with permission from [60] – Copyright 2011 American Chemical Society.

that rough Si nanowires exhibit a thermal conductivity up to 100 times smaller than their smooth counterparts, becoming promising objects to be implemented in thermoelectric devices [87,88]. In addition, a larger roughness effectively increases the available surface, and thus can be an important advantage, e.g., for catalytic and photovoltaic applications. We have been able to tune the surface roughness of the electrodeposited nanowires by selecting suitable polymer membranes: etched tracks in PC result in smooth channel walls, while channels in PET have a rough surface. Figures 12a and 12b display two exemplary nanowires with diameter 90 and 30 nm, respectively, deposited in PET channels. The variations in diameter along the wire axis amount to 30% in the case of 30 nm diameter wires [60].

3.2 Conical shape

Arrays of nanostructures of cylindrical and conical geometry are promising electrodes for field emission, photovoltaic applications, water splitting, or surface-enhanced Raman spectroscopy [112,113]. The individual cones potentially combine the advantages offered by the reduced dimensions of the tip with the enhanced mechanical stability provided by the large base [114]. An array of freestanding conical Cu wires with a large base of 1–3 µm and a small tip of a few tens of nanometres is shown in Figure 12c. As mentioned above, the apex angle of the cones is determined by the geometry of the hosting conical channel (cf. section 2). Different electrodeposition conditions were studied in order to obtain mechanically stable nanocones with good electrical contact to the substrate. Electrodeposition by using a $CuSO_4$-based electrolyte in a two electrode configuration, with $U = -40$ mV leads to a slow growth rate, resulting in a large uniform array of mechanically stable Cu cones of about 28 µm length, 1.2 µm base radius, and 190 nm tip radius [115]. The field-emission properties of similar Cu-nanocone cathodes were investigated by using a field emission scanning microscope (FESM) under ultrahigh vacuum conditions [116]. The improved mechanical stability and solid contact interface of the copper nanocones resulted in much higher emission current values as compared to all previously tested metallic cylindrical nanowires [115,117].

3.3 Nanowire networks

Implementation of nanowire cathodes in fields such as energy harvesting, sensing, or catalysis requires a successful assembly of the nanostructures into 2-D and 3-D architectures [118,119]. Fabrication of 3-D nanowire superstructures by vapour–liquid–solid processes has been reported; however, revealing a limited tunability of the relevant parameters. Recently, Rauber et al. demonstrated the fabrication of highly ordered Pt nanowire networks, consisting of well-defined interconnected nanowires with controlled morphology [120]. Ion irradiation of polymer foils at several incident angles in consecutive steps, followed by chemical etching results in novel etched ion-track membranes with nanochannel arrays tilted at various angles. Electrodeposition in the nanochannel network results in highly ordered 3-D nanowire ensembles. An example of a complex Sb nanowire network is presented in Figure 12d.

3.4 Nanogap structures

Novel nanowire dimer and nanogap structures are interesting for applications in plasmonic sensing as well as nanoelectronics [121,122]. However, the reliable fabrication of such structures remains a challenge. Techniques such as break-junction techniques and gap narrowing by electroplating have been employed, but their precision and reproducibility is limited [123,124]. The template technique offers a promising approach by sequential deposition of multi-material-segmented nanowires grown in porous templates followed by selective etching of one of the deposited elements. This variation of the template method is also known as “on-wire lithography” [125]. Recent experiments yielded segmented Au-rich/Ag-rich/Au-rich nanowires, synthesized by sequential potentiostatic deposition using an electrolyte containing both $[Ag(CN)_2]^-$ and $[Au(CN)_2]^-$ ions [126]. The duration of the sequential pulses controls the length of the silver-rich and gold-rich segments. After dissolution of the polymer membrane, the wires are dispersed in isopropanol. The solution containing the segmented wires is drop-cast onto a substrate. In a subsequent step, the substrate is dipped into concentrated nitric acid to dissolve the silver segments of the wires selectively. The generation of gaps with sizes between

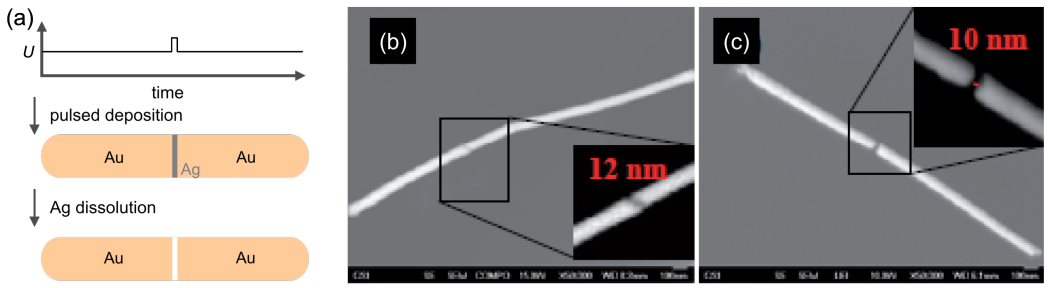

Figure 13: (a) Schema of the electrodeposition and gap-forming process. SEM images of (b) Au-rich/Ag-rich/Au-rich nanowire, and (c) Au nanowire dimer exhibiting a 10 nm gap after selective Ag dissolution. The corresponding insets show details of the Ag segment and the gap, respectively.

7 and 30 nm is demonstrated [127]. Figure 13 displays schematically the fabrication process (Figure 13a) and shows SEM images of Au nanowire dimers before (Figure 13b) and after (Figure 13c) silver dissolution.

4 Size-dependent properties

Nanowires synthesized by electrodeposition in etched ion-track membranes of a large variety of metal, semiconductor and semimetals, whose morphological and crystallographic characteristics can be adjusted in a controlled way as presented above, constitute ideal objects for the investigation of both finite- and quantum-size effects. Due to its technological relevance, size effects on the optical, electrical, and thermal properties are of special interest. The following section presents recent results by the GSI group on electrical, optical, and thermal size effects of electrodeposited nanowires.

4.1 Finite-size effects in electrical properties

Systematic investigations of the electrical transport properties of metal and semiconductor nanowires are necessary in order to better understand classical size effects such as electron scattering at surfaces and grain boundaries. These effects lead to an increase of the specific resistivity of the wire under study compared to its bulk counterpart, which is relevant to nanowire applications such as field-effect transistor sensors, and interconnectors. The influence of grain boundary scattering on the resistivity was predicted decades ago by Mayadas and Shatzkes, and depends on parameters such as electron mean free path, average grain size, and a reflection coefficient at the grain boundaries [128]. The effect of surface scattering was predicted by Dingle et al., and is influenced by nanowire diameter and the specularity of scattering processes at the wire surface [129].

Absolute measurements of the specific resistivity of nanowires require contacting individual nanowires in a reliable manner. The production of low-resistance contacts between nanostructures and macroscopic electronics is a difficult and challenging task. In the case of nanowires, several techniques have been already reported using, for example, the metal-coated tip of a scanning force microscope, optical and electron beam lithography, or manipulators [130-132]. In the case of electrodeposited nanowires, most groups reported the production of large arrays of wires and the subsequent selection of individual wires being contacted with lithographic techniques. Electrical resistivity of individual lithographically contacted Cu nanowires monitored over many hours revealed the critical problem of oxidation. During the measurement, the wire resistance increased from a few hundred ohms to several megaohms. Due to oxidation, the nanowire characteristics change from the metallic to the semiconducting regime [130].

Another possibility for contacting single nanowires is based on single-ion irradiation of polymer foils [51]. The single-wire fabrication and contacting process is schematically presented in Figure 14. The steps include (a) the fabrication of a single-pore membrane by ion irradiation and etching; (b) deposition of a suitable substrate; (c) electrochemical growth of a single nanowire (e.g., Cu, Au, Bi) and continuation of the deposition process until a micrometre-sized cap grows on top of the wire; and (d) contacting of the embedded nanostructure by sputtering

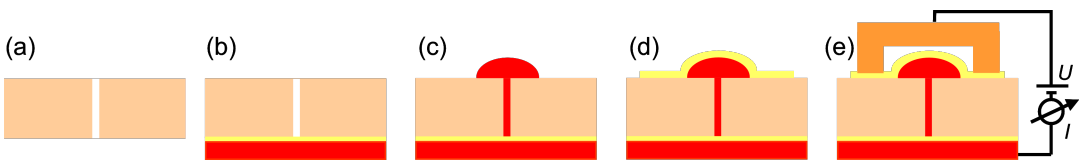

Figure 14: (a–e) Schematic of the fabrication and contacting process for a single nanowire.

a conductive layer on the membrane surface. The process avoids the delicate handling of the nanowires and thus minimizes the risk of mechanical damage. Systematic resistivity measurements were performed with single Bi and Au nanowires of various diameters ranging between 40 nm and 1 µm [133-135].

Figure 15 and Figure 16 display the specific electrical resistivity of individual nanowires as a function of the nanowire diameter for Bi and Au, respectively. In the case of Bi, the electrochemical growth was performed by using three different sets of deposition voltage and temperature. Each of these three wire groups had, thus, a common mean grain size. Figure 15 displays the electrical resistivity of individual Bi nanowires with diameters ranging between 150 nm and 1 µm, which were fabricated by electrochemical deposition in single-pore PC membranes [133].

By using three different sets of deposition voltage and temperature, three groups of single Bi wires could be deposited, each group being characterized by a common mean grain size. The results demonstrate that the resistivity of nanowires with diameters well above 100 nm can be up to eight times higher than for the bulk. For a given diameter, the wire resistivity becomes larger with diminishing grain size due to electron scattering at grain boundaries, providing evidence that the resistivity of nanostructures can be tailored by a suitable choice of the crystalline properties. In the case of Au, all wires show a higher specific resistivity than bulk gold (Figure 16). For diameters larger than 100 nm, the resistivity is nearly constant, with an average value 1.8 times larger than the bulk value,

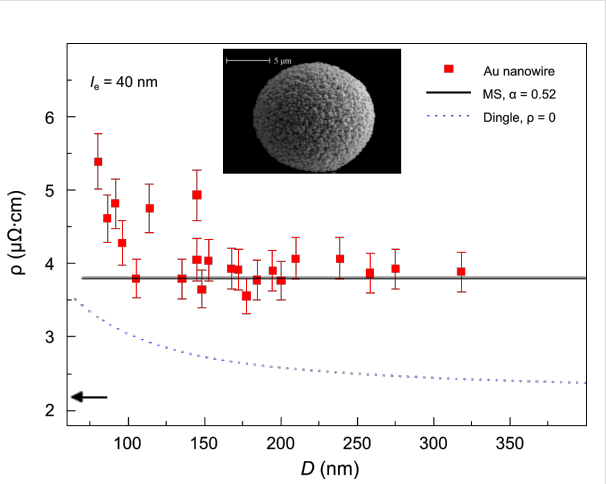

Figure 16: Specific electrical resistivity versus wire diameter for single polycrystalline gold nanowires (ammonium gold(I) sulfite electrolyte, T = 50 °C, U = −0.8 V) together with the cap morphology. The symbols represent the data. The continuous and dashed lines are a fit of the resistivity predicted by the Mayadas and Shatzkes and the Dingle models, respectively. Adapted with permission from [135] – Copyright 2008 Elsevier B.V.

attributed as well to grain-boundary scattering. For d < 100 nm the resistivity increases with decreasing diameter, due to additional scattering at the wire surface [135].

Resistance-versus-temperature curves revealed linear characteristics down to 70 K in the case of Au and a nonmonotonic behaviour in the case of Bi [133,135]. The special configuration of a single nanowire embedded and contacted in single

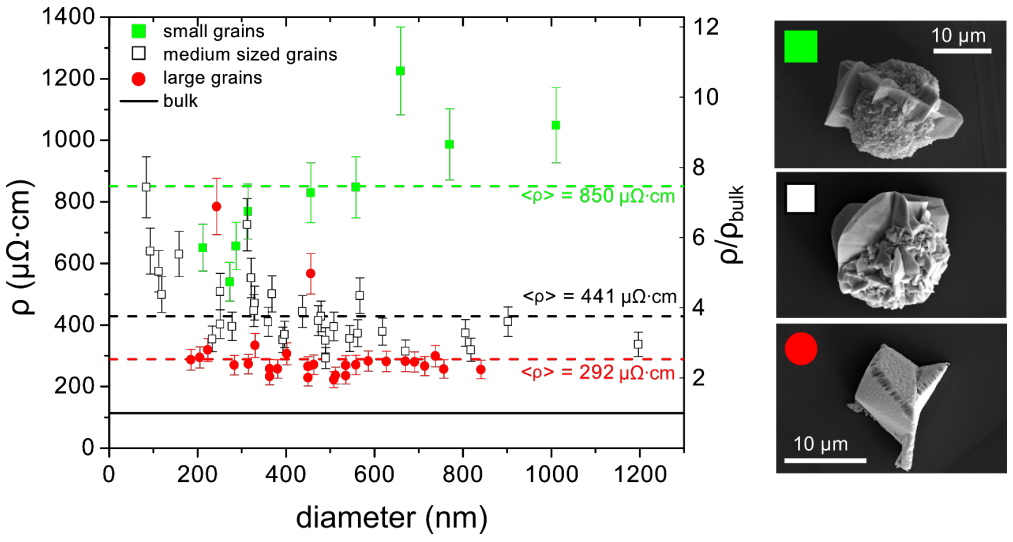

Figure 15: Specific electrical resistivity as a function of diameter of single bismuth nanowires fabricated under three different deposition conditions (T and U): 30 °C and −50 mV (green squares); 50 °C and −25 mV (open black squares); 60 °C and −17 mV (red circles). The solid line represents the classical behaviour, while the dotted lines are the average resistivity values for the indicated deposition conditions. SEM images illustrate the corresponding cap morphology. Adapted with permission from [133] – Copyright 2006 American Institute of Physics.

nanopore membranes also allows the determination of the maximum current density before failure. Embedded Bi nanowires were found to withstand three to four orders of magnitude higher current densities than bulk Bi. The fact that thinner Bi nanowires can carry higher current densities is attributed to more efficient heat dissipation to the surrounding polymer matrix [136]. For Bi nanowires with a diameter comparable to the Fermi wavelength (i.e., $d \approx 100$ nm) theoretical calculations predicted that the charge-carrier confinement leads to splitting of the energy bands into sub-bands, and a shift of conduction and valence bands with respect to each other. Such a quantum-size effect was experimentally observed by infrared spectroscopy, revealing a shift of the absorption edge to higher energies with decreasing wire diameter [137].

4.2 Surface plasmon resonances in Au nanoantennas

Collective charge-density oscillations due to surface plasmons exhibited by metal nanoparticles, and in particular by Au nanowires and nanowire dimers (two nanowires separated by a small gap), are being investigated with great interest due to the strongly enhanced electromagnetic fields formed at the nanowire tips and at the gap [123,138]. These surface plasmon resonances (SPRs) are characteristic of each particle and depend on material, dielectric constant of the surrounding medium, and geometry [65,66]. By controlling the length of the nanowire, antenna nanostructures exhibiting SPR at a given frequency of interest can be synthesized. Suitable Au and Cu nanoantennas with specific micrometre length and about 100 nm diameter were fabricated by electrodeposition in PC etched ion-track templates. After dissolution of the polymer membrane, the nanowires were transferred onto infrared (IR)-transparent substrates. Single nanowires were studied at the synchrotron light source ANKA (Forschungszentrum Karlsruhe), with respect to their antenna-like plasmon resonances [138]. The results showed that the resonances depend not only on length and diameter of the wire but also on the substrate and surroundings. Neubrech et al. demonstrated that the IR vibration signals of one attomol of molecules can be detected with enormous sensitivity when the broadband resonance of the nanoantenna matches the IR active vibration dipoles of the molecules [139]. The application of such single nanoantennas and dimers in fields such as surface-enhanced IR absorption or surface-enhanced Raman scattering requires not only an excellent control over the nanostructure synthesis, but also a fundamental understanding of the near-field characteristics of the antennas.

Near-field investigations were provided by scanning transmission electron microscopy combined with high-resolution electron-energy-loss spectroscopy (STEM–EELS) using a Zeiss SESAM TEM operated at 200 kV with a field-emission gun and equipped with a MANDOLINE energy filter. This technique allows us to study the transversely and longitudinally localized surface plasmon resonances in single nanowires and nanowire dimers excited by the rapidly travelling electron beam depending on the beam position. Figure 17a shows the high-resolution plasmonic field-intensity map obtained by acquisition from top to bottom (red arrow) of 50 electron-energy-loss spectra at equidistant positions along the long axis of a gold–silver alloy nanowire ($L = 907 \pm 5$ nm, $D = 107 \pm 5$ nm). The map reveals different plasmon modes, which we assign to the first five longitudinal LSP modes and a transversal mode, and which are schematically presented at the top of Figure 17a. Figure 17b shows a single spectrum of the mapping in Figure 17a, recorded at one side-end of the wire (red dot in TEM picture). Figure 17c displays the plasmonic mapping of a dimer of two nanowires separated by an ≈8 nm gap ($L_1 = 784 \pm 5$ nm, $D_1 = 112 \pm 5$ nm, $L_2 = 808 \pm 5$ nm, $D_2 = 112 \pm 5$ nm). In the case of nanowire dimers, the splitting of the longitudinal multipole modes into bonding and antibonding modes up to the third order (Figure 17c,d) was investigated. Interestingly, the transversal resonance is not excited when positioning the electron beam at the gap and decays rapidly with increasing distance from the wire surface. Figure 17d displays spectra recorded at the dimer ends (blue and green), and at the dimer gap (red). The positions are marked in the TEM image, with dots of the corresponding colours.

4.3 Thermal instability

A successful implementation of nanowire-based devices requires a knowledge of and ability to control the behaviour of the nanostructures at elevated operation temperatures. The thermal stability of nanomaterials is controlled by surface and diffusion processes and influenced by the material characteristics, temperature, and geometrical parameters [140-144]. In particular, it was predicted that nanowires may fragment into a chain of nanospheres above a temperature that is much lower than the corresponding bulk melting temperature T_m. Based on previous theoretical studies by Plateau and Lord Rayleigh on the instability of liquid cylinders and liquid jets [145,146], Mullins and Nichols performed calculations on the thermal instability of solid cylinders considering mass transport by surface and volume diffusion [147]. For a cylinder with initial radius r and a sinusoidal perturbation $R = r + \Delta r_0 \sin(2\pi x/\lambda)$, perturbations with wavelength $\lambda > 2\pi r$ are expected to increase spontaneously in amplitude and become more pronounced with time. The solid cylinder will finally break up into a row of spheres with an average spacing λ_m and diameter d. Both, λ_m and d should depend on various factors such as the type of diffusion dominating the transformation, the crystallographic characteristics of the structure, or the surroundings (e.g., the substrate).

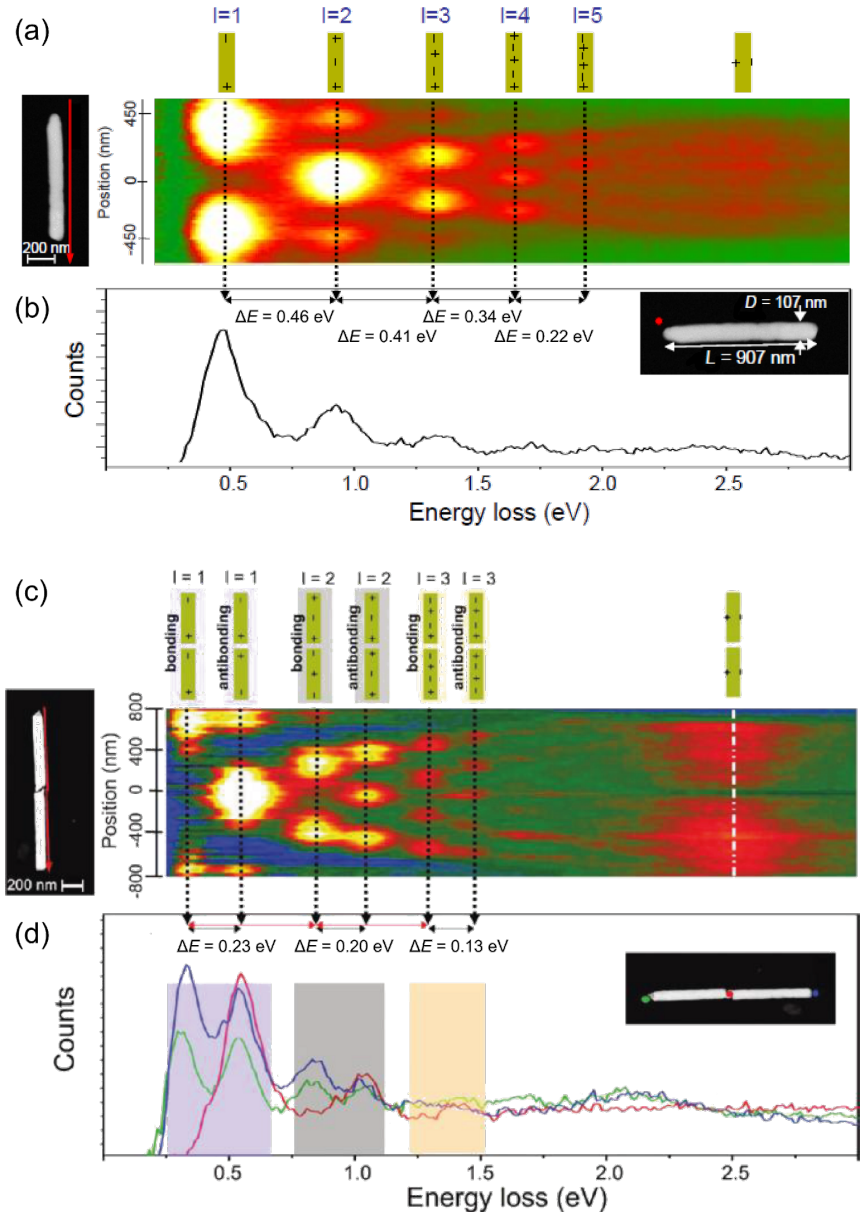

Figure 17: (a) TEM image of the single Au nanowire (length 907 nm, width 107 nm) and the corresponding high-resolution plasmonic field intensity map. The map consists of 50 electron-energy-loss spectra measured along the long axis of the nanowire (cf. direction of arrow next to wire, average distance of scan line to nanowire ≈15 nm). The energy interval, plotted from left to right, ranges from 0.2 to 3.0 eV. The colour indicates the number of counts (white highest). The dotted lines indicate the different multipole modes. (b) Electron energy-loss spectrum measured at one end of the single nanowire (the red dot in the TEM image marks the position of measurement). (c) Plasmonic field intensity map consisting of 60 electron energy-loss spectra measured along a nanowire dimer (red arrow) separated by an ≈8 nm gap. The scan lines have an average distance to the wire of ≈10 nm. The schematics at the top represent the electric-field distribution along the dimer. (d) Electron-energy-loss spectra measured at the two ends of the dimer (blue and green lines) and a spectrum measured in the dimer gap (red line). The coloured dots in the TEM image inset specify the measurement positions for each spectrum. Adapted with permission from [126] – Copyright 2011 American Chemical Society.

Systematic thermal annealing experiments studying the morphological transformation of electrodeposited Cu and Au nanowires confirmed that the Rayleigh instability concept is also applicable to metal nanowires [148,149]. In the case of Cu, the fragmentation of nanowires with diameters below 50 nm occurs at temperatures between 400 and 600 °C. HRSEM beautifully visualizes the different stages of the fragmentation process at different temperatures and for different wire diameters (Figure 18a–d).

After annealing at 400 °C, the wire displays diameter fluctuations along the wire axis (Figure 18a) developing into points of fragmentation (Figure 18b). At this temperature the length of the segments is several hundred nanometres. After annealing at

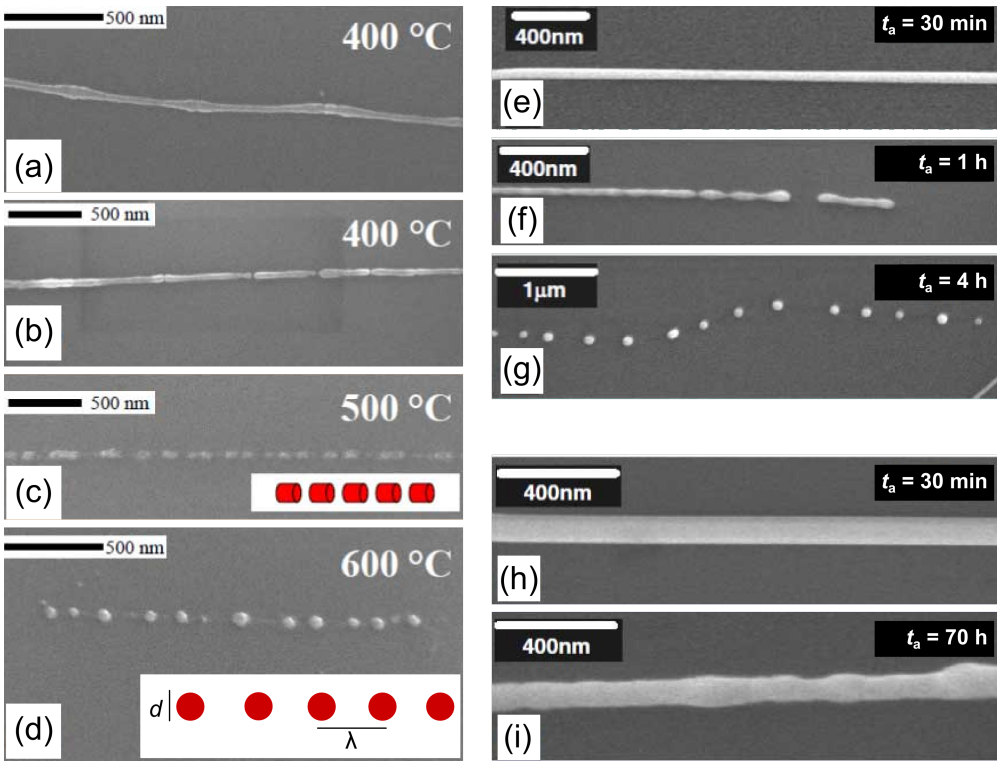

Figure 18: HRSEM micrographs of Cu nanowires of diameter 30 nm after 30 min annealing at different temperatures (a–d), and Au nanowires of two different diameters annealed for various times at 500 °C. The insets represent schematically the fragment geometry, including sphere size and spacing, as modelled by Nichols and Mullins. (e–g) 50 nm diameter Au nanowires after annealing for 30 min (e), 1 h (f), and 4 h (g) at 500 °C. (h–i) 100-nm diameter Au nanowires after 30 min (h) and 70 h (i) annealing. Due to the larger diameter, the wires are more stable and display only soft oscillations after extended annealing. (a–d) Adapted with permission from [148] – Copyright 2004 American Chemical Society; (e–i) adapted with permission from [149] – Copyright 2006 IOP Publishing Ltd.

500 °C, the wires decay into shorter sections of length about 100 nm (Figure 18c). Finally at 600 °C, copper nanowires decay into a linear row of spheres (Figure 18d). In the case of Au, nanowires with a diameter of 25 nm develop radial fluctuations already at 300 °C and decay completely into chains of spheres at 500 °C [149]. Figure 18e–g show evidence for the influence of annealing time on the morphological evolution of ≈50 nm diameter nanowires during annealing at 500 °C. For a given temperature, wider nanowires require significantly larger annealing times to induce Rayleigh instability (Figure 18h–i).

The thermal stability is also influenced by the nanowire structure. Single-crystalline Au nanowires oriented along the <110> direction were found to be more stable and required longer annealing times to complete their geometrical transformation into spheres than their polycrystalline counterparts [150]. For both metals, Au and Cu, the final formation of a chain of nanospheres occurs at a temperature much below the melting point (T_m(Cu) = 1083 °C, T_m(Au) = 1064 °C). Recently Zhou et al. reported the fragmentation of Ni nanowires by the Rayleigh criterion at temperatures of about 900 °C (T_m(Ni) = 1453 °C) [151]. This seems to indicate a direct relationship between the bulk melting temperature of the constituent materials and the maximal temperature at which thermal stability is exhibited. These results reveal that prior to nanoscale device applications, technological problems arising from the thermal instability of nanostructures must be seriously taken into account. The positive aspect of the Rayleigh instability is its potential application for converting nanowires into long chains of nanospheres, and the possibility of controlling surface diffusion processes at the nanoscale by applying elevated temperatures.

An interesting nanoscale diffusion phenomenon was recently observed for micrometre-long electrodeposited Cu nanowires, confined in a graphitic coating. In situ TEM observation showed that at 500 °C nanowires experience a geometrical transformation into single-crystalline nanoparticles of up to 10-fold increased diameter [152]. Real-time movies recorded in situ visualized the Cu draining out of the carbon coating (Figure 19).

Figure 19a shows a TEM image of two encapsulated Cu nanowires (d ≈ 30 nm) intersecting each other on a TEM grid. The wires are covered by a thin carbon layer. The snapshots of

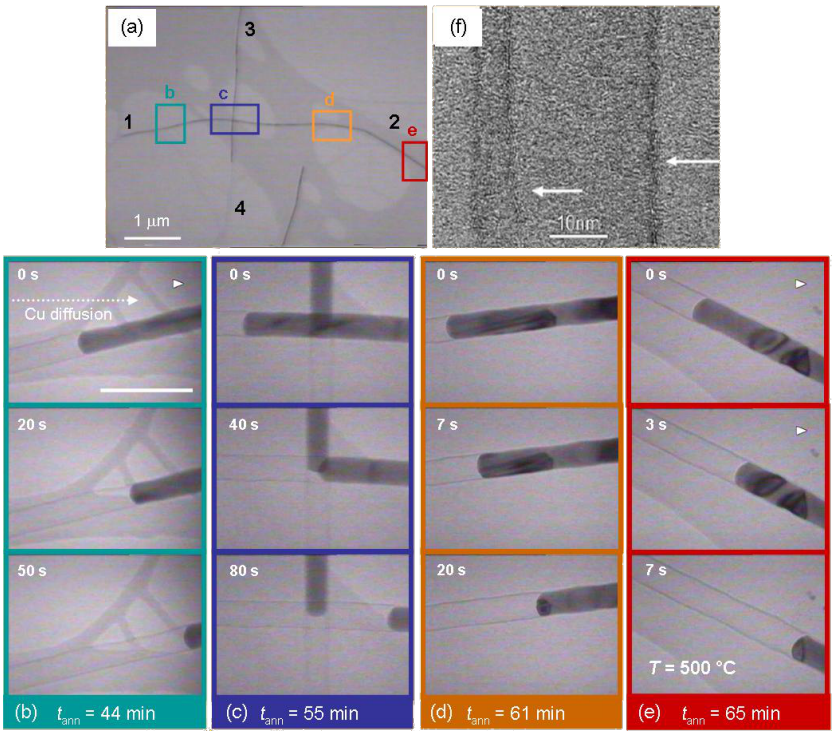

Figure 19: TEM images and video snapshots of Cu nanowire (covered by carbon coating) recorded on four areas marked in (a) at different annealing times: (b) 44, (c) 55, (d) 61, and (e) 65 min. In each case, the time series (from top to bottom) show how the Cu filling moves from left to right, while the carbon shell (f) remains unchanged. The 100 nm scale bar in (a) applies for all snapshots. Adapted with permission from [152] – Copyright 2012 Wiley.

the video recorded on the four areas marked in Figure 19a display the effective evacuation of the solid Cu content out of the carbon tube over micrometre distances towards the open end (labelled as 2). The consecutive images of the video (from top to bottom, Figure 19b–e) were recorded at different annealing times (t_{ann} = 44, 55, 61, and 65 min). Although the temperature is constant (500 °C), the velocity of the Cu front increases with time and location during the annealing process. Details of this drainage process close to the open end of a carbon tube are shown in Figure 20a–c. Figure 20a–c shows TEM images of the Cu nanowire in Figure 19a, close to the end 2, taken at different times during the annealing process. This series of images visualizes the formation and growth of a nanoparticle during the annealing process. Once the process has been completed, each nanowire is transformed into a single monocrystalline, facetted Cu particle (Figure 20d–f).

Based on kinetic Monte Carlo simulations (Figure 20g–i) it is proposed that this dramatic morphological transformation is driven by surface diffusion of Cu atoms along the wire-tube interface, thus minimizing the total free energy of the system. The high-resolution micrograph displayed in Figure 19f displays the multishell graphitic coating presumably formed from polymer residues on the nanowire surface. It is note-

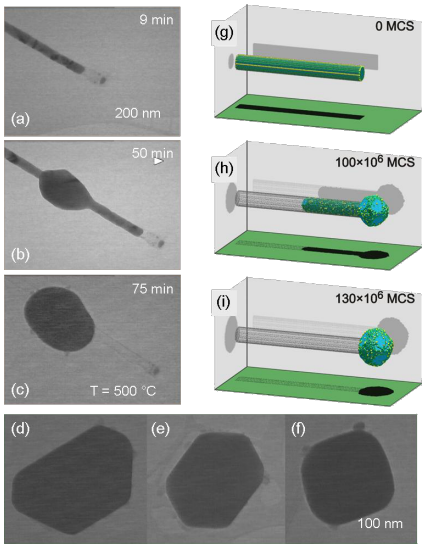

Figure 20: (a–c) TEM images of a Cu nanowire close to the end of a carbon tube (field 2 in Figure 19) visualizing the formation and growth of a nanoparticle during the annealing process. (d–f) Facetted Cu crystals observed at different wire ends after 80 min annealing. (g–h) Snapshots from kinetic Monte Carlo simulations showing the reaction pathway of the draining process. Time is indicated in the number of Monte-Carlo steps (MCS). Adapted with permission from [152] – Copyright 2012 Wiley.

worthy that this carbon layer is resistant throughout the whole process. The formation and characteristics of such fascinating carbon-coated core–shell structures should be investigated in more detail. The results also show that nanowires coated by electron-beam-induced carbon tubes can serve as well-defined nanopipettes. The extraction process is initiated and controlled by temperature. The template-based electrochemical wire synthesis allows control over the wire diameter as well as length and thus provides material for nanocrystals whose size is predefined by the pipette volume.

Conclusion

We have described the synthesis of micro- and nanowires using ion-track technology in combination with electrodeposition. We illustrate how this technique enables the independent and simultaneous control of size (diameter and length), morphology, crystalline structure, and composition of the nanowires. A combination of irradiation of polymer foils with high-energy heavy ions and chemical etching results in templates with micro- and nanochannels (length of several tens of micrometres and diameter from ca. 10 nm to several micrometres). By electrodeposition in the channels, nanowires of different materials, such as Au, Cu, Pt, Bi, Bi_2Te_3, ZnO, and CdTe, are synthesized. The crystallographic characteristics (surface roughness, grain size, and texture) are also well controlled by various electrodeposition parameters, namely voltage, temperature, and electrolyte. Finally, several examples of recent results by the GSI group on electrical, optical and thermal size effects of electrodeposited nanowires have been presented, demonstrating that these electrodeposited nanowires constitute ideal objects for the investigation of both finite- and quantum-size effects.

Acknowledgements

The author thankfully acknowledges financial support from the Helmholtz Association, the Deutsche Forschungsgemeinschaft (DFG) within the SPP 1165 (Nanodrähte und Nanoröhren: von kontrollierter Synthese zur Funktion), and the SPP 1386 (Nanostrukturierte Thermoelektrika: Theorie, Modellsysteme und kontrollierte Synthese). M.E.T.M. thanks all co-workers and collaborators, in particular I. Alber, M. Cassinelli, N. Chtanko, T. W. Cornelius, D. Dobrev, I. Enculescu, S. Karim, J. Krieg, S. Müller, R. Neumann, O. Picht, M. Rauber, C. Schötz, I. U. Schuchert, R. Spohr, C. Trautmann, J. Vetter, and M. F. Wagner for their contributions to the investigations of the synthesis and characterization of micro- and nanowires. Strong support by the members of the Materials Research Group of GSI during beam times for the template irradiation is thankfully acknowledged. M.E.T.M thanks C. Trautmann and R. Neumann for fruitful discussions and their continuous support during our research work, as well as for correcting this manuscript.

References

1. Lieber, C. M.; Wang, Z. L. *Mater. Res. Bull.* **2007,** *32,* 99–108. doi:10.1557/mrs2007.41
2. Hochbaum, A. I.; Yang, P. *Chem. Rev.* **2010,** *110,* 527–546. doi:10.1021/cr900075v
3. Gargas, D. J.; Toimil-Molares, M. E.; Yang, P. *J. Am. Chem. Soc.* **2009,** *131,* 2125–2127. doi:10.1021/ja8092339
4. Seletskiy, D.; Hasselbeck, M. P.; Cederberg, J. G.; Katzenmeyer, A.; Toimil-Molares, M. E.; Leonard, F.; Talin, A. A.; Sheik-Bahae, M. *Phys. Rev. B* **2011,** *84,* 115421. doi:10.1103/PhysRevB.84.115421
5. Chan, C. K.; Peng, H.; Liu, G.; McIlwrath, K.; Zhang, X. F.; Huggings, R. A.; Cui, Y. *Nat. Nanotechnol.* **2008,** *3,* 31–35. doi:10.1038/nnano.2007.411
6. Sun, J.; Liu, C.; Yang, P. *J. Am. Chem. Soc.* **2011,** *133,* 19306–19309. doi:10.1021/ja2083398
7. Holmberg, V. C.; Panthani, M. G.; Korgel, B. A. *Science* **2009,** *326,* 405–407. doi:10.1126/science.1178179
8. Krenn, J. R.; Schider, G.; Rechberger, W.; Lamprecht, B.; Leitner, A.; Aussenegg, F. R.; Weeber, J. C. *Appl. Phys. Lett.* **2000,** *77,* 3379–3381. doi:10.1063/1.1327615
9. Cornelius, T. W.; Toimil-Molares, M. E. Finite- and Quantum-size Effects of Bismuth Nanowires. In *Nanowires;* Prete, P., Ed.; Intech: Rijeka, Croatia, 2010; pp 274–296.
10. Xia, Y.; Yang, P.; Sun, Y.; Wu, Y.; Mayers, B.; Gates, B.; Yin, Y.; Kim, F.; Yan, H. *Adv. Mater.* **2003,** *15,* 353–389. doi:10.1002/adma.200390087
11. Cao, G. *Nanostructures and Nanomaterials: Synthesis, Properties, and Applications;* Imperial College Press: London, 2004.
12. Hulteen, J. C.; Martin, C. R. *J. Mater. Chem.* **1997,** *7,* 1075–1087. doi:10.1039/a700027h
13. Martin, C. R. *Science* **1994,** *266,* 1961–1966. doi:10.1126/science.266.5193.1961
14. Furneaux, R. C.; Rigby, W. R.; Davidson, A. P. *Nature* **1989,** *337,* 147–149. doi:10.1038/337147a0
15. Thurn-Albrecht, T.; Schotter, J.; Kästle, G. A.; Emley, N.; Shibauchi, T.; Krusin-Elbaum, L.; Guarini, K.; Black, C. T.; Tuominen, M. T.; Russell, T. P. *Science* **2000,** *290,* 2126–2129. doi:10.1126/science.290.5499.2126
16. Possin, G. E. *Rev. Sci. Instrum.* **1970,** *41,* 772. doi:10.1063/1.1684640
17. Williams, W. D.; Giordano, N. *Rev. Sci. Instrum.* **1984,** *55,* 410–412. doi:10.1063/1.1137752
18. Vetter, J.; Spohr, R. *Nucl. Instrum. Methods Phys. Res., Sect. B* **1993,** *79,* 691–694.
19. Chakarvarti, S. K.; Vetter, J. *Radiat. Meas.* **1998,** *29,* 149–159. doi:10.1016/S1350-4487(98)00009-2
20. Dobrev, D.; Vetter, J.; Neumann, R. *Nucl. Instrum. Methods Phys. Res., Sect. B* **1998,** *146,* 513–517. doi:10.1016/S0168-583X(98)00437-6
21. Dobrev, D.; Vetter, J.; Angert, N.; Neumann, R. *Electrochim. Acta* **2000,** *45,* 3117–3125. doi:10.1016/S0013-4686(00)00478-3
22. Dobrev, D.; Baur, D.; Neumann, R. *Appl. Phys. A* **2005,** *80,* 451–456. doi:10.1007/s00339-004-3078-z
23. Dobrev, D.; Vetter, J.; Angert, N.; Neumann, R. *Appl. Phys. A* **2001,** *72,* 729–733. doi:10.1007/s003390100872
24. Schönenberger, C.; van der Zande, B. M. I.; Fokkink, L. G. J.; Henny, M.; Schmid, C.; Krueger, M.; Bachtold, A.; Huber, R.; Birk, H.; Staufer, U. *J. Phys. Chem. B* **1997,** *101,* 5497–5505. doi:10.1021/jp963938g

25. Datta, M. *IBM J. Res. Dev.* **1998,** *42,* 563–566. doi:10.1147/rd.425.0563
26. Trautmann, C.; Brüchle, W.; Spohr, R.; Vetter, J.; Angert, N. *Nucl. Instrum. Methods Phys. Res., Sect. B* **1996,** *111,* 70–74. doi:10.1016/0168-583X(95)01264-8
27. Bath, W.; Dahl, L.; Groening, L.; Glatz, J.; Richter, S.; Yaramyshev, S. Development of the UNILAC towards a megawatt beam injector. In *Proceedings of the XXII Linac Conference, Lübeck, 2004,* Schaa, V. R. W., Ed.; DESY: Hamburg, 2004; pp 246–248.
28. Dehaye, F.; Balanzat, E.; Ferain, E.; Legras, R. *Nucl. Instrum. Methods Phys. Res., Sect. B* **2003,** *209,* 103–112. doi:10.1016/S0168-583X(02)02048-7
29. Spohr, R. Method for producing nuclear traces or microholes originating from nuclear traces of an individual ion. US000004369370A, Jan 1, 1983.
30. Spohr, R. *Ion Tracks and Microtechnology: Principles and Applications;* Vieweg und Teubner: Wiesbaden, Germany, 1990.
31. Siwy, Z.; Apel, P.; Baur, D.; Dobrev, D. D.; Korchev, Y. E.; Neumann, R.; Spohr, R.; Trautmann, C.; Voss, K.-O. *Surf. Sci.* **2003,** *532–533,* 1061–1066. doi:10.1016/S0039-6028(03)00448-5
32. Heins, E. A.; Siwy, Z. S.; Baker, L. A.; Martin, C. R. *Nano Lett.* **2005,** *5,* 1824–1829. doi:10.1021/nl050925i
33. Ali, M.; Yameen, B.; Neumann, R.; Ensinger, W.; Knoll, W.; Azzaroni, O. *J. Am. Chem. Soc.* **2008,** *130,* 16351–16357. doi:10.1021/ja8071258
34. Chtanko, N.; Toimil-Molares, M. E.; Cornelius, T. W.; Dobrev, D.; Neumann, R. *J. Phys. Chem. B* **2004,** *108,* 9950–9954. doi:10.1021/jp031368w
35. Toimil-Molares, M. E.; Chtanko, N.; Cornelius, T. W.; Dobrev, D.; Enculescu, I.; Blick, R. H.; Neumann, R. *Nanotechnology* **2004,** *15,* S201. doi:10.1088/0957-4484/15/4/015
36. Enculescu, I.; Toimil-Molares, M. E.; Zet, C.; Daub, M.; Westerberg, L.; Neumann, R.; Spohr, R. *Appl. Phys. A* **2007,** *86,* 43–48. doi:10.1007/s00339-006-3738-2
37. Fischer, B. E.; Metzger, S. *MRS Bull.* **2000,** *25* (2), 39–42.
38. Trautmann, C.; Bouffard, S.; Spohr, R. *Nucl. Instrum. Methods Phys. Res., Sect. B* **1996,** *116,* 429–433. doi:10.1016/0168-583X(96)00083-3
39. Fleischer, R. L.; Price, P. B.; Walker, R. M. *Nuclear tracks in solids;* University of California Press: Berkeley, 1975.
40. De Sorbo, W. *Nucl. Tracks* **1979,** *3,* 13–32. doi:10.1016/0191-278X(79)90026-X
41. Ferain, E.; Legras, R. *Nucl. Instrum. Methods Phys. Res., Sect. B* **1993,** *82,* 539–548. doi:10.1016/0168-583X(93)96008-Z
42. Apel, P. Y.; Blonskaya, I. V.; Dmitriev, S. N.; Orelovitch, O. R.; Presz, A.; Sartowska, B. A. *Nanotechnology* **2007,** *18,* 305302. doi:10.1088/0957-4484/18/30/305302
43. Zhang, H.-Q.; Akram, N.; Skog, P.; Soroka, I. L.; Trautmann, C.; Schuch, R. *Phys. Rev. Lett.* **2012,** *108,* 193202. doi:10.1103/PhysRevLett.108.193202
44. Healy, K.; Schiedt, B.; Morrison, A. P. *Nanomedicine* **2007,** *2,* 875–897. doi:10.2217/17435889.2.6.875
45. Cornelius, T. W.; Apel, P. Y.; Schiedt, B.; Trautmann, C.; Toimil-Molares, M. E.; Karim, S.; Neumann, R. *Nucl. Instrum. Methods Phys. Res., Sect. B* **2007,** *265,* 553–557. doi:10.1016/j.nimb.2007.10.004
46. Apel, P. Y.; Korchev, Y. E.; Siwy, Z.; Spohr, R.; Yoshida, M. *Nucl. Instrum. Methods Phys. Res., Sect. B* **2001,** *184,* 337–346. doi:10.1016/S0168-583X(01)00722-4
47. Karim, S. Fabrication and characterization of gold nanowires. Ph.D. Thesis, University of Marburg, Germany, 2007.
48. Siwy, Z.; Apel, P.; Dobrev, D.; Neumann, R.; Spohr, R.; Trautmann, C.; Voss, K. *Nucl. Instrum. Methods Phys. Res., Sect. B* **2003,** *208,* 143–148. doi:10.1016/S0168-583X(03)00884-X
49. Apel, P. Y.; Blonskaya, I. V.; Orelovitch, O. L.; Ramirez, P.; Sartowska, B. A. *Nanotechnology* **2011,** *22,* 175302–175314. doi:10.1088/0957-4484/22/17/175302
50. Chtanko, N.; Toimil-Molares, M. E.; Cornelius, T. W.; Dobrev, D.; Neumann, R. *Nucl. Instrum. Methods Phys. Res., Sect. B* **2005,** *236,* 103–108. doi:10.1016/j.nimb.2005.03.264
51. Cornelius, T. W. Fabrication and characterisation of bismuth nanowires. Ph.D. Thesis, University of Heidelberg, Germany, 2006.
52. Toimil-Molares, M. E.; Buschmann, V.; Dobrev, D.; Neumann, R.; Scholz, R.; Schuchert, I. U.; Vetter, J. *Adv. Mater.* **2001,** *13,* 62–65. doi:10.1002/1521-4095(200101)13:1<62::AID-ADMA62>3.0.CO;2-7
53. Liu, J.; Duan, J. L.; Toimil-Molares, M. E.; Karim, S.; Cornelius, T. W.; Dobrev, D.; Yao, H. J.; Sun, Y. M.; Hou, M. D.; Mo, D.; Wang, Z. G.; Neumann, R. *Nanotechnology* **2006,** *17,* 1922–1926. doi:10.1088/0957-4484/17/8/020
54. Karim, S.; Toimil-Molares, M. E.; Maurer, F.; Miehe, G.; Ensinger, W.; Liu, J.; Cornelius, T. W.; Neumann, R. *Appl. Phys. A* **2006,** *84,* 403–407. doi:10.1007/s00339-006-3645-6
55. Rauber, M.; Brotz, J.; Duan, J.; Liu, J.; Müller, S.; Neumann, R.; Picht, O.; Toimil-Molares, M. E.; Ensinger, W. *J. Phys. Chem. C* **2010,** *114,* 22502–22507. doi:10.1021/jp108889c
56. Cornelius, T. W.; Brötz, J.; Chtanko, N.; Dobrev, D.; Miehe, G.; Neumann, R.; Toimil-Molares, M. E. *Nanotechnology* **2005,** *16,* S246–S249. doi:10.1088/0957-4484/16/5/020
57. Daub, M.; Enculescu, I.; Neumann, R; Spohr, R. *J. Optoelectron. Adv. Mater.* **2005,** *7,* 865–870.
58. Picht, O.; Müller, S.; Alber, I.; Rauber, M.; Lensch-Falk, J.; Medlin, D. L.; Neumann, R.; Toimil-Molares, M. E. *J. Phys. Chem. C* **2012,** *116,* 5367–5375. doi:10.1021/jp210491g
59. Schuchert, I. U.; Toimil-Molares, M. E.; Dobrev, D.; Vetter, J.; Neumann, R.; Martin, M. *J. Electrochem. Soc.* **2003,** *150,* C189–C194. doi:10.1149/1.1554722
60. Mueller, S.; Schotz, C.; Picht, O.; Sigle, W.; Kopold, P.; Rauber, M.; Alber, I.; Neumann, R.; Toimil-Molares, M. E. *Cryst. Growth Des.* **2012,** *12,* 615–621. doi:10.1021/cg200685c
61. Budevski, E.; Staikov, G.; Lorenz, W. J. *Electrochemical Phase Formation and Growth;* VCH: Weinheim, Germany, 1996. doi:10.1002/9783527614936
62. Steinhögl, W.; Schindler, G.; Steinlesberger, G.; Traving, M.; Engelhardt, M. *J. Appl. Phys.* **2005,** *97,* 023706–023712. doi:10.1063/1.1834982
63. Li, D.; Wu, Y.; Fan, R.; Yang, P.; Majumdar, A. *Appl. Phys. Lett.* **2003,** *83,* 3186–3188. doi:10.1063/1.1619221
64. Fert, A.; Piraux, L. *J. Magn. Magn. Mater.* **1999,** *200,* 338–358. doi:10.1016/S0304-8853(99)00375-3
65. Halas, N. J.; Lal, S.; Chang, W.-S.; Link, S.; Nordlander, P. *Chem. Rev.* **2011,** *111,* 3913–3961. doi:10.1021/cr200061k
66. Kreibig, U.; Vollmer, M. In *Optical Properties of Metal Clusters;* Toennies, J. P., Ed.; Springer Series in Materials Science, Vol. 25; Springer: Berlin, Heidelberg, 1995.
67. Valenzuela, K.; Raghavan, S.; Deymier, P. A.; Hoying, J. *J. Nanosci. Nanotechnol.* **2008,** *8,* 3416–3421. doi:10.1166/jnn.2008.122
68. Kim, C.; Gu, W.; Briceno, M.; Robertson, I. M.; Choi, H.; Kim, K. *Adv. Mater.* **2008,** *20,* 1859–1863. doi:10.1002/adma.200701460

69. Rathmell, A. R.; Bergin, S. M.; Hua, Y.-L.; Li, Z.-Y.; Wiley, B. J. *Adv. Mater.* **2010,** *22,* 3558–3563. doi:10.1002/adma.201000775
70. Datta, M. *IBM J. Res. Dev.* **1998,** *42,* 563–566. doi:10.1147/rd.425.0563
71. Toimil-Molares, M. E.; Brötz, J.; Buschmann, V.; Dobrev, D.; Neumann, R.; Scholz, R.; Schuchert, I. U.; Trautmann, C.; Vetter, J. *Nucl. Instrum. Methods Phys. Res., Sect. B* **2001,** *185,* 192–197. doi:10.1016/S0168-583X(01)00755-8
72. Duan, J.; Liu, J.; Mo, D.; Yao, H.; Maaz, K.; Chen, Y.; Sun, Y.; Hou, M.; Qu, X.; Zhang, L.; Chen, Y. *Nanotechnology* **2010,** *21,* 365605. doi:10.1088/0957-4484/21/36/365605
73. Dobrev, D.; Vetter, J.; Angert, N.; Neumann, R. *Appl. Phys. A* **1999,** *69,* 233–237. doi:10.1007/s003390050995
74. Leopold, S.; Schuchert, I. U.; Lu, J.; Toimil-Molares, M. E.; Herranen, M.; Carlsson, J.-O. *Electrochim. Acta* **2002,** *47,* 4393–4397. doi:10.1016/S0013-4686(02)00515-7
75. Gottstein, G. *Physikalische Grundlagen der Materialkunde;* Springer: Berlin, 1998.
76. Zhong, S.; Koch, T.; Wang, M.; Scherer, T.; Walheim, S.; Hahn, H.; Schimmel, T. *Small* **2009,** *5,* 2265–2270. doi:10.1002/smll.200900746
77. Kelly, K. L.; Coronado, E.; Zhao, L. L.; Schatz, G. C. *J. Phys. Chem. B* **2003,** *107,* 668–677. doi:10.1021/jp026731y
78. Yi, G.; Schwarzacher, W. *Appl. Phys. Lett.* **1999,** *74,* 1746–1748. doi:10.1063/1.123675
79. Ohgai, T.; Gravier, L.; Hoffer, X.; Lindeberg, M.; Hjort, K.; Spohr, R.; Ansermet, J. P. *J. Phys. D: Appl. Phys.* **2003,** *36,* 3109–3114. doi:10.1088/0022-3727/36/24/003
80. Song, S.; Bohuslav, G.; Capitano, A.; Du, J.; Taniguchi, K.; Cai, Z.; Sun, L. *J. Appl. Phys.* **2012,** *111,* 056103. doi:10.1063/1.3692068
81. Lin, Y.-M.; Sun, X.; Dresselhaus, M. S. *Phys. Rev. B* **2000,** *62,* 4610–4623. doi:10.1103/PhysRevB.62.4610
82. Lin, Y.-M.; Cronin, S. B.; Ying, J. Y.; Dresselhaus, M. S.; Heremans, J. P. *Appl. Phys. Lett.* **2000,** *76,* 3944–3946. doi:10.1063/1.126829
83. Edelman, V. S. *Adv. Phys.* **1976,** *25,* 555–613. doi:10.1080/00018737600101452
84. Garcia, N.; Kao, Y. H.; Strongin, M. *Phys. Rev. B* **1972,** *5,* 2029–2039. doi:10.1103/PhysRevB.5.2029
85. Hicks, L. D.; Dresselhaus, M. S. *Phys. Rev. B* **1993,** *47,* 12727–12731. doi:10.1103/PhysRevB.47.12727
86. Sommerlatte, J.; Nielsch, K.; Bottner, H. *Physik Journal* **2007,** *6* (5), 35–41.
87. Hochbaum, A. I.; Chen, R.; Diaz Delgado, R.; Liang, W.; Garnett, E. C.; Najarian, M.; Majumdar, A.; Yang, P. *Nature* **2008,** *451,* 163–167. doi:10.1038/nature06381
88. Boukai, A. I.; Bunimovich, Y.; Tahir-Kheli, J.; Yu, J.-K.; Goddard, W. A., III; Heath, J. R. *Nature* **2008,** *451,* 168–171. doi:10.1038/nature06458
89. Gao, Y.; Niu, H.; Zeng, C.; Chen, Q. *Chem. Phys. Lett.* **2003,** *367,* 141–144. doi:10.1016/S0009-2614(02)01680-9
90. Heremans, J.; Thrush, C. M.; Lin, Y.-M.; Cronin, S.; Zhang, Z.; Dresselhaus, M. S.; Mansfield, J. F. *Phys. Rev. B* **2000,** *61,* 2921–2930. doi:10.1103/PhysRevB.61.2921
91. Duan, X.; Huang, Y.; Cui, Y.; Wang, J.; Lieber, C. M. *Nature* **2001,** *409,* 66–69. doi:10.1038/35051047
92. Lai, M.; Riley, J. *Chem. Mater.* **2006,** *18,* 2233–2237. doi:10.1021/cm051613j
93. Enculescu, I.; Sima, M.; Enculescu, M.; Enache, M.; Vasile, V.; Neumann, R. *Opt. Mater.* **2007,** *30,* 72–75. doi:10.1016/j.optmat.2007.01.002
94. Enculescu, I.; Matei, E.; Sima, M.; Neumann, R.; Granville, S.; Ansermet, J.-P. *IEEE Trans. Magn.* **2008,** *44,* 2678–2680. doi:10.1109/TMAG.2008.2003242
95. Sima, M.; Enculescu, I.; Trautmann, C.; Neumann, R. *J. Optoelectron. Adv. Mater.* **2004,** *6,* 121–125.
96. Enculescu, I.; Sima, M.; Enculescu, M.; Enache, M.; Ion, L.; Antohe, S.; Neumann, R. *Phys. Status Solidi B* **2007,** *244,* 1607–1611. doi:10.1002/pssb.200675109
97. Kum, M. C.; Yoo, B. Y.; Rheem, Y. W.; Bozhilov, K. N.; Chen, W.; Mulchandani, A.; Myung, N. V. *Nanotechnology* **2008,** *19,* 325711. doi:10.1088/0957-4484/19/32/325711
98. Matei, E.; Ion, L.; Antohe, S.; Neumann, R.; Enculescu, I. *Nanotechnology* **2010,** *21,* 105202. doi:10.1088/0957-4484/21/10/105202
99. Mo, D.; Liu, J.; Yao, H. J.; Duan, J. L.; Hou, M. D.; Sun, Y. M.; Chen, Y. F.; Xue, Z. H.; Zhang, L. *J. Cryst. Growth* **2008,** *310,* 612–616. doi:10.1016/j.jcrysgro.2007.11.034
100. Mallet, J.; Molinari, M.; Martineau, F.; Delavoie, F.; Fricoteaux, P.; Troyon, M. *Nano Lett.* **2008,** *8,* 3468–3474. doi:10.1021/nl802352e
101. Al-Salman, R.; Mallet, J.; Molinari, M.; Fricoteaux, P.; Martineau, F.; Troyon, M.; Zein El Abedin, S.; Endres, F. *Phys. Chem. Chem. Phys.* **2008,** *10,* 6233–6237. doi:10.1039/b809075k
102. Endres, F. *ChemPhysChem* **2002,** *3,* 144–154. doi:10.1002/1439-7641(20020215)3:2<144::AID-CPHC144>3.0.CO;2-#
103. Jeong, S.; Garnett, E. C.; Wang, S.; Yu, Z.; Fan, S.; Brongersma, M. L.; McGehee, M. D.; Cui, Y. *Nano Lett.* **2012,** *12,* 2971–2976. doi:10.1021/nl300713x
104. Kline, T. R.; Tian, M.; Wang, J.; Sen, A.; Chan, M. W. H.; Mallouk, T. E. *Inorg. Chem.* **2006,** *45,* 7555–7565. doi:10.1021/ic0601384
105. Paxton, W. F.; Kistler, K. C.; Olmeda, C. C.; Sen, A.; St. Angelo, S. K.; Cao, Y.; Mallouk, T. E.; Lammert, P. E.; Crespi, V. H. *J. Am. Chem. Soc.* **2004,** *126,* 13424–13431. doi:10.1021/ja047697z
106. Nicewarner-Peña, S. R.; Freeman, R. G.; Reiss, B. D.; He, L.; Peña, D. J.; Walton, I. D.; Cromer, R.; Keating, C. D.; Natan, M. J. *Science* **2001,** *294,* 137–141. doi:10.1126/science.294.5540.137
107. Piraux, L.; George, J. M.; Despres, J. F.; Leroy, C.; Ferain, E.; Legras, R.; Ounadjela, K.; Fert, A. *Appl. Phys. Lett.* **1994,** *65,* 2484–2486. doi:10.1063/1.112672
108. Blondel, A.; Meier, J. P.; Doudin, B.; Ansermet, J.-P. *Appl. Phys. Lett.* **1994,** *65,* 3019–3021. doi:10.1063/1.112495
109. Schwarzacher, W.; Attenborough, K.; Michel, A.; Nabiyouni, G.; Meier, J. P. *J. Magn. Magn. Mater.* **1997,** *165,* 23–29. doi:10.1016/S0304-8853(96)00465-9
110. Matei, E.; Preda, N.; Enculescu, M.; Ansermet, J.-P.; Toimil-Molares, M. E.; Enculescu, I. *Digest Journal of Nanomaterials and Biostructures* **2010,** *5,* 1067–1076.
111. Krieg, J. Bachelor Thesis, Faculty of Physics, Technische Universität Darmstadt, 2010.
112. Zhu, J.; Yu, Z.; Burkhard, G. F.; Hsu, C.-M.; Connor, S. T.; Xu, Y.; Wang, Q.; McGehee, M.; Fan, S.; Cui, Y. *Nano Lett.* **2009,** *9,* 279–282. doi:10.1021/nl802886y
113. Maurer, F.; Dangwal, A.; Lysenkov, D.; Müller, G.; Toimil-Molares, M. E.; Trautmann, C.; Brötz, J.; Fuess, H. *Nucl. Instrum. Methods Phys. Res., Sect. B* **2006,** *245,* 337–341. doi:10.1016/j.nimb.2005.11.124

114. Serbun, P.; Jordan, F.; Navitski, A.; Müller, G.; Alber, I.; Toimil-Molares, M. E.; Trautmann, C. *Eur. Phys. J.: Appl. Phys.* **2012,** *58,* 10402. doi:10.1051/epjap/2012110473
115. Serbun, P.; Jordan, F.; Navitski, A.; Müller, G.; Alber, I.; Toimil-Molares, M. E.; Trautmann, C. Field emission proporties of copper nanocones grown in polymer ion-track membranes. In *Proceedings of 24th International Vacuum Nanoelectronics Conference (IVNC), 2011,* Wuppertal, Germany, July 18–22, 2011; pp 183–184.
116. Lysenkov, D.; Müller, G. *Int. J. Nanotechnol.* **2005,** *2,* 239–254. doi:10.1504/IJNT.2005.008062
117. Serbun, P.; Jordan, F.; Navitski, A.; Müller, G.; Alber, I.; Toimil-Molares, M. E.; Trautmann, C. *GSI Scientific Report* **2011,** 432.
118. Wang, M. C. P.; Gates, B. D. *Mater. Today* **2009,** *12,* 34–43. doi:10.1016/S1369-7021(09)70158-0
119. Lindeberg, M.; Hjort, K. *Sens. Actuators, A* **2003,** *105,* 150–161. doi:10.1016/S0924-4247(03)00088-8
120. Rauber, M.; Alber, I.; Müller, S.; Neumann, R.; Picht, O.; Roth, C.; Schökel, A.; Toimil-Molares, M. E.; Ensinger, W. *Nano Lett.* **2011,** *11,* 2304–2310. doi:10.1021/nl2005516
121. Weber-Bargioni, A.; Schwartzberg, A.; Schmidt, M.; Harteneck, B.; Ogletree, D. F.; Schuck, P. J.; Cabrini, S. *Nanotechnology* **2010,** *21,* 065306. doi:10.1088/0957-4484/21/6/065306
122. Chen, X.; Guo, Z.; Yang, G.-M.; Li, J.; Li, M.-Q.; Liu, J.-H.; Huang, X.-J. *Mater. Today* **2011,** *13,* 28–41. doi:10.1016/S1369-7021(10)70201-7
123. Taychatanapat, T.; Bolotin, K. I.; Kuemmeth, F.; Ralph, D. C. *Nano Lett.* **2007,** *7,* 652–656. doi:10.1021/nl062631i
124. Weber, D.; Katzmann, J.; Neubrech, F.; Härtling, T.; Pucci, A. *Opt. Mater. Express* **2011,** *1,* 1301–1306. doi:10.1364/OME.1.001301
125. Qin, L.; Park, S.; Huang, L.; Mirkin, C. A. *Science* **2005,** *309,* 113–115. doi:10.1126/science.1112666
126. Alber, I.; Sigle, W.; Müller, S.; Neumann, R.; Picht, O.; Rauber, M.; van Aken, P. A.; Toimil-Molares, M. E. *ACS Nano* **2011,** *5,* 9845–9853. doi:10.1021/nn2035044
127. Alber, I.; Müller, S.; Picht, O.; Rauber, M.; Toimil-Molares, M. E.; Neumann, R. *GSI Scientific Report* **2010,** 398.
128. Mayadas, A. F.; Shatzkes, M. *Phys. Rev. B* **1970,** *1,* 1382–1389. doi:10.1103/PhysRevB.1.1382
129. Dingle, R. B. *Proc. R. Soc. London, Ser. A* **1950,** *201,* 545–560. doi:10.1098/rspa.1950.0077
130. Toimil-Molares, M. E.; Hoehberger, E. M.; Schaeflein, C.; Blick, R. H.; Neumann, R.; Trautmann, C. *Appl. Phys. Lett.* **2003,** *82,* 2139–2141. doi:10.1063/1.1563741
131. Katzenmeyer, A. M.; Léonard, F.; Talin, A. A.; Toimil-Molares, M. E.; Cederberg, J. G.; Huang, J. Y.; Lensch-Falk, J. L. *IEEE Trans. Nanotechnol.* **2010,** *10,* 92–95. doi:10.1109/TNANO.2010.2062198
132. Talin, A. A.; Léonard, F.; Katzenmeyer, A. M.; Swartzentruber, B. S.; Picraux, S. T.; Toimil-Molares, M. E.; Cederberg, J. G.; Wang, X.; Hersee, S. D.; Rishinaramangalum, A. *Semicond. Sci. Technol.* **2010,** *25,* 024015. doi:10.1088/0268-1242/25/2/024015
133. Cornelius, T. W.; Toimil-Molares, M. E.; Neumann, R.; Karim, S. *J. Appl. Phys.* **2006,** *100,* 114307. doi:10.1063/1.2388857
134. Cornelius, T. W.; Toimil-Molares, M. E.; Karim, S.; Neumann, R. *Phys. Rev. B* **2008,** *77,* 125425. doi:10.1103/PhysRevB.77.125425
135. Karim, S.; Ensinger, W.; Cornelius, T. W.; Neumann, R. *Physica E* **2008,** *40,* 3173–3178. doi:10.1016/j.physe.2008.05.011
136. Cornelius, T. W.; Picht, O.; Müller, S.; Neumann, R.; Völklein, F.; Karim, S.; Duan, J. L. *J. Appl. Phys.* **2008,** *103,* 103713. doi:10.1063/1.2927443
137. Cornelius, T. W.; Toimil-Molares, M. E.; Neumann, R.; Fahsold, G.; Lovrincic, R.; Pucci, A.; Karim, S. *Appl. Phys. Lett.* **2006,** *88,* 103114. doi:10.1063/1.2183823
138. Neubrech, F.; Kolb, T.; Lovrincic, R.; Fahsold, G.; Pucci, A.; Aizpurua, J.; Cornelius, T. W.; Toimil-Molares, M. E.; Neumann, R.; Karim, S. *Appl. Phys. Lett.* **2006,** *89,* 253104. doi:10.1063/1.2405873
139. Neubrech, F.; Pucci, A.; Cornelius, T. W.; Karim, S.; Garcia-Etxarri, A.; Aizpurua, J. *Phys. Rev. Lett.* **2008,** *101,* 157403. doi:10.1103/PhysRevLett.101.157403
140. Glaeser, A. M. *Interface Sci.* **2001,** *9,* 65–82. doi:10.1023/A:1011279015039
141. Li, H.; Biser, J. M.; Perkins, J. T.; Dutta, S.; Vinci, R. P.; Chan, H. M. *J. Appl. Phys.* **2008,** *103,* 024315. doi:10.1063/1.2837053
142. Klinger, L.; Rabkin, E. *Acta Mater.* **2006,** *54,* 305–311. doi:10.1016/j.actamat.2005.08.034
143. Cahn, J. W. *Scr. Metall.* **1979,** *13,* 1069–1071. doi:10.1016/0036-9748(79)90205-9
144. Gurski, K. F.; McFadden, G. B. *Proc. R. Soc. London, Ser. A* **2003,** *459,* 2575–2598. doi:10.1098/rspa.2003.1144 And references therein.
145. Plateau, J. *Smithsonian Institution, Annual Report* **1873,** 1863.
146. Lord Rayleigh. *Proc. London Math. Soc.* **1878,** *10,* 4–13. doi:10.1112/plms/s1-10.1.4
147. Nichols, F. A.; Mullins, W. W. *Trans. Metall. Soc. AIME* **1965,** *233,* 1840–1845.
148. Toimil-Molares, M. E.; Balogh, A. G.; Cornelius, T. W.; Neumann, R.; Trautmann, C. *Appl. Phys. Lett.* **2004,** *85,* 5337–5339. doi:10.1063/1.1826237
149. Karim, S.; Toimil-Molares, M. E.; Balogh, A. G.; Ensinger, W.; Cornelius, T. W.; Khan, E. U.; Neumann, R. *Nanotechnology* **2006,** *17,* 5954–5959. doi:10.1088/0957-4484/17/24/009
150. Karim, S.; Toimil-Molares, M. E.; Ensinger, W.; Balogh, A. G.; Cornelius, T. W.; Khan, E. U.; Neumann, R. *J. Phys. D: Appl. Phys.* **2007,** *40,* 3767–3770. doi:10.1088/0022-3727/40/12/031
151. Zhou, Z. F.; Pan, Y.; Zhou, Y. C.; Yang, L. *Appl. Surf. Sci.* **2011,** *257,* 9991–9995. doi:10.1016/j.apsusc.2011.06.125
152. Toimil-Molares, M. E.; Röntzsch, L.; Sigle, W.; Heinig, K.-H.; Trautmann, C.; Neumann, R. *Adv. Funct. Mater.* **2012,** *22,* 695–701. doi:10.1002/adfm.201102260

Beilstein Journal of Nanotechnology

Low-dose patterning of platinum nanoclusters on carbon nanotubes by focused-electron-beam-induced deposition as studied by TEM

Xiaoxing Ke*[1], Carla Bittencourt[2], Sara Bals[1] and Gustaaf Van Tendeloo[1]

Full Research Paper

Open Access

Address:
[1]EMAT, University of Antwerp, Groenenborgerlaan 171, 2020 Antwerp, Belgium and [2]Chemistry of Interaction Plasma Surface (ChiPS), University of Mons, Place du Parc 20, 7000 Mons, Belgium

Email:
Xiaoxing Ke* - Xiaoxing.Ke@ua.ac.be

* Corresponding author

Keywords:
carbon nanotubes; FEBID; nanocluster; platinum; patterning; radiation-induced nanostructures; TEM

Beilstein J. Nanotechnol. **2013,** *4,* 77–86.
doi:10.3762/bjnano.4.9

Received: 12 September 2012
Accepted: 21 January 2013
Published: 04 February 2013

This article is part of the Thematic Series "Radiation-induced nanostructures: Formation processes and applications".

Guest Editor: M. Huth

Abstract

Focused-electron-beam-induced deposition (FEBID) is used as a direct-write approach to decorate ultrasmall Pt nanoclusters on carbon nanotubes at selected sites in a straightforward maskless manner. The as-deposited nanostructures are studied by transmission electron microscopy (TEM) in 2D and 3D, demonstrating that the Pt nanoclusters are well-dispersed, covering the selected areas of the CNT surface completely. The ability of FEBID to graft nanoclusters on multiple sides, through an electron-transparent target within one step, is unique as a physical deposition method. Using high-resolution TEM we have shown that the CNT structure can be well preserved thanks to the low dose used in FEBID. By tuning the electron-beam parameters, the density and distribution of the nanoclusters can be controlled. The purity of as-deposited nanoclusters can be improved by low-energy electron irradiation at room temperature.

Introduction

Hybrid nanostructures consisting of carbon nanotubes (CNTs) decorated with metal nanoclusters enable access to various electrical and catalytic properties. Therefore, they are considered as building blocks for nanoscopic electronic devices [1]. In such hybrid nanostructures, metals are often deposited onto the CNTs by thermal evaporation [2-6] or wet chemistry [7], which results in a non-site-specific covering. However, when using such structures for nanodevice fabrication, specific sites of the CNTs need to be functionalized in order to create components with specific properties. For instance, in order to fabricate CNT contacts on electrodes, Pd is thermally evaporated onto both ends by using shadowing masks [8]. In earlier reports, it has been shown that Au nanoclusters can be site-selectively decorated on the CNTs by using a focused ion beam (FIB) and

subsequent chemical treatment [9]. However, these approaches either involve several steps or require masks to perform the site-specific deposition. Therefore, a more straightforward strategy to perform site-specific metal deposition is desired. In this paper, we explore the use of focused-electron-beam-induced deposition (FEBID) to pattern CNTs with well-dispersed ultrasmall nanoclusters.

FEBID is a direct-write process where a focused electron beam is used to locally decompose a precursor gas that contains a component such as a metal that is expected to be deposited on the substrate. The process can create nanostructures rapidly in a site-specific manner by scanning the electron beam precisely on the area of interest where the decomposition and deposition should take place. FEBID offers an efficient way of performing site-specific nanostructure deposition in a nondestructive way. A comprehensive review of FEBID can be found in the reviews of Randoph et al. [10], Huth et al. [11], Van Dorp et al. [12], Utke et al. [13,14] and Wnuk et al. [15], etc.

The applications of FEBID on CNTs are mostly focused on the formation of electrical contacts, and therefore much effort is being put into their electrical measurements and resistivity improvement, such as in references [16,17]. Nevertheless, the formation of different patterns of nanostructures at the CNT surface by FEBID is more challenging, since the direct-write process can produce various nanostructures beyond the simple formation of nanocontacts. For instance, by applying different precursor and deposition parameters, nanostructures of different dimensions, different chemical compositions and, thus, different properties can be formed at the CNT surface. Deposition of silicon [18], tungsten [19,20] and cobalt [21,22] nanostructures has been reported. A recent study has demonstrated the successful formation of binary Si–Pt nanostructures by FEBID [23].

Ultrasmall well-dispersed nanoclusters supported on CNTs are of most interest as the (electro-) catalytic activity can be increased [24-27]. The ability of FEBID to write ultrasmall nanostructures has been demonstrated by using scanning transmission electron microscopy (STEM) with an electron probe of 0.2 nm operated at 200 kV [28,29]. By using scanning electron microscopy (SEM)-assisted FEBID, Co nanowires of lateral size below 30 nm have been grown as well [30-32].

In this work, the site-specific deposition of Pt nanoclusters on CNTs by low-dose FEBID is presented. Electron tomography is performed to study the three-dimensional (3D) distribution of the as-deposited nanoclusters on the CNT surface. We observed the formation of a novel stripe-patterning of nanoclusters on the surface of the CNTs, which may open up new prospects of nanostructuring for applications in nanodevices dependent on the distribution of metal clusters. High-resolution transmission electron microscopy (HRTEM) and high-angle annular dark-field scanning transmission electron microscopy (HAADF-STEM) is used to study the morphology and distribution of the nanoclusters deposited by using different electron beam parameters. Although the as-deposited nanoclusters are composed of Pt and amorphous carbon, it is demonstrated that the amount of amorphous carbon due to the fragmentation of the organo-metal [$(CH_3)_3Pt(CpCH_3)$], used as precursor for Pt deposition, can be reduced by using electron-beam irradiation with a low accelerating voltage as a post-deposition treatment.

Results and Discussion

3D distribution of Pt nanoclusters around CNTs

When the CNTs are patterned by FEBID of Pt nanoclusters, the overall distribution of nanoclusters around the CNTs is one of the key factors to evaluate the effectiveness of the deposition process. As one of the most powerful and straightforward approaches to study the nanostructures in a 3D manner, electron tomography is performed to investigate the 3D distribution of as-deposited nanoclusters on CNTs. Figure 1 describes the 3D nanoclusters distribution study of a CNT decorated with Pt nanoclusters deposited by using an electron beam accelerated by 10 kV with a beam current of 0.54 nA; HAADF-STEM images from the tilt series at tilting angles of 0° and 70° and are shown (Figure 1a,b). In HAADF-STEM, the contrast scales with the atomic number *Z*, and therefore Pt nanoclusters yield a higher intensity in comparison to the CNT. Figure 1a,b demonstrates that the ultrasmall nanoparticles are well-dispersed across the whole surface of the CNT. Further 3D reconstruction of a tilt series of images (tilt range of ±70° with a 2° tilt interval, see Experimental section) confirms that the deposition has occurred all around the CNT resulting in a well-dispersed coverage. An orthoslice taken through the 3D reconstruction is presented in Figure 1c, illustrating the cross section of the as-deposited CNT. The dispersion of the Pt nanoclusters over the complete CNT surface verifies that the Pt nanoclusters are present on the entire surface of the CNT. A movie of the 3D reconstruction can be found in Supporting Information File 1.

We have observed that although the Pt nanoclusters are distributed uniformly along the long axis of the CNT, their distribution along the circumference is less homogeneous. A statistical analysis of the nanocluster distribution around the circumference of the CNT has been carried out based on the 3D reconstruction. As shown in Figure 1d, the distribution of nanoclusters has been quantified as a function of the angle α between the electron beam and the tangent plane of the CNT circumference. It can be seen from Figure 1d that the nanocluster distribution

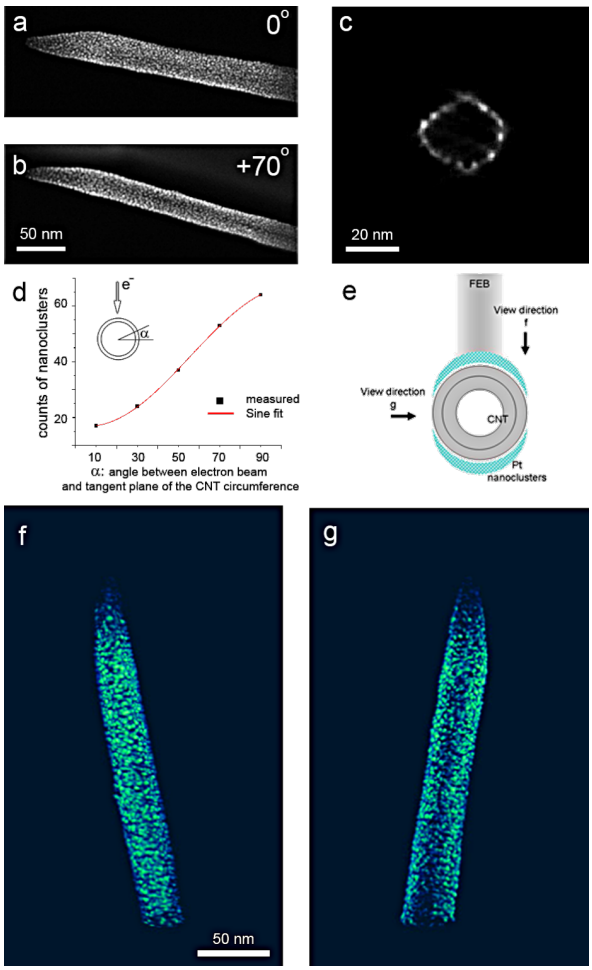

Figure 1: (a,b) HAADF-STEM images of the Pt deposited CNT at tilting angle of 0 and 70 degrees respectively. (c) A cross-section snapshot of the Pt deposited CNT from 3D reconstruction. Pt nanoclusters are shown as bright contrast. (d) Graph showing that the circumferential distribution of nanoclusters fits a sinusoid. (e) Illustration of the Pt distribution around the CNT. (f,g) Snapshots of the 3D reconstructed CNT along the viewing direction of f and g according to the illustration in (e).

can fit into a sinusoid curve. The nonhomogeneous distribution of the nanoclusters can be demonstrated from the snapshots of the reconstruction shown in Figure 1f,g, where the density of nanoclusters at the CNT surface that faces towards the electron beam during deposition (Figure 1f) is higher than the one at the side of the CNT (Figure 1g). A straightforward and likely explanation can be given by considering the curvature of the CNT due to its tubular shape. It has been reported that besides the primary electrons, which are the direct incident electrons used in FEBID, the decomposition of the precursor molecules is to a large extent caused by the secondary electrons from the target surface as well [33]. The effect of the secondary electrons increases as the beam diameter decreases [29]. Due to the curvature at the CNT surface, both the density of primary electrons and the emission of secondary electrons reach a maximum at the surface perpendicular to the electron beam, and decrease for a surface with smaller angles to the primary beam. Therefore, the deposition has lower yields at the side surface parallel to the incident electron beam. As confirmed from the 3D reconstruction, the actual distribution of the as-deposited nanostructures can therefore be schematically illustrated in Figure 1e.

In addition, the 3D reconstruction shows that both the upper surface and the lower surface perpendicular to the beam have a similar distribution of Pt nanoclusters. This can be explained as follows: the CNT is placed on top of a holey carbon film supported by a Cu grid, i.e., the CNT is suspended rather than supported by a substrate. Therefore, when the precursor gas is released, the entire CNT surface is exposed to the precursor molecules (Figure 2a). When the electron beams scan the predefined area, the incident electrons and secondary electrons from the CNT decompose the precursor molecules in the vicinity of the CNT surface. Electrons not only decompose the molecules at the upper surface when they enter the CNT, but also decompose the molecules when they pass through the CNT and exit. Such electrons as well as the secondary electrons from the lower surface of the CNT decompose the precursor molecules in its vicinity as efficiently. Therefore, decomposition has its effect all around the CNT and results in Pt nanoclusters decorating both the upper surface and lower surface of the CNT (Figure 2b).

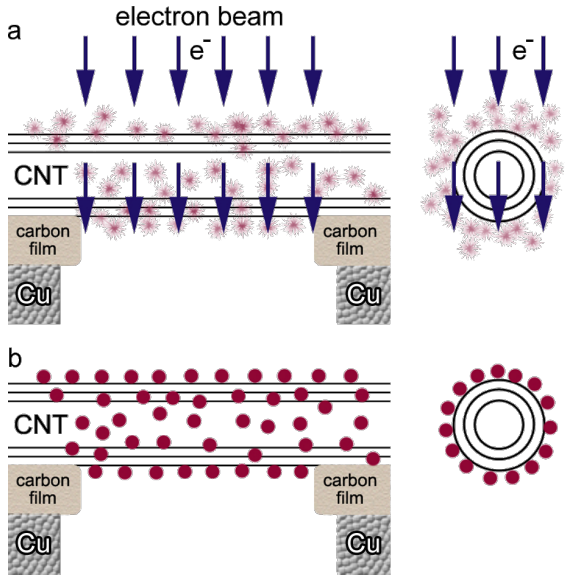

Figure 2: Illustrations of FEBID of nanoclusters on CNT. (a) Precursor gas is all around the CNT since the CNT is not attached to the substrate and is suspended above the support grid. CNT is viewed from both radial and axial directions. Electron beams transmit through the CNT as shown. (b) Pt nanoclusters are found all around the CNT as viewed from both radial and axial directions.

Demonstrating the ability of FEBID to deposit nanoclusters on both sides of the CNTs, we believe that the application of FEBID as a direct patterning approach can be extended to various electron-transparent structures, such as nanowires, thin films and graphene. Furthermore, taking into account that decomposition and further deposition is induced by interaction between electrons and materials, deposition can be tailored by tuning the accelerating voltage of the electron beam to control their transmission through a fixed thickness of target so as to realize the deposition on one or more facets.

Stripe pattern of the Pt nanoclusters on CNTs

When the deposition is performed in the first place, nanoclusters are expected to be confined in the preselected area only. A TEM image of the as-deposited nanostructure at a lower magnification confirms that the site-specificity has been accomplished (Figure 3). As shown in Figure 3a, the dashed box indicates the defined area during deposition and has a dimension of 400 nm × 500 nm. After the deposition, it can be seen that the deposited nanoclusters are strictly restrained in the predefined section of the CNT. The edge of deposited area is sharp and clean and leaves the rest of the CNT unaffected (Figure 3b). The unwanted proximity effect, which is noted to be related to a large dose and charging of the surface [12,34,35], is not seen at this scale. In fact, in this study a low dose is used and the CNTs have an "electron-transparent" thickness, thus the proximity effect can be ignored and the site-specificity is achieved at the nanoscale.

The irradiated and nonirradiated parts of the CNT are investigated by HRTEM (Figure 3c,d). We observe that the graphitic walls under the region covered by Pt nanoclusters (Figure 3c) show similar structure in comparison to the graphitic layers in the nonirradiated part of the CNT next to the deposited area (Figure 3d). This clearly reveals that the nanostructure of the CNT has been preserved during the FEBID process.

The deposition shown in Figure 1 and Figure 3 with uniform coverage of Pt nanoclusters on areas of interest is performed at the right focus of the deposition electron beam, i.e., the defocus value is 0. Nevertheless, if the deposition is carried out with the beam out of the focus, the as-deposited nanoclusters are no longer homogeneously distributed. This effect is demonstrated in Figure 4, where electron beams of different focus of 0 µm (i.e., in focus), 4 µm, 8 µm and 10 µm are applied for deposition onto an amorphous carbon film that was exposed to the Pt precursor gas. Detailed patterning parameters are described in Table S1 of Supporting Information File 2. It is obvious that the 0 µm and 4 µm defoci result in a uniform coverage of deposition (Figure 4a–b), whereas the 8 µm and 10 µm defocused electron beams lead to deposition of nanostructures in a stripe fashion (Figure 4c,d). In Figure 4c, the interstripe distance in the pattern is approximately 35 nm, which agrees with the pitch value of this patterning. In Figure 4d, the interstripe distance is approximately 45 nm, which also agrees to the pitch value during patterning (see Table S1, Supporting Information File 2).

The defocus of the electron beam is reported to have an influence on the volume growth rates [36]. Nevertheless, in this context where only low-dose deposition is studied, the growth rate may not be as important, whereas the formation of the stripe pattern can be attributed to regime shift during pattering along the X and Y axes. In the deposition using a 30 kV electron beam, the working regime is mainly electron-limited (please refer to the discussion of working regime and primary energy in the next section), which is reflected in the patterning

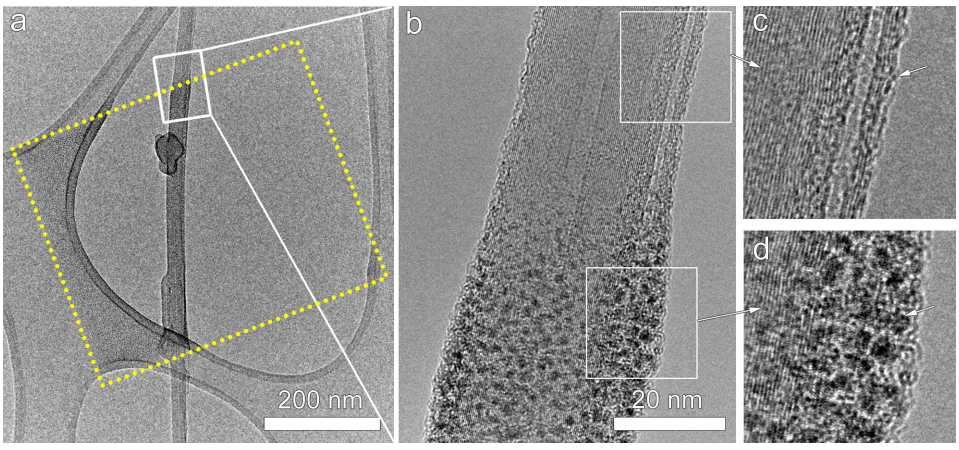

Figure 3: (a) TEM image of Pt nanoclusters deposited by FEBID on a CNT shows that site specific deposition has been achieved. The area indicated by the dotted lines is the predefine area during the deposition process. (b) Shows an enlargement of the rectangular dotted area in (a). The CNT structure has been preserved well during the deposition, as shown by HRTEM images (c–d).

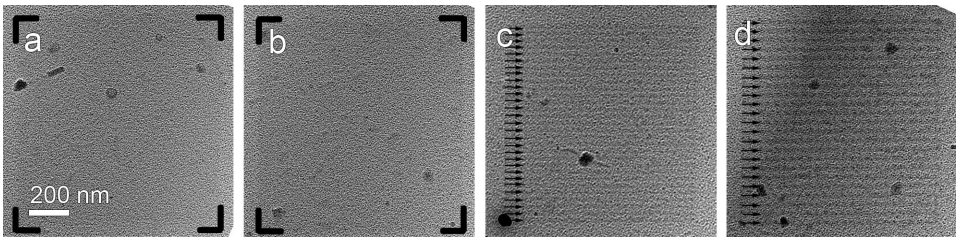

Figure 4: FEBID Pt on amorphous carbon at different defoci of the electron beam. (a) in focus, (b) at 4 µm defocus, (c) at 8 µm defocus and (d) at 10 µm defocus of the 30 kV 0.2 nA electron beam. Stripes with high densities are indicated by arrows and illustrations.

along Y axis, where a high/low density of the Pt nanocluster distribution is presented. Nevertheless, along the X axis, the working regime is likely to be precursor-limited for the serpentine scanning strategy employed during this deposition.

When we use a defocused electron beam for Pt deposition on CNTs, we observe that the Pt nanoclusters can be deposited in a switchable high/low density by fine-tuning the defocus of the electron beam. Figure 5a shows a CNT decorated with a high density of Pt nanoclusters discretely distributed at a regular spacing of approximately 44 nm. A HAADF-STEM tilt series of this nanostructure was performed and a 3D reconstruction was calculated. A movie can be found in Supporting Information File 3. A snapshot through the reconstructed nanostructure is shown in Figure 5b. The high-density stripes of the Pt nanoclusters are parallel to each other, and have an inclined angle of approximately 35° with respect to the long axis of CNT. This inclination can be tuned to any desired angle by positioning the CNTs relative to the scanning direction of the electron beam

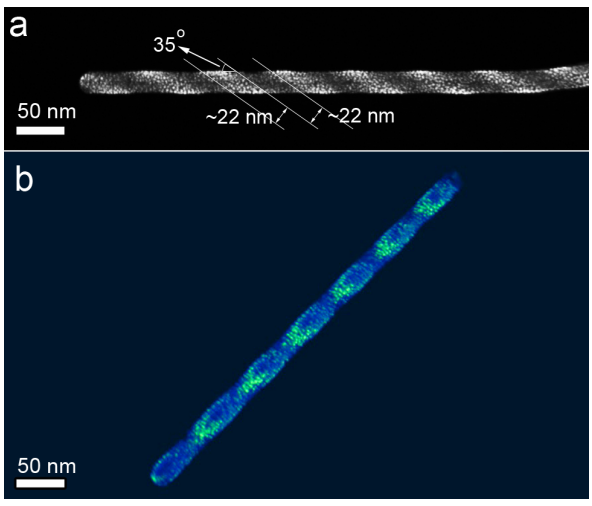

Figure 5: (a) HAADF-STEM image of a CNT with stripe-pattern of Pt nanoclusters from FEBID. (b) A snapshot from the 3D reconstruction of the nanostructure.

during FEBID. Furthermore, the size distribution of the as-deposited Pt nanoclusters is different from the uniform distribution seen in Figure 1. Larger nanoclusters are present in the striped area with higher deposition density, whereas smaller nanoclusters are present in the striped area with lower deposition density. The size distribution of the nanoclusters inside the stripes can be attributed to the regime shift as explained in the previous text. Furthermore, if we imagine a nanotube with a certain inclination angle to the electron beam, we can see that a varying defocus value during deposition can lead to a varying pitch in the stripe pattering along the long axis of the nanotube. The ability to pattern the nanostructure with switchable high/low density of nanoclusters provides new potential applications in tunable wetting, adhesion, catalysis and friction properties for nanodevices [37].

Deposition parameters and the size distribution of Pt nanoclusters

Since the Pt deposition by focused electron beam is essentially a decomposition process of an organometallic precursor using electron beams, the morphology and dimensions of the as-deposited nanoclusters are largely related to the deposition parameter settings, including precursor and gas flow, the nature of the target being deposited, and the electron-beam parameters, etc. [34,38]. As one of the most important parameters, the influence of the different electron-beam settings on the deposited Pt nanoclusters is studied by changing the beam accelerating voltage (primary energy, PE) and dwell time, whereas the beam current is not varied in the current study.

Figure 6 summarizes the deposition of Pt for an increasing PE of 1 kV, 3 kV, 5 kV, 10 kV, 15 kV and 30 kV in each row. For each PE, different dwell times of 50 ns, 100 ns, 500 ns, 1 µs and 100 µs are applied for further comparison. Although the same electron dose is applied for each deposition, which means the same deposition time (2 s) as well as the same beam current is maintained (0.2 nA), the deposited nanoclusters demonstrate a different distribution. Comparing the nanoclusters in the same column in which PE is increasing and dwell time is not varied,

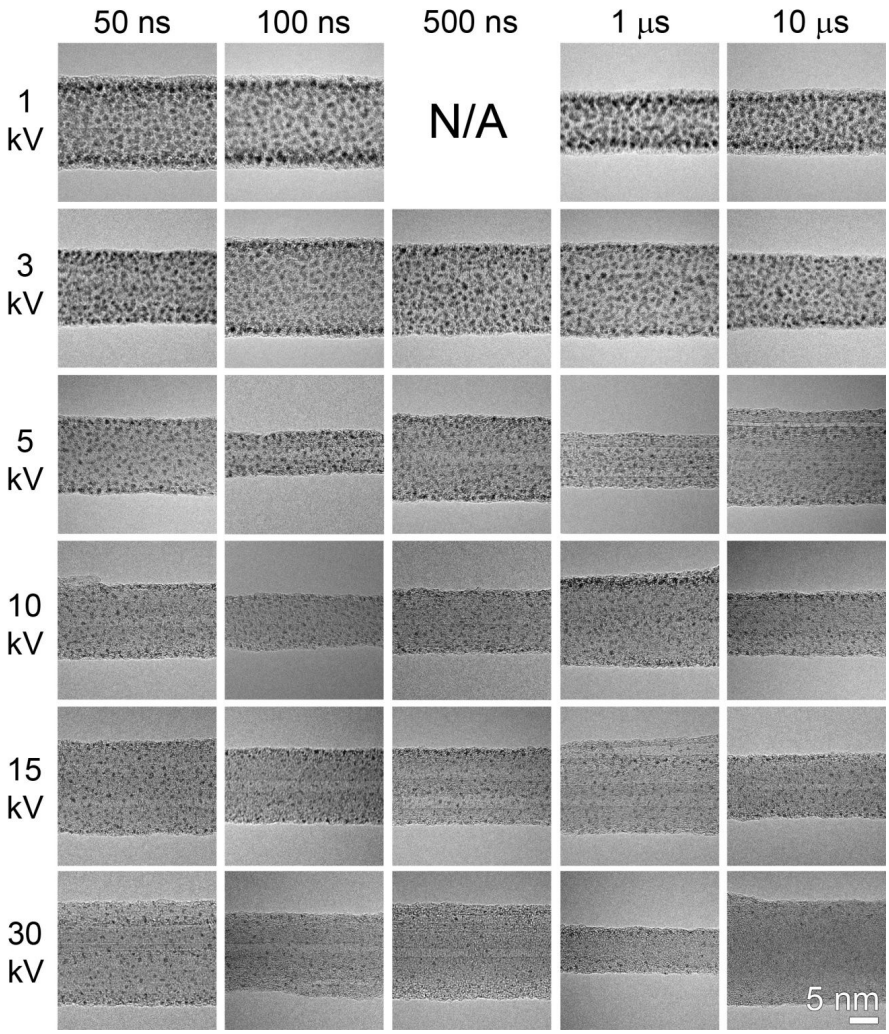

Figure 6: HRTEM images showing Pt nanoclusters deposited on CNTs by using different electron-beam settings. Beam energy is different as indicated in each row, whereas the beam dwell time is different as indicated in each column. The particular beam setting for the corresponding results are listed in Supporting Information File 2. For each beam setting, dwell times of 50 ns, 100 ns, 1 μs, 10 μs and 100 μs are applied for deposition.

it can be seen that their average size and lateral density decreases. The higher lateral density indicates a higher dissociation probability at lower PE, where PE contributes more to the deposition process. Simultaneously, lower PE results in a smaller interaction volume and therefore leads to increasing yields of secondary electrons and backscattered secondary electrons , which all contribute to the dissociation process.

When comparing the deposition in the same row in which PE is kept constant and dwell time is increased, it is noticed that the change in lateral density of the nanoclusters does not follow the same trend. When PE is 1 kV and 3 kV, the deposited nanoclusters have the same high density for all dwell times from 50 ns to 10 μs. Nevertheless, when PE is 15 kV and 30 kV, the nanoclusters show the same low density in the whole range of dwell times from 50 ns to 10 μs. Only when PE is 5 kV and 10 kV do the deposited nanoclusters demonstrate a decrease in the lateral density when the dwell time is increased from 50 ns to 10 μs.

It has been noted before that the precursor regime is largely dependent on the beam dwell time. Short dwell times lead to an electron-limited regime, whereas longer dwell times lead to a precursor-limited regime [10,39]. This well-known effect is reflected in the deposition results by a PE of 5 kV and 10 kV, where nanoclusters show a decrease in lateral density upon increasing dwell time. However, when a lower PE is used for the deposition, the rates of deposition are increased due to the higher number of potentially dissociating electron species (primary, secondary, backscattered, etc.), and therefore results in a working regime which is mainly precursor-limited, where the

lateral density of deposited nanoclusters is higher. In the case of higher PE, a lower contribution of dissociating electron species results in a shift of working regime to electron-limited and thus shows lower nanocluster density.

Improving the crystallinity of the carboneous matrix around Pt

In an ideal FEBID process, the electron beam is supposed to decompose the organoplatinum molecules completely, leaving only the metal atoms on the scanned area, and the volatile by-products should leave the surface. However, in an actual deposition process, the decomposition of the precursor gas is usually incomplete and residual fragments of the precursors as well as of residual gases in the deposition chamber decrease the purity of the as-deposited metal nanoclusters [33]. The chemical composition reported for Pt deposited by FEBID varies from one study to another. Pt relative concentration in the range of 85% to 30% has been reported [40,41]. Since the chemical composition of the as-deposited nanostructures is closely related to their properties, such as electrical conductivity [17] or catalytic activity, the purity of the as-deposited nanoclusters is one of the main concerns in FEBID.

In order to improve the Pt purity in FEBID nanostructures, post-treatment such as annealing or using different precursors [33] has been developed. It has been shown that electron irradiation in SEM can improve the crystallinity and conductivity in the as-deposited Pt nanoclusters [42,43]. Room-temperature phase transformation is also obtained by using low-energy electron irradiation [44]. Another alternative to improve the crystallinity of as-deposited nanostructures is to use higher energy electron irradiation in TEM, with 200 kV electrons used to remove the amorphous carbon [32]. In this context, we used the electron beam in a TEM to reduce the amorphous carbon observed in the as-deposited cluster. The in-situ TEM irradiation has the advantage of site-specificity with simultaneous monitoring of the process.

The electron irradiation in TEM was performed at an accelerating voltage of 80 kV, in order to minimize damage to the CNTs. Figure 7 presents the evolution of the FEBID nanostructures during the irradiation process. Figure 7a shows the as-deposited nanostructure before irradiation, where amorphous carbon is present on the CNT surface. Pt nanoclusters (dark contrast) are embedded within an amorphous carbon layer. After irradiation with a dose of 1.2×10^6 electrons/Å^2 (Figure 7b), 2.0×10^6 electrons/Å^2 (Figure 7c), 2.6×10^6 electrons/Å^2 (Figure 7d) and finally 3.2×10^6 electrons/Å^2 (Figure 7e), the amorphous layer is gradually reduced, as seen by comparing the same area from Figure 7a and Figure 7e as indicated by the circles, whereas the nanostructure of the CNT is well preserved. This effect has been reported in [45], which is attributed to the dissociation of intermediate amorphous carbon and defined as the first phase in electron irradiation. The second phase of graphitization due to the increasing electron–carbon interactions [43,45] can be observed from Figure 7e, where thin graphitic layers have emerged at the CNT surface, adding to the nondamaged CNT nanostructure.

Accompanying the reduction of amorphous carbon, the growth of Pt nanoclusters is noticed. As indicated by the arrows in Figure 7a to Figure 7e, a nanocluster is randomly picked to demonstrate the growth. It is likely that the growth of nanoclusters is due to the aggregation of Pt when the intermediate amorphous carbon is gradually removed. The growth of Pt nanoclusters under electron irradiation has been quantified as shown in Figure 7f. The average diameter of Pt nanoclusters are measured and plotted against electron dose, which shows a linear increase in the range of 0 to 3.2×10^6 electrons/Å^2.

A recent study has shown that FEBID of amorphous carbon on CNT followed by annealing of the structure, can result in a low-resistance electrical contact between CNT and metals, thanks to graphitic carbon layers crystallized from amorphous carbon [46]. Nevertheless, in the deposition of metal nanoclusters by FEBID, conventional annealing of the composite structure may lead to unwanted fast growth of nanoparticles, which can be difficult to monitor and control. Our post-growth experiment through electron irradiation has shown that the crystallization of amorphous carbon can be performed in a controllable manner, where the growth of nanoparticles is seen to increase along with the electron dose, and the graphitization of the carbon layer is present to reduce the resistance between the CNT and the deposited metal effectively.

In summary, focused-electron-beam deposition of Pt nanoclusters on CNTs in a DualBeam system has been demonstrated to be a viable approach to fabricate novel nanostructures. The deposition can be performed in a site-specific manner where the nanoclusters are strictly deposited in the area of interest whereas the rest of the CNT is free of modification and well preserved. Electron tomography is performed in order to reveal the 3D structure of the as-deposited CNTs. It has been found that the deposition takes place all over the CNT, resulting in Pt nanoclusters over the entire surface of the CNT. Some characteristics of the as-deposited nanostructures can be controlled by tuning the electron-beam parameters. Defocus in the electron beam leads to stripe patterning of the Pt nanoclusters across the CNTs. The ability to fine-tune the deposition of ultrasmall nanoclusters with a regular spacing on the nanoscale opens-up the possibility to engineering specific surface electronic states and, thus, catalytic activity.

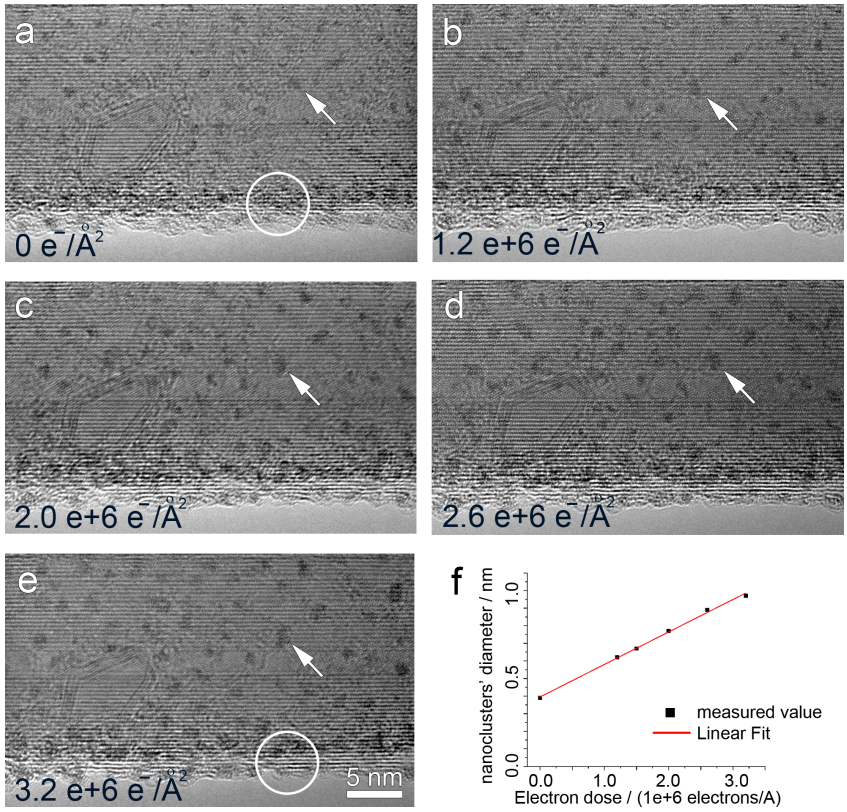

Figure 7: HRTEM images showing that amorphous carbon can be reduced by in-situ electron irradiation in a TEM under 80 kV. (a) shows the FEBID on CNT before electron irradiation. (b–e) show that the amorphous carbon is gradually cleaned by increasing the dose of electrons. Comparing the circled area indicated in (a) and (e), the cleaning of amorphous carbon is obvious. (a–e) also show the growing of nanoclusters by increasing electron dose, one example is indicated by an arrow through the image series. The growth of nanoclusters is quantified as shown in (f), with the diameter of nanoclusters increasing linearly by electron dose.

The distribution of the as-deposited nanoclusters is closely related to the beam primary energy and dwell time during the deposition process. An electron beam of low primary energy has a significant influence on increasing the density of the as-deposited nanoclusters. Furthermore, the Pt purity of the as-deposited nanoclusters can be efficiently improved by reducing amorphous carbon using in-situ electron-beam irradiation in TEM at low kilovolt potentials (80 kV), where a simultaneous growth of a thin graphitic layer and Pt nanoclusters is achieved. The controllable crystallization of amorphous carboneous and Pt nanoclusters could be interesting for contact studies of functionalized CNTs.

Experimental

CNTs supported on a TEM grid are used as the deposition target. The samples are prepared by using commercially available multiwalled carbon nanotubes (MWCNTs) produced by arc discharge or chemical vapor deposition (CVD). The CNTs powder is sonically dispersed in ethanol and then a drop of the solution is deposited onto a holey carbon film supported by a standard TEM copper grid.

FEBID (Figures 1, 3, 5) is performed by using an FEI Nova 200 Nanolab DualBeam SEM/FIB. During the deposition in the DualBeam system, the working distance is set to be 5.0 mm throughout the experiments. The DualBeam system is equipped with a standard gas injection system (GIS) with $(CH_3)_3Pt(CpCH_3)$ as organometallic precursor gas. The reservoir temperature was approximately 43 °C. The electron beam used for deposition can be accelerated between 3 kV and 30 kV with a beam current ranging from 44 pA to 4.3 nA. The electron dose for all experiments is maintained as 2.5×10^9 electrons/μm^2.

FEBID (Figures 4, 6, 7) is performed by using an FEI Helios DualBeam SEM/FIB. During the deposition in the DualBeam system, the working distance is set to be 4.0 mm throughout the experiments. The DualBeam system is equipped with a GIS with the same organometallic precursor gas of $(CH_3)_3Pt(CpCH_3)$. The electron beam used for deposition can be accelerated between 1 kV and 30 kV with varying beam current. The electron dose for Figure 4 was set to be at 8.5×10^8 electrons/μm^2, whereas the electron dose for Figure 6 and

Figure 7 was maintained at 2.5×10^9 electrons/μm^2. The serpentine raster strategy is applied through all experiments, whereas the refresh time is 0 by default.

The as-deposited nanostructures are studied by using an FEI Tecnai G2 microscope operated at 200 kV. In order to investigate the morphology and distribution of the nanostructures in 3D, high-angle annular dark-field scanning transmission electron microscopy (HAADF-STEM) tilt series of the as-deposited CNTs are acquired. The tilt series have an angular range of ±70° with projections taken every 2°, and the tilt axis is set to be parallel to the long axis of the CNTs. Alignment of the tilt series is done by using the FEI Inspect3D software. The same software is used to reconstruct the aligned tilt series through the simultaneous iterative reconstruction technique (SIRT). The volume reconstructed by SIRT is segmented manually and visualized in the Amira software. High-resolution TEM (HRTEM) of the as-deposited nanostructures is performed on the same microscope at 200 kV. Post treatment using electron-beam irradiation is, however, performed using a FEI Titan 80–300 microscope fitted with aberration-correctors for the imaging lens and the probe forming lens, operated at 80 kV.

Supporting Information

Supporting Information File 1

Reconstructed movie of CNT fully covered by Pt.
[http://www.beilstein-journals.org/bjnano/content/supplementary/2190-4286-4-9-S1.mpg]

Supporting Information File 2

Detailed deposition parameters.
[http://www.beilstein-journals.org/bjnano/content/supplementary/2190-4286-4-9-S2.pdf]

Supporting Information File 3

Reconstructed movie of CNT covered by stripe-patterned Pt.
[http://www.beilstein-journals.org/bjnano/content/supplementary/2190-4286-4-9-S3.mpg]

Acknowledgements

X. Ke, S. Bals and G. Van Tendeloo appreciate financial support from the European Union under the Seventh Framework Program (Integrated Infrastructure Initiative N. 262348 European Soft Matter Infrastructure, ESMI). X. Ke and G. Van Tendeloo are grateful to the ERC advanced grant "COUNTATOM". S. Bals thanks the support from the Flemish Fund for Scientific Research (F.W.O. Vlaanderen) through project funding G.0024.10N. C. Bittencourt acknowledges the support of the COST ACTION MP0901 and the FRC-FNRS 2.4577.11F (CHEMOGRAPHENE).

References

1. Terrones, M. *Annu. Rev. Mater. Res.* **2003,** *33,* 419–501. doi:10.1146/annurev.matsci.33.012802.100255
2. Bittencourt, C.; Hecq, M.; Felten, A.; Pireaux, J. J.; Ghijsen, J.; Felicissimo, M. P.; Rudolf, P.; Drube, W.; Ke, X.; Van Tendeloo, G. *Chem. Phys. Lett.* **2008,** *462,* 260–264. doi:10.1016/j.cplett.2008.07.082
3. Suarez-Martinez, I.; Bittencourt, C.; Ke, X.; Felten, A.; Pireaux, J. J.; Ghijsen, J.; Drube, W.; Van Tendeloo, G.; Ewels, C. P. *Carbon* **2009,** *47,* 1549–1554. doi:10.1016/j.carbon.2009.02.002
4. Felten, A.; Suarez-Martinez, I.; Ke, X.; Van Tendeloo, G.; Ghijsen, J.; Pireaux, J.-J.; Drube, W.; Bittencourt, C.; Ewels, C. P. *ChemPhysChem* **2009,** *10,* 1799–1804. doi:10.1002/cphc.200900193
5. Bittencourt, C.; Ke, X.; Van Tendeloo, G.; Thiess, S.; Drube, W.; Ghijsen, J.; Ewels, C. P. *Chem. Phys. Lett.* **2012,** *535,* 80–83. doi:10.1016/j.cplett.2012.03.045
6. Suarez-Martinez, I.; Ewels, C. P.; Ke, X.; Van Tendeloo, G.; Thiess, S.; Drube, W.; Felten, A.; Pireaux, J.-J.; Ghijsen, J.; Bittencourt, C. *ACS Nano* **2010,** *4,* 1680–1686. doi:10.1021/nn9015955
7. Quintana, M.; Ke, X.; Van Tendeloo, G.; Meneghetti, M.; Bittencourt, C.; Prato, M. *ACS Nano* **2010,** *4,* 6105–6113. doi:10.1021/nn101183y
8. Muoth, M.; Helbling, T.; Durrer, L.; Lee, S. W.; Roman, C.; Hierold, C. *Nat. Nanotechnol.* **2010,** *5,* 589–592. doi:10.1038/nnano.2010.129
9. Raghuveer, M. S.; Kumar, A.; Frederick, M. J.; Louie, G. P.; Ganesan, P. G.; Ramanath, G. *Adv. Mater.* **2006,** *18,* 547–552. doi:10.1002/adma.200500181
10. Randolph, S. J.; Fowlkes, J. D.; Rack, P. D. *Crit. Rev. Solid State Mater. Sci.* **2006,** *31,* 55–89. doi:10.1080/10408430600930438
11. Huth, M.; Porrati, F.; Schwalb, C.; Winhold, M.; Sachser, R.; Dukic, M.; Adams, J.; Fantner, G. *Beilstein J. Nanotechnol.* **2012,** *3,* 597–619. doi:10.3762/bjnano.3.70
12. Van Dorp, W. F.; Hagen, C. W. *J. Appl. Phys.* **2008,** *104,* 081301. doi:10.1063/1.2977587
13. Utke, I.; Hoffmann, P.; Melngailis, J. *J. Vac. Sci. Technol., B* **2008,** *26,* 1197–1276. doi:10.1116/1.2955728
14. Utke, I.; Gölzhäuser, A. *Angew. Chem., Int. Ed.* **2010,** *49,* 9328–9330. doi:10.1002/anie.201002677
15. Wnuk, J. D.; Rosenberg, S. G.; Gorham, J. M.; Van Dorp, W. F.; Hagen, C. W.; Fairbrother, D. H. *Surf. Sci.* **2010,** *605,* 257–266. doi:10.1016/j.susc.2010.10.035
16. Botman, A.; Hesselberth, M.; Mulders, J. J. L. *Microelectron. Eng.* **2008,** *85,* 1139–1142. doi:10.1016/j.mee.2007.12.036
17. De Teresa, J. M.; Córdoba, R.; Fernández-Pacheco, A.; Montero, O.; Strichovanec, P.; Ibarra, M. R. *J. Nanomater.* **2009,** 936863. doi:10.1155/2009/936863
18. Kämpken, B.; Wulf, V.; Auner, N.; Winhold, M.; Huth, M.; Rhinow, D.; Terfort, A. *Beilstein J. Nanotechnol.* **2012,** *3,* 535–545. doi:10.3762/bjnano.3.62
19. Huth, M.; Klingenberger, D.; Grimm, C.; Porrati, F.; Sachser, R. *New J. Phys.* **2009,** *11,* 033032. doi:10.1088/1367-2630/11/3/033032
20. Porrati, F.; Sachser, R.; Strauss, M.; Andrusenko, I.; Gorelik, T.; Kolb, U.; Bayarjargal, L.; Winkler, B.; Huth, M. *Nanotechnology* **2010,** *21,* 375302. doi:10.1088/0957-4484/21/37/375302

21. Muthukumar, K.; Jeschke, H. O.; Valenti, R.; Begun, E.; Schwenk, J.; Porrati, F.; Huth, M. *Beilstein J. Nanotechnol.* **2012,** *3,* 546–555. doi:10.3762/bjnano.3.63
22. Bernau, L.; Gabureac, M.; Erni, R.; Utke, I. *Angew. Chem., Int. Ed.* **2010,** *49,* 8880–8884. doi:10.1002/anie.201004220
23. Winhold, M.; Schwalb, C. H.; Porrati, F.; Sachser, R.; Frangakis, A. S.; Kämpken, B.; Terfort, A.; Auner, N.; Huth, M. *ACS Nano* **2011,** *5,* 9675–9681. doi:10.1021/nn203134a
24. Bond, G. C. *Surf. Sci.* **1985,** *156, Part 2,* 966–981. doi:10.1016/0039-6028(85)90273-0
25. Frelink, T.; Visscher, W.; van Veen, J. A. R. *J. Electroanal. Chem.* **1995,** *382,* 65–72. doi:10.1016/0022-0728(94)03648-M
26. Yano, H.; Inukai, J.; Uchida, H.; Watanabe, M.; Babu, P. K.; Kobayashi, T.; Chung, J. H.; Oldfield, E.; Wieckowski, A. *Phys. Chem. Chem. Phys.* **2006,** *8,* 4932–4939. doi:10.1039/b610573d
27. Li, L.; Zhang, Z.; Croy, J. R.; Mostafa, S.; Cuenya, B. R.; Frenkel, A. I.; Yang, J. C. *Microsc. Microanal.* **2010,** *16* (Suppl. S2), 1192–1193. doi:10.1017/S1431927610062562
28. Hagen, C. W.; Van Dorp, W. F.; Crozier, P. A. *J. Phys.: Conf. Ser.* **2008,** *126,* 012025. doi:10.1088/1742-6596/126/1/012025
29. Silvis-Cividjian, N.; Hagen, C. W.; Kruit, P. *J. Appl. Phys.* **2005,** *98,* 084905. doi:10.1063/1.2085307
30. Serrano-Ramón, L.; Córdoba, R.; Rodríguez, L. A.; Magén, C.; Snoeck, E.; Gatel, C.; Serrano, I.; Ibarra, M. R.; De Teresa, J. M. *ACS Nano* **2011,** *5,* 7781–7787. doi:10.1021/nn201517r
31. Nikulina, E.; Idigoras, O.; Vavassori, P.; Chuvilin, A.; Berger, A. *Appl. Phys. Lett.* **2012,** *100,* 142401. doi:10.1063/1.3701153
32. Frabboni, S.; Gazzadi, G. C.; Felisari, L.; Spessot, A. *Appl. Phys. Lett.* **2006,** *88,* 213116. doi:10.1063/1.2206996
33. Botman, A.; Mulders, J. J. L.; Hagen, C. W. *Nanotechnology* **2009,** *20,* 372001. doi:10.1088/0957-4484/20/37/372001
34. Walz, M. M.; Vollnhals, F.; Rietzler, F.; Schirmer, M.; Kunzmann, A.; Steinrück, H. P.; Marbach, H. *J. Phys. D: Appl. Phys.* **2012,** *45,* 225306. doi:10.1088/0022-3727/45/22/225306
35. Plank, H.; Smith, D. A.; Haber, T.; Rack, P. D.; Hofer, F. *ACS Nano* **2012,** *6,* 286–294. doi:10.1021/nn204237h
36. Plank, H.; Gspan, C.; Dienstleder, M.; Kothleitner, G.; Hofer, F. *Nanotechnology* **2008,** *19,* 485302. doi:10.1088/0957-4484/19/48/485302
37. Yin, J.; Yagüe, J. L.; Eggenspieler, D.; Gleason, K. K.; Boyce, M. C. *Adv. Mater.* **2012,** *24,* 5441–5446. doi:10.1002/adma.201201937
38. Donev, E. U.; Schardein, G.; Wright, J. C.; Hastings, J. T. *Nanoscale* **2011,** *3,* 2709–2717. doi:10.1039/c1nr10026b
39. Kohlmann- von Platen, K. T.; Buchmann, L.-M.; Petzold, H.-C.; Brünger, W. H. *J. Vac. Sci. Technol., B* **1992,** *10,* 2690–2694. doi:10.1116/1.586027
40. Li, P. G.; Jin, A. Z.; Tang, W. H. *Phys. Status Solidi A* **2006,** *203,* 282–286. doi:10.1002/pssa.200521292
41. Botman, A.; Mulders, J. J. L.; Weemaes, R.; Mentink, S. *Nanotechnology* **2006,** *17,* 3779–3785. doi:10.1088/0957-4484/17/15/028
42. Botman, A.; Hagen, C. W.; Li, J.; Thiel, B. L.; Dunn, K. A.; Mulders, J. J. L.; Randolph, S.; Toth, M. *J. Vac. Sci. Technol., B* **2009,** *27,* 2759–2763. doi:10.1116/1.3253551
43. Porrati, F.; Sachser, R.; Schwalb, C. H.; Frangakis, A. S.; Huth, M. *J. Appl. Phys.* **2011,** *109,* 063715. doi:10.1063/1.3559773
44. Porrati, F.; Begun, E.; Winhold, M.; Schwalb, C. H.; Sachser, R.; Frangakis, A. S.; Huth, M. *Nanotechnology* **2012,** *23,* 185702. doi:10.1088/0957-4484/23/18/185702
45. Plank, H.; Kothleitner, G.; Hofer, F.; Michelitsch, S. G.; Gspan, C.; Hohenau, A.; Krenn, J. *J. Vac. Sci. Technol., B* **2010,** *29,* 051801. doi:10.1116/1.3622314
46. Yang, C.; Hazeghi, A.; Takei, K.; Hong-Yu, C.; Chan, P. C. H.; Javey, A.; Wong, H. S. P. *IEEE Trans. Electron Devices* **2012,** *59,* 12–19. doi:10.1109/TED.2011.2170216

License and Terms